THE

PHYSICAL REVIEW

VOLUME 76 Second Series NUMBER 10

NOVEMBER 15, 1949

Published for the

AMERICAN PHYSICAL SOCIETY

by the

AMERICAN INSTITUTE OF PHYSICS

LANCASTER, PA. AND NEW YORK, N. Y.

THE PHYSICAL REVIEW

A journal of experimental and theoretical physics established by E. L. Nichols in 1893

Published by the American Institute of Physics for the

AMERICAN PHYSICAL SOCIETY

Officers

President

F. W. Loomis
University of Illinois
Urbana, Illinois

Vice-President

I. I. Rabi
Columbia University
New York, New York

Secretary

K. K. Darrow
Bell Telephone Laboratories
Office:
Columbia University
New York 27, New York

Treasurer

G. B. Pegram
Columbia University
New York 27, New York

Local Secretary for the Pacific Coast

J. Kaplan
University of California at Los Angeles
Los Angeles, California

Managing Editor

John T. Tate
University of Minnesota
Minneapolis, Minnesota

BOARD OF EDITORS

Editor — John T. Tate

Assistant Editor — J. W. Buchta

Associate Editors

H. A. Bethe, L. A. Ridenour, W. H. Zachariasen, S. A. Goudsmit, E. M. Purcell, V. F. Weisskopf, W. E. Lamb, Jr., R. G. Herb, J. Bardeen

Manuscripts for publication should be submitted to John T. Tate, University of Minnesota, Minneapolis, Minnesota. The authors' institutions are requested to pay a publication charge of $4 per page which, if honored, entitles them to 100 free reprints. Instructions will be sent with galley proofs.

Proof and all correspondence concerning papers in the process of publication should be addressed to the Publication Manager, American Institute of Physics, 57 East 55 Street, New York 22, New York.

Subscription Price

United States and Canada.....$25.00
Elsewhere.....$27.00

Back Numbers[1]

Yearly back number rate when complete year is available:
Prior to 1949: $20.00
Thereafter: $27.00
Single copies: $2.00 each, prior to July, 1929;
$1.00 each, July, 1929–December, 1941;
$2.00 each, January, 1942–December, 1946;
$1.00 each, January, 1947–December, 1948.
Current issues: $1.25 each.
General index, 1893–1925: $4.00.

Subscriptions and orders for back numbers should be addressed to Prince and Lemon Streets, Lancaster, Pennsylvania, or to the American Institute of Physics, 57 East 55 Street, New York 22, New York.

Changes of address in the case of members of the American Physical Society should be addressed to the Treasurer; in the case of other subscribers to the Business Manager, American Institute of Physics.

[1] For Series I inquire of Physics Department, Cornell University, Ithaca, New York.

The Physical Review is published semi-monthly at Prince and Lemon Streets, Lancaster, Pennsylvania.

Entered as second-class matter March 6, 1917, at the Post Office at Lancaster, Pennsylvania, under the Act of March 3, 1879.

Acceptance for mailing at special rate of postage provided for in paragraph 4, section 538, P. L. & R., authorized January 27, 1933.

THE
PHYSICAL REVIEW

A journal of experimental and theoretical physics established by E. L. Nichols in 1893

SECOND SERIES, VOL. 76, NO. 10 NOVEMBER 15, 1949

Inversion Frequency of Ammonia and Molecular Interaction

H. MARGENAU
Sloane Physics Laboratory, Yale University, New Haven, Connecticut*
(Received July 18, 1949)

Several experiments on the shape and position of the inversion lines of NH_3 have indicated an effective decrease in the inversion frequency with increasing pressure of the gas. As suggested in a former paper, this is to be expected on theoretical grounds. It is here shown, first with the use of a simple linear model, that the interaction of two NH_3 molecules causes the doublet levels to change their spacing in a manner which produces *two* possible transitions of different frequencies, one smaller and one larger than the normal value. When transition probabilities are calculated it is seen that the smaller frequency gains in strength upon approach of the molecules, at the expense of the other. In Section 2 the effect of rotation upon the distortion of the levels is calculated, and Section 3 contains a schematic calculation of the interaction of three molecules. The pressure for which the reduction in the resonance frequency is experimentally observed agrees surprisingly well with the distance of separation between molecules at which the effect here calculated sets in.

SEVERAL recent investigations[1] have shown beyond doubt the existence of a pressure shift in the inversion frequency of the ammonia molecule, whose normal value is about 0.8 cm^{-1}. In view of the usefulness of this and other microwave lines for frequency stabilization[2] such an effect invites careful study. As a first step, this paper furnishes a calculation of the deformation of the energy levels of an NH_3 molecule as it approaches a like molecule. Only binary interactions are carefully considered, the general problem of simultaneous perturbations by many molecules being left unsolved. But even this simplified model sheds considerable light on the effects observed; it shows why the frequency decreases, and it produces the correct order of magnitude of the frequency shift.

The calculation is carried out for rotating, symmetric-top molecules, each carrying a dipole of moment μ along its figure axis. But to simplify things we shall first proceed with a linear model, which allows the interesting features of the problem to be seen more clearly, though less realistically. This will be done in Section 1, and it results in the following situation. Let E_1 and E_2 be the energies of the normal inversion levels of NH_3, E_1-E_2 being $h\nu_0$ for the microwave line. A system of two molecules at infinite separation has then *three* possible energies: $2E_1$, E_1+E_2, $2E_2$, and the two permitted differences between them both yield the normal E_1-E_2. But the dipole interaction between molecule at finite distances of separation causes the level $2E_1$ to be raised, while level $2E_2$ is lowered by the same amount. The intermediate level, E_1+E_2, suffers a greater downward displacement. Hence there are now 2 different permitted frequencies, one larger and one smaller than normal. Their probabilities are very sensitive functions of the intermolecular distance, and it turns out that the strength of the smaller frequency increases greatly at the expense of the larger.

In Section 2 we allow the molecules to rotate. Instead of the three states of the linear model there now appear a large number of triplets with separations depending on the intermolecular distance. Each of these triplets undergoes the kind of deformation just discussed and yields at sufficiently close approach of the molecules two frequencies, one larger and less probable, and one smaller and more probable than the normal frequency. For slight perturbations (low pressures) the results take on as first approximations the forms discussed in a previous communication.[3]

* Assisted by the ONR.

[1] B. Bleaney and J. H. N. Laubser, Nature **161**, 522 (1948); D. F. Smith, Phys. Rev. **74**, 506 (1948); I. R. Weingarten, dissertation, Columbia University, New York (1948).

[2] W. D. Hershberger and L. E. Norton, RCA Rev. **9**, 38(1948).

[3] H. Margenau, Phys. Rev. **76**, 121 (1949).

1. PERTURBATIONS IN LINEAR MODEL

Our interest is confined primarily to the behavior of the two closely spaced lowest inversion levels of NH_3 under small perturbations. Since all other levels are far away, and since rotation is at present ignored, the variational method to be employed need not include any states other than the two in question. Considered as a linear structure, the NH_3 molecule has two minima corresponding to the position of the nitrogen atom on one side or the other of the plane of the hydrogen atoms.

We recall the following facts about the double-minimum problem.[4] If $V(x)$ represents a potential function of the form drawn in Fig. 1, and $\psi(x)$ a stable state corresponding to the energy E_0, then the double-minimum problem for which the potential energy is $V(x)+V(-x)$ leads to the energies $E_0+(v-u)/(1-\delta)$ and $E_0+(v+u)/(1+\delta)$ in the first order of a suitable variational calculation. The symbols are defined as follows:

$$\delta=\int \psi_+\psi_- dx \tag{1}$$

$$u=\int V_+\psi_+\psi_- dx, \quad v=\int V_+\psi_-^2 dx \tag{2}$$

provided we write ψ_- for $\psi(-x)$, and so forth. The quantities u and v will not be needed in our work; nor shall we require the specific formulas for the two energies given above. We call them henceforth E_1 and E_2 and assume that $E_1>E_2$. The states corresponding to E_1 and E_2 are

$$\psi_1=[2(1-\delta)]^{-\frac{1}{2}}(\psi_--\psi_+), \tag{3}$$

$$\psi_2=[2(1+\delta)]^{-\frac{1}{2}}(\psi_-+\psi_+). \tag{4}$$

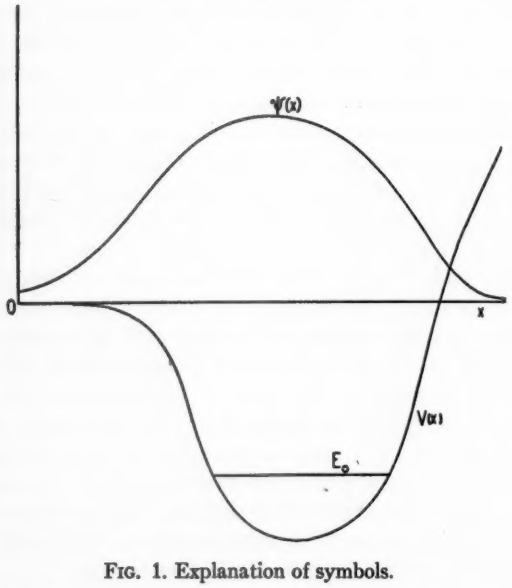

FIG. 1. Explanation of symbols.

[4] D. M. Dennison and G. E. Uhlenbeck, Phys. Rev. 41, 313 (1932).

If a second molecule is placed with its dipole along the axis of the first, a potential energy

$$U=-2q^2\frac{x_1x_2}{R^3} \tag{5}$$

is introduced. Here x_1 and x_2 are the displacements of the mean positive charges (of magnitude q) measured from the center of mass of each molecule, and R is the distance between centers.

The functions ψ_1 and ψ_2 satisfy the Schrödinger equations

$$H\psi_{1,2}=E_{1,2}\psi_{1,2}.$$

The problem is to minimize the Hamiltonian

$$\mathcal{H}(1,2)=H(1)+H(2)+U(1,2)$$

with respect to a linear combination of product functions, each containing two factors of the forms (3), (4). We are thus led to take as trial function

$$\phi=A\psi_1(1)\psi_1(2)+B\psi_2(1)\psi_2(2)+C\psi_1(1)\psi_2(2)+D\psi_2(1)\psi_1(2). \tag{6}$$

This combination will be written as $A\psi_A+B\psi_B+C\psi_C+D\psi_D$.

All diagonal elements of U between ψ_A, ψ_B etc. are zero. In fact the only non-vanishing elements are

$$U_{AB}=U_{CD}=-(2q^2/R^3)x_{12}^2 \tag{7}$$

where

$$x_{12}=\int \psi_1 x\psi_2 dx=-\frac{\bar{x}}{(1-\delta^2)^{\frac{1}{2}}}$$

in view of Eqs. (3) and (4), and

$$\bar{x}=\int x\psi_+^2 dx=-\int x\psi_-^2 dx. \tag{8}$$

One then obtains the following results for the matrix elements of H:

$$\mathcal{H}_{AA}=2E_1, \quad \mathcal{H}_{BB}=2E_2,$$
$$\mathcal{H}_{CC}=\mathcal{H}_{DD}=E_1+E_2; \quad \mathcal{H}_{AB}=\mathcal{H}_{CD}=U_{AB}.$$

All others are zero. Furthermore, the functions ψ_A to ψ_D are orthonormal. Our problem therefore reduces to the simple task of solving the determinantal equation

$$\begin{vmatrix} 2E_1-E & y & 0 & 0 \\ y & 2E_2-E & 0 & 0 \\ 0 & 0 & E_1+E_2-E & y \\ 0 & 0 & y & E_1+E_2-E \end{vmatrix}=0 \tag{9}$$

where we have used the abbreviation

$$y=-\frac{2q^2}{R^3}\cdot\frac{\bar{x}^2}{1-\delta^2}=\frac{-2\mu^2}{(1-\delta^2)R^3} \tag{10}$$

$q\bar{x}$ being the dipole moment, μ.

Now the upper block of the determinant (9) gives rise to a quadratic equation which has two solutions,

$E^{(i)}$, each belonging to a certain choice of the constants A to D which can be computed by well-known rules. With the abbreviations

$$R=\left[1+\left(\frac{y}{E_1-E_2}\right)^2\right]^{\frac{1}{2}}-1, \quad S=\frac{E_1-E_2}{y}R \tag{11}$$

the results become

$$E^{(1)}=2E_1+R(E_1-E_2);$$
$$\Phi^{(1)}=(1+S^2)^{-\frac{1}{2}}[\psi_1(1)\psi_1(2)+S\psi_2(1)\psi_2(2)],$$

$$E^{(3)}=2E_2-R(E_1-E_2);$$
$$\Phi^{(3)}=(1+S^{-2})^{-\frac{1}{2}}[\psi_1(1)\psi_1(2)-S^{-1}\psi_2(1)\psi_2(2)]. \tag{12a}$$

In similar manner, the lower block of the determinant (9) yields

$$E^{(2)}=E_1+E_2+y;$$
$$\Phi^{(2)}=2^{-\frac{1}{2}}[\psi_1(1)\psi_2(2)+\psi_2(1)\psi_1(2)],$$

$$E^{(4)}=E_1+E_2-y;$$
$$\Phi^{(4)}=2^{-\frac{1}{2}}[\psi_1(1)\psi_2(2)-\psi_2(1)\psi_1(2)]. \tag{12b}$$

All but the last of the resulting functions ϕ are symmetric with respect to an exchange of coordinates, 1, 2; hence $\Phi^{(4)}$ cannot combine with any of the other functions and will be ignored hereafter.

The intensities of possible transitions between the remaining states are proportional to the squares of the matrix elements of $X\equiv x_1+x_2$ between the various Φ's. We see at once that $\Phi^{(1)}$ and $\Phi^{(3)}$ are even in X while $\Phi^{(2)}$ is odd. Hence the only transitions permitted by the parity rule are between $E^{(1)}$ and $E^{(2)}$, and between $E^{(2)}$ and $E^{(3)}$. They correspond to the energy differences

$$\Delta_I=E^{(1)}-E^{(2)}=(E_1-E_2)[(1+\lambda^2)^{\frac{1}{2}}+\lambda] \tag{14a}$$

provided λ is written for the perturbation, y, expressed as a multiple of the normal energy difference E_1-E_2. Explicitly,

$$\lambda=\frac{|y|}{E_1-E_2}=\frac{2\mu^2}{(1-\delta^2)R^3}\Big/(E_1-E_2.) \tag{13}$$

Attention is to be called to the fact that y is negative and that we have assumed $E_1>E_2$. The other difference is

$$\Delta_{II}=E^{(2)}-E^{(3)}=(E_1-E_2)[(1+\lambda^2)^{\frac{1}{2}}-\lambda]. \tag{14b}$$

The matrix elements of X are computed with the use of $\Phi^{(1)}$, $\Phi^{(2)}$ and $\Phi^{(3)}$, which are correctly normalized as they are written above. Thus one finds

$$\left.\begin{aligned} w_I&\equiv\left|\int\Phi^{(1)}X\Phi^{(2)}dx\right|^2=2\frac{(S+1)^2}{S^2+1}x_{12}{}^2\\ w_{II}&=\left|\int\Phi^{(2)}X\Phi^{(3)}dx\right|^2=2\frac{(S-1)^2}{S^2+1}x_{12}{}^2\end{aligned}\right\}. \tag{15}$$

Except for an irrelevant factor, these are the probabilities for the transitions denoted by Δ_I and Δ_{II}. Their sum is $4x_{12}{}^2$; it is independent of the perturbation which enters through S. According to Eq. (11), S is a negative quantity because y is negative. It is clear, therefore, that w_{II} increases at the expense of w_I as the strength of the perturbation grows. This result is of course not dependent on the accident of the negative sign in Eq. (5); even if this sign were positive it would still be the *diminished* frequency whose intensity increases with the perturbation. For that reason, the rotation of the molecules which is considered in the next section can not alter this essential fact.

In Fig. 2, the frequencies Δ_I and Δ_{II} are plotted as functions of λ (see Eq. (13)); Fig. 3 shows the corresponding intensities. It is seen that the greater frequency is progressively subdued, becoming insignificant for values of λ greater than 2 or 3. The smaller frequency Δ_{II} grows more intense. An effect of this sort cannot be described accurately by available theories of pressure broadening. If, however, the formula of Van Vleck and Weisskopf[5] is used in representing the pressure-broadened line such use will require the resonance frequency to shift to smaller values at higher pressures, roughly in accord with the lower curve of Fig. 2, since λ increases with the pressure of the gas. Also, the presence of *two* frequencies with changing intensities would destroy proportionality of line widths with pressure.

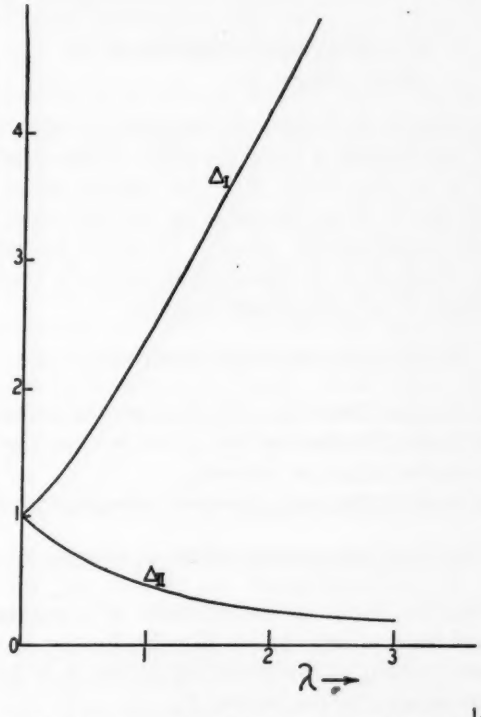

FIG. 2. Δ_I and Δ_{II} in units E_1-E_2 plotted against $\lambda=\frac{|y|}{E_1-E_2}$.

[5] J. H. Van Vleck and V. Weisskopf, Rev. Mod. Phys. **17**, 227 (1945).

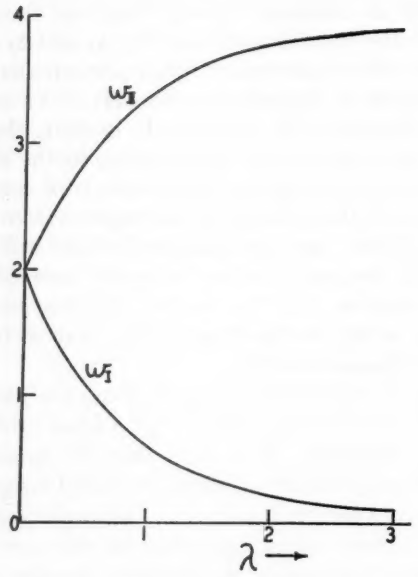

FIG. 3. Transition probabilities in units $\bar{x}^2$, plotted against the perturbation λ.

2. PERTURBATIONS IN ROTATING MOLECULES

When both molecules are allowed to rotate the Hamiltonian for the pair takes the form

$$\mathcal{H}=H_0+Q \tag{16}$$

with

$$\begin{aligned} H_0&=H_r(1)+H_r(2)+H_v(1)+H_v(2)\\ Q&=U\cdot f(\theta,\varphi). \end{aligned} \tag{17}$$

As to notation, H_r is the usual Hamiltonian for a symmetric top in terms of the Euler angles of the molecular dipole, θ, φ and χ. Next, H_v is the operator which was denoted by H in the preceding section and represents the vibrational energy. Finally, Q is the interaction energy (limited to its dipole-dipole part); it contains the former U and the angular function

$$2f=2\cos\theta_1\cos\theta_2-\sin\theta_1\sin\theta_2\cos(\varphi_1-\varphi_2). \tag{18}$$

We understand here that x_1 and x_2 are the scalar distances ordinarily denoted by r_1 and r_2, but they do take negative values on inversion.

The unperturbed state function belonging to H_0 is

$$\Phi_N(x_1x_2)\cdot\Phi_{J_1K_1M_1}(\theta_1\varphi_1\chi_1)\cdot\Phi_{J_2K_2M_2}(\theta_2\varphi_2\chi_2). \tag{19}$$

The function Φ_{JKM} is characteristic of a symmetric top, and Φ_N is a combination like (6). In view of what we have learned in the preceding section it is advantageous to take for the various Φ_N

$$\begin{aligned} \Phi_1&=\psi_1(1)\psi(2),\\ \Phi_2&=(\tfrac{1}{2})^{\frac{1}{2}}[\psi_1(1)\psi_2(2)+\psi_2(1)\psi_1(2)],\\ \Phi_3&=\psi_2(1)\psi_2(2) \end{aligned} \tag{20}$$

which limits our choice at once to symmetric functions. The index N goes from 1 to 3. With respect to (19) and (20), H_0 is diagonal; in fact

$$(NJ_1K_1M_1J_2K_2M_2|H_0|NJ_1K_1M_1J_2K_2M_2)=E_N+E_{J_1K_1}+E_{J_2K_2}$$

provided E_N is given the values $2E_1$, E_1+E_2, $2E_2$ (in terms of the notation of the previous section) as N takes on the values 1, 2, and 3. Also, E_{JK} is the energy of an unperturbed rotating top.

The perturbation Q is, of course, not diagonal. We have

$$\begin{aligned} &(NJ_1K_1M_1J_2K_2M_2|Q|N'J_1K_1M_1'J_2K_2M_2')\\ &\quad=(N|U|N')\cdot(J_1K_1M_1J_2K_2M_2|f|J_1K_1M_1'J_2K_2M_2'). \end{aligned} \tag{21}$$

The element written here is diagonal in the quantum numbers J and K of both molecules. This is the type to which consideration may be restricted for all present purposes; the energies of states with different J and K are sufficiently far away in terms of the inversion frequency to have negligible effects. But the degenerate states with different space quantum numbers M must be retained. The last factor on the right of (21) may therefore be simplified by suppressing the appearance of all J and K, and writing it $(M_1M_2|f|M_1'M_2')$.

Direct calculation of $(N|U|N')$ on the basis of Eq. (5) with the use of the functions (20) yields a simple result for the U-matrix:

$$U=-\frac{2q^2}{R^3}x_{12}^2\begin{pmatrix}0&0&1\\0&1&0\\1&0&0\end{pmatrix}. \tag{22}$$

Comparison with Eq. (10) shows that the coefficient multiplying the matrix is our former y.

We now collect results and form the matrix $\mathcal{H}$ (of Eq. (16)). In doing so it is convenient to introduce a matrix which appears in the construction of H_0, namely

$$T\equiv\begin{pmatrix}E_r+2E_1&0&0\\0&E_r+E_1+E_2&0\\0&0&E_r+2E_2\end{pmatrix}. \tag{23}$$

Then

$$\mathcal{H}=T\times(M_1M_2|1|M_1'M_2')+U\times(M_1M_2|f|M_1'M_2').$$

The crosses in this expression are used to indicate direct products.

Our interest is in the eigenvalues of $\mathcal{H}$, for they are the perturbed energies we are seeking. The problem is, then, to diagonalize $\mathcal{H}$, and this is done by diagonalizing each of the factors in the direct products. As is well known, it is possible to find a transformation that will render $(M_1M_2|f|M_1'M_2')$ diagonal and yet leave $(M_1M_2|1|M_1'M_2')$ a unit matrix. After this trans-

formation, $\mathcal{H}$ will have the form

$$\begin{vmatrix} T & & & & \\ & T & 0 & & \\ & & T & & \\ & & & \cdot & \\ & & & & \cdot \\ 0 & & & & \cdot \end{vmatrix} + \begin{vmatrix} f_1U & & & & \\ & f_2U & & & \\ & & f_3U & & 0 \\ & & & \cdot & \\ & & & & \cdot \\ 0 & & & & \cdot \end{vmatrix}$$

in which the f_i are the diagonal elements of $(M_1M_2|f|M_1'M_2')$. The two remaining matrices can of course be added to form a single one which consists of diagonal blocks, and each diagonal block is a three-square matrix of the simple form $T+f_iU$, where T and U are given by Eqs. (23) and (22).

The problem is now reduced to finding the eigenvalues of

$$T+f_iU=\begin{vmatrix} E_r+2E_1 & 0 & f_iy \\ 0 & E_r+E_1+E_2+f_iy & 0 \\ f_iy & 0 & E_r+2E_2 \end{vmatrix}.$$

Here it is well to put $\epsilon=E-(E_1+E_2)-E_r$, that is, ϵ equals the difference between the perturbed energy E—which is the eigenvalue of the above matrix—and the *intermediate* of our three unperturbed levels. We must then solve

$$\begin{vmatrix} E_1-E_2-\epsilon & 0 & f_iy \\ 0 & f_iy-\epsilon & 0 \\ f_iy & 0 & -(E_1-E_2)-\epsilon \end{vmatrix}=0.$$

The roots are

$$\begin{aligned} \epsilon_i^{(1)}&=[(E_1-E_2)^2+f_i^2y^2]^{\frac{1}{2}}=(E_1-E_2)(R_i+1),\\ \epsilon_i^{(2)}&=f_iy\\ \epsilon_i^{(3)}&=-[(E_1-E_2)^2+f_i^2y^2]^{\frac{1}{2}}=-(E_1-E_2)(R_i+1). \end{aligned} \quad (24)$$

These are in exact agreement with our former results, Eqs. (12), provided we define R_i (formerly given by Eq. (11)) as

$$R_i=\left[1+\left(\frac{f_iy}{E_1-E_2}\right)^2\right]^{\frac{1}{2}}-1$$

and ignore E_r. Equation (24) represents the eigenvalues of $\mathcal{H}$ associated with the ith block of that matrix. *In toto*, then, there will be as many sets of solutions of the form (24) as there are eigenvalues f_i, and their number is $(2J_1+1)(2J_2+1)$. Hence, there are altogether $3(2J_1+1)(2J_2+1)$ perturbed levels.

It is seen that the rotation of the molecules has modified the results of Section 1 only in the following way. Where previously we had two possible transitions, one diminished and one enlarged in frequency, we now have $(2J_1+1)(2J_2+1)$ diminished, and an equal number of enlarged, transitions. Each of these obeys a formula like (14a), (14b), but the perturbation λ is multiplied by a factor f_i. And similarly, the transition probabilities can be computed from Eqs. (15) with substitution of $f_i\lambda$ for λ in S.

As to the f_i, one may see from the definition of f in Eq. (18) that their absolute values cannot be greater than 1. In consequence, the average distortion of the levels will be somewhat smaller than was computed in Section 1, and the effect under consideration will be spread over a considerable frequency range. The values of the f_i can be found only by solving a complicated set of secular equations, no short-cuts being available. The elements $(M_1M_2|f|M_1'M_2')$ are known,[6] and the mean square of the f_i has been calculated.[6] Their arithmetic mean is zero. Typical distributions are also given in the paper cited. But it is hardly worth while to pursue these details further since the model of interacting pairs here treated can not explain the quantitative features of the pressure-broadening problem in any case.

A glance at Eqs. (24) shows that the distortion of the levels $\epsilon^{(1)}$ and $\epsilon^{(3)}$ is quadratic in the perturbation f_iy (or $f_i\lambda$) for small interactions, but the distortion of the intermediate levels $\epsilon^{(2)}$ is linear. For $f_i\lambda\ll 1$; therefore, the upper and lower levels may be regarded as fixed while the middle one is displaced. The two inversion frequencies are then changed by $\pm f_iy$. This is precisely the effect discussed in a recent publication on the self-broadening of the doublet lines at small pressures.[3] One minor modification resulting from the calculation of this paper is occasioned by the appearance of δ^2 in the formula for y (Eq. (10)). But for plausible models of the ammonia molecule $\delta\ll 1$ (see Eq. (1)), and δ^2 may be neglected.

3. THREE MOLECULES

As further illustration of the level distortion we treat briefly the problem of three interacting molecules, excluding rotation. Here again, the conclusions stated at the end of Section 1 will be forced upon us, though in a slightly more elaborate form. To obtain simple answers the arrangement of the three dipoles is assumed to be one of maximum symmetry: each is placed at one corner of an equilateral triangle of side length R, and it extends parallel to the opposite face. This arrangement insures that the Hamiltonian of the problem is symmetric in the x-coordinates of all vibrators and causes the states of the system to have clean symmetries in these variables. The potential energy of this arrangement is

$$U=-(5/4)(q^2/R^3)(x_1x_2+x_1x_3+x_2x_3).$$

Restricting our consideration at once to symmetric functions, we select the variation functions (unnormalized)

$$\begin{aligned} \psi_A&=\psi_1(1)\psi_1(2)\psi_1(3)\equiv 111, & E_A&=3E_1\\ \psi_B&=112+121+211, & E_B&=2E_1+E_2\\ \psi_C&=122+212+221, & E_C&=E_1+2E_2\\ \psi_D&=222 & E_D&=3E_2. \end{aligned}$$

[6] H. Margenau and D. T. Warren, Phys. Rev. **51**, 748 (1937). The present f is the quantity there denoted by V, times $R^3/2\mu^3$.

The zero-order energies corresponding to the functions are also given in the list above. Between these functions, the matrix (U) has the form

$$(U)=\begin{bmatrix}0 & 0 & 3z & 0\\ 0 & 6z & 0 & 3z\\ 3z & 0 & 6z & 0\\ 0 & 3z & 0 & 0\end{bmatrix}$$

where z is the analog of our former y:

$$z=\frac{-5}{4(1-\delta^2)}\frac{\mu^2}{R^3}.$$

This is to be compared with Eq. (10). The determinantal equation reads

$$\begin{vmatrix}3E_1-E & 0 & 3z & 0\\ 0 & 2E_1+E_2+2z-E & 0 & z\\ z & 0 & E_1+2E_2+2z-E & 0\\ 0 & 3z & 0 & 3E-E\end{vmatrix}=0. \quad (25)$$

In constructing it, one must remember that the factor $(B|1|B)$, which multiplies E, is 3; it has been divided out in the determinant above.

The four roots $E^{(i)}$ of Eq. (25), together with the normalized functions belonging to them are as follows:

$$E^{(1)}=3E_1+\eta_1(E_1-E_2)$$

$$\Phi^{(1)}=\left(1+\frac{\eta_1^2}{3\lambda^2}\right)^{-\frac{1}{2}}\left[\psi_A+\frac{\eta_1}{3\lambda}\psi_C\right],$$

$$E^{(2)}=3E_2+\eta_2(E_1-E_2)$$

$$\Phi^{(2)}=\left(1+\frac{\eta_2^2}{3\lambda^2}\right)^{-\frac{1}{2}}\left[\frac{\eta_2}{3\lambda}\psi_B+\psi_D\right],$$

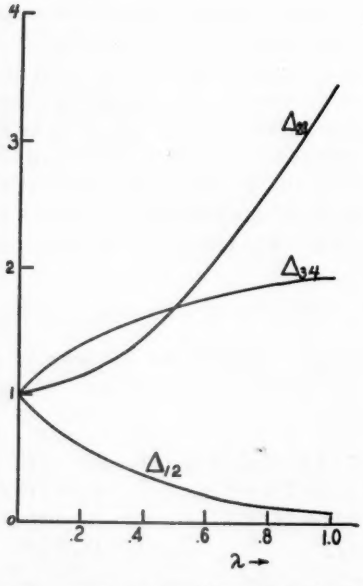

FIG. 4. Frequencies of transitions, in units E_1-E_2, as functions of λ (Eq. (26)).

$$E^{(3)}=3E_1+\eta_3(E_1-E_2)$$

$$\Phi^{(3)}=\left(1+\frac{\eta_3^2}{3\lambda^2}\right)^{-\frac{1}{2}}\left[\psi_A+\frac{\eta_3}{3\lambda}\psi_C\right],$$

$$E^{(4)}=3E_2+\eta_4(E_1-E_2)$$

$$\Phi^{(4)}=\left(1+\frac{\eta_4^2}{3\lambda^2}\right)^{-\frac{1}{2}}\left[\frac{\eta_4}{3\lambda}\psi_B+\psi_D\right].$$

where the parameters are:

$$\lambda=z/(E_1-E_2)$$
$$\eta_1=[(1-\lambda)^2+3\lambda^2]^{\frac{1}{2}}-(1-\lambda)$$
$$\eta_2=[(1+\lambda)^2+3\lambda^2]^{\frac{1}{2}}+(1+\lambda)$$
$$\eta_3=-[(1-\lambda)^2+3\lambda^2]^{\frac{1}{2}}-(1-\lambda)$$
$$\eta_4=-[(1+\lambda)^2+3\lambda^2]^{\frac{1}{2}}+(1+\lambda).$$

Finally, we need the matrix elements of $X=x_1+x_2+x_3$ between the states $\Phi^{(1)}$ to $\Phi^{(4)}$ and the corresponding energy differences. The results are as follows:

$$X_{12}^2=\frac{(\lambda\eta_1+\lambda\eta_2+\frac{2}{3}\eta_1\eta_2)^2}{(\lambda^2+\frac{1}{3}\eta_1^2)(\lambda^2+\frac{1}{3}\eta_2^2)}\bar{x}^2,\quad \Delta_{12}=(3+\eta_1-\eta_2)(E_1-E_2),$$

$$X_{14}^2=\frac{(\lambda\eta_1+\lambda\eta_4+\frac{2}{3}\eta_1\eta_4)^2}{(\lambda^2+\frac{1}{3}\eta_1^2)(\lambda^2+\frac{1}{3}\eta_4^2)}\bar{x}^2,\quad \Delta_{14}=(3+\eta_1-\eta_4)(E_1-E_2),$$

$$X_{23}^2=\frac{(\lambda\eta_2+\lambda\eta_3+\frac{2}{3}\eta_2\eta_3)^2}{(\lambda^2+\frac{1}{3}\eta_2^2)(\lambda^2+\frac{1}{3}\eta_3^2)}\bar{x}^2,\quad \Delta_{23}=(-3+\eta_2-\eta_3)(E_1-E_2),$$

$$X_{34}^2=\frac{(\lambda\eta_3+\lambda\eta_4+\frac{2}{3}\eta_3\eta_4)^2}{(\lambda^2+\frac{1}{3}\eta_3^2)(\lambda^2+\frac{1}{3}\eta_4^2)}\bar{x}^2,\quad \Delta_{34}=(3+\eta_3-\eta_4)(E_1-E_2).$$

Subscripts in this table refer to the functions $\Phi^{(i)}$ listed above and elements not written are zero. Inspection shows that all Δ's except Δ_{14} have the value E_1-E_2 for vanishing perturbation λ, Δ_{14} being 3 times as large. But it will also be noticed that x_{14}^2 is zero for $\lambda=0$ and gains strength only under large perturbations.

Figure 4 shows the behavior of the three significant frequencies as the perturbation increases.[7] Two of the frequencies now increase while only one diminishes with growing λ. Figure 5, however, adds the important information that both increasing frequencies rapidly lose their intensities; indeed at $\lambda=1$, i.e., when the perturbation is equal to the inversion energy, only 15 percent of the total absorption intensity resides within the more energetic transitions. This agrees numerically with our result for the interaction of two molecules, as an examination of Fig. 3 will reveal. But the condition $\lambda=1$ implies a smaller intermolecular distance for 3 molecules than for two. Finally, we note on inspecting Fig. 4 that the dominant frequency contracts more

[7] The anomalous frequency Δ_{14} is not shown in Fig. 4, nor is x_{14}^2 plotted in Fig. 5. This transition probability is so small that it would barely appear on the scale here chosen. For practical purposes it may be ignored.

rapidly with increasing λ in the case of 3 molecules than in the case of two.

On surveying these results the simple model of Section 2 is seen to suffer from two principal faults whose corrections tend in a sense to annul each other. Rotation of the molecules spreads the frequencies, but reduces their distortions; multiple interactions at the same mean distance R increase the distortion, as the present calculation for three molecules indicates. For rough comparison with experiments one is therefore disposed to look with some favor upon the simple results of Section 2.

4. COMPARISON WITH EXPERIMENTS

The bearing upon available experimental data of the schematic theory here presented is semiquantitative at best. Theory does show quite definitely, however, that the frequency of the "ammonia clock" is strongly pressure dependent when the dipole perturbations between the molecules are comparable with the inversion energy. For small pressures, an estimate of the frequency change can be made in the following way.

Taking the results of Section 2 as typical, we easily find the mean frequency, $\bar{\nu}$, of the absorption line ($h\bar{\nu}=w_I\Delta_I+w_{II}\Delta_{II}$) to be $\nu_0(1-\lambda^2)$ for $\lambda\ll 1$. The choice of the intensity-weighted mean as representative of the resonance frequency is indeed arbitrary; it seems to the author for various reasons to be a reasonable measure at very low pressures. Now

$$\lambda=\frac{2\mu^2}{(E_1-E_2)R^3}\approx\frac{2\mu^2 n}{E_1-E_2}$$

if n is the number of molecules per cc. Remembering that $E_1-E_2\approx 0.8$ cm^{-1} and $\mu=1.44\times10^{-18}$ e.s.u. one finds (for a temperature of 0°C)

$$\lambda\approx 0.6p$$

where p is the pressure of the ammonia vapor in atmospheres. Hence the formula

$$\bar{\nu}\approx\nu_0(1-0.36p^2)$$

should give the resonance frequency at small pressures.

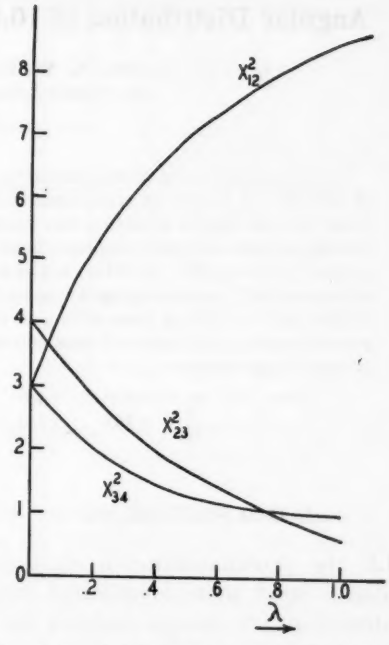

FIG. 5. Transition probabilities in units x^{-2}, plotted against λ.

The *dominant* frequency, computed in the same way, follows the relation

$$\nu_{II}=\nu_0(1-0.6p)$$

at very low pressures.

At one atmosphere, then, $\lambda\approx 0.6$. Figure 3 yields for this perturbation a dominant frequency of 0.44 cm^{-1} whereas the experimental data,[2] interpreted with the use of impact theory,[5] require about 0.5 cm^{-1}. Up to this pressure, then, agreement is excellent.

At still higher pressures the agreement becomes poor. For instance, the resonance frequency computed by Bleaney and Laubser from experimental data drops practically to zero at a pressure of two atmospheres (which is of course embarrassing to the premises on which it was computed), whereas the smaller Δ_{II} in Fig. 2 is down only to 0.29 cm^{-1}. One may take this as evidence that at higher pressures the multiple interactions which, as we have seen, accentuate the frequency reduction, become progressively important.

Angular Distribution of 10.8 Mev Deuterons Scattered by Deuterons*

J. C. ALLRED, K. W. ERICKSON, J. L. FOWLER, AND E. J. STOVALL, JR.
Los Alamos Scientific Laboratory, Los Alamos, New Mexico

(Received July 21, 1949)

Cross sections for the elastic scattering of deuterons by deuterons have been measured for incident energy of 10.8 Mev at laboratory angles from 17.5 degrees to 57 degrees at 2.5 degree intervals. The deuteron beam from the Los Alamos cyclotron was focused on a thin gas target containing deuterium, and the scattered deuterons were detected in a proportional counter. A selsyn-controlled foil shutter mounted in front of the counter prevented He^3, and H^3 at angles greater than 40 degrees, from entering the counter. H^1, and H^3 at the smaller angles, were discriminated against by using a ten-channel pulse amplitude analyzer. Typical values of the elastic scattering cross section at 10.8 Mev, in barns per unit solid angle, are given in the table for several angles in the center of mass system. The experimental curve is symmetrical about 90 degrees in the center of mass system.

θ	35°	40°	50°	60°	70°	80°	90°
σ	0.283	0.235	0.158	0.127	0.109	0.099	0.094

I. D–D SCATTERING

WHILE the deuteron-deuteron scattering interaction is much more complicated than a two-particle interaction, few enough nucleons are involved to make data pertaining to this reaction of value to the development of a nuclear force theory. This is made especially true by the recent advances in modern computing methods.

The differential d–d scattering cross section is fairly well known for bombarding energies below 3.5 Mev,[1,2] and relative values have been obtained at 7 Mev.[3] The results of the measurements given here have been given in an abstract at the Seattle Meeting of the American Physical Society.[4]

II. EXPERIMENT AND RESULTS

The present scattering study was carried out with the 10 Mev deuteron beam from the Los Alamos cyclotron focused into a reaction chamber about 15 feet away from the cyclotron. A proportional counter, mounted so as to rotate to any angle in the horizontal plane, detected the particles produced in a thin gas target mounted in the center of the reaction chamber. The general instrumentation has been discussed in a previous report.[5] For this experiment, however, the gas target has been redesigned so that it is $7\frac{1}{2}$ inches long with a $\frac{9}{16}$-inch$\times 3\frac{1}{2}$-inch Nylon window in each side of the target, through which reaction particles were counted from 17.5 degrees to 57.5 degrees to the direction of the beam in the laboratory system. Besides having the beam collimated to ± 0.6 degree by slits and anti-scattering diaphragms as it enters the $\frac{3}{16}$-inch diameter 2.5-mil Nylon entrance window of the gas target, there was included inside the target $1\frac{1}{32}$ inches behind this Nylon window an anti-scattering diaphragm to remove the deuterons scattered by the front window. A more detailed discussion of this target is soon to be published.[6] On the support of the proportional counter[5] there was mounted a vertical slit adjustable to either $\frac{1}{16}$-inch or $\frac{1}{8}$-inch width to define the beam of scattered deuterons which are detected by the counter. The reaction volume was defined by this slit and the $\frac{1}{8}$-inch diameter hole immediately in front of the proportional counter. Anti-scattering diaphragms between the slits and counter aperture removed deuterons scattered from the slit support. The beam current was measured with a Faraday cage. The accuracy of this measurement has been previously checked.[7] Immediately in front of the proportional counter was mounted a selsyn controlled foil shutter with which 100 combinations of absorbers could be selected.

Before and after the experiment, the position of the beam relative to the counter window was determined by scanning the beam with the counter used as an ionization chamber. The position of the beam had remained constant to 0.1 degree.

The procedure for taking the data was essentially the same as that described in a previous report.[7] For scattered deuterons the absorber foils in front of the counter were adjusted with consideration for the range of triton groups which are produced by the $D(d,p)H^3$ reaction. At angles beyond 40 degrees, the triton group was generally excluded by the absorber foils; near 20 degrees, however, where the range of tritons approaches the range of scattered deuterons, the foils were adjusted so that the tritons' range ended just beyond the counter. The pressure of the counter was such that the air equivalent of the path of particles in the counter was about 10 cm. The amplified pulses from the counter

* This document is based on work performed at Los Alamos Scientific Laboratory of the University of California under Government Contract W-7405-eng-36.

[1] N. P. Heydenburg and R. B. Roberts, Phys. Rev. **56**, 1092 (1939).
[2] W. Sleator, Jr. and J. H. Williams, Phys. Rev. **74**, 1594 (1948).
[3] Guggenheimer, Heitler, and Powell, Proc. Roy. Soc. A **190**, 196 (1947).
[4] Stovall, Allred, Erickson, and Fowler, Phys. Rev. **76**, 589 (1949).
[5] Curtis, Fowler, and Rosen, Rev. Sci. Inst. **20**, 388 (1949).
[6] K. W. Erickson, Rev. Sci. Inst. (to be published).
[7] Erickson, Fowler, and Stovall, Phys. Rev. **76**, 1141 (1949).

were analyzed by means of a ten channel amplitude discriminator. Figure 1 gives a sample deuteron peak obtained. The abscissa gives the amplified pulse height. The ordinate gives the number of pulses per two-volt interval having the magnitude given as the abscissa. Since the tritons were near the end of their range when they entered the counter, the energy lost by them in the counter is higher than that due to the scattered deuterons. Therefore, the peak from the triton group lies above that of the deuteron group. From the known thickness of absorbers in front of the counter, and from the range energy curve of deuterons and tritons, one calculates the expected position of the triton peak relative to the deuteron peak. For almost all of the curves obtained the calculated position and the observed position agreed well. In a few cases, however, where the triton group ended part of the way through the counter, uncertainties in the thickness of absorbers used caused large variations in the ionization due to the triton peak. In such cases where the triton peak was not resolved, the triton pulses were counted in with the deuteron peaks and the resulting data was later corrected for the triton contribution, by use of the measured $D(d,p)H^3$ cross section.

The curve indicated by the crosses was obtained by adjusting the absorbers to stop the deuterons before they entered the counter. This gives the counter background. Since the absorbers were adjusted by remote control while the cyclotron beam was held constant, and since the background run was taken immediately after the peak run, the shift in background due to changing beam conditions was minimized. For the conditions used in this experiment, the background under the peak was, on the average, 8.3 percent of the peak counts. A number of checks were tried to test the validity of the background corrections. For pairs of runs at certain angles, the pressure of deuterium gas in the target was changed by as much as a factor of two. Although the background relative to peak varied by a factor of two, the cross section obtained from the data was the same to within the reproducibility of the measurements (the order of 2.5 percent). In another test, runs were made at certain angles in which the thickness of absorber in the path of the scattered deuterons was decreased from 27-cm air equivalent to 17-cm air equivalent. Under these conditions the number of counts in the peak remained constant to about two percent.

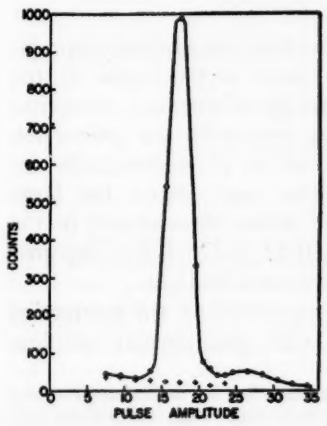

FIG. 1. Distribution of pulses from proportional counter due to deuterons scattered at 32.5 degrees. The crosses represent the background obtained by stopping the deuterons before they reach the counter.

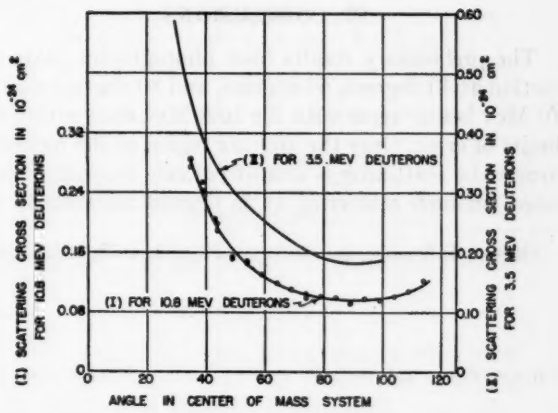
(I) FOR 3.5 MEV DEUTERONS
(I) FOR 10.8 MEV DEUTERONS
(I) SCATTERING CROSS SECTION IN FOR 10.8 MEV DEUTERONS
(II) SCATTERING CROSS SECTION IN FOR 3.5 MEV DEUTERONS
ANGLE IN CENTER OF MASS SYSTEM

FIG. 2. Differential cross section for deuteron scattering in the center of mass system.

Immediately after each run, the energy of the deuteron beam was determined by magnetic deflection.[5] During the course of the experiment the beam energy varied by ± 2.8 percent, but all the data was corrected to the average energy. For this correction, the rate of change of cross section with energy was estimated from interpolation between data from low energy[2] and the present data. Since the maximum correction for energy was only 2.5 percent, this procedure introduced a negligible error.

Figure 2 is a plot of the differential cross section in the center of mass system as a function of center of mass angle. The root mean square deviation of the points from the smooth curve is ± 2.5 percent. This is about the spread expected from the consideration of the statistical error, the variation of the beam position, the random error in current determination, and uncertainty in measuring the background. Systematic errors, such as errors in aligning the slits, measuring distances, and absolute current measurements, amount to 2.5 percent. Combining this error with the random error of the points, we estimate the curve in Fig. 2 is good to ± 3.5 percent.

The curve through the points is accurately symmetrical about 90 degrees, which is a further check of consistency of the data. The points designated by solid circles were obtained by opening the first defining slit for the scattered deuterons from $\frac{1}{16}$-inch to $\frac{1}{8}$-inch wide. The fact that the points so obtained lie on the smooth curve through the previous points is a check on the reliability of the slit measurements. The latter points also indicate that a decrease of the angular resolution of the counter system by 33 percent has no observable effect on the data even in the steep region of the curve.

III. CONCLUSIONS

The preliminary results from photographic plate detection at 40 degrees, 60 degrees, and 80 degrees using a 10 Mev beam[8] agree with the 10.8 Mev data within the limits of error. Over the angular region of the measurements the scattering is almost entirely nuclear. Calculated coulomb scattering at 35 degrees amounts to 4.7 percent of the total differential scattering cross section for 10.8 Mev. For comparison the d–d scattering at 3.5 Mev is included in Fig. 2.[2] The differential cross section is somewhat lower for the higher energy data; at 90 degrees the ratio of the cross section at 10.8 Mev to that at 3.5 Mev is 0.523. For 10.8 Mev scattering the cross section remains more nearly constant over a wider angular region near 90 degrees than for 3.5 Mev scattering.

[8] Rosen, Tallmadge, and Williams, Phys. Rev. **75**, 1632 (1949).

PHYSICAL REVIEW VOLUME 76, NUMBER 10 NOVEMBER 15, 1949

On the Production of π-Mesons by Nucleon-Nucleon Collisions

CECILE MORETTE*
The Institute for Advanced Study, Princeton, New Jersey
(Received June 27, 1949)

Besides the doubts concerning the actual meson theories, and the use of a perturbation method for the study of strongly coupled fields, doubts have been raised as to the validity of some approximations usually made in the computation of the cross section for meson production by nucleon-nucleon collision. This cross section is computed here in a relativistically invariant manner for the pseudoscalar meson (pseudoscalar coupling) with the charged and the charge symmetrical theory. The results are valid for all energies of the incoming particle. The energy distribution and the total cross section derived from the invariant statistical factors are given as a point of comparison. Some computational tools are presented: a projection and a permutation operator and a method for the calculation of the density of states. In the Appendix two different ways of considering the meson production (mesonic analog to the bremsstrahlung or third-order process) are discussed.

THE problem of the production of mesons has interest for the origin of mesons in cosmic rays and for the artificial production of mesons. Many papers have been published on the production of mesons by collision between nucleons.[1–9] In the actual state of the theory, there exists no satisfactory method to compute the cross sections for the production of mesons:

(1) The equation of propagation of the meson field and the form of the interaction between the nucleon field and the meson field are not known.

(2) The perturbation method is not adapted to the study of strongly coupled fields. Attempts to circumvent the inadequacy of the perturbation method for problems involving mesons have not yielded entirely reliable methods. In the absence of an invariant relativistic method which gives the solution to radiative scattering problems without making an expansion in terms of powers of the coupling constant, the study of the multiplicity of the mesons produced in each collision is not really possible.

Besides these basic difficulties, illegitimate approximations have often been made in the course of the calculations. Taking advantage of the new computational techniques, the cross section for the production of a meson is computed here in a relativistically invariant manner. Hence, the result shares the large uncertainty of the present meson theories and of the use of the perturbation method, but it is not impaired by undue and unnecessary approximations.

We compute here the cross section for the production of a pseudoscalar meson with pseudoscalar coupling

* Chargée de recherches au Centre National de la Recherche Scientifique, Paris (now on leave of absence).

[1] L. W. Nordheim and G. Nordheim, Phys. Rev. **54**, 254 (1938). E. Strick, Phys. Rev. **76**, 190 (1949). (Scalar mesons—Born approximation.)

[2] H. S. W. Massey and H. C. Corben, Proc. Camb. Phil. Soc. **35**, 84 (1939). (Vector mesons. Born approximation—non-relativistic approximation. Mesonic analog to bremsstrahlung, see Appendix.)

[3] W. Heitler and H. W. Peng, Proc. Roy. Irish. Acad. **49** A 101 (1943). W. Heitler, Proc. Roy. Irish Acad. **50** A 155 (1945). (Møller and Rosenfeld mixture—Weizsäcker-Williams method—damping theory—extreme relativistic approximation.)

[4] Cécile Morette, Thèse de Doctorat, Paris (1947). (Møller and Rosenfeld mixture—damping theory—non-relativistic approximation—mesonic analog to the bremsstrahlung, see Appendix.)

[5] Cécile Morette and H. W. Peng, Nature **160**, 59 (1947) and Proc. Roy. Irish Acad. **51A** 217 (1948). (Møller and Rosenfeld mixture — damping theory — non-relativistic approximation — third-order process, see Appendix.)

[6] W. G. McMillan and E. Teller, Phys. Rev. **72**, 1 (1947). (Influence of the binding of the nucleons in a nucleus and corrections due to the electromagnetic interactions.)

[7] W. Horning and R. Weinstein, Phys. Rev. **72**, 251 (1947). (Scalar mesons. Born approximation—third-order process, see Appendix.)

[8] Lewis, Oppenheimer and Wouthuysen, Phys. Rev. **73**, 127 (1948). (Multiple meson production.)

[9] L. L. Foldy and R. E. Marshak, Phys. Rev. **75**, 1493 (1949). (Pseudoscalar mesons—pseudovector coupling. Born approximation non-relativistic region, mesonic analog to the bremsstrahlung, see Appendix.) The lists in references 1–9 are not exhaustive, and the notes between brackets are only very rough indications.

between the meson field and the nucleon field. The transitions from a state where two nucleons are present to a state where two nucleons and one meson are present can be represented by the following diagrams (Fig. 1). A full line is the world line of a nucleon; a dotted line is the world line of a meson. The q's and the k's and their combinations are the four-wave vectors of the wave function of the corresponding particle.

According to Dyson[10] and Feynman,[11] the collision operator $\mathbf{O}$, which transforms the wave function of the system in the initial state $\Psi(-\infty)$ to the wave function of the system in the final state $\Psi(\infty)$, is obtained by the following prescription:

Replace each intermediate (or virtual) nucleon and meson line by the inverse of the operator of its equation of motion. Replace each vertex by the Hamiltonian of interaction. The cross section is given by the following relation:

$$\sigma=|\mathbf{O}|^2 1/[\varphi \text{ (initial state)}]\rho \text{ (final states)}, \quad (1)$$

where φ is the flux of the particles in the incident beam, and ρ is the density of the final states.

Natural units will be chosen so that $\hbar=c=1$ and the following notation[12] will be used:

$$\Psi(-\infty)=\Psi(p_0^1,p_0^2),$$
$$\Psi(+\infty)=\Psi(p^1,p^2,k).$$

Hence

$$q_0=p_0^1 \text{ or } p_0^2, \qquad q'_0=p_0^2 \text{ or } p_0^1,$$
$$q=p^1 \text{ or } p^2, \qquad q'=p^2 \text{ or } p^1.$$

p_0^1 is a four vector whose components are $E_0^1=(|\mathfrak{p}_0^1|^2+M^2)^{\frac{1}{2}}$ and $\mathfrak{p}_0^1$. k is a four vector whose components are $\epsilon=(|\mathfrak{k}|^2+\mu^2)^{\frac{1}{2}}$ and $\mathfrak{k}$. The functions φ and ρ in a covariant representation[13] are

$$\varphi(p_0^1,p_0^2)=(\tfrac{1}{2}(p_0^1\times p_0^2)\cdot(p_0^1\times p_0^2))^{\frac{1}{2}} \quad (2)$$

$$\rho(p^1,p^2,k)=\frac{dp^1}{(2\pi)^4}\frac{dp^2}{(2\pi)^4}\frac{dk}{(2\pi)^4}2M2\pi\delta[(p^1)^2-M^2]$$
$$\times 2M2\pi\delta[(p^2)^2-M^2]2\pi\delta[k^2-\mu^2]$$
$$\times(2\pi)^4\delta(p_0^1+p_0^2-p^1-p^2-k). \quad (3)$$

The equations of motion of the field operators are:

$$\text{meson field } (\Box^2-\mu^2)\phi=0,$$

$$\text{nucleon field } (i\nabla-M)\psi=0,$$

$$\nabla=\sum_\mu \gamma_\mu\frac{\partial}{\partial x\mu} \qquad \mathbf{p}=\sum_\mu \gamma_\mu p_\mu, \quad \mathbf{k}=\sum_\mu \gamma_\mu k_\mu,$$

$$a_\mu b_\mu=a_4b_4-\sum_{i=1}^{3} a_ib_i=a\cdot b,$$

$$\gamma_4=\beta=\rho_3,$$

$$\gamma_i=\beta\alpha_i=\rho_1\sigma_i,$$

where β, ρ_1, ρ_3, α_i, and σ_i are the usual Dirac matrices.

$$\bar{\psi}=\psi^*\gamma_4,$$

where ψ^* means the complex conjugate transposed of ψ and $\bar{\psi}$ the adjoint of ψ. The Hamiltonian of pseudoscalar interaction between the nucleon field and the pseudoscalar meson field is

$$H=if\bar{\psi}\gamma_5\tau_c\psi\phi_c.$$

The expression which is to be associated with each vertex of the diagram is simply $if\gamma_5\tau_c$.

$$\gamma_5=\gamma_1\gamma_2\gamma_3\gamma_4,$$

f is the coupling constant, and τ_c are the charge operators. We shall use the charge operators in the representation best suited when one is interested in the charge of the particles.

This representation, in which the charge density is diagonal, is determined by the condition

$$\tau_c\psi_{\mathfrak{N}}=\text{const. }\psi_{\mathfrak{N}}.$$

The index $\mathfrak{N}$ stands for neutron or proton.

$$\tau_c=A_{c\nu}\tau_\nu,$$

where the τ's printed in boldface are the Pauli matrices and A is

c \ ν	1	2	3
+	$\frac{1}{\sqrt{2}}$	$\frac{-i}{\sqrt{2}}$	0
−	$\frac{1}{\sqrt{2}}$	$\frac{i}{\sqrt{2}}$	0
0	0	0	1

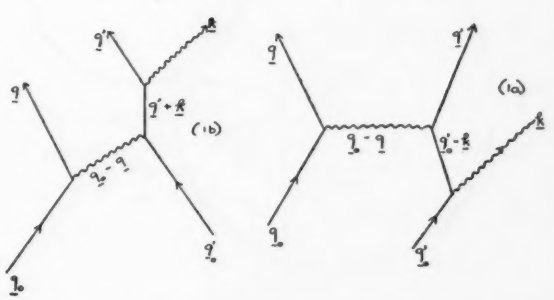

FIG. 1. Diagrams representing meson production by nuclear collision.

[10] F. J. Dyson, Phys. Rev. **75**, 486 (1949).
[11] R. P. Feynman, Phys. Rev. **76**, 769 (1949). We are indebted to Professor Feynman for his most illuminating lectures.
[12] Here is summarized the meaning of the various printings of the vectors: p (italics) is a four vector, $\mathbf{p}$ (boldface) is a matrix, $\mathfrak{p}$ (German type) is a three-vector (momentum); so that $p^2=E^2-\mathfrak{p}^2$ (German type). The lower indices refer to the components of the vector; the upper indices refer to the particles. The primes indicate that the quantity is considered in the laboratory system.
[13] C. Møller, Det. Kgl. Danske Vid. Sels. Math.-Fys. Medd., Bind XXIII, Nr. 1 (1945).

c=+ or − in the charged theory, and c=+, −, or 0 in the charged symmetrical theory. By convention $\tau_+=\tau_-^*$ will be the operator for the emission of a positive meson. The following relations will be used throughout the calculation

$$\tau_{c'}^*\tau_c+\tau_c\tau_{c'}^*=2\delta_{cc'}$$

$$\left(\sum_c \tau_c^{*(1)}\tau_c^{(2)}\right)\tau_{c'}^{(1)}+\tau_{c'}^{(1)}\left(\sum_c \tau_c^{*(1)}\tau_c^{(2)}\right)=2\tau_{c'}^{(2)}. \quad (4)$$

The upper index refers to one or the other particle.

With this notation the operator 0 is:

$$0=-if^3\bar{\psi}(q_0)\gamma_5\tau_{c'}^*\psi(q)\frac{1}{(q_0-q)^2-\mu^2}\bar{\psi}(q_0')$$
$$\times\left\{\gamma_5\tau_{c'}\frac{1}{(\mathbf{q}'+\mathbf{k})-\mathbf{M}}\gamma_5\tau_c+\gamma_5\tau_c\frac{1}{(\mathbf{q}_0'-\mathbf{k})-\mathbf{M}}\gamma_5\tau_{c'}\right\}$$
$$\times\psi(q')\phi(k). \quad (5)$$

The following simplification can be made in Eq. (5):

$$\gamma_5\frac{1}{\mathbf{q}'+\mathbf{k}-\mathbf{M}}\gamma_5\psi(q')=\frac{-\mathbf{k}}{(\mathrm{q}'+\mathrm{k})^2-\mathrm{M}^2}\psi(q'),$$

$$\bar{\psi}(q_0')\gamma_5\frac{1}{\mathbf{q}_0'-\mathbf{k}-\mathbf{M}}\gamma_5=\bar{\psi}(q_0')\frac{+\mathbf{k}}{(\mathrm{q}_0'-\mathrm{k})^2-\mathrm{M}^2}.$$

Before we complete the calculation of the cross section, we shall set up some computational tools to simplify the calculation. We shall set them up in a general form so that they can be used for other calculations. In the paragraph called density of states we give the angular relations and the energy relations of these particles whose total energy and momentum is conserved.

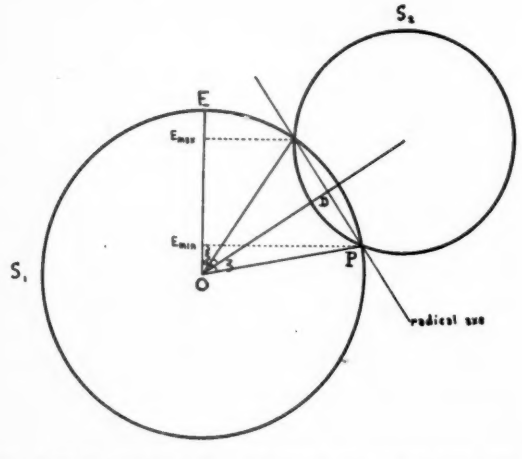

FIG. 2. This drawing is only an analog to the real configuration. The hyperquadrics S_1 and S_2 have been replaced by circles. OP=p^1, OD=D, OE is in the energy direction. $E_{min}\leqslant ch\alpha_1\leqslant E_{max}$.

A. DENSITY OF STATES

The integration over the density of the final states is an integration of the following type:

$$\int F(p_0^1,p_0^2,p^1,p^2,k)\rho(p^1,p^2,k). \quad (6)$$

A convenient way to proceed is the following:

(i) integration of one of the four-vectors (p^2 for instance) with the help of $\delta(p_0^1+p_0^2-p^1-p^2-k)$.

(ii) integration of p^1 say. The two δ-functions $\delta[(p^1)^2-M^2]$ and $\delta[(p_0^1+p_0^2-p^1-k)^2-M^2]$ shows that p^1 is to be integrated on the intersection of the two surfaces.

$$\begin{aligned} &S_1 \quad (p^1)^2-(M^1)^2=0,\\ &S_2 \quad (p_0^1+p_0^2-p^1-k)^2-(M^2)^2=0. \end{aligned} \quad (7)$$

For greater generality we have set the masses of the two nucleons different. The radical plane of S_1 and S_2 is at a distance

$$D=\tfrac{1}{2}(p_0^1+p_0^2-k)\left(1+\frac{(M^1)^2-(M^2)^2}{|p_0^1+p_0^2-k|^2}\right),$$

from the origin of the vector p^1.

Hence, p^1 is to be integrated on S_1 with the condition

$$p^1\cdot\frac{(p_0^1+p_0^2-k)}{|p_0^1+p_0^2-k|}=D, \quad (8)$$

(see Fig. 2). This condition can also be derived immediately analytically from (7). S_1 and S_2 intersect each other only if $D^2\geqslant(M^1)^2$.

(iii) Integration of k. The condition (8) fixes the limit of integration of k on the surface $k^2-\mu^2=0$.

Let us fix a system of coordinates. Let us set

$$\begin{aligned} \epsilon_0&=\mu\mathrm{ch}\theta_1\\ \mathrm{k}_1&=\mu\mathrm{sh}\theta_1\cos\theta_2\\ \mathrm{k}_2&=\mu\mathrm{sh}\theta_1\sin\theta_2\cos\theta_3\\ \mathrm{k}_3&=\mu\mathrm{sh}\theta_1\sin\theta_2\sin\theta_3. \end{aligned} \quad (9)$$

The volume element is then:

$$\delta(k^2-\mu^2)\mathrm{d}k=\mu^2\mathrm{sh}^2\theta_1\mathrm{d}\theta_1\sin\theta_2\mathrm{d}\theta_2\mathrm{d}\theta_3.$$

Similarly, p^1 and p^2 will be expressed in terms of M^1, α_1, α_2, α_3 and M^2, β_1, β_2, β_3, respectively.

The scalar product of two vectors is:

$$k\cdot p^1=\mu M[+\mathrm{ch}\theta_1\mathrm{ch}\alpha_1-\mathrm{sh}\theta_1\cos\alpha_2\mathrm{sh}\alpha_1\cos\alpha_2$$
$$-\mathrm{sh}\theta_1\sin\theta_2\mathrm{sh}\alpha_1\sin\alpha_2\cos(\theta_3-\alpha_3)].$$

Let us now fix a frame of reference: We choose the center of gravity system so that $p_0^1+p_0^2$ has only a component along the energy direction. We choose $\mathbf{f}$ as the polar axis in the $\mathfrak{p}^1$ space. We shall now express the condition (7) for the integration of p^1 and determine the limits of integration of p^1 and k. Let us call ζ the angle between p^1 and $p_0^1+p_0^2-k$ and ξ the angle between $p_0^1+p_0^2$ and $p_0^1+p_0^2-k$. The condition (7) can

be expressed by the following equation:

$$\mathrm{ch}\alpha_1\mathrm{ch}\xi-\cos\alpha_2\mathrm{sh}\alpha_1\mathrm{sh}\xi=\cosh\zeta. \quad (10)$$

It is convenient to consider α_2 as fixed and to introduce the condition (10) into (6) through the following δ-function.

$$\delta(\cos\alpha_2\mathrm{sh}\alpha_1\mathrm{sh}\xi-\mathrm{ch}\alpha_1\mathrm{ch}\xi+\cosh\zeta). \quad (11)$$

α_1 varies then between the following limits

$$\xi-\zeta\leqslant\alpha_1\leqslant\xi+\zeta.$$

Hence,

$$\frac{1}{4M^1M^2}\rho(p^1,p^2,k)=\frac{1}{(2\pi)^5}\frac{\mu M^1}{2}\int_1^{\mathrm{ch}\Theta}\mathrm{dch}\theta_1\int_\pi^0 \mathrm{d}\cos\theta_2$$
$$\times\int_0^{2\pi}\mathrm{d}\alpha_3\int_{\mathrm{ch}(\xi-\zeta)}^{\mathrm{ch}(\xi+\zeta)}\mathrm{dch}\alpha_1\int_\pi^0\mathrm{d}\cos\alpha_2\delta(\cos\alpha_2-A)$$
$$\times\int_0^{2\pi}\mathrm{d}\alpha_3. \quad (12)$$

A is given by Eq. (10) and $\mathrm{ch}\Theta$ is given by Eq. (9). Translated into energy terms the density of states is:

$$\frac{1}{4M^1M^2}\rho(p^1,p^2,k)=\frac{1}{(2\pi)^5}\frac{1}{2}\int_\mu^{\epsilon_{\max}}\mathrm{d}\epsilon\int_\pi^0\mathrm{d}\cos\theta_2\int_0^{2\pi}\mathrm{d}\theta_3$$
$$\times\int_{p^1\min(\epsilon)}^{E^1\max(\epsilon)}\mathrm{d}E_1\int_\pi^0\mathrm{d}\cos\alpha_2\delta(\cos\alpha_2-\mathrm{A})\int_0^{2\pi}\mathrm{d}\alpha_3, \quad (13)$$

$$\epsilon_{\max}=\frac{1}{4E}[4(E_0)^2+\mu^2-(M^1+M^2)^2], \quad (14)$$

$$E_0=E_0^1=E_0^2$$

$$2E_{0\min}=\mu+M^1+M^2. \quad (15)$$

$$\underset{\min}{E^1_{\max}}(\epsilon)=(2E_0-\epsilon)B$$
$$\pm\left((\epsilon^2-\mu^2)\left[B^2-\frac{(M^1)^2}{4(E_0)^2-4E_0\epsilon+\mu^2}\right]\right)^{\frac{1}{2}},$$

with

$$B=\frac{1}{2}\left[1+\frac{(M^1)^2-(M^2)^2}{4(E_0)^2-4E_0\epsilon+\mu^2}\right]$$

$$A=\frac{B[4(E_0)^2-4E_0\epsilon+\mu^2]-E^1(2E_0-\epsilon)}{M^1\mu[(E^1)^2-(M^1)^2]^{\frac{1}{2}}[\epsilon^2-\mu^2]^{\frac{1}{2}}}.$$

The integration over the density of states yields:

$$\frac{1}{4M^1M^2}\int\rho(p^1,p^2,k)=\frac{2}{(2\pi)^3}\int_\mu^{\epsilon_{\max}}\Big((\epsilon^2-\mu^2)(\epsilon_{\max}-\epsilon)E_0$$
$$\times\frac{4E_0(\epsilon_{\max}-\epsilon)+4M^1M^2}{[4E_0(\epsilon_{\max}-\epsilon)+(M^1+M^2)^2]^2}\Big)^{\frac{1}{2}}\mathrm{d}\epsilon. \quad (16)$$

The energy distribution of the nucleon of mass M^1 (or M^2) after the collision is obtained by interchanging μ with M^1 (or M^2) in the formulas (16) and (14). The dummy variable ϵ and the upper limit of integration $\epsilon_{\max}$ would then be called E^1 and $E^1{}_{\max}$ (or E^2 and $E^2{}_{\max}$).

The maximum of the energy distribution is shifted towards E_0 for increasing values of E_0. The shift is more rapid for a light particle than for a heavy particle.

The asymptotic values of $(1/4M^1M^2)\int\rho(p^1,p^2,k)$ are

$$\frac{4}{(2\pi)^3}\left(\frac{2E_0\mu M^1M^2}{(M^1+M^2)^2}\right)^{\frac{1}{2}}\int_\mu^{\epsilon_{\max}}[(\epsilon-\mu)(\epsilon_{\max}-\epsilon)]^{\frac{1}{2}}\mathrm{d}\epsilon$$
$$=\frac{1}{(2\pi)^2}[(\mu+M^1+M^2)\mu M^1M^2]^{\frac{1}{2}}\left(\frac{E_0-E_{0\min}}{\mu+M^1+M^2}\right)^2$$
$$\text{for } E_0-E_{0\min}\ll\frac{M^1+M^2}{2}$$

$$\frac{2}{(2\pi)^3}\int_\mu^{E_0}\epsilon\mathrm{d}\epsilon=\frac{E_0^2}{(2\pi)^3}$$
$$\text{for } E_0\gg\frac{M^1+M^2}{2}.$$

We shall now convert from the rest system to the laboratory system.

Set M, $E_0'\mathfrak{p}_0'$ the mass, the energy, and the momentum of the incoming nucleon; the other nucleon is at rest. The angle between the meson emitted and the incoming nucleon is such that:

$$1-M\frac{(E_0^{2\prime}-M^2)^{\frac{1}{2}}-(\epsilon^{2\prime}-\mu^2)^{\frac{1}{2}}}{(E_0^{2\prime}-M^2)^{\frac{1}{2}}(\epsilon^{2\prime}-\mu^2)^{\frac{1}{2}}}\leqslant\cos(\mathfrak{p}_0',\mathfrak{k}')\leqslant1$$
$$\text{for } (\epsilon^{2\prime}-\mu^2)^{\frac{1}{2}}\geqslant\frac{M}{2}-\frac{M^2}{4(E_0^{2\prime}-M^2)^{\frac{1}{2}}}$$

$$-1\leqslant\cos\mathfrak{p}_0'\cdot\mathfrak{k}'\leqslant1 \quad \text{for } (\epsilon^{2\prime}-\mu^2)^{\frac{1}{2}}\leqslant\frac{M}{2}-\frac{M^2}{4(E_0^{2\prime}-M^2)^{\frac{1}{2}}}.$$

The angle between one of the nucleons after the collision and the incoming nucleon is:

$$1-M\frac{E_0'-E^{n\prime}}{E_0'E^{n\prime}}\leqslant\cos\mathfrak{p}_0'\cdot\mathfrak{p}_n'\leqslant1 \text{ for } E^{n\prime}>M.$$

The asymptotic values of $(1/4M^1M^2)\int\rho(p^{1\prime},p^{2\prime},k')$ are

$$\frac{[(\mu+M^1+M^2)\mu M^1M^2]^{\frac{1}{2}}}{(2\pi)^2 16}\left(\frac{E_0'-E'_{0\min}}{\mu+M^1+M^2}\right)^2$$
$$\text{for } 2\mu<E_0'-M\ll M$$

$$\frac{1}{2}\frac{E_0'M}{(2\pi)^3} \quad \text{for } E_0'\gg M.$$

The density of states of four particles (or more) can be

TABLE I.

	α	β
Charged theory	0	4
Symmetrical theory	6	9

studied in the same way. In Eq. (7) and following k is then replaced by k^1+k^2.

It seems convenient to compare both experimental results and the influence of the various couplings to these invariant statistical factors.

B. PERMUTATION OPERATOR

The number of terms in Eq. (4) can be reduced in the following way: The operation of the emission and absorption operators ψ and $\bar{\psi}$ of the nucleon field on the wave function of the system in the initial and in the final state is equivalent to the anti-symmetrization of the nucleon wave function in the configuration space.

Let us set $\mathcal{P}$ a permutation operator which permutes simultaneously the spin, the charge, and the momentum of the nucleons. The anti-symmetrical wave function ψ of two nucleons can be expressed in terms of the product of the wave function of each nucleon in the following manner:

$$\psi_{\alpha\beta}(p_0^1,p_0^2)=\frac{1-\mathcal{P}}{\sqrt{2}}\psi_\alpha(p_0^1)\psi_\beta(p_0^2).$$

The square of a matrix element symmetrical in the nucleons 1 and 2 is equal to

$$|\psi_{\alpha\beta}(p^1,p^2)\mathrm{A}\bar{\psi}_{\gamma\delta}(p_0^1p_0^2)|^2$$
$$=(1-\mathcal{P})|\psi_\alpha(p^1)\psi_\beta(p^2)\mathrm{A}\bar{\psi}_\gamma(p_0^1)\bar{\psi}_\delta(p_0^2)|^2.$$

Hence, in Eq. (4) we can simultaneously give an identity to the nucleons and multiply the whole expression by $(1-\mathcal{P})$. This procedure simplifies the writing of the cross section. It reduces the number of terms by a factor 4 for transitions involving the same number of particles in the initial and in the final state; it reduces the number of terms by a factor 2 for transitions involving a different number of particles in the initial and in the final states. In the actual case for instance, once a name has been given to the nucleons, two diagrams must be added which describe the emission of the meson by the other nucleon.

Moreover, this procedure separates the terms in the cross section into two groups. The terms which are not proportional to $\mathcal{P}$, are obtained when the Pauli exchange principle is neglected. The other terms are the contribution of the Pauli exchange forces. In some cases these terms can be neglected. In the actual case, these terms are small because the wave-length of the nucleon is small as compared to the range of the nuclear forces. ($\mu c/\mathrm{M}v<1$, v is the velocity of the nucleon.)

The operator which permutes the charge of the nucleons can be expressed algebraically by the expression:

$$\frac{1+\sum_{\nu=1}^{3}\tau_\nu^{(1)}\cdot\tau_\nu^{(2)}}{2}=\frac{1+\sum_{c}\tau_c^{(1)}\tau_c^{(2)}}{2}.$$

The covariant algebraic form of the operator which permutes the spin of the nucleons is derived as follows:

A four component Dirac wave function can be expressed as a wave function with two two-valued indices.

$$\psi_{\alpha^1}(1)\psi_{\alpha^2}(2)=\psi_{\sigma^1\rho^1}(1)\psi_{\sigma^2\rho^2}(2).$$

The indices $\rho^1\sigma^1$ and $\rho^2\sigma^2$ can be permuted simultaneously by the operator.

$$\Gamma=\left[\frac{1+\sum_{i=1}^{3}\sigma_i^{(1)}\cdot\sigma_i^{(2)}}{2}\right]\left[\frac{1+\sum_{i=1}^{3}\rho_i^{(1)}\cdot\rho_i^{(2)}}{2}\right]$$
$$=\frac{1}{4}\left\{1+\sum_{\mu=1}^{5}\left[\gamma_\mu^{(1)}\gamma_\mu^{(2)}+\frac{\delta_{\mu\nu}-1}{2}\gamma_\mu^{(1)}\gamma_\mu^{(2)}\gamma_\nu^{(1)}\gamma_\nu^{(2)}\right]\right\}.$$

One checks that

$$\Gamma\gamma_\mu^{(1)}=\gamma_\mu^{(2)}\Gamma.$$

For the case of Einstein Bose particles, $1-\mathcal{T}$ is replaced by $1+\mathcal{T}$.

C. PROJECTION OPERATOR

The covariant operator $\Lambda(p)=(\mathrm{p}+\mathrm{M})/2\mathrm{M}$ operating on $\gamma_4\psi(p)$ is such that

$$\Lambda(p)\gamma_4\psi_\alpha(p)=\begin{cases}\psi_\alpha(p) & \text{if } \alpha \text{ designates a state whose energy has the same sign as the fourth component of } p.\\ 0 & \text{otherwise}\end{cases}$$

$(\Lambda)^2=\Lambda$.

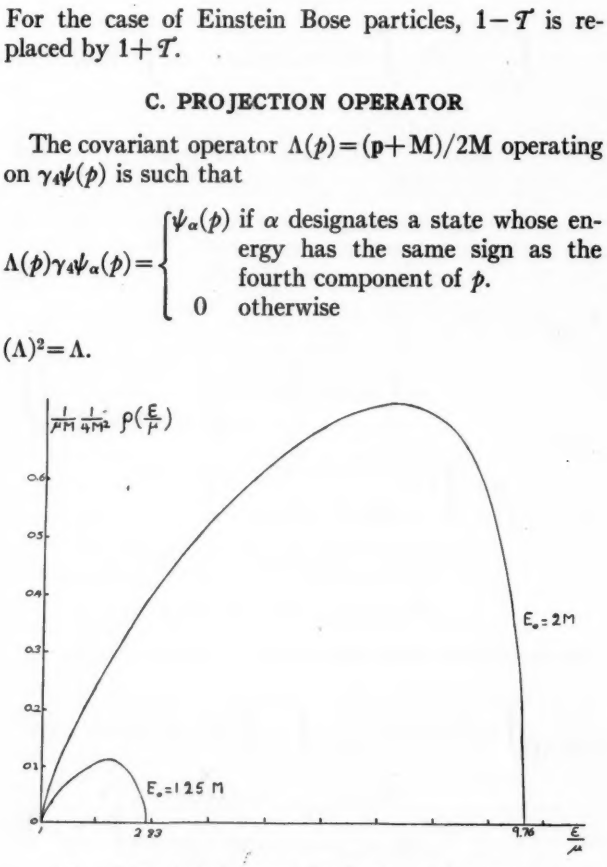

FIG. 3. Statistical energy distribution of the meson emitted (in the rest system).

$\Lambda(p)$ is a "self-selecting" operator: it selects the energy states of the same sign as the fourth component of p. Consequently:

$$\sum|\bar{\psi}(p_0)\mathbf{A}\psi(p)|^2=\mathrm{Spur}\mathbf{A}\Lambda(p_0)\bar{\mathbf{A}}\Lambda(p) \qquad (17)$$

with

$$\bar{\mathbf{A}}=\gamma_4\mathbf{A}^*\gamma_4.$$

The sum is performed over those energy states which have the same sign as the fourth component of p_0 and p.

We notice that we can include the incoming and the outgoing lines in the prescription which give the collision operator and forget at the same time the projection operators: the world line of a nucleon in the final or in the initial state is translated in the collision operator by

$$1/(\mathbf{p}-\mathbf{M})=2\mathbf{M}\Lambda(p)/[(p)^2-\mathbf{M}^2]$$
$$=2\mathbf{M}\Lambda(p)2\pi\delta[(p)^2-\mathbf{M}^2]$$

and the world line of a meson is translated by

$$1/(\mathbf{k}^2-\mu^2)=\delta(k^2-\mu^2)$$

To avoid the mathematical difficulty raised by such expressions as $\{\delta[(p)^2-\mathbf{M}^2]\}^2$, one can also say that the cross section for a process represented by a certain diagram is obtained in the following way:

The diagram and its adjoint (i.e., the same diagram with the time direction reversed) are linked together. The prescription for the collision operator is followed on that "double-diagram" to obtain the probability of the transition.

In any case, the propagation of a particle is described similarly whether the particle is in an observable state or in a virtual state. The propagation of a particle is characterized by its four-wave vector. There is a conservation law for the four-wave vectors of the particles. When the particle is in an observable state the components of the four-wave vector are the energy and the momentum of the particle. When the particle is in a virtual state the 4th component of the wave vector is not the energy of the particle; the three other components are the momentum of the particle.

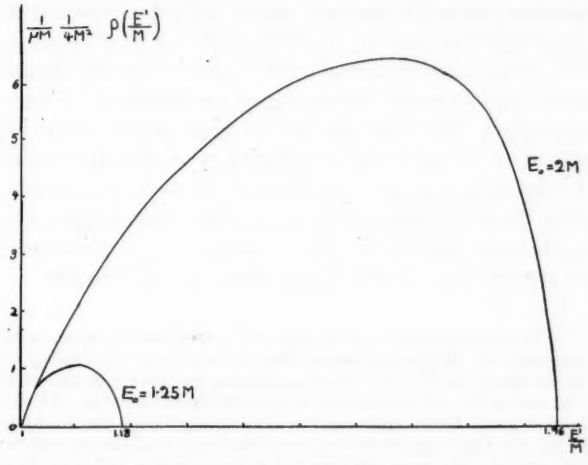

FIG. 4. Statistical energy distribution of one of the nucleons after the collision (in the rest system).

We shall now complete the computation of the cross section.

$$\sigma=\frac{1}{\varphi(p_0^1,p_0^2)}\rho(p^1,p^2,k)\Big\{\phi(k)\psi(p^1)\psi(p^2)$$
$$\times\Big[-\mathrm{if}^3\frac{\gamma_5^{(1)}\mathbf{k}^{(2)}}{(p_0^1-p^1)^2-\mu^2}\Big[\frac{\tau_c^{(2)}\sum_{c'}\tau_{c'}^{(1)}\tau_{c'}^{(2)}}{(p_0^2-k)^2-\mathbf{M}^2}$$
$$-\frac{\sum_{c'}\tau_{c'}^{(1)}\tau_{c'}^{(2)}\tau_c^{(2)}}{(p^2+k)^2-\mathbf{M}^2}\Big]+1\leftrightarrow2\Big]\bar{\psi}(p_0^1)\bar{\psi}(p_0^2)\Big\}^2. \qquad (18)$$

The term explicitly written corresponds to the emission of the meson by the particle 2. The other one "1↔2" corresponds to the emission of the meson by the particle 1. In agreement with the discussion of the paragraph B, the contribution of the Pauli exchange forces has been neglected.

Because of Eqs. (4) and (17) and by use of the following spurs:

$$\frac{\mathbf{M}^2}{4}\mathrm{Spur}(-\Lambda(p_0^1)\gamma_5\Lambda(p^1)\gamma_5)$$
$$=(p_0^1\cdot p^1)-\mathbf{M}^2=-\tfrac{1}{2}(p_0^1-p^1)^2,$$
$$\frac{\mathbf{M}^2}{4}\mathrm{Spur}\Lambda(p_0^2)\mathbf{k}\Lambda(p^2)\mathbf{k}$$
$$=2[2(p_0^2\cdot k)(p^2\cdot k)-k^2(p_0^2\cdot p^2)+k^2\mathbf{M}^2]$$
$$=-\{[-\mathbf{M}^2+(p^2+k)^2][-\mathbf{M}^2$$
$$+(p_0^2-k^2)]+\mathbf{k}^2(p_0^1-p^1)^2\},$$
$$\mathrm{Spur}\Lambda(p_0^1)\gamma_5\Lambda(p^1)\mathbf{k}=0.$$

We obtain:

$$\sigma=\frac{1}{\varphi(p_0^1,p_0^2)}\rho(p^1,p^2,k)\Big(\frac{\mathrm{f}^2}{4\pi}\Big)^3[\alpha\mathrm{A}+\beta\mathrm{B}]$$

where the numerical values of α and β are given by the following table.

$$\mathrm{A}=\frac{1}{(p_0^1-p^1)^2-\mu^2}-\frac{\mu^2}{[(p_0^2-k)^2-\mathbf{M}^2][(p^2+k)^2-\mathbf{M}^2]}$$

$$\mathrm{B}=\frac{1}{(p_0^1-p^1)^2-\mu^2}\Big[\frac{(p_0^2-k)^2-\mathbf{M}^2}{(p^2+k)^2-\mathbf{M}^2}+\frac{(p^2+k)^2-\mathbf{M}^2}{(p_0^2-k)^2-\mathbf{M}^2}\Big]$$
$$-\frac{\mu^2}{[(p_0^2-k)^2-\mathbf{M}^2]^2}-\frac{\mu^2}{[(p^2+k)^2-\mathbf{M}^2]^2}.$$

In this expression μ^2 has been neglected as compared to $\mathbf{M}^2$. Here we have averaged over the charges of the nucleons in the initial state and summed over the

charges of the nucleons and the meson in the final state. The cross sections for the different cases according to the charge of the meson and the nucleons are not equal in the charged theory.

The structure of the cross section is given essentially by the term $1/[(p_0{}^1-p^1)^2-\mu^2]$. The terms proportional to μ^2 are small as compared to the others. The two terms which are functions of k balance each other to give a term nearly equal to two.

$$\int \frac{1}{(p_0{}^1-p^1)^2-\mu^2}\rho(p^1,p^2,k)$$

$$=\frac{(2M)^2}{(2\pi)^3}\int \frac{1}{2[((E_0{}^1)^2-M^2)^{\frac{1}{2}}((E^1)^2-M^2)^{\frac{1}{2}}]}$$

$$\times\log\frac{2[(E_0{}^1E^1+((E_0{}^1)^2-M^2)^{\frac{1}{2}}((E^1)^2-M^2)^{\frac{1}{2}}]-2M^2+\mu^2}{2[(E_0{}^1E^1-((E_0{}^1)^2-M^2)^{\frac{1}{2}}((E^1)^2-M^2)^{\frac{1}{2}}]-2M^2+\mu^2}$$

$$\times\left[((E^1)^2-M^2)\left(\frac{4(E_0{}^1)^2-4E_0{}^1E^1+\mu^2}{4(E_0{}^1)^2-4E_0{}^1E^1+M^2}\right)^2\right.$$

$$\left.-\frac{4\mu^2}{4E_0{}^2-4E_0{}^1E^1+M^2}\right]^{\frac{1}{2}}dE^1. \quad (19)$$

The square root is merely a statistical factor; it corresponds to the integration over all the states of the meson available when the energy of one of the nucleons is equal to E_1. The logarithm divided by $2[(E_0{}^1)^2-M^2]^{\frac{1}{2}}(E_1{}^2-M^2)^{\frac{1}{2}}$ is essentially a function of $E_0{}^1$ alone. Its asymptotic values are

$$\frac{1+M}{(E_0{}^1-M)} \quad \text{for} \quad \frac{\mu}{2}\leqslant E_0{}^1-M\ll M,$$

$$\frac{4M^2}{(E_0{}^1)^2}\log(E_0{}^1) \quad \text{for} \quad E_0{}^1\gg M.$$

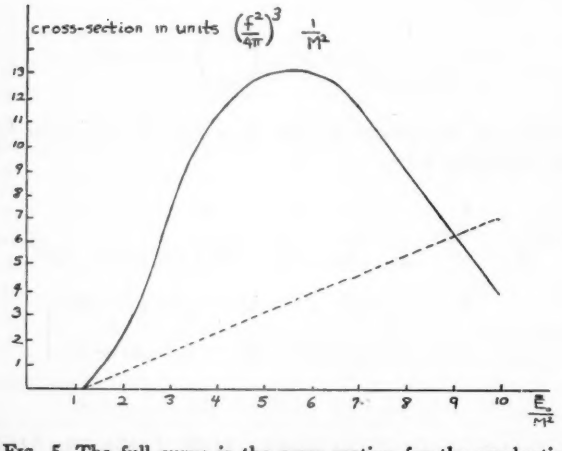

FIG. 5. The full curve is the cross section for the production of a pseudoscalar meson with pseudoscalar coupling in the charge-symmetrical theory (in the laboratory system). The dotted curve is the cross section as obtained from the invariant statistical factors (in the laboratory system). It increases up to a value of 13 which is reached in the neighborhood of $E_0'/M=20$.

Hence, the energy distribution of the meson and the nucleons is nearly the same as the energy distribution obtained from pure statistical considerations (see paragraph A). In Figs. 3 and 4 there is plotted the statistical energy distribution of the meson and the nucleon in the rest system.

The asymptotic expressions for the cross section in the laboratory system are:

$$\sigma=a\pi\left(\frac{f^2}{4\pi}\right)^3\frac{8}{M[M(E_0'-M)]^{\frac{1}{2}}}\left[E_0'-M-\frac{\mu^2-2\mu M}{M}\right]^2 \quad \text{for } 2\mu\leqslant E_0'-M\ll M$$

$$\sigma=a\left(\frac{f^2}{4\pi}\right)^3\left(\frac{8}{ME_0'}\right)\log\frac{ME_0'}{2}. \quad \text{for } E_0'\gg M$$

$a=1$ in the charged theory. $a=3$ in the symmetrical theory. E_0' is the energy of the incoming nucleon, the other nucleon is at rest. The cross section in the charge symmetrical theory is about three times bigger than the cross section in the charged theory. Besides a larger number of mesons transmitted or emitted in the charge symmetrical theory, some transitions are possible only through an exchange of neutral mesons.

The total cross section is plotted on Fig. 4 in the laboratory system. On Fig. 5 there is also plotted the cross section obtained from the statistical factors: density of final states and inverse of the flux of the incoming particles (i.e., the cross section obtained from equation (2) with $O=1$.

This result differs appreciably from the results obtained with a scalar meson field[1] and with the pseudovector coupling of the pseudoscalar meson field.[14] For the scalar and pseudoscalar interactions which do not depend on the energy of the meson, the energy distribution of the particles is nearly the same as the statistical energy distribution. There is no term in the cross section which favors a large or a small momentum transfer from the nucleon to the meson: The strong dependence of the cross section on large momentum transfers, at high energies, which could be expected in a pseudoscalar theory, is eliminated for two reasons: The terms corresponding to the emission of the meson before and after the scattering of the nucleons balance each other. The contribution of high energy particles limited to a small angle scattering is of the same order of magnitude as the contribution of slow energy particles with a large angle scattering; the energy denominators which look like "resonance denominators" are smeared out by the integration over the angles.

[14] The cross section for production of a pseudoscalar meson with pseudovector coupling increases like the square of the energy of the incoming particle E_0'. The cross section reaches the geometrical cross section for a total energy of the particle of the order of twice the rest mass. If the cross section is calculated with the damping theory, the damping terms become effective in that energy region; they reduce the cross section for proton-proton collision to a constant and the cross section for proton-neutron collision to a decreasing function of E_0'.

It is a great pleasure to acknowledge the hospitality of the Institute for Advanced Study and the guidance of Professor J. R. Oppenheimer. We wish to thank also Dr. K. M. Case for very helpful discussions.

APPENDIX

The meson production is considered here from the point of view of the quantum theory of fields (case a). The meson production has been also considered from a phenomenological point of view[2,4,9] as the mesonic analog to the bremsstrahlung (case b). The process is then described as the scattering of a nucleon by another nucleon followed or preceded by the emission of a meson. The knowledge of the scattering can be obtained from experiment; thus this semi-empirical method does not ask the explanation of the momentum transfer between the nucleons from the theory. The difference between these two conceptions is more easily explained in the old form of the perturbation theory. A diagram such as Fig. 1a condenses three different processes which can be unfolded in the following format:

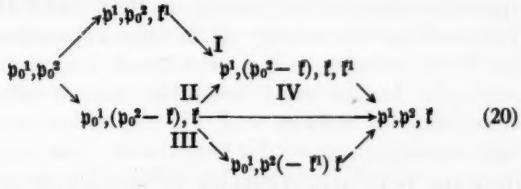

(20)

$f^1 = p_0^1 - p^1$ is the momentum of the virtual meson exchanged between the nucleons.

A circuit will be referred to by the corresponding number on the arrow. Circuit IV describes a direct interaction[15] between the nucleons which may or may not be needed to cancel unwanted singularities in the theoretical derivation of the nuclear potential. The cross sections obtained in the case a and b would be equivalent[5] only if the two following conditions were fulfilled:

(1°) If the matrix element for the circuit II+III+IV could be replaced as a whole by the corresponding matrix element of the nuclear potential. The diagonal elements of these two matrices are equal (elements corresponding to the transitions between two states of the same total energy); but the off diagonal elements are not equal when circuit IV is included or when there is a virtual pair creation in the intermediate state. When there is not equivalence between the circuit II+III+IV and the nuclear potential, it is difficult to speak of a nuclear potential for processes of higher order such as radiative scattering.

(2°) If circuit I were negligible as compared to the circuits II+III+IV. This condition would be necessary because the phenomenological description cannot account for circuit I where the meson is emitted during the exchange of the virtual meson. The ratio of the contribution of circuit I to the contribution of circuit II or III is of the order:

$$\mu/(p_0^1 - p^1) < 1$$

near the threshold. The importance of the contribution of the circuit I at the threshold is due to the finiteness of the meson mass. Two circumstances may affect circuit II and III in such a way that circuit I becomes of major importance. When there is no spin or charge operator, contribution from terms in which scattering precedes meson emission is equal and opposite in sign to that in which scattering follows meson emission.[7] [The contribution of circuit II (and III) cancels with that of the corresponding circuit of the mirror image of (20).] When there is a circuit IV, the contributions of circuit II and III are essentially reduced by that of circuit IV, that of circuit I is unaffected.[5]

We have pointed out the differences of the photon and meson case due to the finiteness of the meson mass. By looking at the meson production in a slightly different manner, we can bring forth another difference between these two fields. Whereas in the bremsstrahlung, the Coulomb potential is accounted for by the longitudinal part of the field, and the photon emission by the transverse part of the field; in the meson production, there is no such distinction between the field responsible for the nuclear potential and the field responsible for the meson emission. Unlike the problem of the bremsstrahlung one cannot take the difference between the total field and the part of the field associated with the nuclear potential to account for the meson emission. In the bremsstrahlung there is no difference between the case a and b.

In conclusion, the phenomenological description avoids the difficulties of the theoretical calculation of the nuclear scattering. It keeps just a part which gives meson production. It overlooks some of the differences between the meson field and the photon field.

---

[15] In the first-order approximation the matrix element for the nuclear interaction $V_{A'A}$ due to the exchange of mesons between two nucleons is

$$V_{A'A} = \Sigma_i [H_{A'i} H_{iA} / (E_A - E_i)]. \quad (1)$$

Contrary to previous opinions on the static nuclear potential, the pseudoscalar mesons do not contribute to the first-order term (they contribute to the second-order term). The vector mesons give a matrix element $V_{A'A}$ which representation in coordinate space is:

$$G^2(e^{-\mu r}/r) + g^2\delta(r). \quad (2)$$

g is the coupling constant for the tensor interaction. G^2 is a linear combination of the square of the coupling constants of the vector and the tensor interactions. The infinite terms occurring from the tensor interaction cannot be cancelled by charge and mass renormalization alone (K. M. Case, Phys. Rev. 75, 1440 (1949)). A treatment which would remove all infinite terms may remove also the term $g^2\delta(r)$. There may not be any δ-interaction in the static potential derived from $V_{A'A}$. If there is one, $V_{A'A}$ is replaced by the following expression:

$$V_{A'A} = \Sigma_i [H_{A'i} H_{iA}' / (E_A - E_i)] + H'_{A'A}. \quad (3)$$

H' is the operator for direct interaction which is chosen so that

$$V(r) = G^2(e^{-\mu r}/r). \quad (4)$$

In Eq. (4) as in Eq. (2) the term in G^2 is obtained only when the static approximation is made, that is to say, when the recoil energy is neglected in Eq. (3) or in Eq. (1). This approximation is justified in Eq. (1); it is not obviously justified in Eq. (3) because $H'_{A'A}$ cancels the main contribution of $\Sigma_i [H_{A'i} H_{iA}/(E_A - E_i)]$ and the remainder is of the same order of magnitude as the first term neglected by the static approximation. It can be shown that the static approximation is justified in Eq. (3) only if the total energy of the states A and A' is the same. Consequently, the representation of $V_{A'A}$ in coordinate space is not $G^2(e^{-\mu r}/r)$.

Relative Cross Sections for Pair Production at 17.6 Mev

R. L. WALKER
Cornell University, Ithaca, New York
(Received August 5, 1949)

The relative cross sections for production of electron pairs by 17.6 Mev gamma-rays have been measured for Li, C, Al, Cu, Sn, and Pb. A gamma-ray pair spectrometer was used to count the number of pairs emitted from thin radiators of these materials when irradiated by 17.6 Mev gamma-rays produced in the $Li^7(p,\gamma)Be^8$ reaction. For each material, the number of pairs counted per atom of radiator has been extrapolated to a radiator of zero thickness, in order to obtain the relative pair cross section. From these measurements some information can be obtained about the probability of pair production in the field of the atomic electrons, and about the errors in the theoretical pair cross sections of heavy elements, which presumably arise from the use of the Born approximation. It is found that the ratio of the pair cross section of an electron to that of a nucleus of unit charge is 0.8 ± 0.3. The data indicate that the pair cross sections of heavier elements are lower than predicted by the Born approximation, in qualitative agreement with measurements of the total absorption cross sections.

I. INTRODUCTION

THE cross sections of different elements for the production of electron pairs by high energy gamma-rays are roughly proportional to Z^2.[1,2] This proportionality is not exact, however, for threee different reasons. These are the screening of the nuclear coulomb field by the atomic electrons; production of pairs in the field of the atomic electrons; and an inadequacy of the Born approximation, by means of which the Z^2 dependence has been obtained in the Bethe-Heitler theory of pair production.

The effect of screening is small at 17.6 Mev and has been calculated with reasonable accuracy by Bethe and Heitler.[1] It may be taken into account by a correction factor $(1-S(Z))$ in the pair cross section. The screening correction, $S(Z)$, varies from 0.01 for lithium, to 0.05 for lead at 17.6 Mev.

The production of pairs in the field of the atomic electrons contributes a term proportional to Z in the cross section per atom. This means the total pair cross section is proportional to $Z(Z+A)$ instead of Z^2, where A is the pair cross section of an electron relative to that of a nucleus of unit charge. For light elements, the effect of the electrons may be rather large. The probability of pair production in the field of an electron has been calculated in a number of papers,[3-6] but its value at 17.6 Mev is not known with certainty. Borsellino[3] gives the (interpolated) value $A=0.68$ at 17.6 Mev, for a free electron. The approximate calculations of Wheeler and Lamb[4] take into account the binding of the electrons in the atom, but are valid for light elements only at higher energies. They give for heavier elements, however, a value $A\approx1.0$.

Finally, the Z^2 dependence of the pair cross section for a bare nucleus depends upon the use of the Born approximation in the theory of Bethe and Heitler.[1] The condition for validity of the Born approximation is $Ze^2/\hbar v\ll1$ where v is the velocity of the electron (or positron). In the most favorable case of relativistic velocities, this reduces to $Z/137\ll1$, which is true for light elements, but not for heavy ones. Thus deviations from the Born approximation values may be expected for heavy elements. These deviations will be expressed by a correction factor $(1-B(Z))$.

Combining the three effects discussed above, one may write the total pair cross section in the form:

$$\sigma_{\text{pair}}\sim Z(Z+A)(1-S(Z))(1-B(Z)). \quad (1)$$

From measurements of the relative pair cross sections of different elements, some information may be obtained about the electron pair cross section, A, and about the correction $B(Z)$ to the Born approximation values.

The above remarks apply not only to the integral pair cross section, but also to the differential cross section, $\sigma(E^+)dE^+$, for production of a pair with positron energy between E^+ and E^++dE^+. However, the magnitude of the three "corrections," A, $S(Z)$, and $B(Z)$, may be different in different regions of the differential cross section, i.e., different E^+. For example, the symmetry of the differential cross section with respect to the positron and electron energies[1,2] is a result of the use of the Born approximation, whereas the true curve is probably asymmetrical. The correction to the Born approximation value is probably different in the region of small positron energies from that at small electron energies.

It will be seen later that in the present experiments the relative cross section measured for each element is not the integral cross section, but an integral over the central region of the differential cross section.

$$\sigma_{\text{obs}}\approx\int_{k/4}^{3k/4}\sigma(E^+)dE^+. \quad (2)$$

This should be kept in mind in interpreting the results.

[1] H. A. Bethe and W. Heitler, Proc. Roy. Soc. **146**, 83 (1934).
[2] W. Heitler, *Quantum Theory of Radiation* (Oxford University Press, London, 1936).
[3] A. Borsellino, Helv. Phys. Acta **20**, 136 (1947).
[4] J. A. Wheeler and W. E. Lamb, Phys. Rev. **55**, 858 (1939).
[5] K. M. Watson, Phys. Rev. **72**, 1060 (1947).
[6] V. Votruba, Phys. Rev. **73**, 1468 (1948).

In addition, pairs produced in the field of an electron are not counted if the "recoil electron" has a high energy (>approx. 1 Mev). Thus these are not included in the observed cross section, but they are probably small in number.[4]

Finally it should be pointed out that information concerning the electron pair cross section and the "Born approximation correction" can also be obtained from measurements of the total gamma-ray absorption cross sections of different elements.[7–9] These measurements have the advantage of being more accurate and less subject to systematic errors than the present experiment. However, at energies below 20 or 30 Mev the effect of pair production in the field of the atomic electrons is much less important in the absorption cross section than in the pair cross section alone. This arises from the fact that Compton scattering contributes more than pair production to the absorption in very light elements. Also, in heavy elements at these energies, nuclear photo-disintegration may contribute a few percent to the total absorption cross section[8,9] but does not affect the relative pair cross section.

II. APPARATUS AND PROCEDURE

Pairs produced in radiators of different elements were counted by means of a magnetic pair spectrometer which has been previously described,[10] and which is shown in Fig. 1. Radiators used in these experiments were 3 by 11 cm in area, and their thicknesses are given in Table I. By counting coincidences between any of the four positron counters and any of the four negative electron counters, the spectrometer measures pairs in seven different energy intervals, separated in energy by about 4 percent. In these experiments, the magnetic field of the spectrometer was always adjusted for each radiator so that the center of the observed 17.6 Mev gamma-ray line fell midway between the central energy channel, number 4, and an adjacent channel, number 3. By adding the counts in channels 3 and 4 (after correcting for a difference in statistical weights arising from the fact that channel 4 is fed by coincidences from four counter pairs whereas channel 3 is fed by only three counter pairs), the flat-topped "resolution function" shown in Fig. 2a may be obtained. The flat top is desirable in order to minimize the effects of small variations in the magnetic field, and of energy loss and scattering of the pair electrons in the radiator. A still broader resolution function, shown in Fig. 2b may be obtained by adding the counts from four channels, numbers 2, 3, 4, and 5 (each corrected for statistical weights). Both of these resolution functions have been used in analyzing the data.

The width of the radiator, and its position with respect to the counters determine the region of the differential pair cross section[1,2] from which pairs may be counted. For example, no pairs in which one electron has a very low energy can be recorded. (The minimum radius of curvature for an electron which is counted is given by one-half the distance from one end of the radiator to the nearest counter.) It may be shown that the counting rate of the spectrometer for a thin radiator is proportional to the integral over the central region of the differential cross section:

$$\sigma_{\text{obs}} \approx \int_{k/4}^{3k/4} \sigma(E^+)dE^+. \qquad (2)$$

Actually, the limits of this integral are not exact, and they depend somewhat upon the particular counter pair giving the coincidences. The important point, however, is that the measured cross section, (2), is different from the total integral cross section. This difference would not be significant, of course, if the unscreened differential cross section had the same shape for all elements, as predicted by the theory of Bethe and Heitler. It is important, therefore, only to the extent that the Born approximation gives wrong results.

The gamma-rays used in these experiments were produced by bombarding thick lithium targets with 0.46 Mev protons from the Cornell cyclotron. The gamma-rays thus produced from the 440-kev resonance in the $Li^7(p,\gamma)Be^8$ reaction have a spectrum which consists of a sharp line at 17.6 Mev, and an apparently broad line near 14.8 Mev.[10] The possible effect on the measurements of the lower energy component (which has a relative intensity about half that of the 17.6 Mev line) will be mentioned later.

The relative number of pairs emitted from each radiator was measured by comparing the counting rate of the spectrometer using this radiator with that obtained from a "standard" 0.006-in. Pb radiator. For

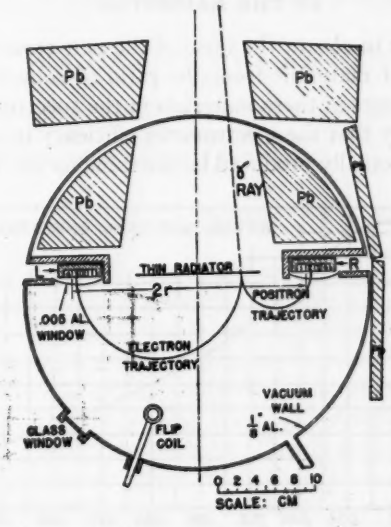

FIG. 1. Diagram of the gamma-ray pair spectrometer. (Horizontal section through the four-inch magnet gap.) The distance between cyclotron target and radiator was about 58 cm in these experiments.

[7] J. L. Lawson, Phys. Rev. **75**, 433 (1949).
[8] R. L. Walker, Phys. Rev. **76**, 527 (1949).
[9] G. D. Adams, Phys. Rev. **74**, 1707 (1948).
[10] R. L. Walker and B. D. McDaniel, Phys. Rev. **74**, 315 (1948).

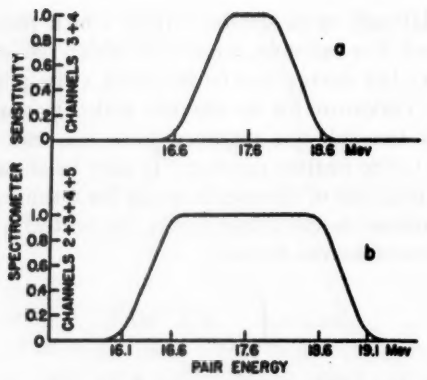

FIG. 2. Resolution functions of the spectrometer under the conditions used in the present experiments: (a) Counting rates of channels 3 and 4 added together, (b) counting rates of channels 2, 3, 4, and 5 added.

this comparison the gamma-ray intensity was monitored by two small Geiger counters mounted in 4.5 cm lead shields. To avoid systematic counting errors, the counting rates of the two radiators being compared were measured alternately, until 7 to 12 readings had been obtained for each one. Enough counts were observed to obtain a statistical accuracy of about 2.0 percent in the ratio of the counting rate of each radiator to that of the standard.

From this ratio has been subtracted a background, which ranged from one to ten percent, depending on the radiator. This background was the counting rate obtained with no radiator in the spectrometer (relative to the counting rate with the standard radiator). Some of the background arises from pairs produced in the mounting frame and Scotch Tape used to support the radiators.

III. EFFECTS OF SCATTERING AND ENERGY LOSS OF THE PAIR ELECTRONS IN IN THE RADIATION

In order to obtain the ratio of the pair cross sections of different materials from the ratio of counting rates with radiators of these materials in the spectrometer, it is necessary that the spectrometer efficiency in counting the pairs actually produced be the same for the different materials. Since this efficiency is affected by energy loss and scattering of the pair electrons in the radiator, an extrapolation was made for each element to a radiator of zero thickness. In making this extrapolation, it is of interest to investigate the effects of energy loss and scattering.

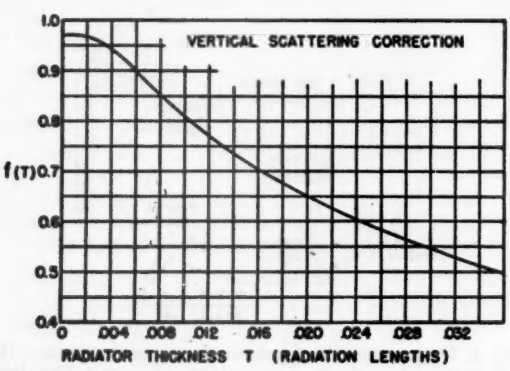

FIG. 3. Vertical scattering correction. $f(T)$ is the fraction of pairs produced which is *not* lost because of vertical scattering.

Scattering of the pair electrons in the radiator has two effects on the efficiency. One of these is that a pair will not be counted if either electron is scattered so far in the vertical direction that it strikes a magnet pole and thus does not enter the counter window. The fraction $f(T)$ of pairs *not* lost because of this vertical scattering has been calculated as a function of the radiator thickness, T, and is shown in Fig. 3. This calculation has been made from the known geometry of the spectrometer, and from the angular distribution of electrons multiply scattered in emerging from the radiator.[11] The angles of emission in the pair production process itself[12] are smaller than those arising from multiple scattering except for very thin radiators. They have been included in a rough way in the curve of Fig. 3. As an aid in extrapolating the data to zero thickness of radiator, corrections have been made for the fraction of pairs lost by vertical scattering. This might appear to introduce significant errors, since the calculated curve of Fig. 3 is certainly not exact, especially at large radiator thicknesses. However, it is felt that the errors in the relative cross sections introduced by this procedure are unimportant since the same correction curve, $f(T)$, has been applied to all elements.

The second effect of scattering of the pair electrons is an apparent lowering of the energy of the pair. This results from the properties of 180 degrees focusing, by means of which the spectrometer measures the momentum component of an electron normal to the radiator. This apparent energy loss, combined with the actual energy loss by inelastic collisions, means that the apparent spectrum of pairs produced by 17.6 Mev gamma-rays is not a sharp line at 17.6 Mev, but a continuous spectrum in a small energy interval just below 17.6 Mev. If this energy interval is larger than the flat region of the resolution functions shown in Fig. 2, then a loss in efficiency will result from this "line broadening." Sample corrections for these effects have been calculated, but no corrections have been applied to the data. The calculations indicate a sizable loss of efficiency for thicker radiators of light elements if the narrow resolution function 2a is used. No significant losses (except perhaps for the two or three heaviest radiators) are expected if the wider resolution function 2b is used.

IV. RESULTS

The relative pair counting rate per atom for each radiator measured is shown in Table I. The column R_{3-4}/N gives this data as obtained from channels 3 and

[11] See, for example, B. Rossi and K. Greisen, Rev. Mod. Phys. 13, 263-265 (1941).
[12] M. Stearns, Phys. Rev. 76, 836 (1949).

4 of the spectrometer, corresponding to the narrow resolution function 2a. The column headed R_{2-5}/N gives the data obtained from channels 2, 3, 4, and 5, corresponding to the wide resolution function 2b. Also shown in Table I are the vertical scattering corrections $f(T)$.

The relative counting rates, corrected for vertical scattering losses, have been plotted in Fig. 4 as a function of the radiator thickness for each material. These curves have then been extrapolated to zero thickness to obtain the relative pair cross sections. The slopes of the curves for light elements using the narrow resolution function 2a are probably a result of energy loss in the radiator. As discussed above, the effect of this energy loss is unimportant if the broad resolution function 2b is used, and the slopes of the corresponding curves are seen to be greatly reduced. In fact, the curves for heavy elements have a slight positive slope. This may reflect errors in the vertical scattering correction $f(T)$, but it may also be a result of the broad 14.8 Mev lithium gamma-ray line. Because of the way in which the magnetic field was adjusted for each radiator the fraction of counts arising from the tail of the 14.8 Mev line

TABLE I. Relative counting rate per atom for each radiator.*

Radiator material	Thickness (g/cm²)	Thickness (Radiation lengths)	$f(T)$	N (10^{24} atoms	R_{3-4}/N	R_{2-5}/N	Statistical standard error
Li	0.2061	0.00181	0.969	0.590	0.194	0.181	1.4%
C	0.1138	0.00220	0.967	0.1883	0.703	0.620	1.7%
C	0.1937	0.00374	0.947	0.3206	0.644	0.591	1.9%
C	0.3462	0.00669	0.882	0.5731	0.548	0.567	2.1%
C	0.5902	0.01141	0.781	0.9768	0.371	0.442	2.0%
Al	0.1099	0.00419	0.940	0.0810	2.95	2.68	1.8%
Al	0.2897	0.01104	0.787	0.2135	2.26	2.24	1.5%
Al	0.4729	0.01803	0.673	0.3485	1.71	1.94	1.5%
Cu	0.0489	0.00369	0.947	0.01528	14.29	12.54	2.0%
Cu	0.1383	0.01044	0.800	0.04326	12.08	11.16	1.8%
Sn	0.0368	0.00423	0.939	0.00617	38.8	34.5	1.7%
Sn	0.0962	0.01106	0.787	0.01610	34.0	31.2	1.9%
Pb	0.0315	0.00534	0.917	0.003023	95.3	84.4	1.7%
Pb	0.0599	0.01015	0.807	0.005747	83.0	75.7	2.1%
Pb	0.1233	0.02090	0.637	0.01183	64.6	62.1	2.0%
Pb	0.1861	0.03154	0.532	0.01785	55.5	55.3	

* N is the total number of atoms in the radiator.
R_{3-4} and R_{2-5} are ratios, corrected for background, of the spectrometer counting rate when the listed radiator is in position, to the counting rate with the "standard" Pb radiator, (0.1861 g/cm²).
R_{3-4} is this ratio measured by channels 3 and 4 of the spectrometer, corresponding to the narrow resolution function 2a.
R_{2-5} is this ratio obtained from channels 2, 3, 4, and 5 of the spectrometer, corresponding to the wide resolution function 2b.

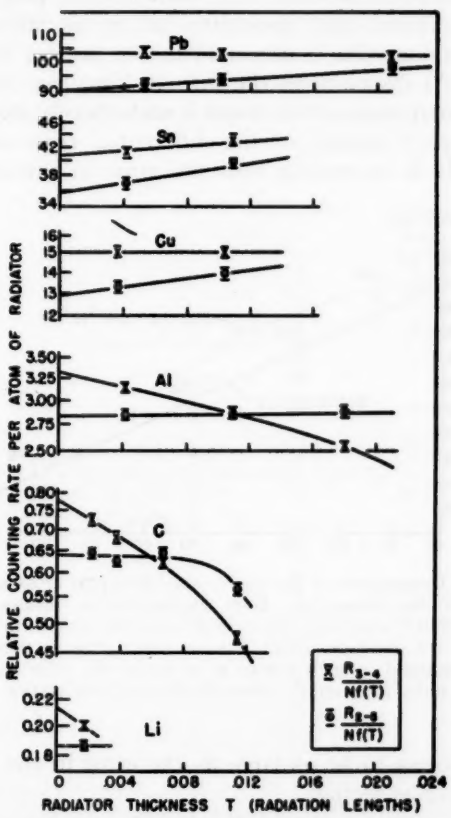

FIG. 4. Relative counting rates per atom for each radiator, corrected for vertical scattering. The crosses represent data obtained from channels 3 and 4, corresponding to the narrow resolution function of Fig. 2a. The circles are data obtained from channels 2, 3, 4, and 5, corresponding to the wide resolution function 2b. For each of these sets of data the relative pair cross section of each element is obtained from the extrapolation to zero radiator thickness.

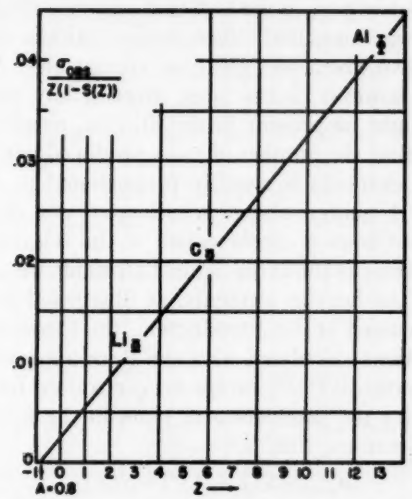

FIG. 5. Graph of $\sigma_{obs}/Z[1-S(Z)]$ *vs.* Z. The intercept on the Z-axis gives the electron pair cross section, $A=0.8$, relative to the pair cross section of a nucleus of unit charge.

would be expected to increase with the radiator thickness.

The relative pair cross sections obtained from data taken with the two resolution functions of Fig. 2 are listed in Table II. Both sets of values have been arbitrarily normalized so that the measured (relative) cross sections of the lightest elements will agree numerically with the theoretical Born approximation values for the integral cross sections (see Fig. 6). This normalization is convenient even though the measured cross section (2) differs from the total integral cross section. (In the "theoretical" values, the electron cross section $A=0.8$ has been used.) Also shown in Table II are the screening corrections, $S(Z)$ calculated from the

TABLE II. Observed relative pair cross sections and their comparison with the theoretical Born approximation values. The value $A=0.8$ for the electron pair cross section has been used in the "theoretical" cross sections.

Element	Screening correction $S(Z)$	σ_{3-4} normalized (10^{-24} cm²)	σ_{2-5} normalized (10^{-24} cm²)	Average $=\sigma_{obs}$ (10^{-24} cm²)	$\frac{\sigma_{obs}}{\sigma_{Born}}$
Li	0.010	0.0342 ±4%	0.0347 ±2%	0.0344 ±4%	0.997
C	0.014	0.1248 ±3%	0.1194 ±2%	0.1221 ±3%	0.991
Al	0.021	0.531 ±2%	0.530 ±2%	0.530 ±2%	0.987
Cu	0.031	2.416 ±3%	2.406 ±3%	2.411 ±2%	0.942
Sn	0.040	6.54 ±3%	6.70 ±3%	6.62 ±3%	0.890
Pb	0.050	16.48 ±2%	16.80 ±2%	16.64 ±2%	0.845

low energy formula of Bethe and Heitler[1] involving the function $C(\gamma)$.

Assuming that the Born approximation is valid for light elements (i.e., $B(Z)\approx 0$), if one plots $\sigma_{obs}/Z[1-S(Z)]$ against Z, the negative intercept on the Z axis should give the electron pair cross section, A (see Eq. (1)). This has been done in Fig. 5 and the value $A=0.8\pm 0.3$ obtained. The rather large estimate of error arises from the fact that the measured cross section of lithium (for which the electron effect is greatest) is less reliable than those of the other elements. This is due in part to the fact that only one thickness of lithium was measured, since thicker lithium radiators would have given too great an energy loss. Also important, however, is the large effect of any impurities which might be present in the lithium, resulting from the fact that the number of pairs produced per gram in different elements is roughly proportional to Z.* The error in A quoted above is estimated not only from Fig. 5, but from a consideration of the relation of the cross sections of the three lightest elements measured to those of the heavier elements, as illustrated in Fig. 6.

As discussed in the introduction, the theoretical pair cross sections calculated with the Born approximation, are proportional to Z^2, except for corrections for screening and for the production of pairs in the field of the atomic electrons; that is,

$$\sigma_{Born}\sim Z(Z+A)(1-S(Z)). \quad (3)$$

In order to find the deviations of the measured cross sections from the Born approximation values (i.e., the correction $B(Z)$ of Eq. (1)), the ratio $\sigma_{obs}/\sigma_{Born}$ has been plotted as a function of Z, in Fig. 6. In this graph, the relative cross sections, σ_{obs}, have been normalized to make the ratio $\sigma_{obs}/\sigma_{Born}$ approach 1 at small Z, where the Born approximation should be valid. The values of σ_{Born} are not purely theoretical, since the experimental electron cross section, $A=0.8$, has been used in (3). The curve of Fig. 6 indicates that the correction to the Born approximation is linear in Z,

$$B(Z)=(0.0019\pm 0.0005)Z,$$

but the data are not accurate enough to actually determine the Z-dependence of this correction. For example, the data are not greatly inconsistent with a Z^2-dependence, as suggested by Lawson,[7] and as might seem more reasonable from consideration of the total absorption cross sections.[8]

According to Fig. 6, the correction to the Born approximation is about 0.16 ± 0.4 for lead, whereas a measurement of the total absorption cross section[8] indicates a correstion of 0.10. The latter figure is based on the assumption that the absorption of 17.6 Mev gamma-rays takes place only by pair production, Compton scattering, and atomic photoelectric effect, and that the theoretical cross sections for the latter two processes are correct. It will be too low if any other processes contribute to the absorption. Actually the nuclear (γ,n) process may make a contribution of a few percent, and if a correction for this effect is made, it is possible that the value of $B(Z)$ obtained from the absorption data would agree within the experimental error with that found from Fig. 6.

Exact agreement between the two values of the Born approximation correction might not be expected since the absorption involves the total, integral pair cross section, whereas only the central half of the differential cross section, (2), is measured in the present experiments. As discussed in the introduction, the error in the Born approximation result is undoubtedly different in different regions of the differential cross section curve. It is interesting that the error in the central region seems to be as large as the error in the total, integral cross section.

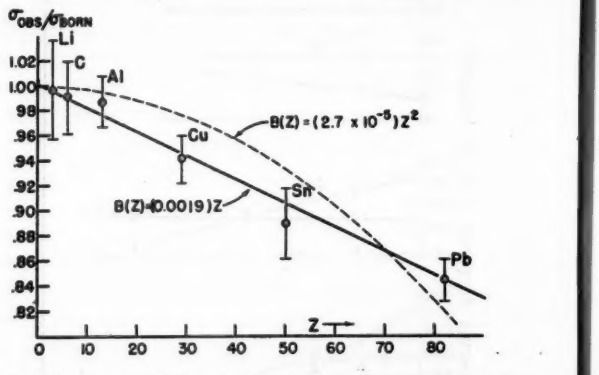

FIG. 6. Comparison of the observed relative pair cross sections σ_{obs}, with the theoretical, Born approximation results, $\sigma_{Born}=(3.055\times 10^{-27}\text{ cm}^2)Z(Z+A)(1-S(Z))$. (In the above curve, the value $A=0.8$ has been used.) The measured cross sections have been normalized in such a way as to make the ratio $\sigma_{obs}/\sigma_{Born}$ approach unity for small Z, where the Born approximation should be valid.

ACKNOWLEDGMENTS

I am indebted to Professor B. D. McDaniel for many discussions concerning these experiments, and to Bruce Dayton for help in the operation of the cyclotron.

This work was supported in part by the Office of Naval Research.

* A spectrographic analysis of the lithium radiator, made by the New England Spectrochemical Laboratories of Ipswich, Massachusetts, showed only small amounts of impurities (0.1 percent ± a factor 10). However, the qualitative nature of this analysis, together with the fact that the likely surface impurities, *C*, *N*, and *O* were not included in it, make it impossible to rule out the effects of impurities.

Yield and Angular Distribution of the D-D Neutrons*

G. T. HUNTER** AND H. T. RICHARDS
Department of Physics, University of Wisconsin, Madison, Wisconsin

(Received August 10, 1949)

The differential and total cross sections for neutron emission from the d—d reaction have been measured for deuteron energies between 0.5 and 3.7 Mev. A "thin" deuterium gas target and an energy insensitive neutron detector were used in the measurements. The yield in the center of mass coordinates was of the form $N(\theta)=K(1+A\cos^2\theta+B\cos^4\theta+C\cos^6\theta)$; the total cross section was essentially constant (0.1 barn) for deuteron energies above 1 Mev. The coefficient A was found to be negative above 1.4 Mev and appreciable $\cos^4\theta$ was needed at all energies. Above 2.5 Mev, a $\cos^6\theta$ term was also appreciable. The angular distribution results can be understood qualitatively in terms of penetration of Coulomb and centrifugal barriers plus spin-orbit coupling.

INTRODUCTION

ACCURATE information concerning the neutrons from the

$$D+D\rightarrow He^3+n+3.27 \text{ Mev}$$

reaction is of both experimental and theoretical importance since (a) for most laboratories the reaction is the only practical source of monochromatic neutrons of energy between 1.8 and 7 Mev, and (b) it is a simple enough reaction that detailed theoretical considerations about yield and angular distribution become feasible.[1]

Both the neutron and proton emission from this reaction have been investigated extensively for deuteron energies below 500 kev.[2–4]† However, most of the low energy data are "thick" target data and are difficult to translate with any certainty to differential and total cross-section measurements.

At higher deuteron energies data of Bennett, Mandeville, and Richards[5] and the recent work of Blair, Freir, Lampi, Sleator, and Williams[6] are available. The former data give only relative neutron yields and are limited to but two angles of observation to the deuteron beam. The Minnesota data[6] includes differential cross sections for both disintegration protons and He^3 particles for deuteron energies of 1 to 3.5 Mev. The angular range (~15° to 85° in c.m.s. coordinates) investigated in that work was limited in the forward direction by the geometry of the charge measuring system and at large angles by the low energy of the He^3 particle. The counting of charged particles in a known geometry did, however, permit the Minnesota group to obtain quite accurate differential cross-section values for the above angular range.

There are also recent differential neutron and pro-

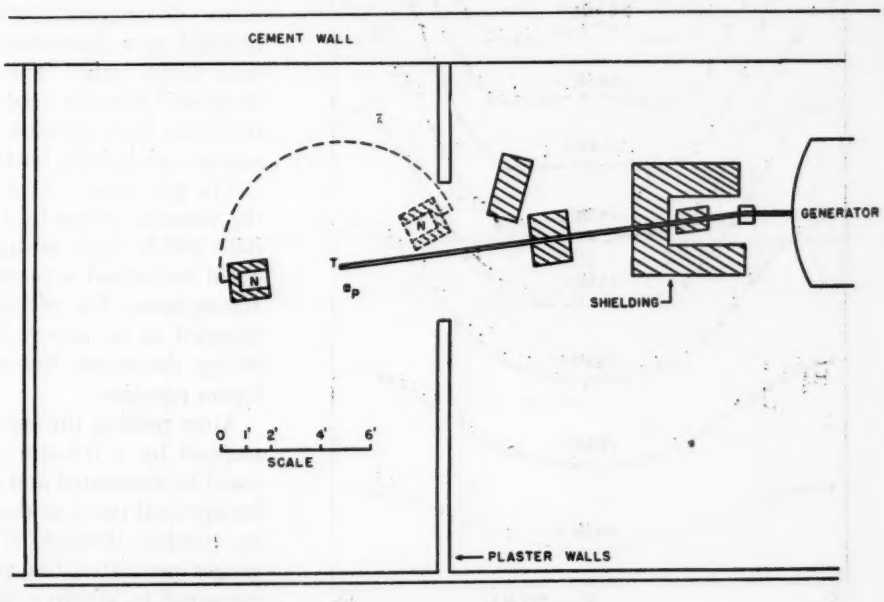

FIG. 1. Schematic experimental arrangement. T is the gas target and P is the proton monitor counter. N is the shielded neutron detector.

* This work was supported in part by the AEC and in part by the Wisconsin Alumni Research Foundation.
** Now at the U. S. Naval Postgraduate School, Annapolis, Maryland.
[1] E. J. Konopinski and E. Teller, Phys. Rev. **73**, 822 (1948).
[2] Bretscher, French, and Seidl, Phys. Rev. **73**, 815 (1948).
[3] Manley, Coon, and Graves, Phys. Rev. **70**, 101A (1946).
[4] Graves, Graves, Coon, and Manley, Phys. Rev. **70**, 101A (1946).
† References to earlier work may be found in references 1, 2, and 5.
[5] Bennett, Mandeville, and Richards, Phys. Rev. **69**, 418 (1946).
[6] Blair, Freier, Lampi, Sleator, and Williams, Phys. Rev. **74**, 1599 (1948).

ton cross-section measurements for 10-Mev deuterons.[7,8]

EXPERIMENTAL ARRANGEMENTS

In the present investigation it was decided to observe the neutrons rather than the charged He^3 so that measurements could include all angles in the c.m.s.

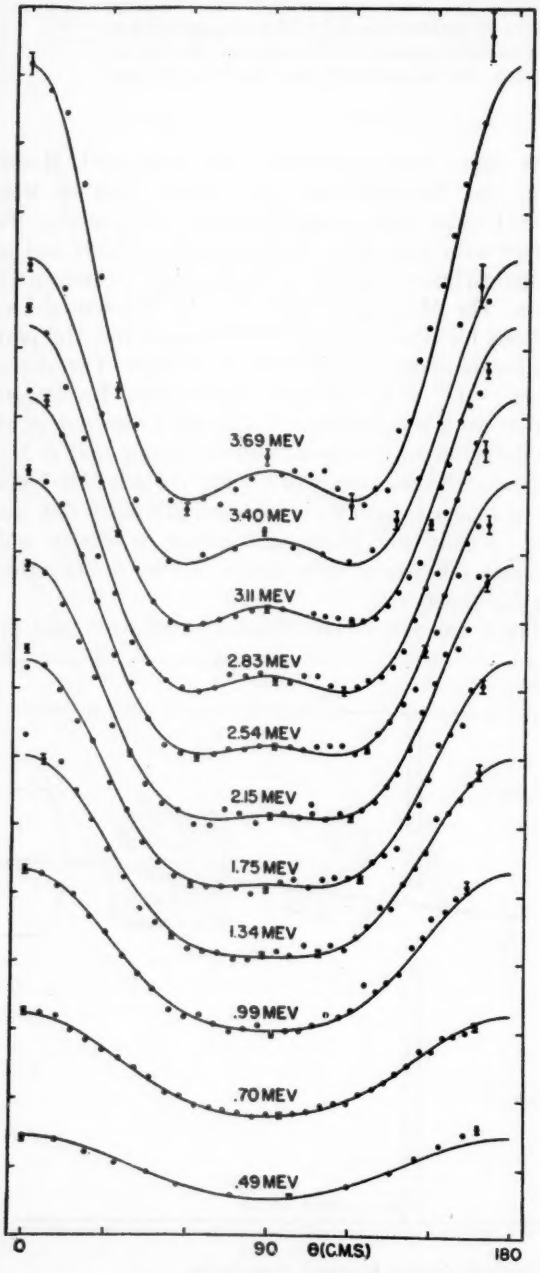

FIG. 2. Observed angular distribution plotted in c.m.s. coordinates after correction for background and for neutron counter efficiency. The ordinate scale for each successive energy has been displaced one unit to prevent overlapping of data. The curves drawn through the experimental points are of the form $N(\theta) = K(1+A\cos^2\theta+B\cos^4\theta+C\cos^6\theta+\cdots)$.

[7] Erickson, Fowler, and Stovall, Jr., Phys. Rev. 75, 894 (1949).
[8] Leiter, Meagher, Rodgers, and Kruger, Phys. Rev. 76, 167 (1949).

from 0° to nearly 180°. At 180° (laboratory coordinates) the neutron energy varies only between 1.9 and 1.6 Mev for deuteron energies between 0.5 and 4 Mev, but in the forward direction the corresponding variation of neutron energies is from 3.5 to 7.0 Mev. Hence an energy insensitive neutron detector is desirable for measurement of the angular distribution. A shielded long counter[9] was used for this purpose. From the measurements of reference 9, the efficiency of such a counter is almost independent of neutron energy in the range from 1.5 to 3 Mev and is down about 5 percent at 5 Mev (average energy of Ra—Be neutrons). Extrapolation of Hanson and McKibben's data would indicate a relative efficiency of almost 90 percent even for 7 Mev neutrons.

Because of the identity of the two particles initiating the d-d reaction, the differential cross section must be symmetrical about the equatorial plane in the c.m.s. One might, therefore, use any experimentally observed asymmetry about this equatorial plane as a measure of the variation of the detection efficiency with energy. Our data, Fig. 2, after correction for counter efficiency according to the data of reference 9, was always symmetric about 90° in the c.m.s. This efficiency correction was small for most angles and energies and never exceeded 11 percent. The observed symmetry may then be taken as verification of Hanson and McKibben's efficiency curve, or if their efficiency curve is accepted, be taken to indicate the absence of large systematic error in our angular distributions.

Figure 1 shows the schematic experimental arrangement. A magnetically analyzed deuteron beam was brought to a deuterium gas target through a 20-foot long brass tube. The high resolution electrostatic analyzer[10] was not used since targets of 50–150 kev in thickness were desirable for satisfactory counting rates and for minimizing background neutrons.

The gas target (2 cm in length) was separated from the vacuum system by a 0.00005-inch (1 micron) nickel foil[11] which when unsupported over a 6-mm aperture could withstand a pressure differential of almost two atmospheres. The effective thickness of the foil[12] corresponded to an energy loss of 150 kev for the lowest energy deuterons, but only about 75-kev loss for the higher energies.

After passing through the gas target the beam was stopped by a 0.1-mm gold foil. The target chamber could be evacuated and filled with either hydrogen (for background runs) or deuterium gas which was purified by passing through a palladium tube. Appropriate gauges permitted the gas density in the target to be measured to within a few percent. Beam current was integrated by observing with a string electrometer the potential difference across a known capacitance.

A small end window proportional counter fixed at

[9] A. O. Hanson and J. L. McKibben, Phys. Rev. 72, 673 (1947).
[10] Warren, Powell, and Herb, Rev. Sci. Inst. 18, 559 (1947).
[11] Available from the Chromium Corporation of America, Waterbury 90, Connecticut.
[12] As measured by observing the shift in the $Li^7(p,n)Be^7$ threshold resulting from the foil being inserted ahead of the target.

90° to the beam was used to count disintegration protons from $D(d, p)H^3$. This reaction was used to monitor conditions while the angular distribution of neutrons was being investigated.

Background neutrons (from the foil, defining apertures, etc.) were troublesome only at high deuteron energies. Thus at 0.7-Mev deuteron energy, background neutrons amounted to only 2 percent of the d-d yield and at 3.1-Mev background was 7 percent of the total yield in the forward direction but 22 percent at 110°. At 3.7-Mev background was 20 percent of the forward yield and 68 percent of the 110° yield. This large and somewhat fluctuating background makes our highest energy data somewhat unreliable.

RESULTS

Angular distribution results after conversion to c.m.s. coordinates and correction for counter efficiency are shown in Fig. 2. The deuteron energy associated with each curve is the average energy of the deuteron beam in the gas target. Because of non-uniformities in the foil and voltage fluctuations, this average bombarding energy is probably not known better than ±10 kev. The ordinates (yield in arbitrary units) of each curve have been displaced one unit to display more clearly the experimental data associated with each curve. The indicated error is statistical only.

The curves drawn through the experimental points of Fig. 2 are expressions of the form

$$N(\theta)=K(1+A\cos^2\theta+B\cos^4\theta+C\cos^6\theta+\cdots).$$

This is the conventional representation. The experimental data can also be represented as a linear expansion in Legendre polynomials of the first kind:

$$F(\mu)=A_0P_0+A_2P_2+A_4P_4+A_6P_6+\cdots$$

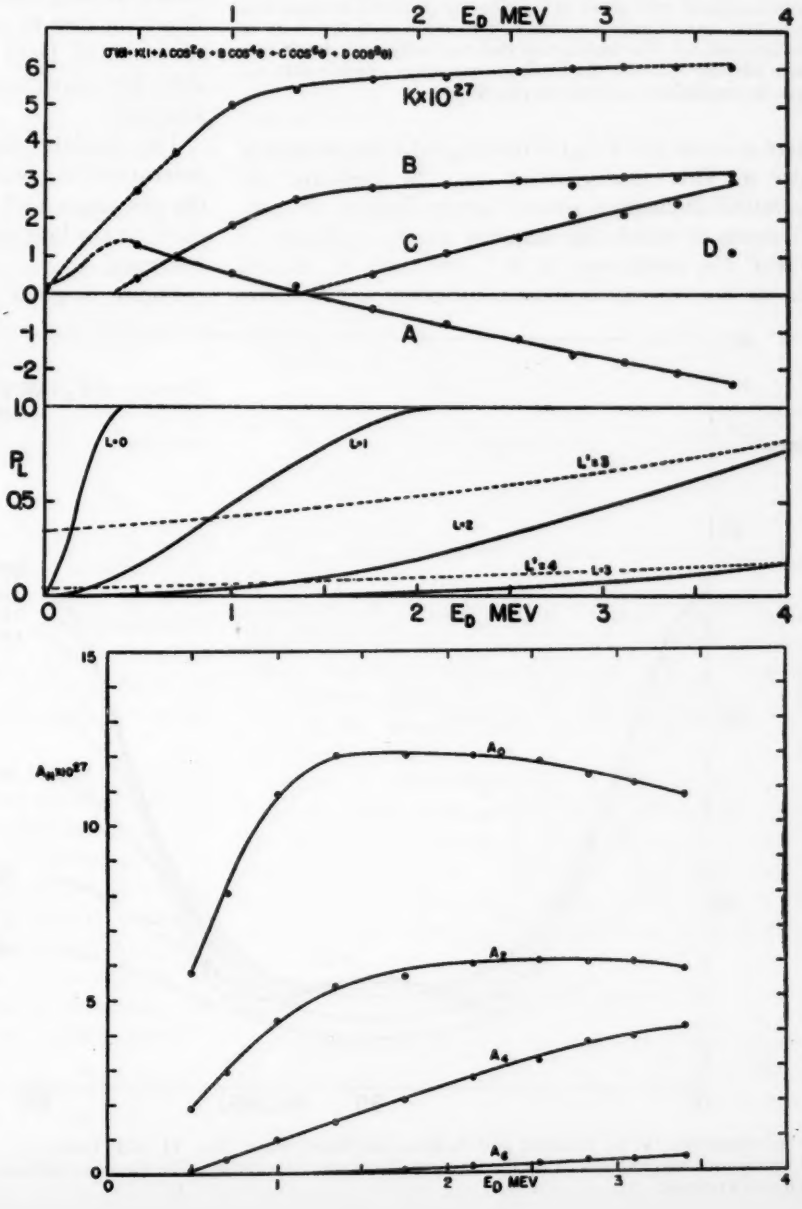

FIG. 3. Variation with deuteron energy (E_d) of the coefficients K, A, B, etc. of the $\cos^n\theta$ representation of the data. The extrapolation to zero energy is based on the low energy data of reference 2. Solid circles indicate that the normalization of these points was not checked because of generator difficulty. Also is included a plot of the penetrabilities P_L for the incoming deuterons (solid curve) and outgoing neutrons (dashed curve).

FIG. 3a. Variation with deuteron energy E_d of the coefficients of the Legendre polynomial fit to the outgoing neutron intensity in c.m.s. coordinates.

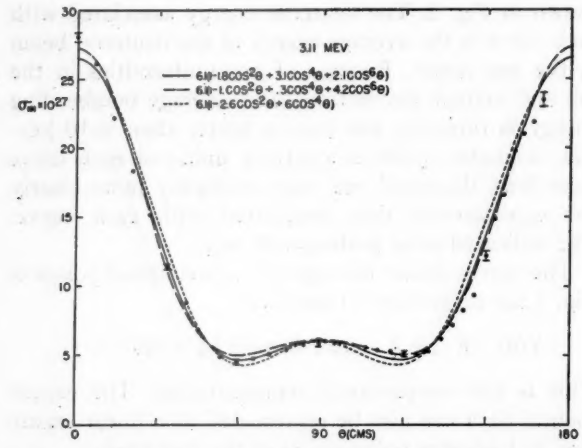

FIG. 4. Illustration of the latitude in choice of parameters which can be used to fit a given experimental curve. The dashed curve is from a Legendre polynomial analysis. The solid curve has coefficients consistent with those of neighboring deuteron energies and the dotted curve shows the best fit possible if only terms up to $\cos^4\theta$ are included. The assumption that the coefficients should be a slowly varying function of the deuteron energy considerably reduces the ambiguity in choice of parameters.

where $\mu=\cos\theta$ and $P_n(\mu)$ is the Legendre polynomial of order n. This representation may be preferred for theoretical discussions since it better displays the partial waves of which the outgoing neutron intensity is formed. The coefficients A, B, C, etc., and A_0, A_2, A_4, etc., for the two representations are given as a function of energy in Fig. 3 and in Fig. 3a. In either case the coefficients were obtained from the experimental data by a Legendre polynomial analysis similar to that developed by F. Reines[13] except that in some instances the coefficients were modified to give a smoother variation of the coefficients as a function of deuteron energy.

When only two parameters are used to describe the angular distribution, their values are quite closely fixed by the experimental data. However, for higher deuteron energy, three parameters are needed and in this case considerably more leeway is available in the choice of coefficients. This is best illustrated by the 3.11-Mev data, where in Fig. 4 it is seen that reasonable fit of the data is possible for significantly different expressions. The dashed curve is that obtained by the straight Legendre polynomial analysis. The solid curve has had the coefficients modified to be consistent with values at neighboring energies, and the dotted curve shows the best fit possible if no terms higher than $\cos^4\theta$ are included. Data at other energies required considerably less modification of the Legendre polynomial analysis.

The absolute value of the reaction cross section was determined by placing a calibrated[14] Ra-Be source at the gas target and by use of Hanson and McKibben's data[9] on the long counter detection efficiency for Ra-Be neutrons.

Figure 5 gives the resulting absolute differential

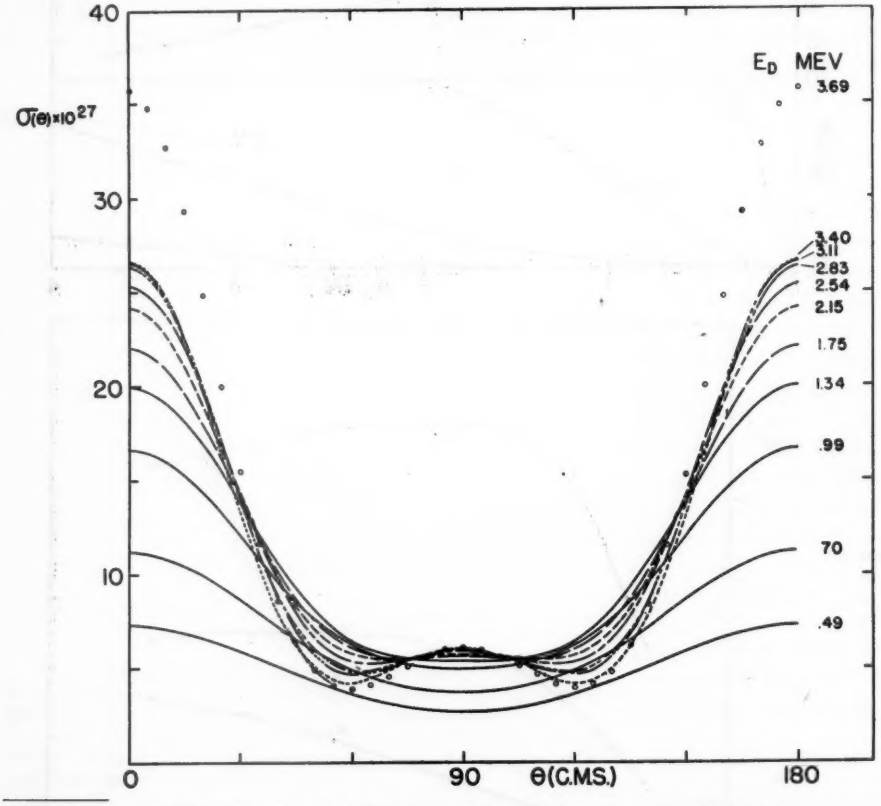

FIG. 5. Differential cross section for $D(d, n)He^3$ in c.m.s. coordinates. The 3.69 and 3.4-Mev data are somewhat unreliable because of large and fluctuating backgrounds.

[13] See Appendix IV, R. Taschek and A. Hemmendinger, Phys. Rev. 74, 373 (1948).

[14] The source was calibrated by the Argonne National Laboratory. The absolute calibration of this source may be uncertain by as much as 10 percent.

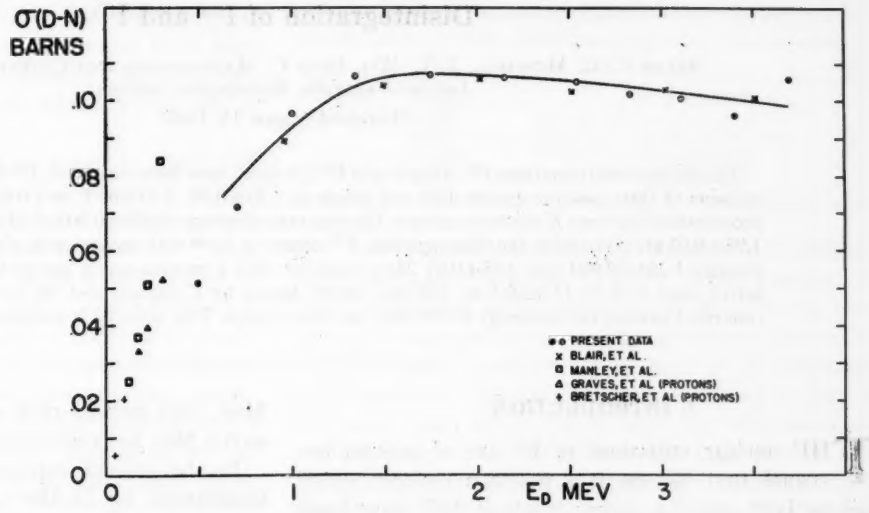

FIG. 6. Total cross section for $D(d, n)He^3$.

cross sections for the analytic expressions which have been fitted to the data of Fig. 2. The ordinates of the 3.4 and 3.69-Mev curves have considerable uncertainty because generator and background difficulties at the time prevented a careful normalization of this data to that at lower energies.

The total cross section (obtained by integrating the differential cross sections) is displayed in Fig. 6 along with comparison values from other experimenters. There is remarkably good agreement with the results of Blair *et al.*,[6] but the present data does not extrapolate to the very low energy data of Manley *et al.*[3]

The laboratory differential cross-section curves, Fig. 7, are included for the convenience of the experimentalist who uses this reaction as a source of neutrons.

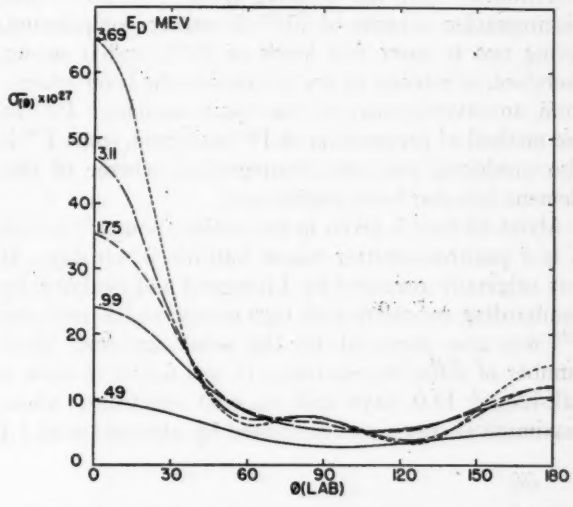

FIG. 7. Laboratory differential cross section for $D(d, n)He^3$.

DISCUSSION

Since the present data show no evidence of sharp resonances, we may attempt to explain qualitatively the behavior of the differential cross section solely on the basis of Coulomb and centrifugal barrier penetrabilities. These penetrabilities (with $R=7\times10^{-13}$ cm as assumed in reference 1) are plotted in Fig. 3 for both the incident deuterons and the outgoing neutrons of various orbital angular momentum.

These penetrabilities indicate that for low deuteron energies the outgoing angular neutron distribution will be influenced chiefly by the penetrabilities of the incoming deuterons[15] and therefore the angular distribution will change rapidly with deuteron energy. However, at higher deuteron energies it will be the outgoing penetrabilities which limit the complexity of the angular distribution. Under these circumstances one expects the angular distribution to be a much less sensitive function of the deuteron energy. Experimentally this result is evidenced in the plot of Legendre polynomial coefficients (Fig. 3a) and would indicate that even for much higher deuteron energies than those here investigated, the angular distribution would not change drastically. The 10-Mev deuteron data of references 7 and 8 support this contention.

It will be noted that spin and orbital angular momentum do not appear to be conserved independently. For example, outgoing D neutron waves are of quite appreciable intensities even for very low penetrabilities of incoming D deuterons. This result is consistent with the large spin-orbit coupling advocated by Konopinski and Teller.[1]

[15] According to a theorem of Eisner and Sachs, Phys. Rev. 72, 680 (1947), the outgoing wave intensities cannot contain spherical harmonics of order greater than $2L$ where L is the order of the incoming wave.

ACKNOWLEDGMENTS

Valuable assistance in recording data and in operation of the electrostatic generator was provided by Messrs. Stanley Bashkin, Gerson Goldhaber, James Hamilton, Virgil Johnson, and Raymond Smith.

Disintegration of I^{124} and I^{126}

ALLAN C. G. MITCHELL, J. Y. MEI, FRED C. MAIENSCHEIN, AND CHARLES L. PEACOCK
Indiana University, Bloomington, Indiana

(Received August 15, 1949)

The nuclear radiations from I^{124} (4 days) and I^{126} (13 days) have been measured. I^{124} decays to Te^{124} with the emission of three positron groups with end points at 2.20±0.01, 1.50±0.01, and 0.67±0.05 Mev, possibly accompanied by some *K*-electron capture. Gamma-rays of energy 0.603±0.002, 0.73±0.01, 1.72±0.02, and 1.95±0.05 are given off in the disintegration. I^{126} decays to Xe^{126} with the emission of two beta-ray groups of energies 1.268±0.010 and 0.85±0.01 Mev, together with a gamma-ray of energy 0.395±0.005 Mev. An active state of I, of 13.0±0.5 hr. half-life, which decays by *K*-capture and the emission of an internally converted gamma-ray of energy 0.159 Mev, has been found. This activity is assigned to I^{128}.

I. INTRODUCTION

THE nuclear radiations of I^{124} are of interest because that isotope is a positron emitter which goes to Te^{124}, and the energy levels of Te^{124} have been determined from the disintegration[1,2] of Sb^{124}. The disintegration scheme of Sb^{124} is rather complicated, giving rise to some five levels of Te^{124}, and it seems, therefore, of interest to try to confirm the level scheme from an investigation of the "pair nucleus," I^{124}. In the method of preparation of I^{124} used here, some I^{126} is also produced, and the disintegration scheme of this element has also been worked out.

About all that is given in the tables about I^{124} is that it is a positron emitter whose half-life is 4.0 days. It was originally prepared by Livingood and Seaborg[3] by bombarding antimony with high energy alpha-particles. I^{126} was also prepared by the same authors,[3] by a number of different reactions. It was found to have a half-life of 13.0 days and to emit electrons, whose maximum energy was determined by absorption as 1.1 Mev, and gamma-rays whose energy was determined as 0.5 Mev by lead absorption.

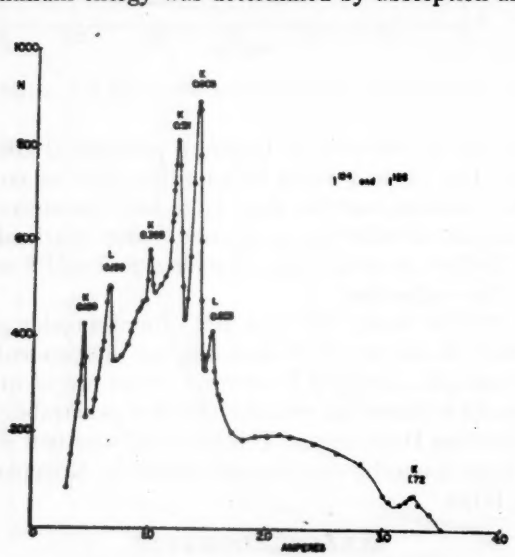

FIG. 1. Spectrum of photoelectrons ejected from lead radiator by gamma-rays of I^{124} and I^{126}.

In the present experiments, metallic antimony was bombarded by 23-Mev alpha-particles in the Indiana University cyclotron. For most of the measurements described here, bombardments of approximately 100 μa-hr. were used.

In order to separate the iodine from the target material, the (powdered) antimony was scraped off the target into a distilling flask. A small amount of a solution of KI, of known iodide concentration, was added to act as carrier. Nitric acid was then added to the mixture and a condenser was connected to the distilling flask. On boiling the mixture, iodine collected in the condenser and was washed out with carbon tetrachloride. The iodine in carbon tetrachloride was then transferred to a separatory funnel, the iodine reduced to iodide by $NaHSO_3$, and the resulting iodide ion was precipitated from the water layer as AgI.

II. APPARATUS AND RESULTS

The spectrum of the photoelectrons ejected from a radiator was measured by a magnetic lens spectrometer which has been described by Kern, Zaffarano, and Mitchell.[1,4] The Geiger-Müller counter used in these experiments was of the end window type with a window thin enough to transmit electrons of around 10 kev and above. Since the window was not supported on a grid, it was possible to measure the complete spectrum with this counter. Sources of active AgI were placed in a copper capsule thick enough to stop all beta-rays. Lead radiators of various thicknesses and one uranium radiator were used in the series of experiments.

In the first experiment, the source was placed in the spectrometer approximately 24 hours after the end of the bombardment. Figure 1 shows the distribution of photoelectrons from a lead radiator of surface density 31 mg/cm². Photoelectron peaks can be seen corresponding to the following gamma-ray lines: *K* and *L* for 0.159 Mev; *K* for 0.395 Mev; *K* for 0.511 Mev, annihilation radiation; *K* and *L* for 0.603 Mev; and a weak *K* line for a gamma-ray of 1.72 Mev. The photoelectron peak for annihilation radiation served as a

[1] Kern, Zaffarano, and Mitchell, Phys. Rev. **73**, 1142 (1948).
[2] C. S. Cook and L. M. Langer, Phys. Rev. **73**, 1149 (1948).
[3] J. J. Livingood and G. T. Seaborg, Phys. Rev. **54**, 775 (1938).
[4] Kern, Mitchell, and Zaffarano, Phys. Rev. **76**, 94 (1949).

calibration point for the spectrum. The strong line at 0.603±0.002 Mev corresponds to the line at 0.603 Mev found in Sb^{124} and the line at 1.72±0.02 Mev, though weak and poorly defined, corresponds to a line seen in Sb^{124} of 1.71-Mev energy.

In order to check on which lines might be due to I^{124} and which to I^{126} the same source was measured on two additional occasions each a weak apart. On the second running, about five days after the run shown in Fig. 1, it was found that the K and L lines corresponding to the gamma-ray at 0.159 Mev were entirely absent. It was shown later that this line has a half-life of 13 hours. Of the remaining lines, successive experiments showed that those due to annihilation radiation, the gamma-ray at 0.603 Mev and that at 1.72 Mev all decayed with a half-life of 4 days, while that corresponding to the gamma-ray of 0.395 Mev decayed with a half-life of 13 days.

Subsequent experiments, in which a uranium radiator was used, confirmed the existence of the line at 1.72 Mev and showed in addition a higher energy line at 1.95±0.05 Mev. A careful search, using the same source, but a lead radiator, brought to light another weak line at 0.73 ±0.01 Mev.

The line at 0.395 Mev has a half-life of 13 days and must be attributed to I^{126}. Those at 0.603, 0.73, 1.72, and 1.95 Mev are attributed to I^{124}. The lines shown by Sb^{124} and those exhibited by I^{124} are compared in Table I. The origin of the line at 0.159 Mev will be discussed below.

The measurement of the particle spectrum—electrons and positrons—was accomplished through the use of two instruments. Since the magnetic lens spectrometer was not equipped with a spiral baffle to separate positive from negative electrons, a small 180°-type spectrometer, described by Peacock and Wilkinson,[5] was used. Actually, spectra were measured in both instruments and analysis of the data showed that quite good agreement was obtained between the two.

TABLE I. Gamma-ray lines from Sb^{124} and I^{124}.

Sb^{124}	I^{124}
0.603	0.603±0.002
0.651	—
0.71	0.73±0.01
1.705	1.72±0.02
2.06	1.95±0.05

The complete spectrum of all particles as measured in the magnetic lens spectrometer is shown in Fig. 2. This spectrum, taken in its entirety with the thin window counter, stretches from approximately 10 kev to 2.2 Mev. The features of the spectrum are: an Auger line, A, at 21.6 kev, K and L conversion lines for the gamma-ray at 0.159 Mev, and K lines for the gamma-rays at 0.395 and 0.603 Mev, together with the electron and positron distribution.

Since the line at 0.159 Mev had been found, in the photoelectron investigation, to decay with a short half-life, measurements were made over this region of the spectrum for a period of several days. The intensity of the K and L lines of the 0.159-Mev gamma-ray was found to decay with a half-life of 13.0±0.5 hr. Since the chemical procedure involved ensures that only iodine is used as the source material and since the activity decays with a 13-hr. period, rather than being observed to grow and eventually reach secular equilibrium with the longer-lived decay products, the 0.159-Mev line is either connected with a metastable state of iodine, or arises from the reaction $Sb(\alpha,2n)I$.

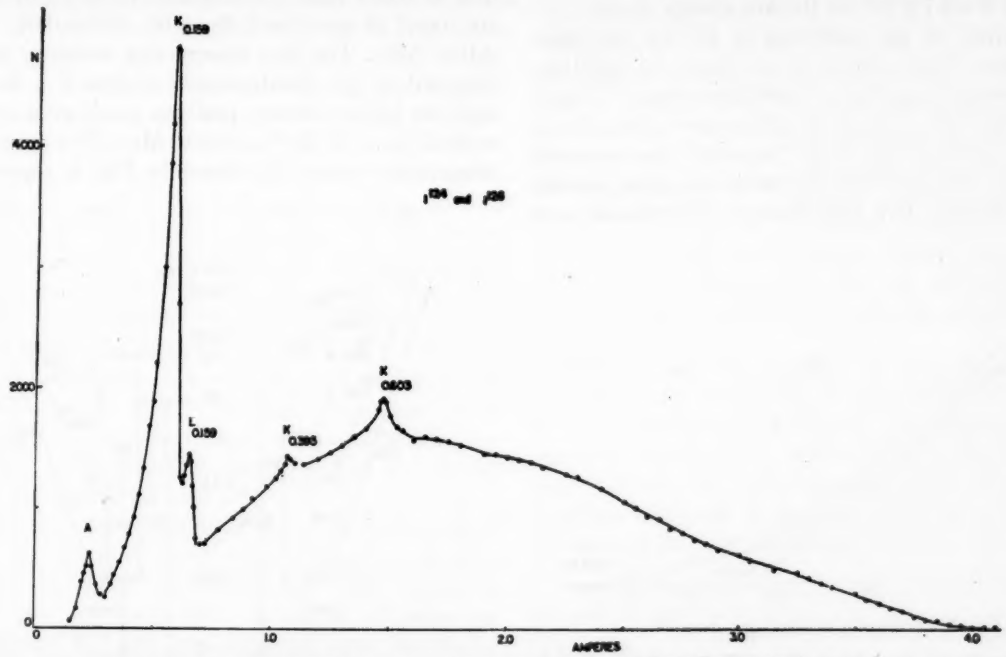

FIG. 2. Particle spectrum (electrons and positrons) of I^{124} and I^{126}.

[5] C. L. Peacock and R. G. Wilkinson, Phys. Rev. 74, 297 (1948).

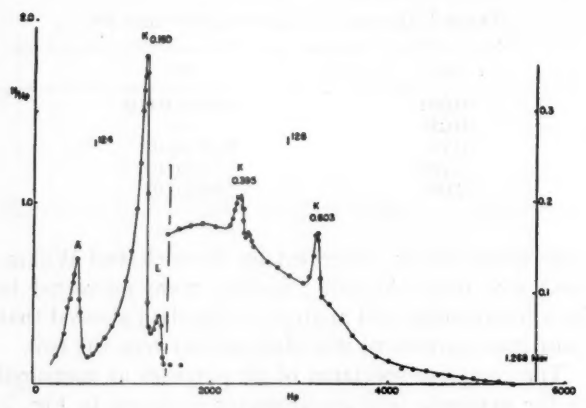

FIG. 3. Internal conversion lines from I^{124} and I^{126} superimposed on beta-ray spectrum of I^{126}.

Figure 3 shows the electron-spectrum taken on the 180° spectrometer. Figures 4 and 5 show the Fermi-plots of the electron spectrum and the positron spectrum, respectively. As in the investigation of the photoelectrons, the internal conversion line associated with the 0.603-Mev gamma-ray decays with a 4-day half-life and is due to I^{124}, while that associated with the 0.395-Mev line decays with a 13-day half-life and is due to I^{126}. In addition, the positron spectrum shows a 4-day half-life and the continuous electron spectrum, one of 13 days.

The analysis of the continuous electron distribution, I^{126}, by the method of Fermi-plots, shows that there are two groups of beta-rays; one with an end point energy of 1.268±0.01 Mev (27 percent abundance) and the other with an end point energy of 0.85±0.03 Mev (73 percent abundance). The comparative half-lives for the two groups are: $ft=2.5\times10^8$ for the high energy group; and $ft=2.7\times10^7$ for the low energy group.

The analysis of the positrons of I^{124} by the same method shows three groups of positrons. In addition, the high energy group has a "forbidden-shape." This is shown in the inset of Fig. 5, in which curve *A* is a plot of the data employing the usual "allowed" functions and curve *B* that obtained when the correction term, usually called "*a*" is used.[6] This type of shape is attributed to an

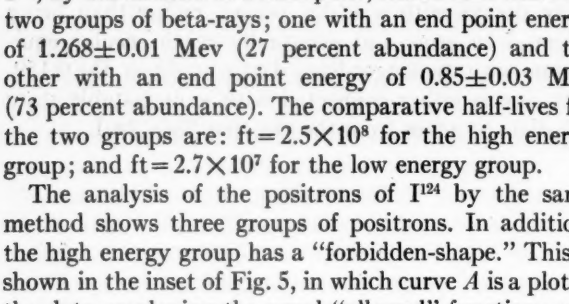

FIG. 4. Fermi-plot of electrons from I^{126}.

[6] E. J. Konopinski, Rev. Mod. Phys. **15**, 209 (1943). For the application of this method, see also C. L. Peacock and A. C. G. Mitchell, Phys. Rev. **75**, 1272 (1949).

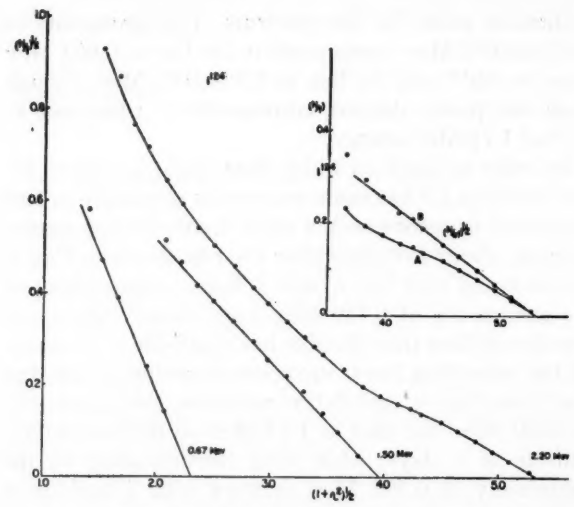

FIG. 5. Fermi-plot of positrons from I^{124}.

axial vector type interaction and is *first forbidden*, with $\Delta j=\pm2$ and a change of parity. The three groups obtained by this analysis have end point energies at 2.20 ±0.01 Mev (51 percent abundance), 1.50±0.01 Mev (44 percent abundance), and 0.67±0.05 Mev (5 percent abundance). The comparative half-lives for the three groups are: 26.8×10^6, 6.8×10^6, and 1.4×10^6, respectively.

III. DISCUSSION OF RESULTS

(a) $I^{124}\rightarrow Te^{124}$. Half-Life 4 Days

I^{124} goes to Te^{124} with the emission of positrons, and with possibly some *K* electron capture. Gamma-rays of energy 0.603±0.002, 0.73±0.01, 1.72±0.02, and 1.95±0.05 Mev are observed, the strongest line being that at 0.603 Mev. In addition, three positron groups are found of energies 2.20±0.01, 1.50±0.01, and 0.67 ±0.05 Mev. The best energy and intensity fit can be obtained in the disintegration scheme if it is assumed that the highest energy positron group goes to the first excited state of Te^{124} at 0.603 Mev. The proposed disintegration scheme is shown in Fig. 6 together with

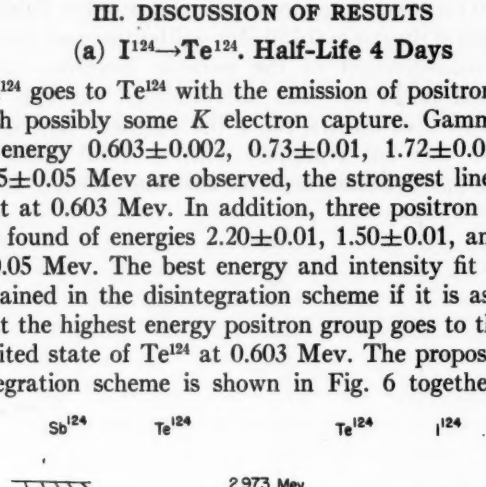

FIG. 6. Disintegration scheme of I^{124}, also showing disintegration scheme of Sb^{124}.

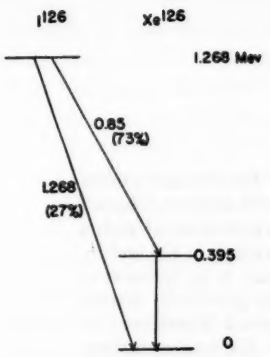

FIG. 7. Disintegration scheme of I^{126}.

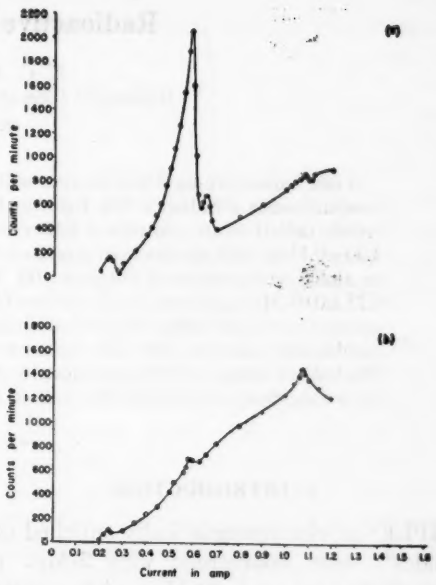

FIG. 8. Low energy particle spectrum of radiations from iodine. (a) Normal antimony bombarded by alpha-particles; (b) antimony 123 bombarded by alpha-particles.

that of Sb^{124}. The levels fit quite well, within the limit of the experimental errors, with those previously determined. The fit obtained for the lowest energy positron group is not good, but this group is quite weak and is determined as a result of two previous subtractions. The fact that the line at 1.72 Mev appears, where there is apparently no associated positron group, suggests that it arises as a result of *K*-capture.

(b) $I^{126} \rightarrow Xe^{126}$. Half-Life 13 Days

The spectrum of I^{126} consists of two beta-ray groups of energies 1.268 ± 0.010 (27 percent) and 0.85 ± 0.01 (73 percent) Mev together with one internally converted gamma-ray of energy 0.395 ± 0.005 Mev. The disintegration scheme is given in Fig. 7.

(c) Remarks on the 13-Hour Activity

From the chemical procedures involved and from the fact that the line at 0.159 Mev is observed to decay with a 13-hr. half-life, rather than to grow and eventually reach secular equilibrium with one of the longer periods, it is supposed that the 0.159-Mev line arises from an isotope of *iodine*. A careful search was made for any positrons or beta-ray groups which might decay with a 13-hr. half-life but none was found. It is therefore certain that this state decays by the emission of an internally converted gamma-ray only. The question now arises as to whether this activity belongs to I^{124}, to I^{126}, or to an iodine formed from $Sb(\alpha,2n)I$. In order to get information on this point, I^{127} was bombarded with fast neutrons—Li(*d*, *n*)—at the cyclotron. The source was, unfortunately, not strong enough to measure in a spectograph. The period was followed with a counter. Measurements of the electrons on the one hand and the gamma-rays on the other, showed only the 25-min. period of I^{128} and the 13-day period of I^{126}. No 13-hr. component was observed. While not conclusive, this experiment suggests that the 13-hr. period is not connected with I^{126}.

A conclusive experiment, however, was performed in which the results obtained using ordinary antimony, on the one hand, and separated Sb^{123} (96.7 percent) on the other, were compared. A sample of separated Sb^{123}, weighing 100 mg, was obtained from the Stable Isotopes Division of the Oak Ridge National Laboratory. In order to make the comparison, a sample of ordinary antimony, weighing 100 mg, was given a total irradiation of 80-μa-hr. of 23-Mev alpha-particles, and a source of iodine prepared in the usual manner. The low energy part of the beta-ray spectrum from this source was investigated in the magnetic lens spectrograph. A source was prepared in the same manner from the separated Sb^{123} sample, precautions being taken to avoid, as far as possible, any contamination from ordinary antimony. The results of both measurements are shown in Fig. 8, in which curve (a) gives the results for the ordinary sample and (b) those for the separated sample. It will be seen at once that, although the separated sample had a somewhat stronger activation as judged from the intensity of the beta-ray spectrum and the internal conversion line for the 0.395-Mev gamma-ray, the internal conversion line for the 0.159-Mev gamma-ray is extremely weak in the separated sample while the peak for this line, in the normal sample, gives a counting rate of about 2000 counts/min. This activity is therefore connected with the alpha-particle bombardment of Sb^{121} and is probably to be attributed* to I^{123}.

This research was assisted by the joint program of the ONR and AEC. The authors wish to thank Drs. B. D. Kern and D. J. Zaffarano who helped in the early stages of this investigation, and also Miss E. Lanterman for her help with the chemistry. They are also indebted to Dr. M. B. Sampson and the cyclotron crew for making the bombardments.

* *Note added in proof:* Drs. I. Perlman and L. Marquez have informed us that they obtained this activity from the reaction $Sb^{121}(\alpha,2n)I^{123}$. This isotope probably decays by *K*-electron capture to Te^{123} which emits the 159 kev gamma-ray. [See R. D. Hill, Phys. Rev. 76, 186A (1949)].

Radioactive In^{107}, In^{108}, In^{109}, and Sn^{108}

E. C. MALLARY* AND M. L. POOL
Mendenhall Laboratory, Ohio State University, Columbus, Ohio
(Received August 1, 1949)

A new indium isotope which decayed with a 33±2-min. half-life has been produced by deuteron and proton bombardments of cadmium 106. Evidence for the assignment of the activity to indium 107 is given. Characteristic radiations are positrons of 2-Mev energy and gamma-rays. An indium isotope which decayed with a 4.30±0.15-hr. half-life has been produced by a deuteron and proton bombardment of cadmium 108 and by an alpha-bombardment of cadmium 106. The assignment is made to indium 109. Decay is by emission of 0.75±0.05-Mev positrons, by *K*-electron capture, and by emission of gamma-rays. Two genetically related isotopes in tin and indium have been assigned to mass number 108. The tin isotope, which is produced by bombarding cadmium 106 with alpha-particles, decays with a half-life of 4.5 hr. by *K*-electron capture. The indium isotope, which is produced by the decay of the tin isotope and by bombarding cadmium 108 with deuterons, decays with a half-life of about 55 min. by emitting positrons of 2-Mev energy and gamma-rays.

I. INTRODUCTION

SAMPLES of electromagnetically enriched cadmium oxides** were bombarded with 5-Mev protons, 10-Mev deuterons, and 20-Mev alpha-particles. In Table I are given the isotopic abundance supplied with each sample of enriched cadmium and the impurities found by spectroscopic analysis. Included in this table for purposes of comparison are the abundances of natural cadmium.

The samples were prepared for bombardment by pressing the cadmium oxide into slots in chemically pure aluminum target blocks. Resulting activities were measured with a spectrometer counter[1] and with a Wulf unifilar electrometer connected to a calibrated Freon-filled ionization chamber placed below an electromagnet.

Calcium impurity, though not listed in Table I, was found in all enriched cadmium isotopes. Initially this resulted in considerable confusion because calcium bombarded with alpha-particles produced a large yield of scandium 43 which decayed with 3.92-hr. half-life by emission of 1.13-Mev positrons. The most satisfactory method found to remove the scandium from the indium and the tin was to separate the tin by distillation and then to precipitate the scandium from the indium.

After proton bombardments of cadmium oxide, fluorine was removed. If the oxide could be efficiently reduced to the metal prior to the proton bombardment, this would not be necessary. In the reduction of natural cadmium oxide there was too much loss of cadmium by sublimation to jeopardize the small available supply of enriched cadmium oxide.

TABLE I. Isotopic abundance of enriched cadmium.

	Percent abundance of isotope of mass numbers 106	108	110	111	112	113	114	116	Impurities
Sample enriched in Cd 106	*32.9*	1.5	9.4	7.7	13.5	11.1	19.1	4.7	None
Sample enriched in Cd 108	1.5	*24.8*	33.2	12.0	10.6	4.5	10.3	3.6	0.08% Pb 0.04% Ag 0.04% Cu
Sample enriched in Cd 110	0.1	0.2	*70.0*	18.6	7.0	1.3	2.3	0.5	None
Natural cadmium	1.2	0.9	12.4	12.7	24.1	12.3	28.9	7.6	

II. 33-MINUTE INDIUM 107

No previous assignment to indium 107 and no radioactive isotope in indium with a 33-min. half-life has been reported.

When cadmium enriched in isotope 106 was bombarded with deuterons and with protons, there was produced in the indium fraction a new radioactive isotope which decayed with a 33±2-min. half-life by emitting positrons and gamma-rays in excess of the annihilation radiation. The activity was followed for more than seven half-lives. After bombarding cadmium enriched in isotopes 108 or 110 with deuterons and with protons, no such activity was found. Therefore, the activity is attributed to either indium 106 or 107.

The evidence in favor of indium 107 comes from the fact that cadmium 107, which is known to decay with a half-life of 6.7 hr., was found by irradiating cadmium 106 with protons. However, it is conceivable that a very short-lived isotope could be located at indium 107 instead of the isotope which decays with a 33-min. half-life. The mass assignment is thus made to isotope 107 instead of 106.

The positron energy of about 2 Mev was determined with the spectrometer counter.

III. 4.3-HOUR INDIUM 109

It has been reported that the bombardment of silver with alpha-particles produced a radioactive indium isotope which decayed with a half-life of 6.5 hr.[2] The

* Lt. Col. USAF, research under auspices of USAFIT, Wright-Patterson Field, Ohio.

** Supplied by the Y-12 plant, Carbide and Carbon Chemicals Corporation, through the Isotope Division, U. S. AEC, Oak Ridge, Tennessee.

[1] L. L. Woodward and D. A. McCown, Rev. Sci. Inst. **19**, 823 (1948).

[2] D. J. Tendam and H. L. Bradt, Phys. Rev. **72**, 527, 1118 (1947).

assignment of this isotope was to mass number 109. Later a similar experiment indicated a half-life of 5.2 hr.[3]

When cadmium enriched in isotope 106 was bombarded with alpha-particles and cadmium enriched in isotope 108 was bombarded with deuterons and protons, there was produced in the indium fraction a radioactive isotope which decayed with a half-life of 4.30±0.15 hr. by emitting positrons and gamma-rays in excess of the annihilation radiation. The activity was followed for more than six half-lives. The positron- and gamma-activities both decrease with this half-life. The ratio of the ionization produced by the alpha-induced positron- and gamma-activities is about 12 for the ionization chamber used. This ratio for the same activities induced by protons is also about 12. However, for the alpha-induced activities of scandium 43 which decays with a 3.92-hr. half-life, this ratio is about 93.

This indium activity was not found after bombarding cadmium enriched in isotopes 106 or 110 with deuterons and protons, nor after bombarding cadmium enriched in isotopes 108 or 110 with alpha-particles. Therefore, this activity is attributed to either indium 108 or 109. If it is attributed to indium 108, the reaction $Cd^{106}(\alpha,np)In^{108}$ would be required. The similar reaction $Cd^{108}(\alpha,np)In^{110}$ would produce indium 110 which decays with a 1.1-hr. half-life, but this reaction was not detected with the energy used. If this 4.30-hr. activity is attributed to indium 109, the reaction $Cd^{106}(\alpha,p)In^{109}$ would be required. The similar reaction $Cd^{108}(\alpha,p)In^{111}$ was easily observed. Indium 111 decays with 2.84-day half-life. Therefore the isotope which decays with a 4.3-hr. half-life is assigned to indium 109. The expected daughter, silver 109 which decays with a 470-day half-life,[4] was not found as would be surmised from a consideration of the amount of this long-lived x-ray emitter that would be produced.

The x-ray decay curve indicates also a 4.3-hr. half-life. Thus indium 109 decays also by K-electron capture. By the use of the calibrated ionization chamber the ratio of the modes of decay by K-electron capture to positron emission is found to be about 8 to 1.

The energy of the positrons from indium 109 is 0.75±0.05 Mev. The absorption curve and the histograms from which this was determined are shown in Fig. 1.

Indium 109, which decays with a 4.3-hr. half-life is not to be confused with the well-known indium 115 which decays with a half-life of 4.5 hr. The latter is characterized by gamma-emission and by 0.34-Mev internally converted electrons.

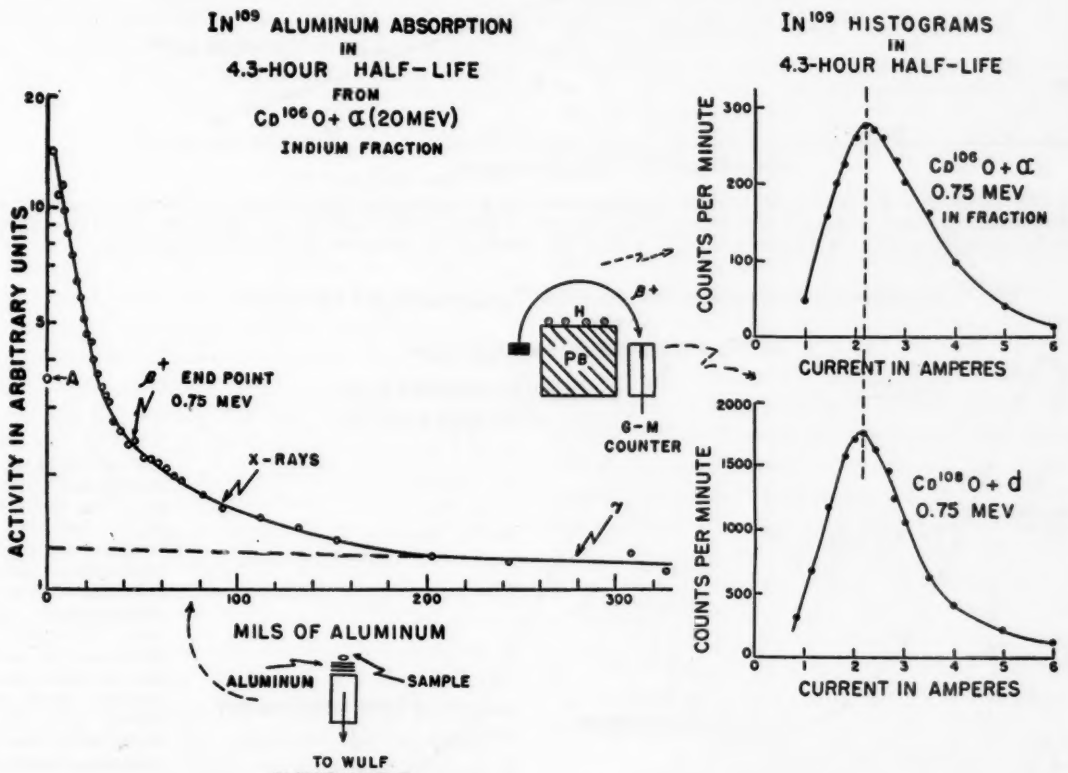

FIG. 1. Aluminum absorption of the alpha-induced activity and histograms of alpha- and deuteron-induced activities in indium 109. The energy of the positrons is shown to be 0.75 Mev. Point A on the ordinate scale of the absorption plot is the intensity of the total electromagnetic radiation from indium 109 for zero absorber thickness.

[3] S. N. Ghoshal, Phys. Rev. **73**, 417 (1948).
[4] Gum, Thompson, and Pool, Phys. Rev. **76**, 184 (1949).

IV. 55-MINUTE INDIUM 108

An isotope decaying with a 5-hr. half-life has been questionably assigned to indium 108. The reaction postulated is $Ag(\alpha,3n)$.[3]

When cadmium enriched in isotope 110 was bombarded with deuterons, indium 110 was produced. Indium 110 is known to decay with a 1.1-hr. half-life by emitting 1.6-Mev positrons. When cadmium enriched

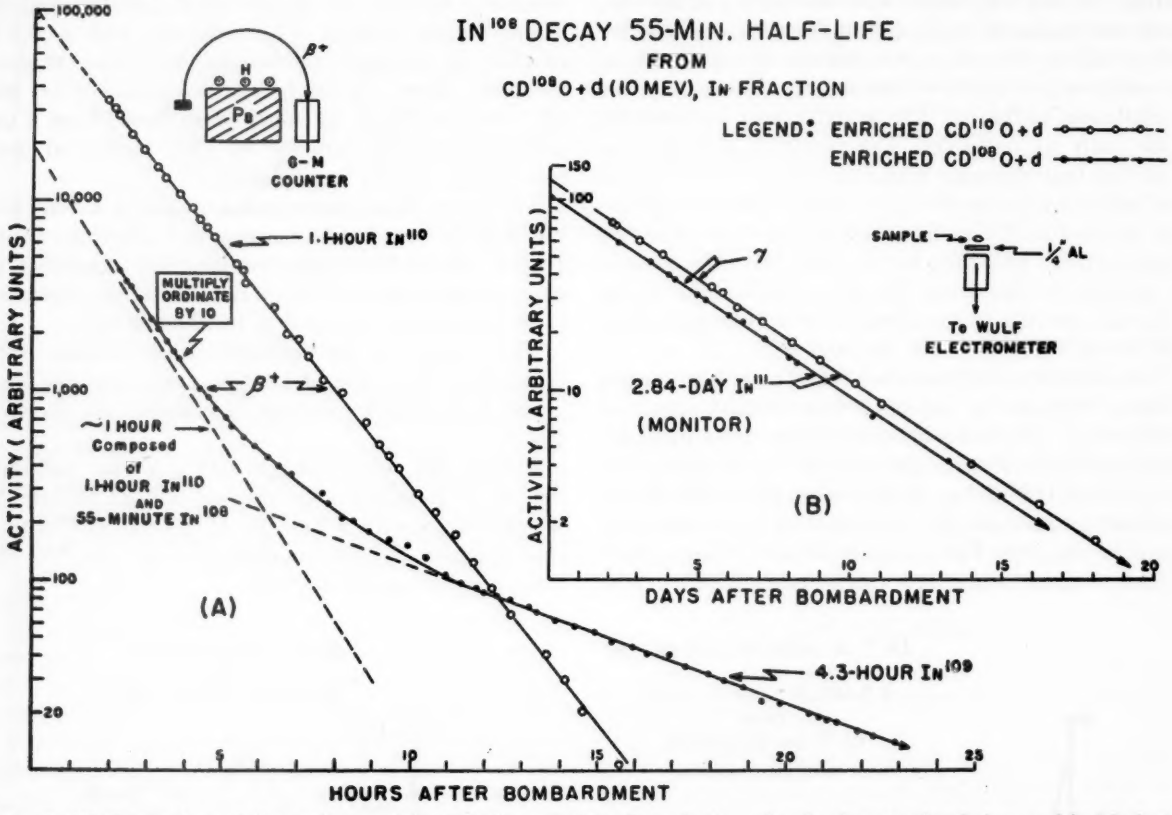

FIG. 2. (A) Comparison of the positron-activity in indium resulting from deuteron bombardments of cadmium enriched in isotope 110, and cadmium enriched in isotope 108. Indium 108 is shown to decay with a half-life less than 1 hr. (B) The comparison was facilitated by monitoring with the gamma-activity of indium 111 produced by the same deuteron bombardments.

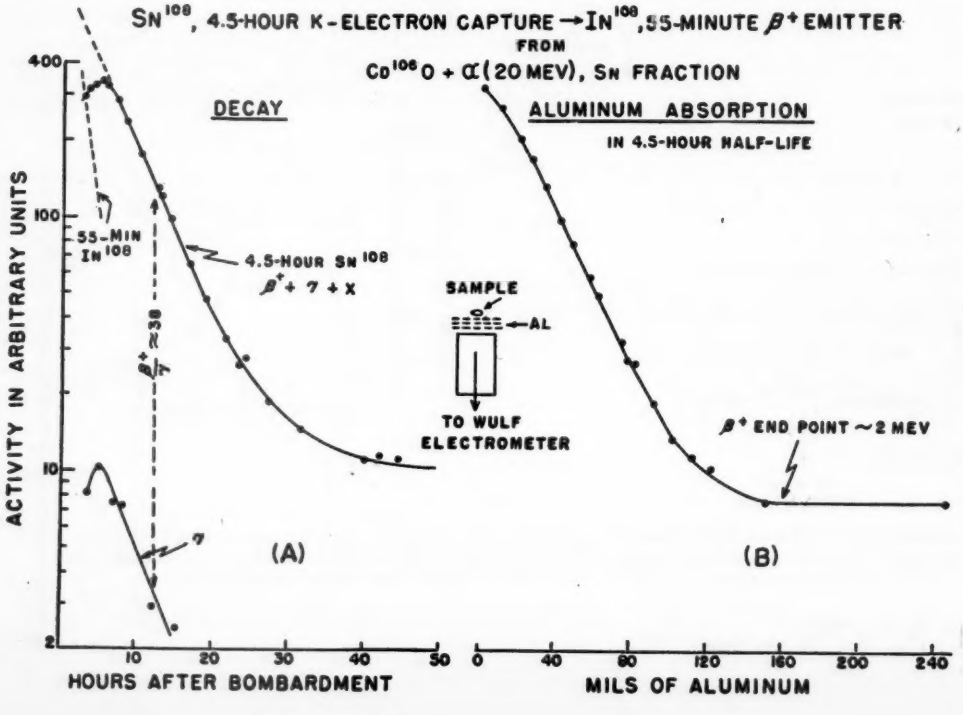

FIG. 3. (A) Build-up of the activities in the tin fraction and the subsequent decay of tin 108 with a 4.5-hr. half-life. The activities were produced by bombarding cadmium enriched in isotope 106 with alpha-particles. (B) Aluminum absorption of the alpha-induced activity in the tin fraction. The absorption which was taken shortly after the activity of the tin fraction reached a maximum, shows that only one positron component was present.

in isotope 108 was given an equal bombardment there was produced in the indium fraction radioactive isotopes which decayed with about a 1-hr. half-life by emitting about 2-Mev positrons. The positron energy was measured with the spectrometer counter. The decay curves for both of these bombardments are shown in Fig. 2(A). Comparison of these positron-activities was facilitated by monitoring with the gamma-radiation from indium 111 which was also produced. Indium 111 decays with a 2.84-day half-life. Figure 2(B) shows the decay curves for indium 111 produced by each of these bombardments. More than twice as much positron-activity resulted from the bombardment of cadmium enriched in isotope 108 than could be attributed to the cadmium 110 present in the cadmium enriched in isotope 108. Therefore, the activity observed must have been composed of the positron-activity of indium 110 which decays with a 1.1-hr. half-life and the positron-activity of another indium isotope which decays with a half-life shorter than the approximate 1-hr. half-life measured. No indium isotope decaying with a comparable half-life is produced by bombarding either cadmium 106 or 110 with deuterons. Therefore, this isotope is either indium 108 or 109.

Cadmium 106 bombarded with alpha-particles does not produce this activity in a measurable quantity. Since the reaction Cd(α,p)In has been observed and the reaction Cd(α,np)In has not been detected with the energy used, the isotope which decays with a half-life less than 1 hr. is assigned to indium 108.

V. 4.5-HOUR TIN 108

No previous assignment to tin 108 has been reported. It has been reported that a tin isotope was produced by a deuteron bombardment of antimony. The tin isotope decayed with 4.5-hr. half-life by K-electron capture to an indium isotope which decayed with a 72-min. half-life by emitting 2.2-Mev positrons.[5]

When cadmium enriched in isotope 106 was bombarded with alpha-particles the intensity of the positron- and gamma-activities of the tin fraction increased initially; the tin fraction then decayed with a 4.5-hr. half-life. Figure 3(A) shows this initial build-up and the subsequent decay of the tin fraction. No such activities were found when cadmium enriched in isotopes 108 or 110 were bombarded with alpha-particles. Therefore this activity results from bombarding cadmium 106 with alpha-particles.

When the activity of the tin fraction reached a maximum, indium was separated chemically. The activity of the remaining tin fraction then increased initially as shown in Fig. 4. The shortest half-life observed in the indium fraction was about 55 min. as also shown in Fig. 4. Positrons were emitted by the indium fraction.

The energy of the positrons emitted by the tin fraction was about 2 Mev. The energy was measured by an aluminum absorption taken shortly after the activity reached a maximum. Figure 3(B) shows the absorption curve. Only one positron component was observed in the tin fraction and the indium, formed from the tin, decays by positron emission; therefore, the tin must decay primarily by K-electron capture.

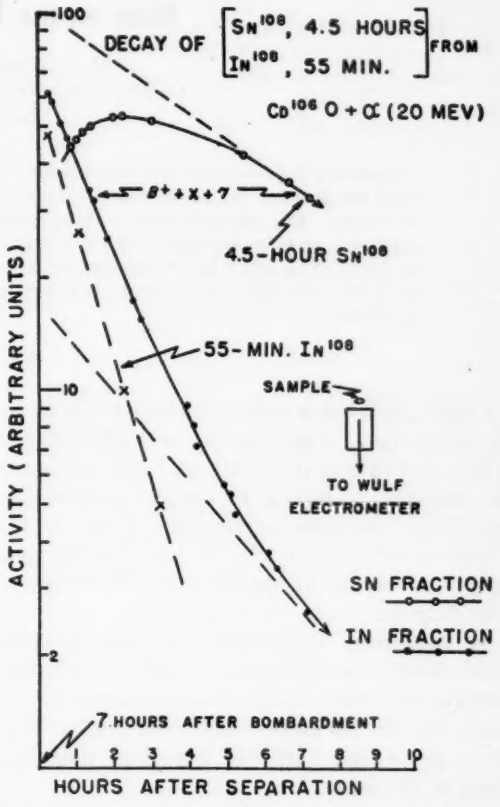

FIG. 4. Decay of indium 108 and the build-up of the activity in the tin from which the indium was removed. Indium 108 was produced by the decay of tin 108. Tin 108 was produced by bombarding cadmium 106 with alpha-particles. Indium 108, which emits positrons, is shown to decay with about a 55-min. half-life.

Since this tin isotope was made from an alpha-particle bombardment of cadmium 106, it must be either tin 108 or 109. The daughter isotope in indium must be either indium 108 or 109. However, it has already been shown that indium 109 decays with a half-life of 4.3 hr. and that indium 108 decays with a half-life of less than 1 hr. Therefore, the daughter isotope of the tin fraction is indium 108, and the parent tin isotope is tin 108.

The gamma-activity of the tin fraction increases during the growth of the daughter indium 108. Thus gamma-radiation is associated with the decay of indium 108. The gamma-radiation is in excess of the annihilation radiation.

VI. ACKNOWLEDGMENTS

Thanks are due to Mr. H. L. Finston and to Mr. R. M. Dyer for the chemical separation. Grateful acknowledgment is made for the support received from the Ohio State Development Fund and the Graduate School.

[5] G. T. Seaborg and I. Perlman, Rev. Mod. Phys. 20, 613 (1948).

Note on the Decay of the π-Meson

M. RUDERMAN AND R. FINKELSTEIN
California Institute of Technology, Pasadena, California
(Received July 25, 1949)

Assuming the symmetric coupling scheme proposed by Wheeler and Tiomno, and others, we have calculated the ratio of the decay rate π-meson$\rightarrow$electron+neutrino to the decay rate of π-meson$\rightarrow\mu$-meson +neutrino. The electron-neutrino decay proceeds faster, in disagreement with experiment, unless the π-meson is pseudoscalar and the β-decay coupling is pseudovector. Hence if the symmetric coupling scheme is corect and no other direct couplings are introduced, the π-meson must be pseudoscalar and β-decay must be at least partially pseudovector. If symmetric coupling is not assumed, no conclusion of this kind can be drawn.

ALTHOUGH the π-meson appears to decay into a μ-meson and a neutrino at least 100 times faster than into an electron and neutrino, the latter process is to be expected according to certain formulations of meson theory. We have therefore calculated the rate of the decay $\pi\rightarrow e+\nu$, and wish to mention the possible bearing of our results on the nature of the π-meson and nuclear β-decay.

It is customary to assume that the π-meson is coupled directly to nucleons, in order to explain its production in nuclear collisions and to account, at least partially, for nuclear forces. Assuming further that the nucleons are Dirac particles, one then postulates a coupling of the form

$$G(\varphi_P{}^{+}O\varphi_N)\psi_\pi, \tag{1}$$

or a similar coupling involving first derivatives of ψ_π, where O is some Dirac operator. This interaction leads to the real capture process

$$N+\pi^{+}\rightarrow P^{+},$$

but it also permits the virtual decomposition of the π:

$$\pi^{+}\rightarrow P^{+}+N_{-}, \tag{2}$$

where N_- signifies an anti-neutron.

On the other hand, to account for β-decay along the general lines of the Fermi or Gamow-Teller theories, one postulates the interaction

$$g(\varphi_N{}^{\dagger}A\varphi_P)(\varphi_e{}^{\dagger}A\varphi_\nu),$$

where A is also a Dirac operator. This interaction leads to the observed β-process

$$N\rightarrow P^{+}+e^{-}+\nu,$$

but it also leads one to expect the reaction

$$P^{+}+N_{-}\rightarrow e^{+}+\nu. \tag{3}$$

The virtual decomposition (2) followed by (3) leads to the real decay

$$\pi^{+}\rightarrow e^{+}+\nu. \tag{4}$$

It can then be concluded that any theory which couples π-mesons to nucleons also predicts the $\pi\rightarrow(e,\nu)$ decay. This argument depends not on the existence of real anti-neutrons, but only on the role of such particles in virtual processes.

Since (4) has not been observed experimentally, we have compared its rate with that of the observed decay

$$\pi^{+}\rightarrow\mu^{+}+\nu. \tag{5}$$

To do this, a further hypothesis must be introduced by postulating the nature of the field interaction responsible for (5). One may assume a direct coupling between the π- and μ-fields,[1] or one may assume that (5) goes indirectly. We have tested the symmetrical coupling scheme proposed by Wheeler and others,[2] according to which (5) goes indirectly. According to this scheme the following three processes

$$\mu\text{-capture}\quad \mu^{-}+P\rightarrow N+\nu, \tag{6a}$$

$$\beta\text{-decay}\quad N\rightarrow P+e^{-}+\nu, \tag{6b}$$

$$\mu\text{-decay}\quad \mu^{-}\rightarrow e^{-}+\nu+\nu, \tag{6c}$$

result from the direct couplings

$$g_a(\varphi_N{}^{+}A\varphi_P)(\varphi\nu^{+}A\varphi_\mu), \tag{7a}$$

$$g_b(\varphi_N{}^{+}B\varphi_P)(\varphi_\nu{}^{+}B\varphi_e), \tag{7b}$$

$$g_c(\varphi_\nu{}^{+}C\varphi_\mu)(\varphi_\nu{}^{+}C\varphi_e). \tag{7c}$$

All fields in (6) are spinor fields; A, B, and C are Dirac operators.

It has been found[2] that $g_a\cong g_b\cong g_c$. We have assumed

$$g_a=g_b=g_c$$

and

$$A=B=C. \tag{8}$$

These three couplings are thus assumed to be of the same nature and strength. According to the sym-

[1] R. E. Marshak and H. A. Bethe, Phys. Rev. **72**, 506 (1947); R. Latter and R. F. Christy, Phys. Rev. **75**, 1459 (1949); Taketani, Nakamura, Ono, and Sasaki, Phys. Rev. **76**, 60 (1949).

[2] J. Tiomno and J. A. Wheeler, Rev. Mod. Phys. **21**, 153 (1949); O. Klein, Nature **161**, 897 (1948); Lee, Rosenbluth, and Yang, Phys. Rev. **75**, 905 (1948).

[3] Pseudoscalar β-decay does not give the agreement in coupling constants which makes the symmetric coupling scheme so attractive.

TABLE I. Ratio of $\pi\to(e,\nu)$ to $\pi\to(\mu,\nu)$-decay for couplings (1) and (7).

Meson \ Type of β-decay	Scalar	P-scalar	Vector	P-vector	Tensor
Scalar	5.1	f	f	f	f
P-scalar	f	5.1	f	1.0×10^{-4}	f
Vector	f	f	4.0	f	2.4
P-vector	f	f	f	4.0	f

metrical scheme (5) is a second-order process

$$\pi^+\to P^+ + N_-, \tag{9a}$$

$$P^+ + N_-\to\mu^+ + \nu. \tag{9b}$$

The matrix element for (9b) is contributed by (7a). We have compared the rates of the two second-order decays (4) and (5) for various operators in the fundamental interaction (7) and several meson field couplings in (1). The decay may progress through either of two intermediate states: (a) A π-meson disappears with the production of a pair of virtual nucleons which in turn are annihilated with the creation of a (μ,ν)-pair. (b) A vacuum fluctuation produces a (μ,ν)-pair and a nucleon pair. The latter disappear with the absorbtion of the π-meson. The transition probability is given by:

$$\tau^{-1}=2\pi|H|^2\rho(E)=\sum_{\sigma_\nu\sigma_\mu}2\pi g^2G^2\left|\int d\mathbf{p}\sum_{\sigma P\sigma N}\left(\frac{1}{2\mu_\pi}\right)^{\frac{1}{2}}\right.$$
$$\times\left(\frac{\varphi_\pi\cdot\langle u_P{}^\dagger Ou_N\rangle\langle u_N{}^\dagger Au_P\rangle\cdot\langle u_\mu{}^\dagger Au_\nu\rangle}{2E_P-\mu_\pi}\right.$$
$$\left.\left.+\frac{\langle u_P{}^\dagger Au_N\rangle\cdot\langle u_\mu{}^\dagger Au_\nu\rangle\varphi_\pi\cdot\langle u_N{}^\dagger Ou_P\rangle}{2E_P+\mu_\pi}\right)\right|^2\rho(E), \tag{10}$$

$\hbar=c=1$. μ_π is the mass of the π-meson. u_P, u_N, u_μ, u_ν are the spinors for free protons, anti-neutrons, mesons, and anti-neutrinos, respectively. φ_π is the amplitude of the π-meson wave function. $2E_P$ is the energy of the virtual nucleon pair and the integration is over all momenta of the nucleons. This integration leads to a divergent answer for the two rates of decay $\pi\to e+\nu$ and $\pi\to\mu+\nu$. The same divergent integral appears in both. If this integral can be made finite the ratio of decay rates is independent of how this is accomplished.

Taking $\mu_P=\mu_N$ and using the masses $\mu_\pi=286$, $\mu_\mu=215$, $\mu_e=1$, $\mu_\nu=0$, the ratio of density of final states for the competing decays is

$$\frac{\rho_e(E)\text{decay into }(e,\nu)}{\rho_\mu(E)\text{decay into }(\mu,\nu)}=3.3$$

Table I gives the ratio of $\pi\to(e,\nu)$ to $\pi\to(\mu,\nu)$-decay for couplings (1) and (7). Table II gives this ratio when the coupling of (1) involves first derivatives of ψ_π. f signifies a forbidden transition for both processes. In most instances the decay of the π-meson is forbidden. The symmetric coupling scheme is in agreement with

TABLE II. Ratio of $\pi\to(e,\nu)$ to $\pi\to(\mu,\nu)$-decay when the coupling of (1) involves first derivatives of ψ_π.

Meson	Scalar	P-scalar	Vector	P-vector	Tensor
Scalar	f	f	f	f	f
P-scalar	f	5.1	f	1.0×10^{-4}	f
Vector	f	f	4.0	f	2.4
P-vector	f	f	f	f	2.4

experimental facts only if the π-meson is pseudoscalar (with either pseudoscalar or pseudovector coupling to nucleons) and the β-decay coupling contains a pseudovector term. According to the table the β-decay coupling may also contain arbitrary admixtures of scalar, vector, and tensor terms, since these do not contribute to the $\pi-\mu$ or $\pi-e$ decays. This result is in agreement with Wigner's conclusion[4] that the evidence from nuclear β-decay requires a pseudovector coupling and does not exclude scalar or pseudoscalar terms.

The transition probability for the pseudoscalar meson decay is

$$\tau^{-1}=\left(\frac{G^2}{\hbar c}\right)\left(g^2\frac{\mu_\pi{}^2\mu_P{}^2c^8}{\hbar^6c^6}\right)\left(\frac{\mu_\pi c^2}{\hbar}\right)\left(\frac{\mu_\pi{}^4-\mu_\mu{}^4}{\mu_\pi{}^4}\right)$$
$$\times\left(\frac{\mu_\pi{}^2-\mu_\mu{}^2}{64\pi^5\mu_\pi{}^2}\right)\left(1-\frac{cp_\mu}{E_\mu}\right)$$
$$\times\left[\ln(\theta+\{\theta^2+1\}^{\frac{1}{2}})-\frac{\theta}{(\theta^2+1)^{\frac{1}{2}}}\right]^2, \tag{11}$$

where θ is the cut-off momentum in units of μ_PC. A covariant calculation using an invariant cut-off procedure of Feynman[5] leads to the same expression with the bracket replaced by

$$\left[\ln\left(\frac{\lambda}{\mu_P}\right)+1-\frac{(4\mu_P{}^2-\mu_\pi{}^2)^{\frac{1}{2}}}{\mu_\pi}\sin^{-1}\left(\frac{\mu_\pi}{2\mu_P}\right)\right]^2, \tag{11a}$$

where terms of order μ_P/λ and higher have been dropped. λ is a cut-off with the dimensions of mass. For large cut-offs both expressions are essentially equal. Although the expressions (11) are only logarithmically divergent, they are sensitive to the choice of cut-off. Choosing $G^2/\hbar c=\frac{1}{3}$ and $g=2\times10^{-49}$ erg-cm^3, if $\theta=1$, $\tau=9\times10^{-6}$ sec.; $\theta=10$, $\tau=6\times10^{-8}$ sec.; $\theta=100$, $\tau=1\times10^{-8}$ sec. Steinberger[6] has also calculated the lifetime for this decay, and after cutting off with Pauli regulators, he finds 2×10^{-2} sec. (pseudoscalar coupling). In view of the sensitivity of the result to the cut-off procedure, and in the absence of any reliable theory, we believe that no conclusion, either for or against symmetric coupling, can be drawn from a consideration of the *absolute* rate. We emphasize, however, that the *ratios* in the table are independent of the divergent integrals. The above calculation is also open to the

[4] E. P. Wigner, Phys. Rev., to be published.
[5] R. P. Feynman, Phys. Rev. 74, 1430 (1948).
[6] J. Steinberger, Phys. Rev., to be published.

objections (1) that it is based on the Dirac theory for the nucleons, including, in particular, the virtual role of the anti-nucleons and (2) that it employs the usual perturbation methods of field theory. If these objections are tentatively ignored, the calculation suggests that the symmetric coupling scheme is tenable only if the π-meson is pseudoscalar and β-decay coupling is at least partially pseudovector. On the other hand, it is possible that a correct calculation of the divergent integrals will not agree with experiment even in the pseudoscalar case. In that event it would seem natural to reject the symmetric coupling scheme in favor of direct π–μ-coupling.[7]

We wish to thank Dr. R. F. Christy for helpful discussion.

[7] According to Lopes, Phys. Rev. **74**, 1722 (1948) the hypothesis of *direct* π–μ-coupling demands a pseudoscalar meson with pseudovector coupling if one wishes to retain the Yukawa scheme for β-decay. Yukawa (Rev. Mod. Phys. **21**, 474 (1949)) has pointed out that this peculiarity of the pseudoscalar case can also be inferred from the earlier work of Sakata. However, according to more detailed calculations the direct coupling scheme does not give satisfactory lifetimes for β-decay, even if the π-meson is pseudoscalar.

PHYSICAL REVIEW VOLUME 76, NUMBER 10 NOVEMBER 15, 1949

Precise Measurement of the Gyromagnetic Ratio of He^3

HERBERT L. ANDERSON
Argonne National Laboratory and Institute for Nuclear Studies, University of Chicago, Chicago, Illinois
(Received July 18, 1949)

The gyromagnetic ratio of He^3 was compared to that of H_2 gas by the magnetic resonance method with the result

$$|\gamma(He^3)|/|\gamma(H_2)| = 0.7617866 \pm 0.0000012.$$

To obtain the nuclear gyromagnetic ratios, a diamagnetic correction must be made which raises this by approximately 38 parts in 10^6 to

$$|\gamma_{He^3}|/|\gamma_p| = 0.761815.$$

Intensity measurements were consistent with a spin of $\frac{1}{2}$. In nuclear magnetons, the magnetic moment $\mu_{He^3} = (-)2.12815$ based on the value $\mu_p = 2.79353$ obtained by Taub and Kusch. The negative sign has not yet been verified.

A PRELIMINARY measurement of the gyromagnetic ratio of He^3 has already been reported in this journal.[1] In the present paper, a new series of measurements also based on the magnetic resonance method[2,3] is reported using the same sample of He^3, but in which the capabilities of the method were more fully exploited.

MAGNETIC RESONANCE METHOD

The technique used was a refinement of the one which was used in a measurement of H^3,[4] being quite similar to that developed by Bloembergen, Purcell, and Pound.[5] The sample formed the core of a small coil which was one element of a radiofrequency bridge. The coil and sample were placed in the magnetic field between the poles of an electromagnet, with the axis of the coil at right angles to that of the poles of the magnet. Under these circumstances, a nucleus with spin I may orient itself in $2I+1$ ways with respect to the direction of the magnetic field, each having a different energy value. Transitions between neighboring states will be induced when the frequency of the signal applied to the coil satisfies the resonance condition,

$$2\pi\nu = |\gamma| H. \tag{1}$$

Here, $\gamma = \mu/\hbar I$ is the ratio of the magnetic moment to the angular momentum of the nucleus, ν is the frequency in cycles per second, and H is the magnetic field intensity in gauss at the nucleus.

The magnetic field is modulated about the resonance value by a small amount at 30 cycles per second. Under suitable conditions,* the transitions which occur each time the resonance value of the field is traversed produce a change in the impedance of the coil and an unbalance of the bridge. Thus, the magnetic resonance effect produces a 30-cycle modulation in the radiofrequency signal which feeds the bridge, and this may be detected by means of an ordinary radio receiver. The extreme sharpness of the resonance which may be obtained makes possible the great accuracy of the method.

It is seen that a measurement of γ requires a measurement of both the frequency ν and the magnetic field H. Since ν can be measured with much greater accuracy than H, it is preferable and also convenient to compare the value of ν with that of some standard nucleus in

[1] H. L. Anderson and A. Novick, Phys. Rev. **73**, 919 (1948).
[2] Purcell, Torrey, and Pound, Phys. Rev. **69**, 37 (1946).
[3] Bloch, Hansen, and Packard, Phys. Rev. **69**, 127 (1946); **70**, 474 (1946); F. Bloch, Phys. Rev. **70**, 460 (1946).
[4] H. L. Anderson and A. Novick, Phys. Rev. **71**, 372 (1947).
[5] Bloembergen, Purcell, and Pound, Phys. Rev. **73**, 679 (1948).

* A detailed exposition of the theory of the method and the conditions for observing the magnetic resonance effect may be found in the pioneer papers, references 2 and 5.

the same magnetic field. If, as is usual, the comparison is made with the light hydrogen nucleus, such an experiment measures

$$\frac{\gamma}{\gamma(H^1)}=\frac{\nu}{\nu(H^1)}. \tag{2}$$

The absolute value of γ may be obtained by using the value of $\gamma(H^1)=(2.6752\pm0.0002)\times10^4$ gauss^{-1} sec.$^{-1}$ obtained by Thomas, Driscoll, and Hipple.[6] To obtain a result in units of the Bohr magneton, the value $\mu(H^1)=(15.2106\times10^{-4}\pm0.005$ percent) Bohr magnetons for the magnetic moment of the proton obtained by Taub and Kusch[7] should be used.

SIGNAL INTENSITY

The signal from the magnetic resonance is small at ordinary temperatures because only a small fraction of the nuclei in the sample contributes to it. This fraction is the excess of nuclei which, in thermal equilibrium, exists in the lower of the two energy states between which the transitions occur. It has the value $(1/2I+1)\times h\nu/kT=1.5\times10^{-6}$ for spin $I=\frac{1}{2}$ at 20 megacycles and room temperature, the conditions of the present experiments.

The occurrence of these transitions tends to equalize the population of the two energy states, and unless there is a mechanism which restores the thermal equilibrium rapidly enough, the magnitude of the signal will decay during the course of the observations. The nuclear magnetic relaxation effects, the processes which bring about thermal equilibrium in nuclear systems, have been studied in considerable detail by Bloembergen, Purcell, and Pound.[5] Some of their results are used in the discussion which follows.

In He^3 gas, the atoms are in an S state, and the only important relaxation mechanism is the interaction of the nuclear magnetic moments during collisions in the gas. The order of magnitude of the relaxation time may be estimated from the formula

$$T_1\approx\lambda v\{d^2/\gamma\mu\}^2, \tag{3}$$

where γ is the gyromagnetic ratio of He^3, μ the magnetic moment of the atom with which it collides, d is the distance of closest approach, v is the relative velocity of the colliding atoms, and λ the collision mean free path. For pure He^3 at 10 atmospheres, this formula gives $T_1\approx10^6$ seconds. If, however, following a suggestion of Purcell, Pound, and Bloembergen,[8] ten atmospheres of oxygen gas are introduced, the relaxation time is reduced to $\frac{1}{2}$ second. The amplitude of the signal which may be observed is increased more than a thousand-fold thereby.

The other factors which determine the detectability of the magnetic resonance effect are evident from the following formula for the signal-to-noise ratio which has been given by Bloembergen, Purcell, and Pound,[5]

$$\frac{A_s}{A_n}=\frac{V^{\frac{1}{2}}Q^{\frac{1}{2}}\alpha\zeta h^2N\gamma\nu^{\frac{1}{2}}T_2^{\frac{1}{2}}I(I+1)}{24kT(kTBF)^{\frac{1}{2}}T_1^{\frac{1}{2}}}, \tag{4}$$

where V is the volume of the coil in cm^3; Q is the ratio of the reactance to the series resistance of the coil; α is a coefficient appropriate to the shape of the signal, the amount of the modulation swing, the shape of the modulating wave, and the characteristics of the indicating meter; ζ is the fraction of the coil volume occupied by the sample; h is Planck's constant; N is the number of He^3 atoms per cm^3; ν is the resonance frequency in cycles per second; T_2 is the inverse line width expressed in seconds; I is the nuclear spin; k is Boltzmann's constant; B is the equivalent bandwidth of the detecting system in cycles per second; F is the noise figure of the detecting system including the bridge; and T_1 is the relaxation time in seconds. The factor 24 appears in the denominator instead of the factor 48 of the original formula because phase unbalance rather than amplitude unbalance of the bridge was used in the present experiments.

The following values, appropriate to the present experiment, were either measured or estimated in a manner which will be made clear in the sections to follow. $V=1.2$ cm^3, $Q=240$, $\alpha=0.4$, $\zeta=0.46$, $N=2.7\times10^{20}$ cm^{-3}, $\gamma=2.0\times10^4$ gauss^{-1} sec.$^{-1}$, $\nu=20\times10^6$ sec.$^{-1}$, $T_2\cong1.6\times10^{-3}$ sec., $I=\frac{1}{2}$, $T=300°$K, $B=\frac{1}{2}$ sec.$^{-1}$, $F\cong4$, $T_1\cong1$ sec. These values give $A_s/A_n=7$ in good

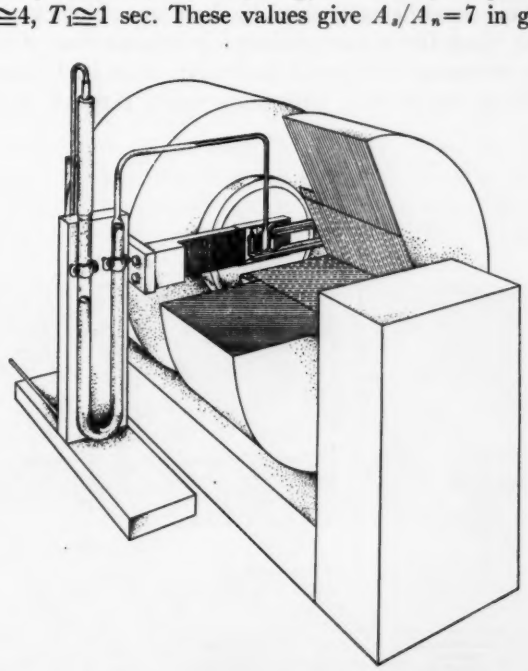

FIG. 1. Experimental arrangement for observing magnetic resonance of He^3 and H_2O simultaneously. The mercury U tube is used to compress a mixture of He^3, O_2, and H_2 gases into a small bulb in the center of the magnetic field. The small water comparison sample is close by but electrically shielded from the He^3 sample.

[6] Thomas, Driscoll, and Hipple, Phys. Rev. **75**, 902 (1949).
[7] H. Taub and P. Kusch, Phys. Rev. **75**, 1481 (1949).
[8] Purcell, Pound, and Bloembergen, Phys. Rev. **70**, 986 (1946).

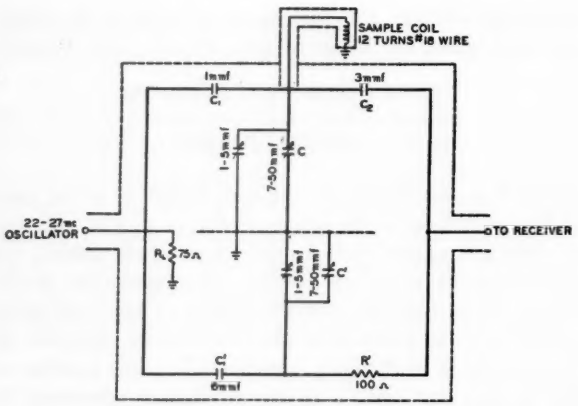

FIG. 2. Twin "T" Bridge: This was used for observing the He^3 resonance at 20.22 mc, and for the H_2 resonance at 26.54 mc. The bridge was first adjusted to null by varying C and C'. By shifting C slightly off balance, the dispersion signal was obtained. By shifting C' slightly off balance, the absorption signal was obtained.

accord with the signal-to-noise ratio which was obtainable with careful adjustment of the equipment.

A spin of $\frac{3}{2}$ would predict a signal-to-noise ratio 5 times greater. Thus, the observed intensity is a strong indication that the spin of He^3 is $\frac{1}{2}$.

HELIUM SAMPLE

The He^3 sample was obtained from the radioactive decay of tritium. The tritium was made by neutron bombardment of Li^6 in the Hanford pile according to a method described elsewhere by Anderson, Novick, and Weil. Since He^4 is also produced in this reaction, it was first necessary to separate the tritium from it. This was done by means of a palladium valve, through which the tritium was passed and collected in a Pyrex bulb. At a subsequent time, the tritium (and light hydrogen impurity) was removed from the bulb by passing it through another palladium valve, leaving the He^3 gas behind. Gaseous impurities which may have accumulated in the course of these manipulations were removed by means of a charcoal trap. In this way, about 10 cm^3 at N.T.P. of isotopically pure He^3 gas was prepared.

In order to obtain a detectable signal from this sample, it was mixed with an equal amount of oxygen gas and then sealed off in a Pyrex glass system in which it was possible to compress the mixture into a small bulb whose volume was nearly 1 cm^3. A sketch of this system is shown in Fig. 1. The sample was isolated from a tank of compressed nitrogen by a mercury U tube. The compression of the sample could be adjusted by means of a pressure-reducing valve on the nitrogen tank.

This sample of He^3 was prepared by Dr. Aaron Novick of the Chemistry Division of the Argonne National Laboratory, who carried through the extraction of tritium from irradiated Li^6. The detection of the magnetic resonance signal from this sample was reported shortly thereafter.[1]

The initial experiments were made with a mixture of equal volumes of oxygen and He^3 at a total pressure of 20 atmospheres. Later, hydrogen gas was added to this mixture through the mercury U tube by means of a fine stainless steel capillary which was flexible enough to be bent around the bend in the U tube. The volumes of the gases He^3, O_2, and H_2 were then in the proportions 1:1:0.37, respectively, and the experiments were carried out at a pressure of 24 atmospheres.

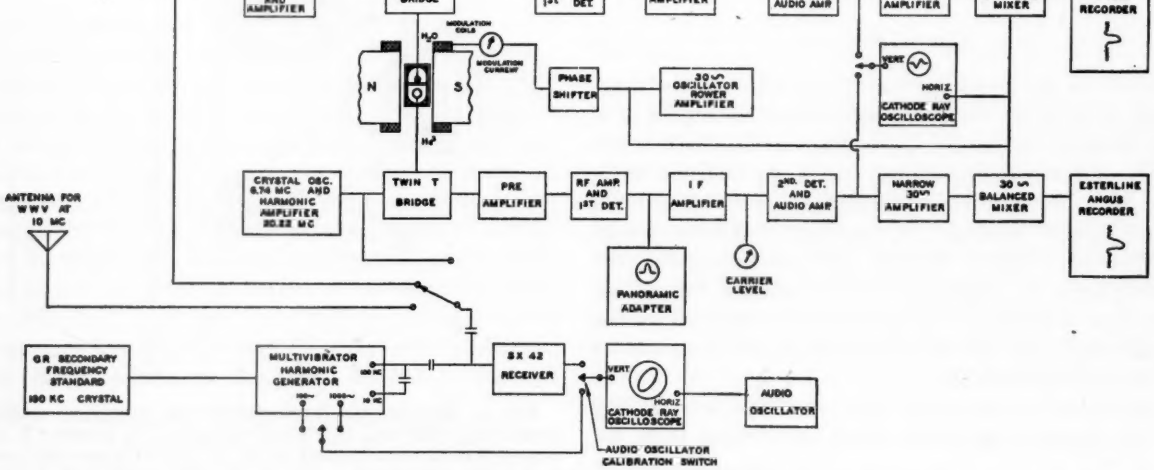

FIG. 3. Block diagram of radiofrequency system for simultaneous observation of magnetic resonance in He^3 and H_2O. The means for precise measurement of frequency are also shown.

EXPERIMENTAL METHOD

The He^3 sample was located within a small r-f coil and placed between the poles of an electromagnet. The magnetic field was modulated by a small amount by means of a 30-cycle current in a pair of modulation coils wound around the pole tips. At a steady value of the field sufficiently near the correct value, the magnetic resonance effect could be expected to produce a 30-cycle modulation of the radiofrequency signal. The problem was to detect this signal and distinguish it from the noise background.

The coil was made a part of a bridge circuit between an r-f source and detector. By balancing the bridge, the carrier signal level was reduced enough so that it would not overload the detector. A narrow band 30-cycle lock-in amplifier was used which responded to the 30-cycle modulation produced by the magnetic resonance effect and discriminated strongly against noise and other undesired signals. This is the method of Bloembergen, Purcell, and Pound,[5] and differs only in the type of bridge used. The weakness of the signal made it necessary to adjust the experimental parameters with considerable care. In what follows the experimental conditions will be elucidated in sufficient detail to permit a reasonable evaluation of all the factors which affect the signal to noise ratio (Eq. (4)).

The coil was made of 12 turns of No. 18 enameled copper wire, and fitted snugly over the outside of the small Pyrex bulb in which the sample was contained. The coil was 14 mm long and had an inside diameter of 9 mm. The sample bulb extended beyond the coil by about 2 mm at each end. Since the wall thickness of the bulb was about 1 mm, the filling factor ζ was 0.46. The volume of the coil V was 1.17 cm^3.

In order to provide electrical shielding, this assembly was mounted inside a cavity in a copper block. The sample was centered in this cavity by means of small Bakelite wedges which served to reduce microphonic effects which would result from the vibration of the coil.

TWIN "T" BRIDGE

The coil was a part of a radiofrequency twin "T" bridge,[9] connection to which was made with copper coaxial line, 1 foot long, $\frac{3}{8}$-in. O.D., and having a capacity of 16 mmf. The circuit for the twin "T" bridge is shown in Fig. 2. This bridge has the advantage that the reactive and the resistance balance are controlled separately and independently by the variable condensers C and C', respectively. The balance conditions are

$$\text{reactive balance:}\quad \frac{1}{\omega^2 L}=C+C_1+C_2\left(1+\frac{C_1}{C_1'}\right), \quad (5)$$

$$\text{resistive balance:}\quad \frac{1}{R}=\omega^2 C_1 C_2\left(1+\frac{C'}{C_1'}\right)R'. \quad (6)$$

[9] W. N. Tuttle, Proc. I.R.E. 28, 23 (1940).

Here, R is the equivalent shunt resistance of the coil, ω is the angular frequency. The Q of the coil is the ratio $R/\omega L$ and may be obtained from the circuit constants at balance. The resistor R_L was inserted to terminate properly the coaxial line from the oscillator and thereby facilitate input voltage measurements. The condensers C and C' were of the conventional variable type, but were provided with special trimmers. Each trimmer was made of two small disks arranged with a fine slow-motion screw which could advance one toward the other. These made it easy to obtain a balance of better than 1 part in 10^4 for both the resistive and the reactive components. Since the balance of the bridge is frequency dependent, care was taken to avoid frequency modulation effects in the r-f generator. Best results were obtained with a crystal-controlled oscillator, and this was used in most of the work with the He^3 sample.

The conditions of operation of the bridge were determined by balancing it at 20.22 megacycles and then measuring the capacity of C and C'. The values $C=65$ mmf and $C'=39$ mmf were obtained. The first value includes 18 mmf of distributed capacity in the connections to the coil. Equations (5) and (6) lead to $L=0.89\mu h$ and $Q=240$. The last value is fairly approximate because of an uncertainty in the values of C_1 and C_2. The r-f voltage across the coil may be obtained from a knowledge of the input voltage applied to the bridge by means of the following formula, obtained from an analysis of the bridge circuit at balance.

$$\frac{|e_c|}{|e_s|}=\left\{\left(\frac{C_2}{C_1'}\right)^2+\left[\omega C_2\left(1+\frac{C'}{C_1'}\right)R'\right]^2\right\}^{-\frac{1}{2}}, \quad (7)$$

which, in the present case, yields $|e_c|/|e_s|=1.74$.

An analysis of the twin "T" bridge showed that the signal-to-noise ratio at the coil is reduced by a factor of 1.3 at the output terminals. The signal from the bridge was detected with a National HRO-5A radio

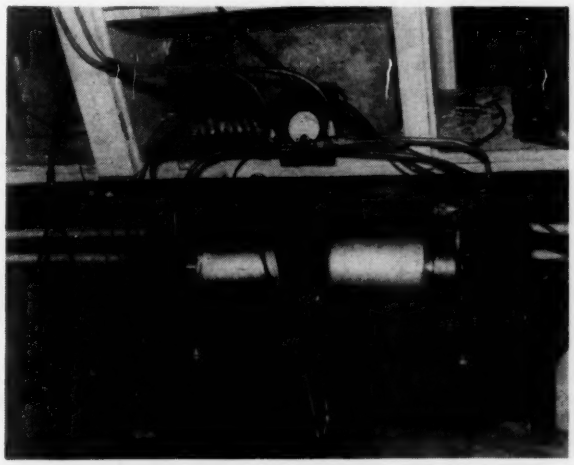

FIG. 4. Photograph of the experimental arrangement: The magnet has a 5-in. diameter pole and a 1-in. gap, and is shown with the He^3 sample in place.

receiver. The noise figure of this receiver is reported to be about 12. This noise figure was improved by preceding the receiver with a single tuned preamplifier, using a 6AK5 tube so that a reasonable value for the noise figure of the detecting system including the bridge was 4.

A panoramic adapter connected to the output of the first detector allowed visual observations of the carrier signal and proved to be exceedingly useful in balancing the bridge and in the rapid adjustment of the circuits. The audio output of the receiver had to be modified slightly to improve its response at 30 cycles. It was fed into a narrow band 30-cycle amplifier followed by a lock-in amplifier copied from one described by Dicke.[10] This system had an equivalent band width of about $\frac{1}{2}$ cycle, and its response was recorded by means of an Esterline-Angus recording milliammeter. A block diagram of the general arrangement is shown in Fig. 3.

COMPARISON SAMPLE

All of this equipment was duplicated to permit simultaneous observations of the proton resonance in water. Various water samples were used, but in the last and best measurements, 0.06 cm^3 of water was used with a manganous ion concentration of 6.7×10^{17} ions/cm^3. According to the data of Bloembergen, Purcell, and Pound,[5] Fe^{+++}, which should have the same paramagnetic behavior as Mn^{++}, in this concentration produces a relaxation time of about 0.1 second. The center of this sample was 1.4 cm from the center of the He^3 sample and electrically shielded from it. The r-f coil which was wound on the outside of the glass tube had 8 turns of No. 18 enameled copper with an inside diameter of 4 mm. This coil was operated at 26.54 megacycles.

The oscillator for the water sample was not crystal controlled as was that for the He^3, but could be adjusted in frequency so that both resonances could be recorded simultaneously. The water signal was strong enough to be seen visually on a cathode-ray oscilloscope connected to the audio output of the radio receiver. The horizontal sweep of this oscilloscope was driven by the same 30-cycle oscillator which was used to modulate the magnet. Visual observation of the water signal was used to find the resonance value of the magnetic field quickly. A preamplifier was not needed for the water sample.

ELECTROMAGNET

The electromagnet used in this work is shown in the photograph of Fig. 4. It has 5-in. diameter poles with a 1-in. plane parallel gap. A high voltage winding was used to allow the use of a rectified and filtered d.c. supply capable of delivering 1 ampere at 2500 volts. This winding was cooled by circulating oil. In the experiments described here, it was operated at 8640 gauss with 0.695 ampere and at 6240 gauss with 0.430 ampere.

The magnet power supply and regulator is shown schematically in Fig. 5. The rectified output was well filtered to reduce to an unnoticeable extent the ripple in the current from the rectifier. The magnet current was regulated by means of a d.c. vacuum tube amplifier, the reference voltage for which was obtained from a manganin-wound 185-ohm resistor in series with the magnet. This resistor was cooled by the same oil which

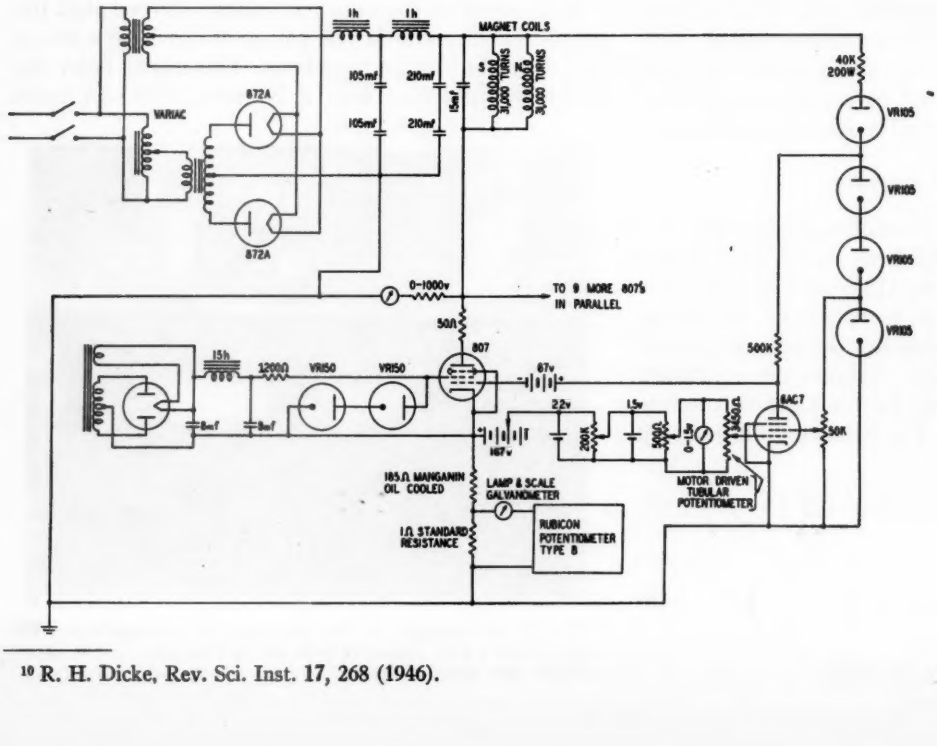

FIG. 5. Electronically stabilized magnet current supply. At 2500 volts, the total magnet current was 1 ampere, and the magnetic field in the gap was 10,000 gauss.

[10] R. H. Dicke, Rev. Sci. Inst. 17, 268 (1946).

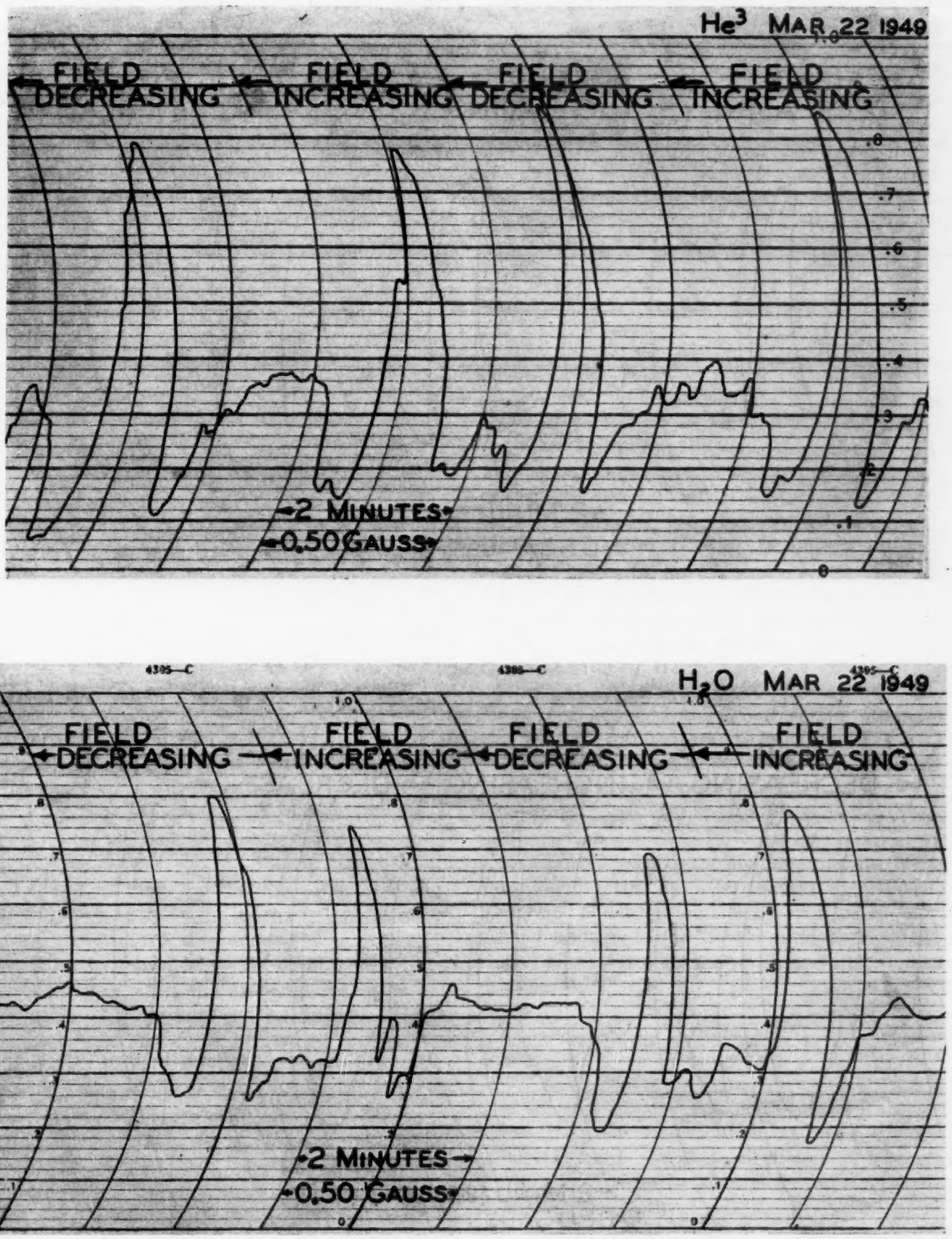

FIG. 6. Typical records of simultaneous observation of the He^3 and H_2O magnetic resonance signals with reactive unbalance of the bridge. The 30-cycle modulation amplitude was $H_m = 0.064$ gauss. The resonance was traversed four times in the above portion of the record, twice from above and twice from below. The jogs which appear in the pattern are due to an unsteadiness in the magnetic field of about 1 part in 10^5. Other irregularities were due to noise. The H_2O receiver was more noisy than usual when this particular record was taken.

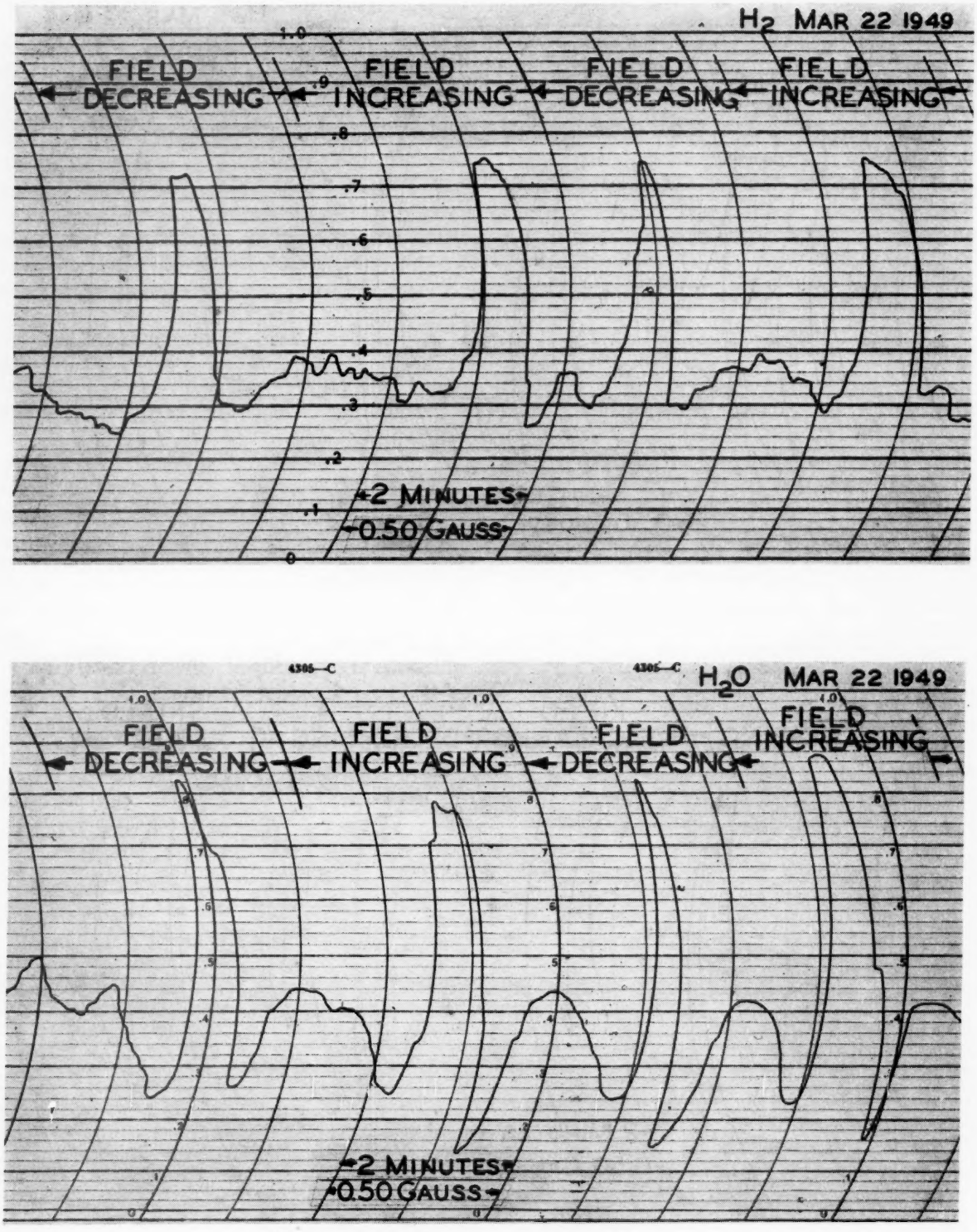

FIG. 7. Typical records of simultaneous observations of the H_2 and H_2O magnetic resonance signals with reactive unbalance of the bridge.

circulated through the magnet windings. The magnet current was adjusted by selecting the proper voltage from a battery box which bucked the voltage developed across this resistor, and then raising the input voltage of the high voltage power supply to the point where the regulator operated in the sensitive part of its range. A motor-driven tubular potentiometer in this battery circuit was arranged so that the bucking voltage could be automatically varied slowly and linearly through the resonance value of the field. In some cases, the rate was as small as 0.005 volt/cm corresponding to a magnetic field change of 0.25 gauss/min. in the vicinity of 6240 gauss. When the resonance value of the field was traversed in this way, the Esterline-Angus instruments would record the amplitude of the 30-cycle component of the magnetic resonance signal. The fluctuation in the regulated magnetic field which occurred during the traversal of a resonance was usually less than 1 part in 10^5. These fluctuations are responsible for some of the irregularities in the resonance patterns which are evident in the sample records shown in Figs. 6 and 7.

A great deal of effort was devoted to the improvement of the uniformity of the magnetic field. Most of this was done by means of a lapping tool. The uniformity of the field was checked after each lapping operation by means of a small water sample having 7×10^{17} manganous ions per cm^3. This probe was mounted on a micro manipulator and could be moved about between the poles and so explore the field. The spatial variation of the field was followed visually by observing the position of the magnetic resonance signal on the cathode-ray oscillograph screen. The best uniformity which was achieved was a variation of 1 part in 10^5 over an area 1 inch in diameter. The mechanical stability of the magnet was not sufficient to maintain this degree of uniformity for very long. When the magnet was turned on again on the following day, the region which was uniform to this amount was noticeably smaller. Some improvement could be obtained by recycling the magnet, but the extended region of uniformity could only be regained by further lapping. Since even a fairly slight pressure on the magnet pole could alter the value of the field by 1 part in 10^5, it was clear that it would be necessary to redesign the magnet to obtain a further improvement in the uniformity.

It was possible to obtain a measure of the inhomogeneity of the magnetic field over the He^3 sample in the following way: A sample of water having the same size as the He^3 sample was placed in the same position as was standard for the He^3. Moreover, the radiofrequency coil was made the same as for He^3. The water sample had added to it 7×10^{17} manganous ions per cm^3 so that the relaxation time was about $\frac{1}{10}$ second. The proton resonance signal from this sample could be observed on the cathode-ray oscilloscope screen. These signals showed a number of oscillations. These occur when the inverse line width T_2 is not too small.[5,11] The oscillations are due to beats between the radiofrequency signal from the oscillator and the magnetic resonance signal. The frequency of the latter varies as the magnetic field is shifted off resonance, and its amplitude decreases as $\exp(t/T_2)$. By analyzing the decay of the oscillations, it was found that the inverse line width was $T_2=1.6\times10^{-3}$ second. This is small compared to T_1 and, provided the r-f input to the bridge is small enough, it must be due almost entirely to an inhomogeneity in the magnetic field of 3.8 parts in 10^6.

ADJUSTMENT

With proper adjustment of the amplifiers, the response of the Esterline-Angus instrument is proportional to the 30-cycle Fourier coefficient of the input signal. In the present experiments, the dispersion signal (obtained by reactive unbalance of the bridge) was used. This signal increases with increasing values of the rotating component of the r-f field H_1. It is desirable to set $(\gamma H_1)^2T_1T_2>1$ for the largest signal amplitude. However, excessive values of H_1 broaden the signal in a manner unsuited to a precise location of the center. For any given value of H_1, there is an optimum value for H_m, the amplitude of the 30-cycle modulation field. Again, a large response requires $(\gamma H_m)^2T_2^2>1$. With excessive values of H_m, however, the signal as it appears on the Esterline-Angus record is broadened. There is also an optimum adjustment of the phase of the modulation current relative to the lock-in signal.

Because of the weakness of the He^3 signal, it was necessary to accept some amount of broadening in the interest of signal amplitude. What seemed to be an optimum compromise was found by empirical adjustment of H_1 and H_m. In the final experiments, the values were found to be $H_1=0.005$ gauss, $H_m=0.064$ gauss. The value of H_1 was obtained from a measurement of the r-f voltage output to the bridge ($e_s=0.05$ volt r.m.s.) and by making use of (7) and the approximate formula,

$$H_1\cong\left(\frac{2\pi e_c^2\times10^7}{\omega^2LV}\right)^{\frac{1}{2}}. \tag{8}$$

The value of H_m was obtained by measuring with an audio frequency vacuum tube voltmeter the 30-cycle voltage induced in a pick-up coil of known number of turns and area inserted between the poles of the magnet at the sample position.

A reliable measurement of the relaxation time was not made in the present work. However, the response obtained with the above value of T_2 and several values of H_1 and H_m were consistent with $T_1\cong1$ second. These values lead to $a^2=(\gamma H_m)^2T_2=4$, $b^2=(\gamma H_1)^2T_1T_2$

[11] B. A. Jacobsohn and R. K. Wangsness, Phys. Rev. 73, 942 (1948).

TABLE I. The difference in the resonance value of the magnetic field for He^3 and H_2 for various frequencies.

$\nu(H_2)$ cycles/sec.	$\nu(He^3)$ cycles/sec.	$\nu(He^3)/\nu(H_2)$	$H(He^3)-H(H_2)$ gauss
26,543,725	20,221,180	0.7618064	+0.173
3,755	1,180	0.7618056	+0.184
4,648	1,180	0.7617799	−0.046
4,677	1,180	0.7617791	−0.065
4,702	1,180	0.7617784	−0.058
2,670	1,180	0.7618367	+0.391
2,683	1,180	0.7618363	+0.402
2,700	1,180	0.7618358	+0.388
3,816	1,180	0.7618038	+0.151
3,850	1,180	0.7618028	+0.132
3,880	1,180	0.7618020	+0.132
3,909	1,180	0.7618011	+0.132
3,944	1,180	0.7618001	+0.115
3,963	1,180	0.7617996	+0.110
3,982	1,180	0.7617990	+0.108
4,720	1,180	0.7617779	−0.081
4,745	1,180	0.7617771	−0.113
4,760	1,180	0.7617767	−0.081
4,765	1,180	0.7617766	−0.079

$=16$, and

$$\alpha=\frac{1}{\pi}\int_0^{2\pi}\frac{ab\sin^2 p\,dp}{a^2\sin^2 p+b^2+1}=0.4, \tag{9}$$

the first harmonic Fourier coefficient of the Bloch dispersion formula. A somewhat larger signal was obtained with $H_m=0.12$ gauss. This setting was used in some of the measurements. In this case, the value of α is 0.56.

The signal obtained from the hydrogen gas in the sample was considerably stronger than the He^3 signal. This is due to the shorter relaxation time in H_2. A preamplifier was not used in detecting the H_2 signal. The H_2 signal disappeared completely when the pressure in the sample bulb was reduced to 1 atmosphere. This was also the case for the He^3 signal. Thus, there was no doubt that these signals originated in these gases and not in any of the surrounding material.

FREQUENCY MEASUREMENT

Precise measurements of frequency were made using a General Radio secondary frequency standard. This unit contains a temperature-controlled 100-kilocycle crystal oscillator followed by a set of multivibrators which produce square wave outputs at 100 kc and 10 kc, and also at 1000 cycles and 100 cycles. The output of the 100-kc multivibrator contains useful harmonics of 100 kc beyond 36 megacycles. These harmonics were readily detected with a Hallicrafters SX42 communications receiver. By mixing the output of the 10-kc multivibrator with the 100-kc multivibrator, it was easy to interpolate at 10-kc intervals between the 100-kc markers. Finally, mixing one of the oscillators at the input to the receiver produced an audible beat of this signal with each of the two neighboring 10-kc markers. This beat signal was connected to the vertical plates of an oscilloscope. By adjusting the frequency of an audio oscillator connected to the horizontal plates of this oscilloscope, it was possible to obtain a circular pattern which symbolizes frequency equality of the two signals. The calibration of the audio oscillator was checked against the 100-cycle and 1000-cycle multivibrator outputs of the frequency standard; the frequency standard itself was checked against the 10-megacycle transmissions of WWV. In this way, the magnetic resonance frequencies could be determined as closely as the audio oscillator dial could be read. No attempt was made to improve this reading to better than ± 10 cycles. The block diagram of this arrangement is shown in Fig. 3.

The drift in the frequency of the crystal oscillator was usually not detectable. The frequency of the variable frequency oscillator was measured every two minutes during a run. A drift of about 50 cycles in 10 minutes was typical and easily followed.

PROCEDURE

Measurements were made by observing the magnetic resonance signals of He^3 and of H_2O on the Esterline-Angus recorders, at the same time. The frequencies of the He^3 and the H_2O oscillators were fixed so that the two resonance signals would appear at almost the same value of the magnetic field. The magnet current was then slowly and automatically varied through the two resonances by means of the motor-driven potentiometer of Fig. 5. The two resonances were traversed first with the magnet current increasing and then with the magnet current decreasing. This was repeated a number of times. The measured quantity is the displacement between the centers of symmetry of the two signals as recorded on the Esterline-Angus instruments. A typical pair of records is shown in Fig. 6. This displacement was measured alternately with field increasing and with field decreasing, always taking the average of these. By proceeding in this way, certain systematic errors were eliminated which might arise from time lags in

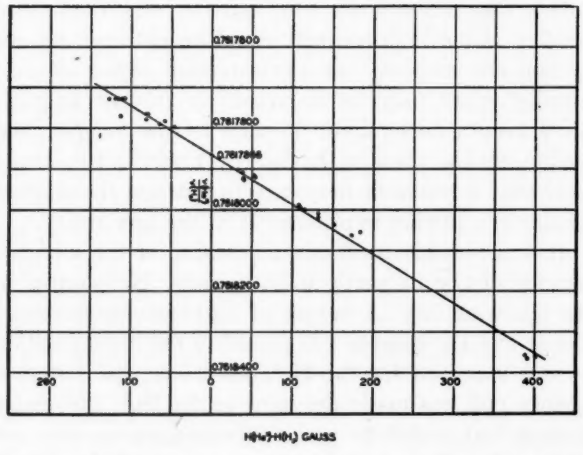

FIG. 8. Ratio of frequency of He^3 and H_2 oscillators plotted against difference in the resonance value of the magnetic field. The straight line is the least squares solution. The intercept at $H(He^3)-H(H_2)=0$ is the ratio of the gyromagnetic ratios of He^3 and H_2.

the apparatus or from non-linear inhomogeneities in the magnet field at the two samples.

The H_2O oscillator was then connected to both bridges so that the signal from the hydrogen gas which was mixed with the He^3 sample could be compared with the signal from the water sample. This is essentially a measurement of the difference in the value of the magnetic field at the positions of the two samples. The significant quantity is the difference between the displacements He^3-H_2O and H_2-H_2O. This difference is a true measure of the difference in the resonance values of the magnetic field for He^3 and H_2 for any given pair of frequencies. Since both the He^3 and the H_2 signals were recorded with the same apparatus, possible instrumental errors were largely eliminated. The frequency of the H_2 oscillator was adjusted so as to give both positive and negative values of the He^3-H_2 difference. Thereby, the frequency ratio for which the resonance value of the magnetic field for He^3 and H_2 was the same could be established by interpolation. Observations made in this way on March 8 and 9, 1949, are recorded in Table I. The measurements were taken with the magnetic field near 6234 gauss. Each difference in the resonance value of the magnetic field for He^3 and H_2 was obtained by taking the average of the pair of displacements found for He^3-H_2O with increasing and with decreasing magnet currents, and subtracting the average displacement found for H_2-H_2O which was -0.079 gauss. The value of $\nu(He^3)/\nu(H_2)$ at $H(He^3)-H(H_2)=0$, was found by a least squares solution to be

$$\frac{\nu_0(He^3)}{\nu_0(H_2)}=0.76178649\pm0.00000045.$$

The precision measure indicated above is merely a measure of the self-consistency of the observations. The experimental error is certainly greater than this.

A search was made for obvious systematic errors in the experiment. One possibility was an effect of the slight asymmetry in the signal as recorded on the Esterline-Angus instrument. This was due in part to friction in the recording pen and in part to residual charge effects in the condensers of the lock-in amplifier. The presence of the asymmetry made it uncertain how to judge correctly the center of the magnetic resonance pattern. In the above experiment, the signal due to H_2 was about twice as large as that from He^3, thereby opening the possibility of a small systematic error in the judgment of the centers of the two patterns.

Accordingly, a new experiment was carried out and care was taken to adjust the receiver gain when observing H_2 to give a signal amplitude more nearly equal to that of He^3. Several other parameters were changed as well. The 30-cycle modulation amplitude was reduced from 0.123 gauss to 0.064 gauss, and the rate at which the magnetic field was varied was reduced from 0.600 gauss/minute to 0.252 gauss/minute. Typical records for He^3 and H_2O and for H_2 and H_2O are given in Figs. 6 and 7, respectively. The observations are collected in Table II. In this case, the result was

$$\frac{\nu_0(He^3)}{\nu_0(H_2)}=0.76178650\pm0.00000025,$$

in excellent agreement with the previous result. This argues against the presence of instrumental systematic errors due to obvious causes.

TABLE II. The difference in the resonance value of the magnetic field of He^3 and H_2 for various frequencies.

$\nu(H_2)$ cycles/sec.	$\nu(He^3)$ cycles/sec.	$\nu(H_2)/\nu(He^3)$	$H(He^3)-H(H_2)$ gauss
26,544,266	20,221,180	0.7617909	+0.037
240	180	916	+0.051
225	180	921	+0.053
215	180	924	+0.038
205	180	927	+0.039
900	180	727	−0.111
900	180	727	−0.119
900	180	727	−0.127
900	180	727	−0.115
900	180	727	−0.107

In Fig. 8, all the above measurements are plotted, together with the least squares straight line solution. The result is

$$\frac{\gamma(He^3)}{\gamma(H_2)}=0.7617866\pm0.0000012.$$

In starting this result, a limit of error is given which is four times larger than the precision measure obtained by calculating $(\langle\epsilon^2\rangle_{Av}/N)^{\frac{1}{2}}$ where ϵ^2 is the mean square deviation from the mean, and N is the number of observations. The limit is more than twice as large as the uncertainty in the frequency measurements, and more than 70 percent of all the observations fell within it.

The systematic error which arises from the fact that an oscillating rather than a rotating r-f field is used[12] was, because of the small value of H_1 used here, too small to be significant.

The paramagnetism of the oxygen present in the sample alters the value of the magnetic field at a given atom of He^3. The time average value of the local field is increased by the fraction $4\pi\chi/3$ because the time-averaged situation of the He^3 atom is that it is in a spherical cavity surrounded by a paramegnetic medium of volume susceptibility χ. If the sample vessel had a spherical shape, it would cause a *decrease* in the value of the local field by an amount $4\pi\chi/3$ so that the net result would be zero, at least in the first order in χ. For the non-spherical vessel used here, the fractional *decrease* in local field was about $\pi\chi$. Thus, the net increase in the local field for 10 atmospheres of oxygen at 20°C was about 0.5 part in 10^6. However, since the situation

[12] F. Bloch and A. Siegert, Phys. Rev. 57, 522 (1940).

for the H_2 molecules was almost exactly the same, no correction was needed for this cause.

DIAMAGNETIC CORRECTION

The above frequency ratio is not strictly equal to the ratio of the nuclear gyromagnetic ratios of He^3 and H^1, but refers rather to the gyromagnetic ratio of He^3 *atoms* and H_2 *molecules*.

To obtain the *nuclear* gyromagnetic ratio, a correction has to be made for the shielding effect of the atomic electrons. Such corrections have been discussed by Lamb[13] and can be made reliably, provided the electronic wave functions are sufficiently well known. Lamb's formula, derived for a spherically symmetric electronic distribution, may be written

$$\frac{H'}{H}=-\tfrac{1}{3}\alpha^2 Z\langle 1/r\rangle_{Av}, \tag{10}$$

where H' is the magnetic field in the z direction produced by the electron at the nucleus, H is the external magnetic field (taken in the z direction), α is the fine structure constant ($1/\alpha=137.02$), Z is the number of electrons, and where the radial distance r is measured in units of the Bohr radius. In both H_2 and He^3, the shielding is due to two electrons so that the shielding in the two cases differs only in the value of $\langle 1/r\rangle_{Av}$. Although the electron distribution in H_2 is not spherically symmetric, the above formula should hold approximately, since, in the present case, it is required to average the correction over all orientations of the hydrogen molecule. Further consideration of this point is in progress.

For H_2, the formula for the electron density given by Nordsieck[14] was used to calculate $\langle 1/r\rangle_{Av}$. For He^3, several of the simpler variational wave functions given by Hylleraas[15] gave fairly concordant results. The reduction of the magnetic field at the nucleus produced by the electrons was found** to be 32 parts in 10^6 for H_2 and 70 parts in 10^6 for He^3. Accordingly, the ratio of the *nuclear* gyromagnetic ratios is increased to,

$$|\gamma_{He^3}|/|\gamma_p|=0.761815.$$

MEASUREMENT AT HIGHER FIELD

The earlier measurements in He^3 were made at a higher value of the magnetic field, namely, 8641 gauss. At this time, the hydrogen had not yet been added to the He^3 sample. Measurements were made in the same manner as described above except that only He^3-H_2O comparisons were made. Comparisons were made with tiny water samples placed at three different positions around the He^3 sample and at a distance of about 1 cm from its center. A survey of the magnetic field was made using the probe so that differences in the value of the magnetic field at the positions of the samples could be taken into account. The result obtained was

$$\gamma(He^3)/\gamma(H_2O)=0.761779\pm 0.000014.$$

The uncertainty given here is due to the uncertainty in the knowledge of the magnetic field at the samples. This result is of interest because it shows that within the limits of error which are given, the ratio of the gyromagnetic ratios is independent of the magnitude of the magnetic field which is used in its measurement.

REMARKS

Villars[16] has interpreted the anomalous moments of H^3 and He^3 as being due to the existence of an exchange moment in these nuclei. In an earlier note to this journal,[17] the value of this exchange moment was calculated by correcting the observed moments for the effect of the orbital motions using the theory developed by Sachs and Schwinger[18] and of Sachs.[19] At that time, there was a possibility that the anomaly might be due to orbital motions. The moment of He^3 is now known accurately enough so that this possibility can be definitely excluded.

It is to be hoped that this addition of precise knowledge about the magnetic moment of He^3 will provide a clue to the nature of the nuclear field.

ACKNOWLEDGMENTS

It is a pleasure to acknowledge the capable assistance of Mr. Edward Yasaitis of the Argonne National Laboratory, who built most of the equipment and maintained it in operating order. I wish to thank Dr. R. G. Sachs, who stimulated my interest in this experiment, and Professor Enrico Fermi for his valuable discussions concerning this work, and for his continued interest in it.

[13] W. E. Lamb, Phys. Rev. **60**, 817 (1941).
[14] A. Nordsieck, Phys. Rev. **58**, 310 (1940).
[15] E. A. Hylleraas, Zeits. f. Physik **54**, 347 (1929).
** I am indebted to Mr. Herbert Kanner for checking these calculations for me.

[16] F. Villars, Phys. Rev. **72**, 256 (1947); Helv. Phys. Acta **20**, 476 (1947).
[17] H. L. Anderson, Phys. Rev. **73**, 919 (1948).
[18] R. G. Sachs and J. Schwinger, Phys. Rev. **70**, 41 (1946).
[19] R. G. Sachs, Phys. Rev. **72**, 312 (1947).

On the Production of Electron Pairs in the Field of an Electron*,**

J. A. PHILLIPS*** AND P. GERALD KRUGER
Physics Department, University of Illinois, Urbana, Illinois
(Received May 19, 1949)

The ratio, $R=\sigma$-pairs/σ-triplets$=C(Z^2)_{ef}/Z_{ef}$ for three gases, CH_4, air, and argon, has been studied and C found to be 3.63, 3.97, and 4.11, respectively. The average value of C from these data is 3.92±0.26. The gamma-rays from $F^{19}(p,\alpha)\gamma O^{16}$ were used in this experiment. The measured energies of the gamma-rays as deduced from pairs formed in CH_4 are 6.13±0.06 and 7.12±0.07 Mev. Data on the energy distribution of the low energy negative electron of the triplet are included.

INTRODUCTION

THE production of an electron pair by a gamma-ray has been known for some time. In order that both energy and momentum be conserved, a third particle must be present in this process.

It is known that the threshold energy for pair production is

$$h\nu=2mc^2(1+m/M),$$

where $h\nu$ is the threshold energy, m the rest mass of the electron, and M the rest mass of the particle in whose field the pair is created.

In general, the formation of an electron pair takes place in the field of the nucleus of the absorbing atom. The threshold energy is then approximately $2mc^2$ and the cross section is proportional to Z^2 where Z is the atomic number of the absorbing medium.

Perrin[1] in 1933 suggested the possibility of the formation of an electron pair in the field of an electron. The threshold energy for this case is $4mc^2$. The cross section should be proportional to Z, there being Z electrons about a nucleus of charge Z.

One of the significant differences between these two cases of pair production is that in the former, although the nucleus may take considerable momentum, the energy it receives is small, whereas in the case of pair formation in the field of an electron, the energy of the recoil electrons may be appreciable. In a Wilson cloud chamber the latter process will give rise to a "triplet"—three electron tracks starting at one apex, one positive and two negative (one of the two negative electrons being the electron about which the electron pair was formed).

In 1938 da Silva[2] reported finding one triplet starting in a lead foil. In 1941 Shinohara and Hatoyama[3] observed one triplet which occurred in the gas of a cloud chamber. Groshev[4] looked for triplets while examining pairs produced in nitrogen, krypton, and xenon. While observing 435 pairs, no triplets were found. K. Zuber[5] also looked for triplets in argon and although 142 pairs were found, no triplets were observed.

Ogle and Kruger[6] in 1945 obtained two triplets in a cloud chamber using the gamma-rays from radioactive sodium. Momentum and energy were found to be conserved in both triplets within experimental error.

It was the purpose of this investigation to determine as accurately as possible the ratio of the cross section for pair production in the field of a nucleus to that for triplet production at one gamma-ray energy. Examples of electron pairs and triplets are shown in Figs. 1, 2, and 3.

SOURCE OF GAMMA-RAYS

The source of gamma-rays was obtained by bombarding crystals of CaF_2 by protons accelerated in the cyclotron of the University of Illinois. The reaction that is believed to occur is as follows:

$$_9F^{19}+{}_1H^1\rightarrow[{}_{10}Ne^{20}]\rightarrow{}_8O^{16*}+{}_2He^4,$$
$$\downarrow$$
$$_8O^{16}+h\nu.$$

The above scheme is necessary since it has been found that the gamma-ray energy is independent of the bombarding energy of the protons.

For some time the gamma-ray spectrum was thought to consist of a single line at 6.4 Mev.[7] Recently, Walker and McDaniel[8] and Rasmussen, Hornyak, and Lauritsen[9] have reported two lines. The reported values including those from this study are given in Table I.

Protons are accelerated in the cyclotron to an energy of 5 Mev. A molecular hydrogen beam could be obtained with the same cyclotron adjustments as for deuterons. During the greater part of the experiment, a 4 μa molecular hydrogen beam, equivalent to 8 μa of atomic hydrogen, was used.

* Assisted by the joint program of the ONR and the AEC.
** Preliminary reports on these data have been given, (a) J. A. Phillips and P. Gerald Kruger, Phys. Rev. **72**, 164 (1947); (b) J. A. Phillips and P. Gerald Kruger, Phys. Rev. **74**, 1259 (1948); (c) J. A. Phillips and P. Gerald Kruger, Phys. Rev. **75**, 1289 (1949).
*** This report is part of a thesis submitted in partial fulfillment of the requirements for the degree of the Doctor of Philosophy at the University of Illinois, 1949.
[1] F. Perrin, Comptes Rendus **197**, 1100 (1933).
[2] A. M. da Silva, Ann. d. Physik **11**, 504 (1939).
[3] K. Shinohara and M. Hatoyama, Phys. Rev. **59**, 461 (1941).
[4] L. V. Groshev, J. Phys. Acad. Sci. U.S.S.R. **5**, 135 (1941).
[5] K. Zuber, Helv. Phys. Acta **15**, 38 (1942).
[6] W. E. Ogle and P. Gerald Kruger, Phys. Rev. **67**, 282 (1945).
[7] Fowler, Lauritsen, and Lauritsen, Rev. Mod. Phys. **20**, 236 (1948).
[8] R. L. Walker and B. D. McDaniel, Phys. Rev. **74**, 315 (1948).
[9] Rasmussen, Hornyak, and Lauritsen, Phys. Rev. **75**, 1462 (1949).

Large pieces of natural CaF_2 crystals were used as the target. Six inches in front of the CaF_2 target was a "beam shutter" made of copper which normally kept the beam from striking the CaF_2 target. Immediately before an expansion of the cloud chamber this shutter was pulled aside by an air ram.

THE APPARATUS

A 12-in. Wilson cloud chamber operating at a pressure of 1.75 atmos. was used. Since the cyclotron was to be used with the cloud chamber, it was desirable to decrease the cycle time of the chamber as much as possible. James L. Lawson[10] has pointed out that the cycle time of a cloud chamber can be reduced by overcompression. Following his suggestion a second piston was installed, designed so as to allow an overcompression of the main chamber (for a few seconds immediately after an expansion) before coming back to the normal compressed position. This allows the chamber to come to thermal equilibrium earlier than would otherwise occur, and old tracks evaporate faster. Thus, not only has the cycle time of the chamber been reduced but more radiation can be allowed to enter the chamber during each expanison. It has been found that with a normal expansion ratio of 1.19 for methane the overcompression ratio (i.e., normally compressed volume to overcompressed volume) was 1.03 for best performance. This resulted in a decrease of the cycle time of the cloud chamber, methane-filled, from 36 sec. to 23 sec. and permitted operation with twice the gamma-radiation entering the chamber as compared to non-overcompression.

FIG. 1. Two stereoscopic views obtained in a cloud chamber filled with air of an electron pair created in the field of a nucleus. The gamma-rays are incident in the direction of the arrow.

The cloud chamber is provided with two field coils, placed one above the other so as to give a uniform field in the usuable portion of the chamber. A current regulator kept the current (for a few seconds before and during the expansion of the cloud chamber) to within ± 0.5 percent and usually to within ± 0.25 percent of a predetermined value.

The magnetic field was measured by two different methods. Using a super-regenerative detector method of Roberts[11] of measuring a magnetic field with the magnetic moment of the proton, a resonant frequency of 6.895 ± 0.011 mc/sec. was obtained. Using a value for the gyromagnetic ratio of the proton of 2.675×10^4 radians/sec. gauss, the calculated magnetic field was 1619.6 ± 9.1 gauss. Also, a separate determination was made using flip coils and a standard mutual inductance. Averaging the results of the latter method where three coils were used gives 1623 ± 11 gauss. An average value of the two methods (1621.5 ± 7.3 gauss) was used throughout the experiment.

The camera, which was automatic, was provided with an Eastman Kodak Ektar $f/2$ coated lens. Eastman Kodak Super XX 35-mm film was used with an exposure of 1/20 sec. The film gate of the camera was so designed that the film could be repositioned accurately after an exposure in the camera.

A mirror box, between the camera and cloud chamber, allowed stereoscopic pictures of the chamber to be taken during each expansion. Thus, when an exposure is reprojected through the optical system it is possible to determine accurately the position of any track in the cloud chamber.

COLLIMATION OF THE GAMMA-RAYS AND SHIELDING OF THE CHAMBER

The cloud chamber is located outside of the 4-ft. thick water tanks which completely surround the cyclotron as shown in Fig. 4. A 6-in. I.D. pipe extends through the water tank on a line between the target and the cloud chamber. A paraffin plug 3 ft-long and 6 in. O.D. lies inside this pipe at either end of which is a 6-in. long lead plug. Extending through these plugs and

[10] James L. Lawson, private communication.

[11] A. Roberts, Rev. Sci. Inst. 18, 845 (1947).

lined up between the target and the cloud chamber is a 1-in. diameter hole. The 7-in. long target is so tilted that the front faces of the crystals are exposed to this 1-in. hole. A 1-in. diameter hole was machined in the side of the target box in line with the collimator and covered with a 0.005-in. aluminum foil. As neutrons caused a number of recoil protons which badly fogged the chamber, a 4-in. block of paraffin was placed immediately in front of the collimator passing through the water tanks on the cyclotron side.

Appreciable gamma-ray shielding around the chamber was necessary. A partial shield from general radiation from the cyclotron is afforded by the 4-ft. thick water tank in front of the chamber. Two and one-half tons of lead has been placed around the cloud chamber most of which has been concentrated between the water tanks and the cloud chamber with only a small fraction around the sides and backs of the chamber. Satisfactory shielding has been achieved, since, of the several thousand electron pairs observed in the chamber, none were found to lie outside the collimated region.

MEASUREMENT OF GAMMA-RAY ENERGIES

Gamma-ray energies were determined by measuring the energies of electron pairs which were formed in the gas of the cloud chamber. A set of criteria were established and if a pair could satisfy these, measurements of the radii of the electron tracks were made. The criteria to be satisfied for the acceptance of a measurable pair were as follows:

(a) Both electron tracks, one positive and the other negative, must be of the same age and density and have a sharp and clearly defined apex.

(b) Both electron tracks had to lie within 10° of the plane of the cloud chamber which is perpendicular to the magnetic field.

(c) Each track of the pair must have no obvious large angle single scattering unless the track was long enough to obtain a good measurement without including the scattered region.

The measurement of a pair consisted in reprojecting the photograph through the camera and mirror system used to take the picture. The two stereoscopic images (one the direct view and the other the reflected view from the mirror) were observed through a ground glass screen. By manipulating the ground glass screen the two images could be made to coincide and thus, if no errors were present in the system, the original position and shape of the track in the cloud chamber could be determined.

Several tests have been carried out to determine with what accuracy the optical system could reproduce a given set of circles. A system of circles was photographed, reprojected, and measured. Measurements made a few weeks after processing, when the film was completely dry, showed that the optical system could reproduce a circle to within an accuracy of ± 0.5 percent.

A measuring engine has been used by which the sagitta for a given cord of a circle can be measured. These data are then sufficient to determine the radius of curvature. The practice which has been followed in measuring the energies of electron tracks is to measure the sagitta of each track five times for each of 2 cords. These measurements are repeated several days later. Thus four values for the radius of curvature of each track are obtained. If a measurement cannot be repeated to within at least 3 percent, the pair has been discarded. Pairs will then be discarded if the film cannot be repositioned in the camera or if large angle single scattering is treated differently in the two sets of measurements.

A serious limitation to this method of gamma-ray energy determinations is the small angle scattering which occurs in the gas of the cloud chamber. To obtain an estimate of the probable error introduced by scattering the treatment of Rossi and Greisen[12] has been used

FIG. 2. A photograph of an electron pair created in the field of an electron. The direction of the gamma-ray is shown by the arrow and one of the two negative electrons is the electron in whose field the pair was formed.

[12] B. Rossi and K. Greisen, Rev. Mod. Phys. 13, 268 (1941).

TABLE I. Gamma-ray energies from $F^{19}(p, \alpha)\gamma O^{16}$.

Walker and McDaniel	6.13±0.06 Mev	6.98±0.07 Mev
Rasmussen, Hornyak, and Lauritsen	6.16±0.04 Mev	7.06±0.06 Mev
Authors	6.13±0.06 Mev	7.12±0.07 Mev

Their results have been verified by Smith and Kruger[13] within experimental error.

MEASURED ENERGIES OF THE GAMMA-RAYS

Eighty-seven electron pairs in CH_4 were found to satisfy the above selection criteria. Each pair was measured as has been described. A histogram of the distribution of energies of the pairs is shown in Fig. 5. It appears that there are two gamma-ray lines. Averaging the energies of the individual pairs in each peak, the energies 6.13±0.06 and 7.12±0.07 Mev are obtained. The assigned errors have been determined by considering the probable error in the magnetic field measurement, non-uniformity of the magnetic field in the plane of the chamber, reproducibility of tracks by the optical system, and the probable error from the mean of the energies of the individual electron pairs.

The number of pairs under the 6.13-Mev peak is 30 and under the 7.12-Mev peak there are 57 pairs. The cross section[14] for pair production at 6.13 Mev is $1.37\times10^{-27}\ Z^2$ and at 7.12 Mev is $1.57\times10^{-27}\ Z^2$. Thus, correcting for the cross sections at these energies, the 7.12-Mev line is about 1.7±0.4 times as intense as the 6.13-Mev line at a bombarding energy of 5 Mev.

Early in this investigation**[a] two strong lines with some evidence for three weaker lines were reported from measurements of 40 electron pairs formed in air. Subsequently, the magnetic field was remeasured as described above and found to be higher than had been previously determined.

Two of these lines, when corrected by use of the more accurate magnetic field value, agree with the data here presented, but it appears that small angle scattering in air is sufficient to make this gas unreliable for electron energy determinations.

DETERMINATION OF THE RATIO OF PAIR TO TRIPLET PRODUCTION

From the present experiment, in agreement with others, the gamma-ray energies from $F(p, \alpha)\gamma O$ lie between 6 and 7 Mev. Since the ratio of the cross sections for pair and triplet production is not expected to vary widely over this interval, the energy of each pair and triplet has not been measured. Thus only the total number of pairs and triplets observed are considered sufficient to determine the ratio of the cross sections for a gamma-ray energy of about 6.5 Mev.

[13] L. W. Smith and P. Gerald Kruger, Phys. Rev. **72**, 357 (1947).
[14] W. Heitler, *The Quantum Theory of Radiation* (Oxford University Press, London, 1936), p. 200.

The criteria for a countable pair were as follows:

(a) Two electron tracks of the same age appear to start at a single point in both stereoscopic views, the curvature of the tracks being such that one would have been made by a positron and the other by a negative electron.

(b) The density of the two electron tracks must be constant along the tracks near the apex.

(c) The region immediately about the apex must be free of other tracks such that if there were another electron track leaving the apex it would of a certainty be observed.

The criteria for a countable triplet were similar:

(a) Three electron tracks of the same age must start from a single point, the curvature of the tracks being such that if all three tracks originated at the apex one would be a positive electron and the other two negative electrons.

(b) The density and sharpness of the three electron tracks must be the same and constant along the track near the apex in so far as the relative energies of the three electrons allow.

(c) When reprojected through the camera and mirror system and observed by means of a ground glass screen the three tracks must be seen to converge and meet at a single point.

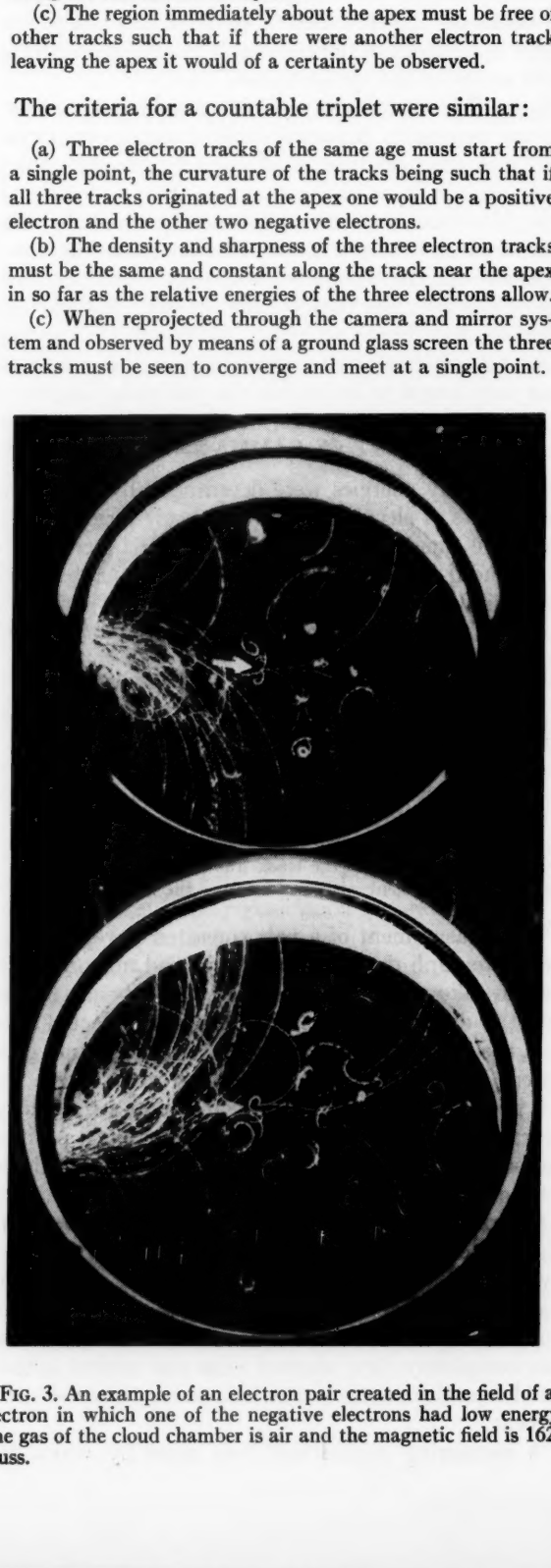

FIG. 3. An example of an electron pair created in the field of an electron in which one of the negative electrons had low energy. The gas of the cloud chamber is air and the magnetic field is 1622 gauss.

The pictures were all examined twice by means of a Spencer delineascope. Any doubtful pair was examined by a magnifying lens or reprojected through the camera and mirror system and examined more critically.

DETERMINATION OF $(Z^2)_{ef}/Z_{ef}$

Three gases (methane, air, and argon) were used in the present experiment. The ratio $(Z^2)_{ef}/Z_{ef}$ for each gas was calculated per molecule of the gas; for example, in methane the effective Z^2 for the production of pairs per molecule will be 40 (36 for the carbon atom and 1 for each of the four hydrogen atoms). The total number of electrons in each molecule is ten. Hence, if the cross section for pair production is purely additive, the ratio of $(Z^2)_{ef}$ to Z_{ef} for methane will be 40/10 or 4. Throughout the experiment a 50:50 mixture by volume of alcohol and water was used. At 20°C the vapor pressure[15] of alcohol is 2.19 cm Hg and of water 1.46 cm Hg. When the presence of these vapors are included the effective Z^2/Z for each gas was calculated to be as shown in Table II.

RESULTS FOR THE RATIO OF PAIR TO TRIPLET PRODUCTION

The data that were obtained for the three gases are shown in Table III.

From these data a weighted average of 3.92 ± 0.26 Z^2/Z is obtained for the ratio of pair production in the field of a nucleus to pair production in the field of an electron.

Six hundred and sixteen pictures were taken with hydrogen in the cloud chamber and 728 pictures with helium. The sensitive time of the chamber when filled with these gases was found to be so short that the number of pictures necessary to obtain enough triplets to determine the cross section for triplet production with some accuracy was so large as to make the use of these gases impractical.

SOURCES OF ERROR

(1) There was some concern as to whether a few triplets would be missed and counted as pairs owing to the low energy negative electron having such a small energy that its range would not be long enough to be detected in the cloud chamber. A simple calculation, however, from the conservation of energy and momentum shows that the minimum energy this electron may have is $2\ mc^2(mc^2/h\nu)^2$. At a gamma-ray energy of 6.5 Mev this corresponds to an energy of about 6 kev which will have a range of about 0.2 cm in the cloud chamber. An electron of this range is probably just too short to be observable. The lowest energy negative electron of a triplet observed had an energy of about 20 kev with a range of 0.65 cm. As triplets having a track of 0.5 cm in length should be easily seen it is believed that there is not an appreciable number of triplets having a track too short to be seen.

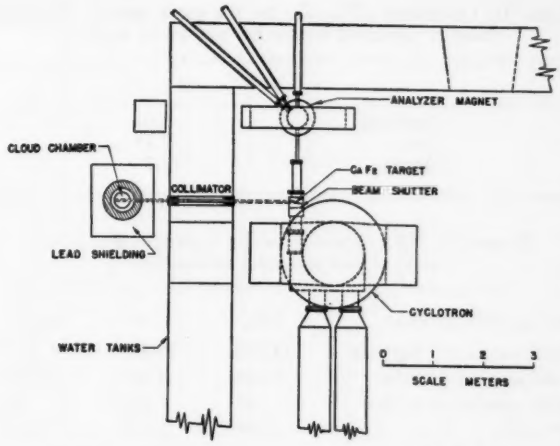

FIG. 4. A schematic diagram showing the location of the cloud chamber with respect to the cyclotron. A 1-in. hole through lead plugs in the water tanks surrounding the cyclotron collimates the radiation from the target.

(2) Selections of triplets are based only on observations made on the projected image of the triplet by the optical system. To satisfy the selective criteria the tracks would have to be sharp and distinct, especially near the apex with the region immediately about the apex free from all other tracks. With so many variables affecting the operation of a cloud chamber it is difficult to keep the quality of tracks unchanged over long periods of time. There may have been a few real triplets which were rejected as there was some doubt as to whether the tracks met at a point or crossed due to fuzzy broad tracks. Since any doubtful triplet was discarded, the number of triplets accepted is probably too small rather than too large. The number of triplets about which there was some doubt was about 1 percent of the total number of triplets.

(3) There is a possibility that a pair and a photoelectric or Compton electron may start so close together that they might appear to form a triplet. In order to estimate the probability of this happening, the number of photoelectric and Compton electrons in each of several expansions were counted. A cylindrical volume about the apex of a pair 1 mm in diameter and 2 mm long was defined as that volume such that if a photoelectric or Compton electron started in this region a possible "confusable" triplet would result. The data on this point for the three different gases is shown in Table IV.

The probability of a "confusable" triplet is still smaller than that shown in Table IV. Here the average total number of photoelectric and Compton electrons appearing per picture were used. Many of the photoelectric and Compton electrons are of so high an energy that if one such electron appeared in a "confusable" region the triplet would be discarded since it would obviously have too high a total energy. Again, the

[15] N. Das Gupta and S. K. Ghosh, Rev. Mod. Phys. 18, 280 (1946).

TABLE II. Calculated $(Z^2)_{ef}/Z_{ef}$ for the gases used in the cloud chamber corrected for alcohol and water vapors.

Gas	$(Z^2)_{ef}/Z_{ef}$
Methane	4.07
Air	7.35
Argon	17.7

TABLE III. Data obtained for the determination of the ratio of pair to triplet production.

Gas in cloud chamber	CH_4	Air	Argon
Total number of pictures	13,362	19,295	11,672
Total number of pairs	1,430	3,441	6,484
Total number of triplets	97	118	89
$(Z^2)_{ef}/Z_{ef}$	4.07	7.35	17.7
$\frac{\sigma\text{-pairs}}{\sigma\text{-triplets}}\left(\frac{Z_{ef}}{(Z^2)_{ef}}\right)=C$	3.63±0.41	3.97±0.41	4.11±0.53

photoelectric and Compton electrons were of all ages and densities while in an acceptable triplet the ages and densities of all three tracks must be the same. Therefore, the probable number of "confusable" triplets in air and methane are negligible and in argon might be as high as 1 percent of the total triplets observed.

ENERGY DISTRIBUTION OF THE RECOIL ELECTRON

Measurements have been made on the energy of all the low energy negative electrons of the triplets observed in CH_4 and air. This proved difficult since only a small fraction of these tracks can be expected to lie in the plane of the chamber perpendicular to the magnetic field. Also, these tracks, caused by slow electrons, will suffer appreciable scattering in the gas of the chamber. In general, the energy was determined by measuring the radius of the track in the plane of the track which approximated its curvature most closely. The angle of the plane of the track with the direction of the magnetic field was measured and the component of the magnetic field perpendicular to this plane calculated. (This is an approximation since such a track in reality is a helix. A detailed analysis, however, was impossible since most tracks were short—the usable portion of the chamber being only $1\frac{1}{4}$ in. high.) The lowest energy electrons were measured by range if it was certain that the entire track could be seen. Range energy relationships of Das Gupta and Ghosh[16] were used. It is estimated that the measured energies are correct to within about 50 percent for electrons having energies between 20 and 500 kev and about 30 percent for those electrons having energies above 500 kev. The results of these measurements are shown in Table V and Figs. 6 and 7.

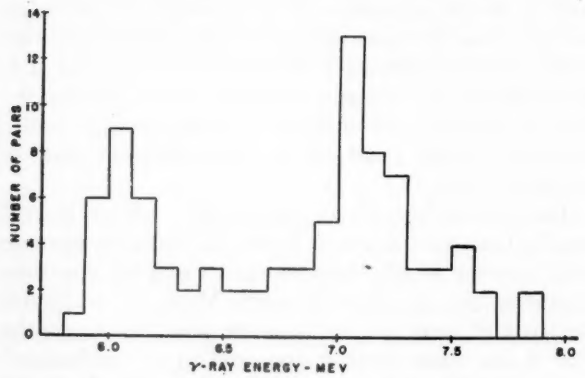

FIG. 5. A histogram of the distribution of energies of electron pairs formed in the gas of the cloud chamber.

TABLE IV. Data for the determination of the possible number of "confusable" triplets.

Gas in cloud chamber	CH_4	Air	Argon
Number of photoelectric or Compton electrons per picture	7.0	9.22	16.2
Percent of total pairs that might form a confusable triplet	0.012	0.016	0.028
Percent of triplets which might be a confusable triplet	0.18	0.46	2.0

CONSERVATION OF MOMENTUM

Since it is possible to observe all the particles taking part in the formation of a triplet (the direction and energy of the gamma-ray known from the collimation of the radiation and measurements of the energies of the three electrons), it should be possible to show that momentum is conserved in the process. There were 25 cases in which this measurement was attempted. A life-size enlargement was made of the triplet through the original optical system. From this enlargement the centers of the circles which most closely approximated the tracks of the electrons were determined. Then the angles at which the electrons left the apex were measured.

Since in most cases the energy of the low energy electron is small and the effects of scattering on angles and energy measurements so large the results are not very significant. The triplets measured show a large spread in energies, and in many cases just as good agreement could be made with the known gamma-ray energies if the energy of the low energy negative electron were ignored. About the most that can be said is that momentum is conserved within experimental error, but as a criterion for the selection of triplets formed in a cloud chamber, conservation of momentum is impossible.

DISCUSSION OF RESULTS

1. Energy and Intensity of the Gamma-Rays

There seem to be two gamma-ray energy lines when CaF_2 is bombarded with 5-Mev protons—one at 6.13 ±0.06 Mev and the other at 7.12±0.07 Mev. The ratio of the intensities of these lines from these data is about

[16] N. R. Das Gupta and S. K. Ghosh, Rev. Mod. Phys. 18, 225 (1946).

TABLE V. Measured energies of the low energy negative electron of triplets formed in methane and air.

(Three triplets have E_{min}^- tracks not measurable.)

Methane				
0.020 Mev	0.057 Mev	0.15 Mev	0.28 Mev	0.54 Mev
0.027	0.061	0.15	0.29	0.64
0.030	0.062	0.15	0.30	0.68
0.030	0.063	0.15	0.30	0.74
0.031	0.070	0.16	0.30	0.75
0.031	0.074	0.16	0.30	0.81
0.034	0.080	0.16	0.31	0.83
0.034	0.080	0.17	0.32	0.87
0.034	0.083	0.17	0.32	0.95
0.035	0.084	0.17	0.33	0.97
0.036	0.084	0.17	0.38	1.00
0.038	0.098	0.18	0.39	1.11
0.039	0.098	0.18	0.39	1.36
0.040	0.10	0.19	0.39	1.56
0.044	0.11	0.19	0.40	1.59
0.050	0.11	0.20	0.42	1.60
0.052	0.11	0.21	0.42	1.80
0.054	0.11	0.25	0.42	
0.054	0.12	0.26	0.45	
0.056	0.12	0.27	0.50	
Air				
0.022 Mev	0.073 Mev	0.16 Mev	0.28 Mev	0.49 Mev
0.023	0.087	0.17	0.29	0.49
0.025	0.089	0.18	0.29	0.50
0.027	0.092	0.19	0.29	0.54
0.027	0.093	0.19	0.30	0.58
0.035	0.095	0.19	0.30	0.59
0.037	0.095	0.20	0.30	0.61
0.038	0.099	0.20	0.30	0.62
0.042	0.10	0.20	0.32	0.64
0.044	0.10	0.20	0.33	0.67
0.048	0.11	0.22	0.34	0.68
0.049	0.11	0.22	0.34	0.72
0.049	0.11	0.23	0.34	0.76
0.056	0.12	0.23	0.34	0.77
0.056	0.12	0.23	0.36	0.78
0.059	0.12	0.24	0.37	0.78
0.060	0.12	0.24	0.37	0.81
0.061	0.12	0.24	0.37	0.90
0.066	0.13	0.26	0.38	0.93
0.069	0.14	0.26	0.39	0.99
0.069	0.14	0.26	0.40	1.07
0.069	0.16	0.26	0.40	1.17
0.070	0.16	0.26	0.43	1.92

TABLE VI. The ratio of the intensities of the two gamma-ray lines when CaF_2 is bombarded with protons as a function of the bombarding energy.

Observer	Bombarding energy	$I_{7.1}/I_{6.1}$
Walker and McDaniel	0.45 Mev	0.044
	0.70	0.17
	1.15	0.38
Goldhaber*	2.6	~1.0
Authors	5.0	1.7±0.4

* G. Goldhaber, Phys. Rev. **74**, 1725 (1948).

1.7±0.4 (see above). The ratio of the intensities of the two lines in the present data compared with the results of other observers is shown in Table VI.

2. Cross Section for Triplet Production

At a gamma-ray energy of about 6.5 Mev the ratio of the cross sections for the production of a ± electron pair in the field of a nucleus to that in the field of an electron from the data here presented is 3.92±0.26. Within statistical limits the ratio of the cross sections is proportional to Z^2/Z of the absorbing medium.

Several calculations[17] have been made of the total cross section for triplet production as a function of energy. The results differ markedly from each other and none are in good agreement with the value obtained in the present experiment. It appears that this experiment

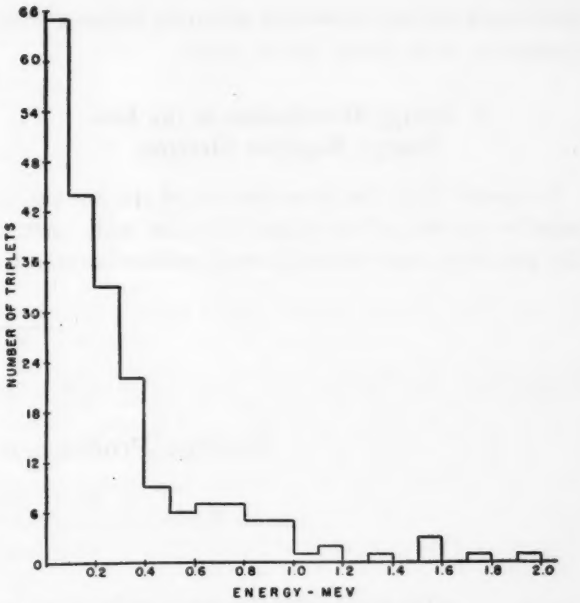

FIG. 6. The distribution of measured values of the kinetic energy of the low energy negative electron of triplets formed in air and methane.

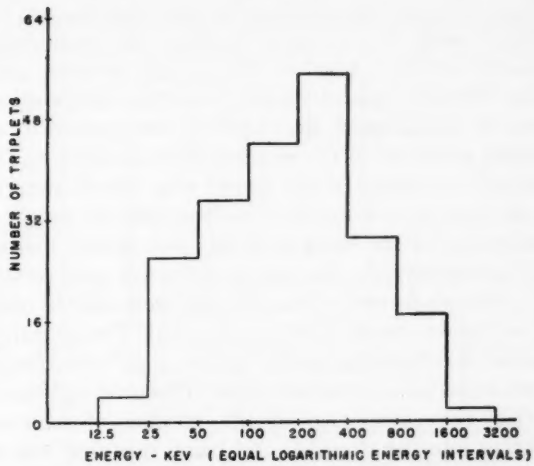

FIG. 7. The distribution of measured values of the kinetic energy of the low energy negative electron of the triplets plotted in equal logarithmic energy intervals.

[17] (a) K. M. Watson, Phys. Rev. **72**, 1060 (1947). (b) A. Borsellino, Nuovo Cimento **IV**, 1 (1947). (c) P. Nemirovsky, J. Phys. Acad. Sci. U.S.S.R. **11**, 94 (1947). (d) V. Votruba, Phys. Rev. **73**, 1468 (1948).

must await further theoretical attention before a valid comparison with theory can be made.

3. Energy Distribution of the Low Energy Negative Electron

It appears from the measurements of the low energy negative electron of the triplet that the main part of this process is connected with small momentum transfer to the recoil electron. This is in agreement with predictions of Bethe,[18] Votruba, and Nemirovsky.

ACKNOWLEDGMENTS

The authors are grateful to Professor H. A. Bethe for valuable discussions during the course of this experiment. They also express their thanks to Mr. E. Hahn for helpful assistance in making the magnetic field measurement.

[18] H. A. Bethe, Proc. Camb. Phil. Soc. **30**, 524 (1934).

PHYSICAL REVIEW VOLUME 76, NUMBER 10 NOVEMBER 15, 1949

Neutron Production at Mountain Altitudes*

C. G. MONTGOMERY AND A. R. TOBEY**
*Sloane Physics Laboratory, Yale University,*** *New Haven, Connecticut*
(Received August 1, 1949)

The rate of production of neutrons by cosmic rays was measured at 3510 meters elevation in lead, aluminum, and paraffin, and in paraffin at 1640 meters elevation by means of an ionization chamber filled with boron trifluoride. The variation with elevation for production in paraffin differs slightly from that in the heavier elements, but agrees well with observations by other observers of the production in air at higher altitudes and with the variation of extensive showers. The neutrons are produced with a larger multiplicity in lead than in paraffin. Comparison with measurements of star production in photographic plates results in the value of 3 to 6 neutrons per star. Bursts of ionization resulting from other cosmic-ray phenomena were also observed.

INTRODUCTION AND APPARATUS

DURING the spring of 1948 measurements were made[1] of the rate of production of cosmic-ray neutrons in several materials at sea level. The experiment was so designed that absolute rates of neutron production could be accurately calculated from known nuclear cross sections, both total and capture, for the elements used. The detector consisted of a cylindrical ionization chamber filled to atmospheric pressure with boron trifluoride gas of standard isotopic composition. Bursts of ionization in the chamber were caused by α-particles produced in the reaction $B^{10}+n=Li^{7}+\alpha$. The chamber was placed at the center of a pile of material consisting of approximately equal amounts by weight of paraffin and of the element to be investigated, distributed homogeneously. Enough paraffin was used so that only neutrons formed within the pile were able to reach the ionization chamber and be detected. The ionization chamber was furnished with "guard rings" constructed of borax and other chambers filled with boron trifluoride, so that the calculation of the number of neutrons diffusing into the chamber and being captured was reduced to a one-dimensional problem with axial symmetry which could be solved rigorously. The ionization chamber was connected to an electrometer tube with a balanced amplifier. The output voltage was applied to a galvanometer which produced a trace on moving photographic paper. Thus the size of the ionization pulse in the chamber could be measured. The background was determined by surrounding the chamber with a layer of borax within the pile of paraffin. For further details of the experimental arrangement, reference should be made to the thesis mentioned. Since the rates to be reported here depend on the nuclear cross sections chosen, these values are reproduced in Table I.

OBSERVATIONS

During the summer of 1948 the sea level observations were extended by others taken in Colorado at Denver, 1640 meters elevation, atmospheric depth 865 g/cm², magnetic latitude 48.5°N and at Climax, 3510 meters elevation, atmospheric depth 675 g/cm², magnetic latitude 48.1°N. The experiments were performed in a truck with a light roof of approximately 1.3 g/cm² thickness in open areas.

The direct result of the observations is a set of curves giving the rate of occurrence of pulses of a given size in the ionization chamber. Figure 1 shows three such curves taken at Climax. The abscissas are given in arbitrary units (a deflection of $\frac{1}{32}$ inch on the photographic paper) and the ordinates are rates per hour of occurrence of pulses per unit interval of size. The highest curve shows the observations obtained when the pile contained 517

* Presented at the Echo Lake Cosmic-Ray Symposium (June, 1949).
** Now at Washington State College, Pullman, Washington.
*** Assisted by the Joint Program of the ONR and the AEC.
[1] A. R. Tobey, Ph.D. thesis, Yale University (1948); Phys. Rev. **75**, 894 (1948).

lb. of lead and 770 lb. of paraffin, the middle curve for the paraffin alone and the lowest curve shows the background and was obtained with the chamber surrounded by borax which in turn was surrounded by the paraffin. The peaks resulting from the disintegration alpha-particles are well marked. The neutron production in any case is proportional to the area between the background curve and a higher one.

The counting rates at high altitude were so large that a correction had to be applied for the resolving time of the apparatus. The galvanometer used had a period of 1.1 sec. and it was estimated that if two neutrons were captured in the chamber within an interval of less than 0.36 sec. $= 10^{-4}$ hr., the resultant pulse would be classed as a single pulse but of larger size. The occurrence of a subsidiary peak at twice the abscissa of the main peak is evident in Fig. 1. The true counting rate N is related to the observed rate N_0 by the equation

$$N_0 = Ne^{-\sigma N},$$

where σ is the resolving time. From the corrected counting rates the rates of neutron production were calculated and the results obtained are given in Table II. For convenience the sea level values are included also.

The probable errors that are indicated in Table II are those arising from the statistics of counting only. The rates are uncertain also because of uncertainties in the values of the nuclear constants assumed. Since no tests of the purity of the substances used were made, no estimate of the inaccuracy arising from this source is possible. Small amounts of boron will, of course, make large changes in the neutron rates. Probably no contamination resulted from the use of borax to determine the background of the chamber since the values determined from two different amounts of lead agree well. The values listed for carbon are based on the assumption that the hydrogen in the paraffin does not contribute and that the composition of the paraffin could be represented by C_nH_{2n}. Neutron production in the chamber walls, which were thin, was neglected.

VARIATION WITH ELEVATION

The observed variation with elevation of the rates of neutron production is illustrated in Fig. 2 where the ratio to the sea level value is plotted on a logarithmic scale against the atmospheric depth. It is seen that the variation is approximately exponential but that the neutron production in paraffin increases more rapidly than that in lead or aluminum. Measurements at higher elevations of the neutron production in air have been reported by Agnew, Bright, and Froman,[2] by Simpson,[3] and by Yuan.[4] All these observers agree that an exponential absorption occurs with a mean free path of approximately 160 g/cm² of air. For comparison with these observations the dashed line in Fig. 2 is drawn which has a slope corresponding to this value of the mean free path.

TABLE I. Nuclear cross sections used for calculations.

Substance	Total cross section	Capture cross section
H	41.0×10^{-24} cm²	0.29×10^{-24} cm²
B	830.0	830.0
C	4.6	0.0045
Al	1.6	0.23
Pb	11.0	0.17
CH_2	86.4	0.59

It is of interest to compare the neutron rates with some observations of the counting rate of a set of Geiger counters arranged to record extensive showers. These observations[5] were made at the same locations and simultaneously with the neutron observations. They are represented by the circles in Fig. 2. It is apparent that the agreement with the paraffin observations is very close.

The variation with elevation can be used to correct the neutron-production rates given in Table II for the absorption of neutron-producing rays within the pile. The detecting chamber was covered with a layer of 30 g/cm² of paraffin and consequently the neutron production in the vicinity of the chamber corresponds to a primary intensity at a somewhat lower elevation than that at which the observations were made. A similar correction can be applied for the case in which lead is present in the pile. However, when the total quantity of lead in the pile was reduced by a factor of nearly 2, the rate of production of neutrons per gram remained unaltered to within the accuracy of the counting as shown in Table II. Hence we conclude that the absorption in the lead is negligible.

This conclusion is strengthened by a separate experiment in which the pile of paraffin was shielded on the top

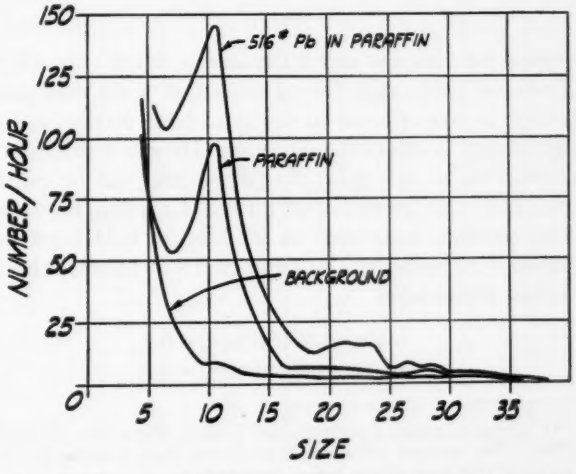

FIG. 1. Neutron distribution at Climax: (a) for 517 pounds of lead and 770 pounds of paraffin. (b) for paraffin alone. (c) for chamber surrounded by borax and paraffin (background).

[2] Agnew, Bright, and Froman, Phys. Rev. 72, 203 (1947).
[3] J. A. Simpson, Jr., Phys. Rev. 73, 1389 (1948).
[4] L. C. L. Yuan, Phys. Rev. 74, 504 (1948).
[5] J. Wei and C. G. Montgomery, Phys. Rev. 76, 1488 (1949).

TABLE II. Observed rates of neutron production. Values are in units of 10^{-5} g^{-1} sec.$^{-1}$.

Material	Mass of material	Neutron production rate (10^{-5} g^{-1} sec.$^{-1}$)
Climax, 675 g/cm²		
Paraffin	770 lb.	24.7 ±0.5
Carbon calculated from paraffin		28.8 ±0.6
Aluminum	749 lb.	30.0 ±1.2
Lead	517 lb.	55.7 ±1.5
	346 lb.	54.3 ±2.1
Mean value for lead		55.0 ±1.3
Denver, 865 g/cm²		
Paraffin	770 lb.	7.98±0.18
Carbon calculated from paraffin		9.32±0.21
New Haven, 1030 g/cm²		
Paraffin	770 lb.	1.98±0.07
Carbon calculated from paraffin		2.31±0.08
Aluminum	749 lb.	3.49±0.20
Lead	517 lb.	6.47±0.24

and four sides by 1 inch of lead. Without the lead shield the neutron counting rate corrected for the background was 505±10 hr.$^{-1}$. With the shield in place 492±11 counts per hour were observed. The absorption in the lead is thus observed to be 2.6±3.0 percent or less than could be detected. This conclusion as well as the observations on the variation with elevation are in good agreement with the observations of Mrs. Cocconi.[6]

MULTIPLICITY OF NEUTRON PRODUCTION

The differences in the rates of production of neutrons in different substances are to be ascribed to two factors: the cross section σ for star production and the multiplicity, or number ν of neutrons per star. In fact the rate R of neutron production per gram is

$$R=k\sigma\nu/A,$$

where k is a constant and A the atomic weight. Now it is extremely likely that the cross section σ for star production is proportional to the total cross section σ_t for high energy bombarding particles.[7] Hence, if values are adopted for σ_t, the ratio of multiplicities can be calculated from the present observations. Choosing the total cross sections measured[8] at 90 Mev of 0.55 barn for carbon, 1.12 barns for aluminum and 4.53 barns for lead, we find at sea level

$$\nu\text{ (lead)}/\nu\text{ (carbon)}=6.4,$$
$$\nu\text{ (lead)}/\nu\text{ (aluminum)}=3.5.$$

These ratios are, of course, subject to some uncertainty on account of the variation of the transparency of nuclei as light as carbon with the energy of the fast neutrons in this energy range. These results are also in agreement with those of Mrs. Cocconi.[6]

It is possible to find the value of ν by a comparison of the neutron rates reported here with the number of stars produced in photographic plates. We assume that the neutron production R can be represented empirically as a function of the atomic weight A by the relation

$$R=CA^{\alpha},$$

where C and α are constants. With this interpolation function the rate of production of neutrons in photographic plates can be calculated. The values so calculated for Climax are given in Table III. The composition of the Ilford nuclear research plates Type C1 was taken from Gardener and Peterson.[9] The total of 157×10^{-5} neutron cm^{-3} sec.$^{-1}$ represents the rate of production under 30 g/cm² of paraffin at Climax. Correction for absorption with a mean free path of 160 g/cm² increases this value to 190×10^{-5} cm^{-3} sec.$^{-1}$.

Two sets of observations of stars in photographic plates at this elevation have been made.[10] Both can be represented by the relation

$$N=N_0e^{-p/2.08},$$

where N is the rate of occurrence of stars having more than p prongs. This relation can be shown to be valid for $p\geqslant3$. If it can be used also for $p<3$, then the total number of stars is simply N_0. The observations of George and Jason give $N_0=41\times10^{-5}$ cm^{-3} sec.$^{-1}$ whereas those of Bernardini and collaborators give $N_0=73\times10^{-5}$ cm^{-3} sec.$^{-1}$. From these values, the multiplicity ν of neutron production is found to be 4.6 or 2.6 averaged

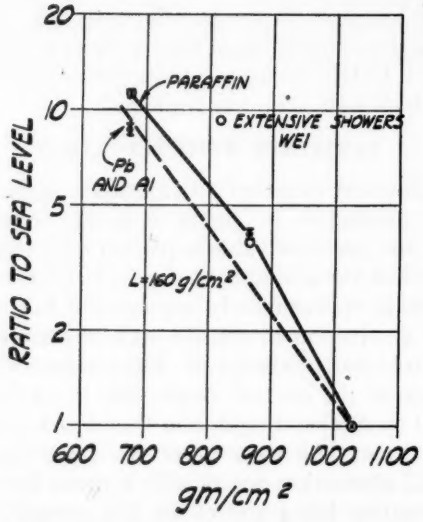

FIG. 2. Variation of production of neutrons with elevation.

[6] Cocconi, Coconni Tongiorgi, and Greisen, Phys. Rev. 76, 1020 (1949). The authors are much indebted to Mrs. Cocconi for the receipt of this manuscript before publication.

[7] See De Juren, Knable, and Moyer, Phys. Rev. 76, 589 (1949); and Fox, Leith, McKenzie, and Wouters, Phys. Rev. 76, 590 (1949).

[8] Cook, McMillan, Peterson, and Sewell, Phys. Rev. 75, 7 (1949).

[9] E. Gardener and V. Peterson, Phys. Rev. 75, 367 (1949).

[10] Reported by B. Rossi, Technical Report No. 26, Laboratory for Nuclear Science and Engineering, M.I.T. (April 4, 1949).

over all stars and over all substances in the photographic plate. A value in this range is entirely satisfactory since the average number of charged particles per star is 2.1.

THE CHAMBER BACKGROUND

It is evident from Fig. 1 that some bursts of ionization occur in the chamber even when it is surrounded by a layer of borax which excludes all thermal neutrons. The size-frequency distribution of these bursts shows no characteristic peak caused by neutrons. Moreover, it is found that these background pulses vary rapidly with elevation. The same large background is observed by other experimenters[11] and it is of some interest to ascertain its nature. The integral frequency-distribution curves observed at the three elevations are shown in Fig. 3 on a log-log plot. The increase with elevation is mostly confined to the small sizes, and the curves show a characteristic shape. This shape can be interpreted as follows.

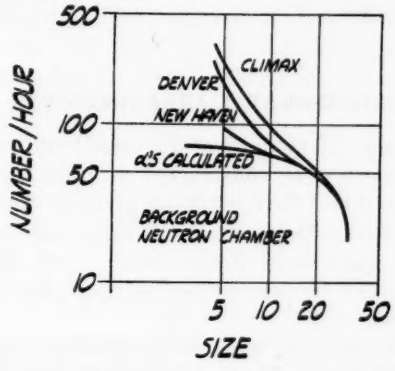

FIG. 3. Background in neutron chamber at three elevations.

At sea level alpha-particles arising from radioactive contamination in the walls of the chamber certainly contribute an appreciable portion of the bursts of ionization. Such contamination is the result of small amounts of uranium and thorium in equilibrium with their daughter substances and the shape of the integral distribution curve can be calculated easily.[12] Such a calculated curve has been drawn to fit the large bursts in Fig. 3. The total number of contamination alpha-particles so determined is of the correct order of magnitude for clean surfaces.[13]

TABLE III. Neutron production in plates—Ilford NR plates Type C1.

Substance	Density ρ	Atomic weight	R	$R\rho$
Ag	1.85 g/cm³	108	45 $\times 10^{-5}$ g^{-1} sec.$^{-1}$	83.3 $\times 10^{-4}$ cm^{-3} sec.$^{-1}$
Br	1.34	80	41	55
I	0.052	127	47	2.4
C, H, O, N	0.661	(as paraffin)	25	16.3
S	0.010	32	31	0.3
Total	3.923			157.3

The bump in the differential distribution curve, Fig. 1, near the abscissa 30 does not vary with elevation and probably represents a surface contamination. The pulses under consideration here are the more frequent smaller ones.

The contribution of alpha-particles can then be subtracted from the curves at the three elevations to yield the burst distribution curves arising from cosmic-ray phenomena. It has been shown[14] that bursts of such a range of sizes are the result of nuclear disintegrations taking place principally in the walls of the chamber. A qualitative comparison with observations of bursts in other chambers made simultaneously at Climax[12] shows that the rate of occurrence and the frequency distribution are in approximate agreement with this explanation. Since the background measurements were taken with a complicated borax and paraffin shield it is difficult to draw further conclusions.

ACKNOWLEDGMENTS

The authors wish to express their thanks to Mr. C. J. Abrams of the Climax Molybdenum Company and to Professor Marcel Schein and Mr. E. F. Fahy for their generous hospitality and the use of laboratory facilities at Climax, Colorado. The observations at Denver were made possible through the kindness of Professors Byron Cohn and Mario Iona of the University of Denver, whose help is gratefully acknowledged.

[11] A good example is shown in reference 3.
[12] H. Carmichael, Phys. Rev. 74, 1667 (1948). Also C. G. Montgomery and D. D. Montgomery, Phys. Rev. 76, 1482 (1949).
[13] J. A. Bearden, Rev. Sci. Inst. 4, 271 (1933).
[14] C. G. Montgomery and D. D. Montgomery, Phys. Rev. 72, 131 (1947); Bridge, Hazen, and Williams, Phys. Rev. 74, 1689 (1948); and also reference 12.

The Analysis of Bursts of Cosmic-Ray Ionization

C. G. MONTGOMERY AND D. D. MONTGOMERY
Sloane Physics Laboratory, Yale University, New Haven, Connecticut*
(Received August 1, 1949)

The agents responsible for the production of bursts of ionization in small chambers have been analyzed on the basis of observations taken at 3510-meters elevation. Three methods of separation were employed: (1) the coincidences between ion chambers and between chambers and counters, (2) the variation of burst rate with a small thickness of lead placed over the chamber, and (3) the variation of burst rate with the size of the ionization chamber. Three components of the burst distribution curve are identified with (1) small locally produced electron showers, (2) nuclear disintegrations, and (3) extensive air showers of high density. Each component predominates at a certain range of burst sizes.

INTRODUCTION

IN a recent paper,[1] evidence has been presented that bursts of ions occurring at sea level in an unshielded ionization chamber are produced by at least two separate phenomena, (1) extensive Auger showers of electrons and photons produced in the air, and (2) nuclear disintegrations produced in the chamber walls. The principal basis for the separation of the bursts of two origins was the effect of thin shields on the frequency distribution of bursts with respect to size. Since then Bridge, Hazen, Rossi, and Williams[2,3] have performed similar analyses of bursts occurring at an altitude of 3500 meters on the basis of the coincidences observed among several ionization chambers.[4] Carmichael[5] has also separated the bursts observed in chambers at sea level according to the agents producing them, using the shapes of the observed frequency distribution curves as a guide. The present paper describes some experiments on bursts observed at 3510-meters elevation. Three independent methods were employed to analyze the bursts: (1) the effect of thin lead shields as previously employed at sea level, (2) coincidence experiments similar to those of Bridge *et al.* and (3) a comparison of the frequency of bursts observed in chambers of three different areas.

TABLE I. Characteristics of the ion chambers.

Chamber	Inside diameter inches	Inside length inches	Area cm²	Diameter collecting electrode inch	Coefficient of induction cm	Maximum time of ion collection sec.	Efficiency, for electron collection
2-inch	$1\frac{15}{16}$	$7\frac{3}{4}$	92	$\frac{1}{8}$	7.78	0.09	0.82
3-inch	2.87	$9\frac{3}{4}$	174	$\frac{1}{4}$	9.44	0.17	0.80
4-inch	$3\frac{15}{16}$	$15\frac{1}{2}$	394	$\frac{1}{4}$	11.7	0.37	0.82

* Assisted by the Joint Program of the ONR and the AEC.
[1] C. G. Montgomery and D. D. Montgomery, Phys. Rev. **72**, 131 (1947).
[2] Bridge, Hazen, Rossi, and Williams, Phys. Rev. **74**, 1083 (1948).
[3] R. W. Williams, Phys. Rev. **74**, 1689 (1948).
[4] See also C. G. Montgomery and D. D. Montgomery, Phys. Rev. **75**, 980 (1949).
[5] H. Carmichael, Phys. Rev. **74**, 1667 (1948).

EXPERIMENTAL ARRANGEMENTS

Three pairs of cylindrical ion chambers were used. The chambers were constructed of brass $\frac{1}{32}$ inch in thickness and had the dimensions given in Table I. The collecting electrodes were coaxial brass rods supported by Kovar glass seals. Each chamber was filled with argon of about 99 percent purity to a pressure of 4.8 atmospheres.

In order to cover a large range of burst sizes and frequencies, two methods of observation were employed. In the first, Method A, each ion chamber was connected to an electrometer tube, Type 38, followed by an amplifier and a galvanometer. The galvanometer deflections were recorded photographically on sensitive paper moving at a rate of 70 cm per hour. The time constants of the amplifier were several seconds long and hence the low frequency limit of the amplifier was a small fraction of 1 cycle per second; the high frequency limit was determined by the period of the galvanometer which was one second. The sensitivity was determined by means of a calibrating pulse of known potential applied to the ion chamber, together with a measurement of the proper coefficient of induction by comparison with a standard capacitor. The burst sizes were therefore expressed in terms of ion pairs formed within the chamber, by an absolute calibration. The over-all precision is probably about 10 percent. A representative value is 4×10^4 ion pairs per millimeter deflection of the galvanometer, Observations were taken with two chambers of the same size with the axes parallel and separated by 6 inches. The two galvanometer traces were recorded on the same photographic paper.

In Method A, the central rod of each ion chamber was operated near ground potential and the outer cylinder at a positive potential of 300 volts. Both positive and negative ions were collected fast enough to be recorded by the galvanometer. The maximum traversal time T for an ion is

$$T=\frac{\ln b/a}{2\mu V}(b^2-a^2),$$

where a and b are the inner and outer radii, μ the mobility, and V the potential applied to the chamber.

Values of T calculated with $\mu = 1.5$ cm^2 volt^{-1} sec.$^{-1}$ at one atmos. are given in Table I. Since the positive ions moved inward to the high field region, most of the potential change of the collecting electrode was the result of the motion of positive ions.

On the same photographic paper with the galvanometer traces, the counts of two sets of shower counters were recorded by means of flashes of small argon-filled lamps. The first shower set considered of three counters, each of 20-cm^2 area, arranged in a triangular array. The second set, which was also in use for another investigation, consisted of three counter trays, each of area 320 cm^2. The two sets were placed in roughly the same horizontal plane as the chambers and at various distances, usually between 1 and 2 meters, from the chambers. From the photographic record, coincidences between chambers, and between a chamber and one or both counter sets could be detected. The resolving time for such coincidences was determined by measuring chance coincidences between galvanometer traces and lamp flashes caused by unrelated events. It was found to be 1.5 sec. which represents a distance on the photographic record of 0.3 millimeter. Corrections have been made for accidental coincidences in the few instances where this was necessary.

The second method of observation, Method B, was suitable for recording the more frequent smaller bursts of ionization. The collecting field in the chamber was reversed and the outer shell of the chamber was fixed at a negative potential with respect to the rod. Most of the change of potential was therefore produced by the rapid motion of electrons to the high field regions. The fast pulse so produced was amplified by a four-stage feed-back amplifier with an upper frequency limit of about 20 kc/sec. The low frequency cut-off was determined by a time constant of 10^{-3} sec. and therefore the

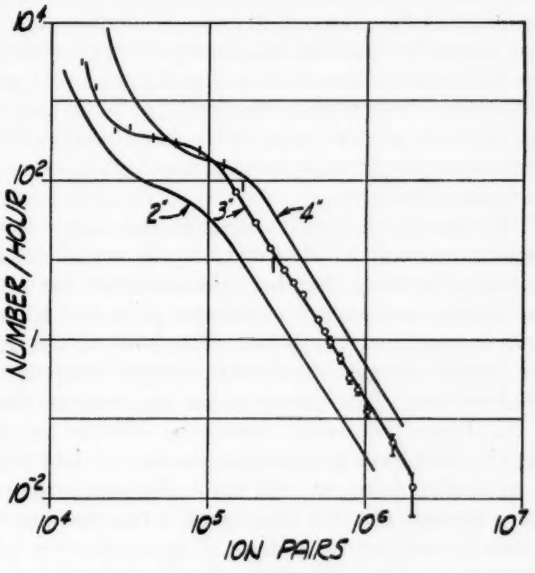

FIG. 1. Burst frequency distribution curves for chambers of 2-, 3-, and 4-inch diameters.

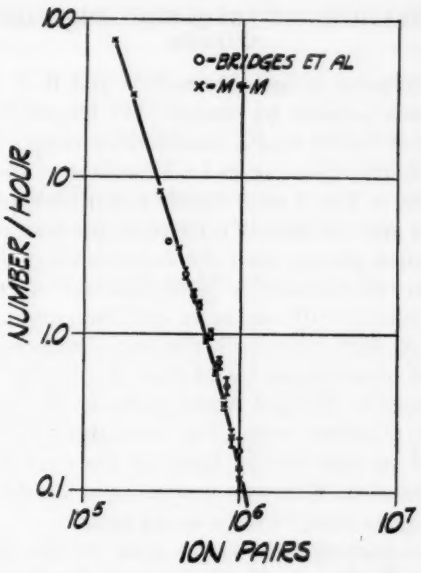

FIG. 2. Comparison with results of Bridge, Hazen, Rossi, and Williams.

effect of the motion of the positive ions was very little amplified. The directly observed potential changes depend in this situation on the distribution of ionization within the chamber.[2] If the ionization is uniform throughout the volume, the correcting ratio or efficiency for electron collection is given by

$$1-1/(2\ln b/a),$$

for $b \gg a$. The values of this efficiency are given also in Table I.

It is well known that accurate quantitative measurements of ionization cannot be made employing electron collection unless precautions are taken to obtain extremely pure gas in the chamber. If impurities are present electron attachment takes place, the speed of the negative charges is much reduced, and the change of potential of the collecting electrode takes place too slowly to be amplified. In the present experiments argon of only commercial purity was used and hence some electron attachment occurred. Advantage was taken of this circumstance as described in a section to follow.

The amplifier was followed by a discriminator circuit to select pulses larger than a given size. These pulses could then be counted with a mechanical recorder or used to flash another argon lamp. This made it possible to operate several chambers simultaneously; two chambers using Method A, the others with Method B. As seen below, too few coincidences were found to justify long periods of such operation.

All of this equipment was installed in a 2½-ton truck with a light roof of approximately 1.3 g/cm^2 thickness. The truck was located at Climax, Colorado at an altitude of 3510 meters during July and August of 1948. The mean atmospheric pressure corresponded to 675 g/cm^2.

OBSERVATIONS OF FREQUENCY DISTRIBUTION CURVES

By utilization of both Methods A and B of observation it was possible to measure the frequency of occurrence of bursts over a considerable range. The frequency distribution curves for chambers of three sizes are shown in Fig. 1 on a double logarithmic plot. The ordinates give the rates of occurrence per hour of bursts of ionization greater than the corresponding abscissas. The observations made by Method A cover sizes greater than about 1.5×10^5 ion pairs and the curves are the average of data taken with the two chambers of each size. The observations by Method B overlap to some extent those by Method A and represent the results for a single chamber only. The statistical accuracy is indicated by the vertical lines for the data from the 3-inch chamber. Where no vertical lines are drawn, the errors are too small to show in the figure.

It is of interest to compare these curves with data taken by Bridge *et al.*[2] at the same location. These observers employed several ionization chambers of 3-inch diameter but longer than the ones used by us. The chambers were filled with argon to the same pressure. Two important differences exist however. First, Bridge *et al.* employed electron collection similar to our method but with more rapid amplifier response although the range of burst sizes is comparable to our observations by Method A. Second, our calibrations for burst sizes are absolute ones depending on measurements of potential and capacitance whereas Bridge *et al.* used for calibration a source of polonium alpha-particles inside their chambers and expressed the burst sizes in terms of the energy released in the chamber relative to that released by an alpha-particle. To compare the observations it is necessary only to multiply the burst rates by the ratio of the lengths of the chambers and to convert from electron volts to ion pairs. The value of 25.4 ev per ion pair was chosen. Figure 2 shows that the agreement is excellent. The plotted points are those of Bridge *et al.*, the curve represents the present observations.

The principal task before us is to analyze these curves and attempt to establish the nature of the phenomena responsible for the production of these bursts of ionization.

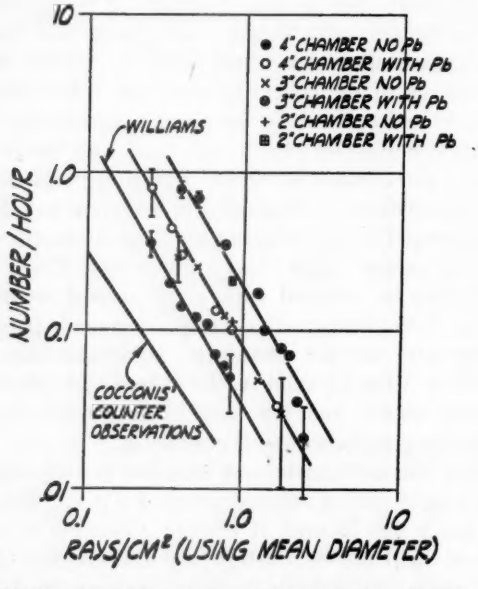

FIG. 3. Distribution of bursts caused by extensive showers with and without lead over the chambers.

EXTENSIVE SHOWERS

The component most easily separated is the bursts produced by the extensive showers of cosmic rays. Such showers cover an area large compared with the area of the chambers and spread over distances of 100 meters or more. Consequently, if an extensive shower produces a burst of ionization in one chamber, it will produce bursts of nearly equal size in the other chambers near it and also cause a discharge of the counter sets. Thus by rejecting all but coincident bursts, the effects of such showers can be isolated. The actual criterion chosen was that at least a triple coincidence occur. Both of the chambers must show in the galvanometer a trace a burst of ionization greater than a given size and in addition at least one other chamber or one or both shower counter sets must simultaneously discharge.

When this is done it is found that most of the bursts shown in the curves of Fig. 1 are rejected. The relatively few remaining bursts constitute not more than 5 percent of the total; these are plotted in Fig. 3. The coordinates used here are somewhat different. Since the spreading of the showers is large, the number of bursts of ionization should be independent of the size of the chamber. The size of the burst measured in ion pairs is, however, proportional both to the area of the chamber and to the chamber diameter or in fact proportional to the volume of the chamber. In order to compare directly these ionization-chamber measurements with observations by counters, the data in Fig. 3 are plotted with the ordinates representing the rate per hour and the abscissas rays per unit area. It has been assumed that a shower ray produces 80 ions pairs per cm in argon at atmospheric pressure.

This value of the specific ionization was chosen in the following manner. R. H. Frost,[6] by means of droplet counting in a cloud chamber, has measured the minimum specific ionization for electrons to be 53.1 ± 2.8 in argon at standard conditions. The shower electrons have higher energies than that corresponding to the minimum since their energy is on the average about 10^8 ev. From theoretical curves an electron of this energy should have a specific ionization of 1.44 times the minimum value or 76.5 cm^{-1}. Extensive showers passing through the thin brass walls of the chamber will increase in number[8] by a factor of approximately 1.12.

[6] R. H. Frost, Ph.D. thesis, University of California (1947), quoted by R. B. Brode, Rev. Mod. Phys. 21, 37 (1949).

Hence the effective specific ionization in argon at 20°C is $1.12\times76.5\times273/293$ or 80 cm^{-1}.

The bursts plotted in Fig. 3 for the 4-inch chamber were selected by requiring a triple coincidence between *three* ionization chambers; the shower counters were not used. The strictness of this requirement eliminated some extensive showers, and the results for the 3- and 4-inch chambers are not comparable. The single point for the 2-inch chamber agrees well with the data for the 3-inch chamber.

Observations were also taken with lead shields over the chambers. The shields were 6 mm thick and covered the upper half of the cylindrical surfaces. Electrons and photons from the air, impinging on this lead, increase in number since the critical cascade energy for lead is much less than that for air. The burst sizes would therefore be increased by this multiplication. It is evident from Fig. 3 that such multiplication is observed, and the factor seems to be about 1.7 for all chambers.

The observed multiplication can be compared with that expected from the cascade-shower theory. Since the lead shield is curved, the effective thickness is larger than the actual thickness by a factor of $4/\pi$ as can be shown by a simple calculation. The effective thickness is thus 7.6 mm or 1.5 radiation units. Since the average energy of an electron from the air is approximately equal to the critical energy for air or 100 Mev and that for lead only 7 Mev, a simple estimate from Arley's[7] calculations predicts a factor of 2.2. Although this factor is somewhat larger than the observed multiplication, the discrepancy can probably be removed by a more accurate calculation.

In Fig. 3 are plotted also the observations of the Cocconis[8] and of Williams.[3] The Cocconis measured the density distribution of extensive showers by means of counters at the somewhat lower elevation of 3260 meters. The measured rates have been multiplied by a factor, obtained from unpublished observations of Kraybill,[9] amounting to 1.25 to correct for the increase with elevation. Williams' observations were made with ionization chambers at the same location as the present experiment. In order to compare the data directly it has been necessary to alter the sizes of Williams' bursts to the value of specific ionization used above. Williams assumed that the energy loss of shower electrons in argon was 2.1 Mev cm^2 g^{-1}, a theoretical value, and that the brass walls introduced multiplication by a factor of 1.12. Thus the effective specific ionization used was 157 ion pairs/cm at 20°C. The shower densities have therefore been increased before plotting by a factor of $157/80 = 1.96$.

Williams' observations are represented by the line drawn in the figure and the agreement with our observations is good. Both sets of data show the same slope on the logarithmic plot of -1.7 which is the value of the exponent in the integral density spectrum of the showers. The Cocconis' observations are lower in absolute value and have a slope of -1.46. The range of sizes observed by the Cocconis is somewhat smaller (less than 0.1 ray/cm^2) than that covered by the ionization-chamber measurements, and an extrapolation to larger densities may not be justified.

[7] N. Arley, Proc. Roy. Soc. A168, 519 (1938).
[8] G. Cocconi and V. Tongiorgi, Phys. Rev. 75, 1058 (1949).
[9] H. Kraybill, Ph.D. thesis, University of Chicago (1949).

NUCLEAR DISINTEGRATIONS

Bursts of ionization which are not coincident with bursts in other chambers or with the discharges of the counter set comprise the greater part of the bursts of sizes between 2×10^5 and 10^6 ion pairs. According to one criterion then, they result from nuclear disintegrations occurring within the chamber walls. A second check of this conclusion can be found from a comparison of the observations in chambers of different sizes. The rate of occurrence should be proportional to the area of the chamber and the amount of ionization produced should be proportional to the path length within the chamber or to the chamber diameter. The observations reduced in this manner are plotted in Fig. 4. The frequency is expressed in number $hr.^{-1}$ cm^{-2} and the burst size in ion pairs per cm obtained by dividing by the diameter of the chamber. It is seen that there is rather close agreement between the various chambers, but that a systematic difference appears to exist, with the rates of the largest chamber being least. Two possible explanations suggest themselves. First, some of the rays from the nuclear event may not complete their range within the chamber or, second, some

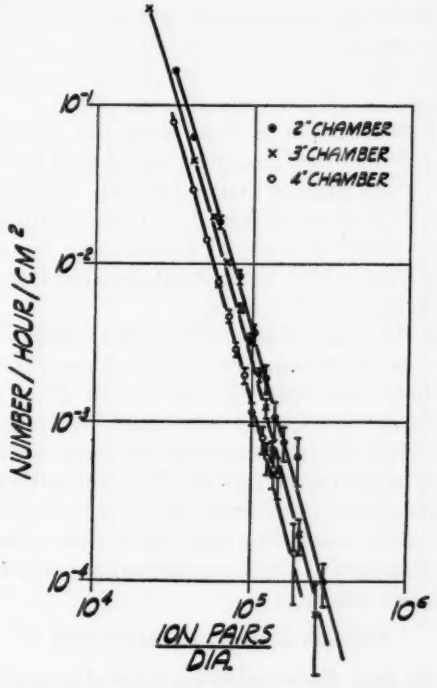

FIG. 4. Distribution of bursts caused by stars.

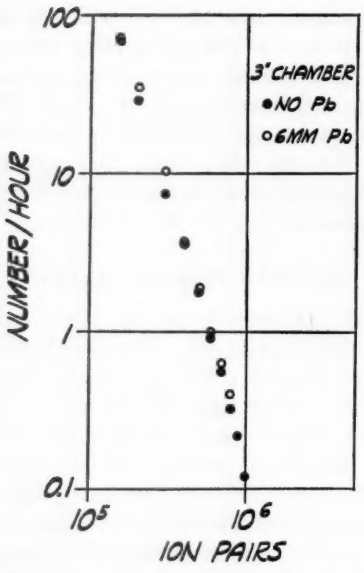

FIG. 5. Effect, on the star distribution, of a lead shield placed over the chamber.

recombination may be present and present to the greatest extent in the largest chamber where the electric field is smallest. Probably both factors contribute to some extent. It should be noted that the distribution curves have a slope of about -3.2, much steeper than the slope of the distribution curves for extensive showers. A similar behavior was also found at sea level.[1]

The third test also confirms the supposition that the bursts are the result of nuclear disintegrations. A small thickness of lead placed over the chamber should have no effect on the burst size and little effect on the burst rate if electronic radiations are not involved. The effect of the 6-mm lead shield on the bursts in one chamber is shown in Fig. 5. Although a small increase in rate may be present, it scarcely exceeds the errors of measurement. Consideration of these data and corresponding curves for the other chambers shows that the increase in rate is not greater than 5 percent. Thus the three criteria: lack of coincidences, variation with chamber size, and effect of lead, all substantiate the assertion that the bursts of the sizes considered arise from nuclear events in the chamber walls.

From the observations with lead an additional conclusion can be drawn. Since the lead contributes little to the burst rate observed, the ranges of the particles produced in the nuclear events must, to a large extent, be less than the thickness of the brass walls of the chamber or less than 0.7 g/cm². This fact is in agreement with observations of cosmic-ray stars on photographic plates. Some stars, however, have been observed in cloud chambers to contain penetrating particles with a much larger range.

OBSERVATIONS BY METHOD B

All the data discussed so far were obtained from the galvanometer traces by Method A. It remains to discuss the observations dealing chiefly with bursts of sizes smaller than about 2×10^5 ion pairs obtained by counting (Method B). The most striking feature of the observations in this region is the existence of a "knee" in each of the burst distribution curves shown on Fig. 1. In this region of small sizes no coincidence data nor data on the effect of lead shields are available and we must rely on the variation with chamber size alone to guide the analysis. We can, however, realize the advantage of the use of gas in which some electron attachment and recombination takes place. The range of burst sizes in question, of the order of 10^5 ion pairs, is the same as that of the alpha-particles from natural radioactive contamination in the chamber walls. In the alpha-particle tracks the density of ionization is high. Moreover, the tracks are short and, at high pressure, confined to within a few millimeters of the chamber wall where the electric field is lowest. The free electrons formed are quickly attached either to a positive ion or to an impurity molecule and the pulse resulting from the motion of negative ions is slow and hence greatly reduced. For protons from nuclear disintegration, the situation is different. Protons have much longer ranges and are not confined to regions of low field strength and in addition the density of ionization along a track is much less. Attachment and recombination are therefore much less likely and a large fraction of the free electrons formed are collected by the electrode of the chamber and a large pulse is produced.

To demonstrate that these processes are taking place, observations were made at sea level with only one atmosphere of argon present in the chamber. Under this condition the attachment in the alpha-particle ionization is small and nearly all of the negative charge moves across the chamber as electrons. The ionization from high energy protons is, on the other hand, reduced since in crossing the chamber only one-fifth as much gas is traversed. Most of the pulses recorded, therefore, are the result of contamination alpha-particles. The results

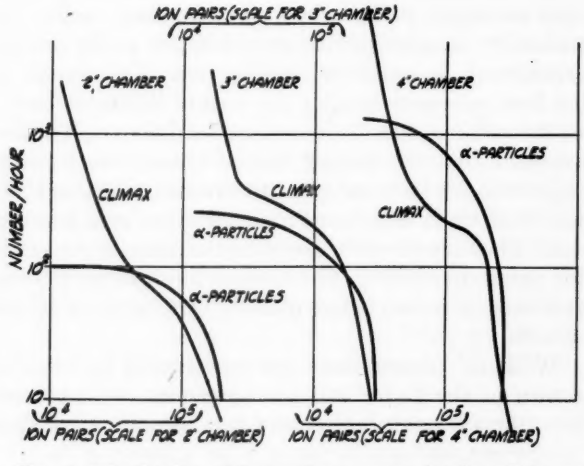

FIG. 6. Distribution of bursts from contamination alpha-particles compared with the total burst distribution at 3510 meters, showing knee and effect of recombination.

of these measurements are shown in Fig. 6 together with the observations at 4.8 atmos. pressure taken at 3510 meters. It is evident that, for some range of burst sizes in each chamber, the number of alpha-particles exceeds the measured number of bursts at the high elevation. The difference is particularly large in the 4-inch chamber where the number of contamination alpha-particles per unit area is much larger than in the other chambers. The curves drawn for the alpha-particles are calculated on the assumption that the uranium and thorium series are present distributed uniformly through the volume of the brass walls and that the disintegration rates of the two series are equal. The experimental points, not shown in the figure, fit the calculated curves very well.

It is evident that the alpha-particle distributions show a "knee" quite similar to those observed in the burst distributions, and indeed, for the same reasons. Charged particles ejected from nuclei must have a differential energy distribution that is cut off at the low energy end somewhat below the energy corresponding to the Coulomb potential barrier of the residual nucleus. Since the pentration through the barrier is improbable, the ejected particles must possess at least the energy gained from the repulsive electric forces as the particle moves away. This minimum energy will be of the order of several million electron volts. In an ionization chamber where the particles originate in the walls, not all of this energy is effective in producing ions but a large part may be lost in the chamber walls before the particle emerges into the gas. The differential energy distribution of the particles emerging from the walls does not show, therefore, the low energy cut-off but instead is flat from zero energy to the cut-off energy. The integral distribution of the amounts of ionization produced in the chamber must consequently approach the zero-energy axis with a finite slope. On a double logarithmic plot there will be a corresponding leveling off of the distribution curve for small burst sizes and the knee results.

It should be noted from Fig. 1 that the burst size at which the knee occurs decreases with the diameter of the chamber. This suggests that these small bursts are also the result of nuclear disintegrations and hence the data from the different chambers should be compared on this basis. Figure 7 shows the observations reduced in the manner of Fig. 4. It is evident that the correspondence here is much less marked than for bursts of larger sizes. Nevertheless we think that the observed knees are representative of the low energy cut-off in the energy distribution of protons and other long-range particles from nuclear disintegrations. Electron attachment undoubtedly affects the observed pulse sizes from protons to some extent and, since the process is sensitive to small amounts of impurities in the gas, inconsistencies in the observations near the knee as shown in Fig. 7 are readily understandable.

The existence of a flat portion of the size distribution

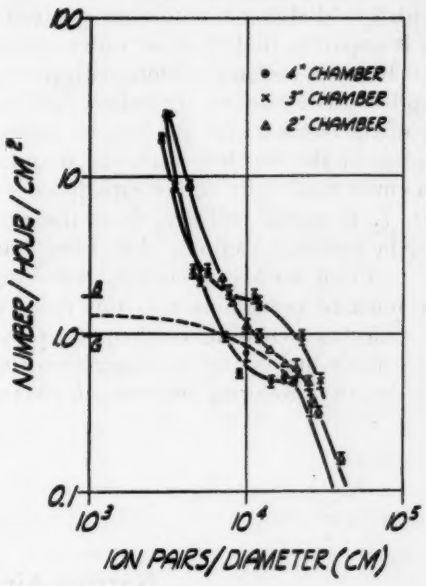

FIG. 7. Comparison of extrapolated star burst rate with observations of Bernardini (B) and of George (G) with photographic plates.

curve allows an estimate to be made of the total number of nuclear disintegrations and a comparison with the rates observed in photographic plates becomes possible. Bernardini and collaborators and George[10] have recently reported the rate of occurrence of stars having three prongs or more to be 15.3 and 8.5, respectively, in units of cc^{-1} day^{-1} at an elevation of 3500 meters. If the relative frequencies of stars with different numbers of prongs are extrapolated from 3 prongs to 1, the corresponding rates become 39 and 22 cc^{-1} day^{-1}. If we assume that the emulsion density is 3.9 g cc^{-1} and that the brass in the chamber walls is all as effective as the emulsion in the production of disintegrations containing ionizing particles which emerge into the gas of the chamber, the expected total frequency of bursts that result from disintegrations can be calculated. The values corresponding to Bernardini's and to George's data are plotted at the levels labeled B and G, respectively, in Fig. 7. The distribution curve for nuclear bursts should thus flatten and approach these levels as the burst size is decreased, as indicated by the dashed line in the figure.

This dashed line was drawn taking into account the following arguments. The line should lie above the curve for the 4-inch chamber since we know that some electron attachment is taking place. The curve for the 3-inch chamber is much higher than the other two and probably contamination alpha-particles contribute appreciably to the observed rates. The most reliable estimate can therefore be made from the curve for the 2-inch chamber where the alpha-contamination is low

[10] Results reported by Rossi, ONR Technical Report No. 26, M.I.T. (April 4, 1949).

and the high field strength minimizes electron attachment. It is apparent that there is order-of-magnitude agreement between the observations with photographic plates and with ionization chambers although the accuracy of the check leaves much to be desired.

For bursts of the smallest sizes, the frequency distribution curve rises again rather rapidly as is evident from Fig. 7. It seems unlikely, from the arguments presented in previous sections, that these bursts are also the result of nuclear processes. Some new phenomenon must be predominant in this range of sizes. Only a few electrons crossing the chamber are necessary to produce these bursts and it is suggested that these represent locally produced showers of electrons. In support of this contention, we can only point out that the number of single rays through the chambers amounts to 250 cm^{-2} $hr.^{-1}$. Since many of these are electrons and since there is an approximately equal number of photons, small showers occurring with the observed frequency are not unreasonable. It should be noticed that the number of these small showers appears to be proportional to the chamber area.

In conclusion, the authors wish to express their thanks to Mr. C. J. Abrams of the Climax Molybdenum Company and to Mr. E. F. Fahy and Professor Marcel Schein of the University of Chicago for their generous hospitality that made the observations at high altitude possible.

PHYSICAL REVIEW VOLUME 76, NUMBER 10 NOVEMBER 15, 1949

Narrow Air Showers of Cosmic Rays*

JOHN WEI AND C. G. MONTGOMERY
*Sloane Physics Laboratory, Yale University,** New Haven, Connecticut*

(Received August 1, 1949)

Observations are reported of the decoherence curves for air showers of cosmic rays at sea level, 1640 meters and 3510 meters elevation. The variation of the decoherence curves with counter area and the absorption of narrow showers were also measured at the highest elevation. It was found that narrow showers (that is, showers observed at small counter separations) differ from ordinary extensive air showers with respect to variation with elevation, variation with area of the counters, and penetrating power. Consideration of the effects of pressure on the spreading function show that the altitude variation cannot be taken as a certain indication that narrow showers differ in nature from extensive ones, nor can the variation with counter area. The relative penetration, however, of narrow showers in lead, iron, and aluminum cannot be explained except by differences in the nature of the particles involved.

INTRODUCTION

SHOWERS of cosmic rays which originate in the atmosphere have been the subject of many investigations since their discovery by Auger.[1] Auger and many others have measured the coincident counting rate of two or more counters as a function of the separation between them up to large distances. The lateral spread of such showers as measured by this "decoherence curve" agrees well with theoretical predictions[2,3] of the cascade theory of electron-photon showers for separations from 1 to 1000 meters. Between about 1 and 10 meters separation there is a well defined plateau in the decoherence curve, and Molière's calculations, as well as those of others, predict only a negligibly small increase of counting rate as the separation is decreased to zero. Observations, however, deviate from the theoretical predictions, and a sharp rise in counting rate is found which attains many times the expected value at separations of 20 or 30 cm. The showers that are responsible for this discrepancy at small separations we call "narrow air showers." Although this discrepancy was noted long ago, no detailed investigations were made concerning it until the experiments of Alichanian *et al.*[4] Many questions concerning narrow showers were still unanswered precisely and hence the present experiments were undertaken. The observations to be described consist of measurements of the decoherence curve for different elevations and different counting areas, some absorption measurements, and subsidiary experiments to test the importance of local showers.

THE DECOHERENCE CURVE

Most of the experiments were performed with the arrangement of counters indicated in Fig. 1. Four trays of four counters each were arranged as two telescopes of wide angle in order to minimize the accidental coincidences. The counters had copper cathodes 20.5 cm by 4.3 cm in glass envelopes and were filled with argon

* Part of a dissertation to be presented by the first author for the degree of Doctor of Philosophy at Yale University.

** Assisted by the Joint Program of the ONR and the AEC.

[1] Auger, Maze, Ehrenfest, and Freon, J. de phys. et rad. **10**, 39 (1939).

[2] G. Molière, *Lectures on Cosmic Radiation* (Dover Publications, New York, 1946), edited by W. Heisenberg.

[3] G. Cocconi, Phys. Rev. **72**, 350 (1947).

[4] A. Alichanian *et al.*, J. Phys. U.S.S.R. **10**, 296, 518 (1946); **11**, 16 (1947).

mixed either with alcohol or with ethyl ether vapor. The resultant efficiencies were more than 99 percent. Each tray thus had an effective area of 320 cm². Triple coincidences (T) between counters 123 and quadrupole coincidences (Q) were simultaneously recorded as a function of the distance d for three elevations: New Haven, Connecticut, 10 meters above sea level, Denver, Colorado, elevation 1640 m, and Climax, Colorado, elevation 3510 m. The counters were placed either in a truck or in small houses close to thin wooden roofs of thickness about 1.3 g/cm². The effect of such a covering is small, as discussed in more detail below.

The coincidence circuits were simple Rossi circuits with 6SJ7 tubes, and thyratrons were used to drive mechanical recorders. The resolving time was of the order of 8μ sec. and corrections to the counting rates were made for accidental coincidences.

The six curves obtained are shown on a log-log scale in Fig. 2. The long plateau and the increase in counting rate for small separations are evident in each case.

The portion of the curves for separations greater than about 1 meter results entirely from extensive cascade showers. Hence, if the separation is measured in radiation units in air at the pressure where the observations were taken, the three curves should be identical except for an intensity factor dependent on elevation. It is possible to compare the curves on this basis if the ordinates and abscissas are reduced by the factors given in Table I. The decoherence curves reduced in this fashion are shown in Fig. 3. It is apparent that for large separations all the observations can be considered to lie on a common curve. The variation of the occurrence of extensive showers with elevation as given in the last column of Table I is in good agreement with that determined by Kraybill.[5]

For small values of d the situation is quite different. The decoherence curves do not reduce to a common shape and hence disagree with the predictions of the cascade theory. We can separate the narrow showers from the extensive ones by extrapolating the observed plateaus of Fig. 2 to the smallest separations and subtracting. The resultant curves are shown in Fig. 4 on a linear scale. It has been assumed that the decoherence curve for extensive showers has zero slope for distances less than about 1.5 meters and the counting rate at this distance has been subtracted from those at smaller distances. The standard deviations of the points have been correspondingly increased. No reduction to compensate for a change in pressure has been made.

It is evident that the variation with elevation is much less for narrow showers than for extensive ones. The increase from sea level to 3510 m is only by a factor of 4 for $d=20$ cms instead of by a factor of 12 as for extensive showers. This slow variation with elevation is characteristic of only the hard component of cosmic radiation and suggests that a genetic relation exists. As will become evident, corrections for the pressure variation may modify this conclusion.

TABLE I. Factors by which d and the counting rate should be divided to reduce the decoherence curves to sea level.

Location	Elevation	Pressure	Factor for d	Factor for counting rate
New Haven	10 m	1030 g/cm²	1	1
Denver	1640	865	0.84	4
Climax	3510	675	0.65	12

Some observations were also made at Climax of the decoherence curves for different sensitive areas in each counter tray. These data are presented in Fig. 5. It is evident that the narrow showers become relatively less prominent, compared with extensive showers, as the area is decreased.

PROBABILITY CONSIDERATIONS

To interpret experiments on showers, it is always essential to calculate the probability that a count be recorded when the desired phenomenon occurs. Let us consider a simple model that should apply to our observations. Assume first that the showers under consideration come from the vertical direction and have an axis such that the N rays in the shower are distributed at random in azimuth about this axis. The probability distribution with respect to distance r from the axis we shall denote by $\rho(r)$ and assume that $\rho(r)$ is normalized according to

$$\int_0^\infty 2\pi r\rho(r)dr=1. \quad (1)$$

Let the number of showers with N rays be $f(N)$ per unit area per second. Suppose two counters of areas S_1 and S_2 are arranged as shown in Fig. 6. It can be shown[6] that the probability P that a shower of N rays with an axis through the point $(r, 0)$ will give at least one ray through each counter is

$$P=1-(1-p_1)^N-(1-p_2)^N+(1-p_1-p_2)^N, \quad (2)$$

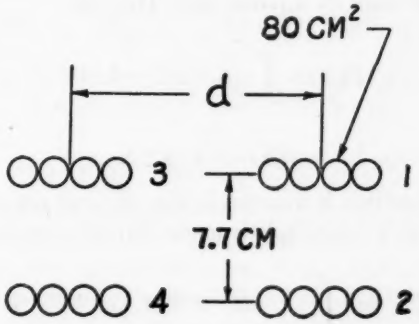

FIG. 1. Arrangement of 4 trays of counters to form 2 telescopes.

[5] H. L. Kraybill, Phys. Rev. 73, 632 (1948) and private communication.

[6] C. G. Montgomery and D. D. Montgomery, J. Frank. Inst. 221, 59 (1936).

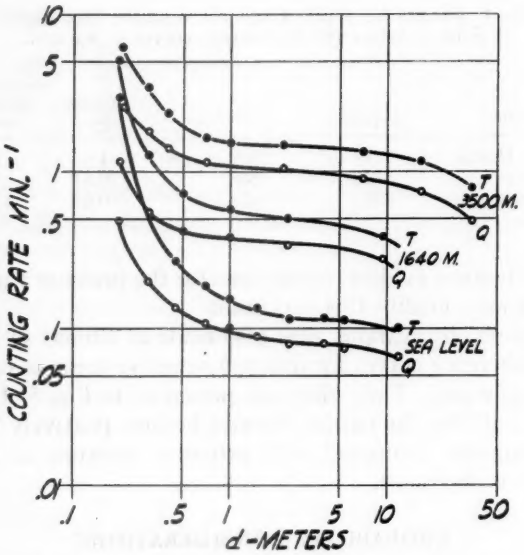

FIG. 2. Decoherence curves for triple and quadruple coincidences at three elevations.

where the *a priori* probabilities p_1 and p_2 are given by

$$p_1=S_1\rho(r_1), \quad p_2=S_2\rho(r_2). \tag{3}$$

The coincident rate C of the two counters is then

$$C=\int_{\text{plane}} rdrd\theta \sum_{N=2}^{\infty} Pf(N). \tag{4}$$

The lower limit of the sum could as well have been taken as 1 or 0 in Eq. (4) since P is zero for these values of N. If the probabilities p_1 and p_2 are not too large, P can be approximated by

$$P=(1-e^{-p_1N})(1-e^{-p_2N}), \tag{5}$$

and the sum in (4) replaced by an integral. Hence

$$C=\int_{\text{plane}} rdrd\theta \int_{N=2}^{\infty} (1-e^{-p_1N})(1-e^{-p_2N})f(N)dN. \tag{6}$$

It is customary to represent the integral distribution of shower sizes by a power law. Thus let

$$F(N)=\int_N^{\infty} f(N)dN=A/N^{\gamma} \tag{7}$$

and

$$f(N)=\gamma A/N^{\gamma+1}. \tag{8}$$

If this function is inserted in Eq. (6) and the substitution $x=p_1N=\rho(r_1)S_1N$ is made, Eq. (6) becomes

$$C=\int_{\text{plane}} rdrd\theta \int_{x=(r_1)S_1}^{\infty} (1-e^{-x})(1-e^{-(P_2/P_1)x}) \times\frac{\gamma A}{x^{\gamma+1}}[\rho(r_1)S_1]^{\gamma}dx. \tag{9}$$

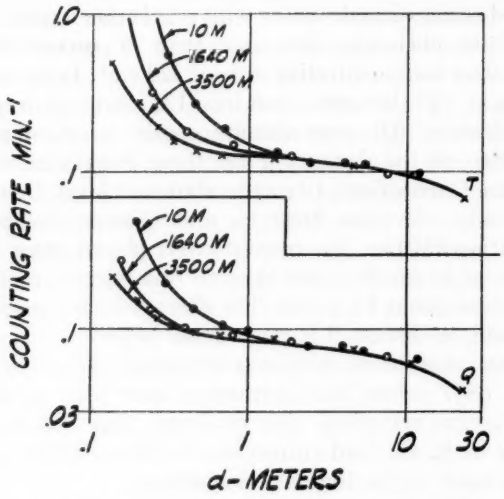

FIG. 3. The data of Fig. 2 reduced according to Table I.

Now if the counting rate resulting from showers containing only a few rays is small, the lower limit of the second integral can be replaced by a small constant. In this case it is evident that, if the counter areas are altered by the same factor, so that p_2/p_1 remains constant, the counting rate C is proportional to S^{γ}. The observations shown in Fig. 5 can be used to test this relation and to determine the parameter γ. In Fig. 7 the data have been replotted on a double logarithmic scale. It can be seen that the variation with area can indeed be approximated by a power law, but with an exponent γ which is different for the narrow and the extensive showers. For the latter γ is 1.4 in agreement with other observers,[5] but for the narrow showers the observed slope corresponds to a value of γ between 3.0 and 3.6 with a most probable value of 3.2. Again in

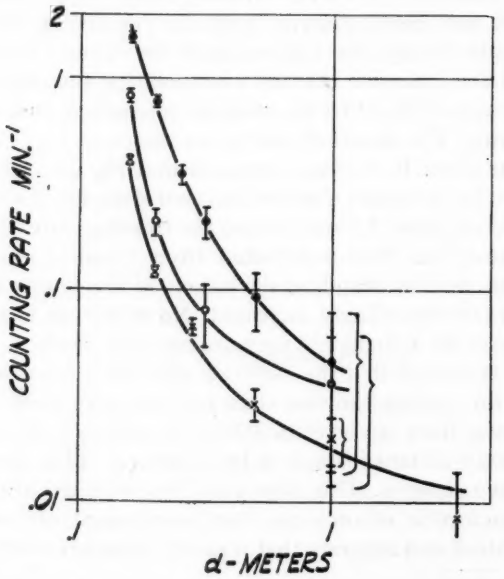

FIG. 4. Decoherence curves with extensive showers subtracted.

this respect the behavior of narrow showers appears to be characteristically different from that of extensive ones. Caution must be observed here, however. For such a large value of γ it may not be permissible to neglect the effect of the lower limit of the second integral in Eq. (9). In fact if the lower limit were zero, the integral diverges at this limit for $\gamma>2$. In a rigorous calculation Eqs. (2) and (4) should be employed.

It is perhaps suggestive that γ so determined is close to 3. Such an exponent in the power-law distribution of the frequency of showers of N rays would be expected for cascade showers produced by knock-on and disintegration electrons of mesotrons.

Equation (9) can also be employed to find the shape of the decoherence curve. For extensive showers the function $\rho(r)$ has been calculated by Molière[2] and can be expressed as shown by Bethe[7] by the approximate analytic form

$$\rho(r)=\frac{0.45}{r_0r^2}\left(1+4\frac{r}{r_0}\right)\exp\left[-4\left(\frac{r}{r_0}\right)^1\right],\quad \frac{r}{r_0}<0.5, \quad (10)$$

where the unit length r_0 is given by

$$r_0=\frac{E_sX_0}{E_c}, \quad (11)$$

E_c and X_0 being the familiar cascade parameters and E_s the characteristic scattering energy[8] which is equal to 21 Mev.

The occurrence of the singularity in ρ at the origin prompts one to suspect that a peak also occurs in the decoherence curve at the origin, contrary to Molière's calculations.[9] It should be noticed that ρ occurs raised

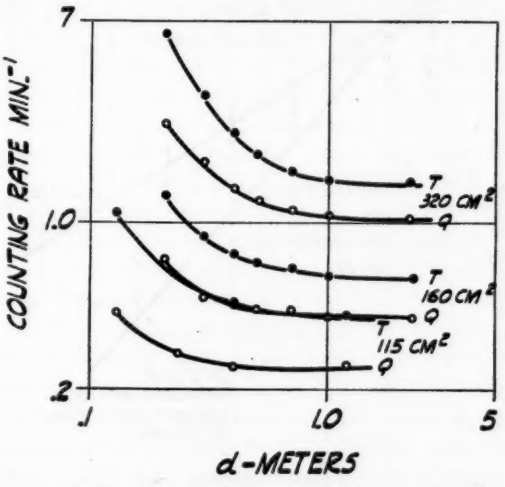

FIG. 5. Decoherence curves for different sensitive areas.

[7] H. A. Bethe, Phys. Rev. **72**, 172 (1947).
[8] B. Rossi and K. Greisen, Rev. Mod. Phys. **13**, 240 (1941).
[9] Similar conclusions have been drawn for ionization chambers by J. M. Blatt, Phys. Rev. **75**, 1584 (1949). The authors are indebted to Dr. Blatt for allowing them to see before publication a manuscript dealing with this question.

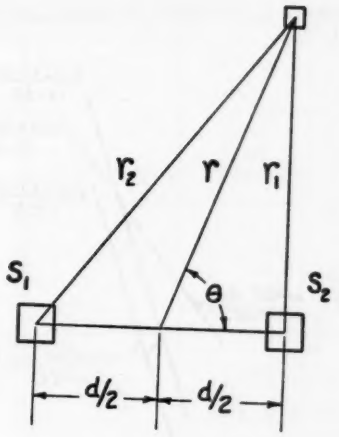

FIG. 6. Definition of symbols.

to the γ-power in the integrand of Eq. (9). Consequently, the exact manner in which the probability P approaches zero and the lower limit of the integral are important in the determination of the value of the counting rate C.

The interpretation of the variation of the counting rate with elevation is complicated by the change in atmospheric pressure. From Eq. (11) it is evident that the unit length r_0 is proportional to the cascade parameter X_0 which is in turn inversely proportional to the pressure. Comparison at two elevations should not, therefore, be made for the same values of the counter separation d nor for the same counter area A at the two elevations. The counting rate must depend on pressure, by Eqs. (6) and (8), as

$$C=C_0(p^2S, pd)A(p). \quad (12)$$

If C is proportional to S^γ, then

$$C=p^{2\gamma}S^\gamma A(p)g(pd), \quad (13)$$

where g is the function giving the decoherence curve. To find the ratio of the intensities A at two elevations with pressures p_1 and p_2, such values of d should be chosen that pd and therefore $g(pd)$ remains constant. If the area A is also taken constant, then

$$\frac{A(p_1)}{A(p_2)}=\frac{C(p_1)}{C(p_2)}\left(\frac{p_2}{p_1}\right)^{2\gamma}. \quad (14)$$

For extensive showers, taking for p_1 and p_2 the pressures at Climax and sea level, respectively, we have $\gamma=1.4$ and

$$A(p_1)/A(p_2)=12(1030/675)^{2\times1.4}=39.$$

For the narrow showers, from the data of Fig. 4, the counting rate at $d=50$ cm at Climax can be compared with that for $d=33$ cm at sea level. The exponent $\gamma=3.2$ but may be as small as 3.0 or as large as 3.6. The intensity ratio is thus most probably

$$\frac{A(p_1)}{A(p_2)}=1.9\left(\frac{1030}{675}\right)^{2\times3.2}=29,$$

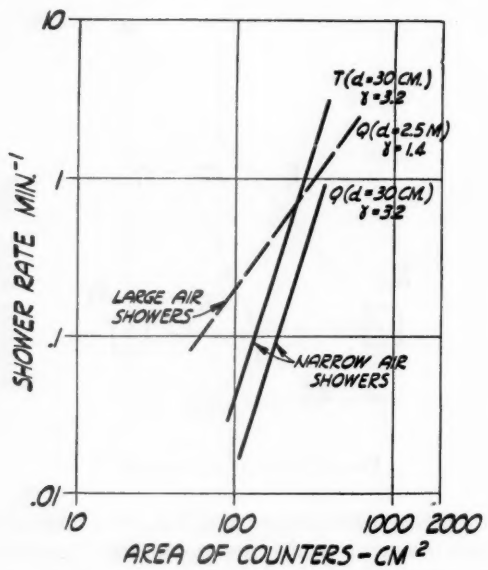

FIG. 7. Dependence of shower rate on counter area.

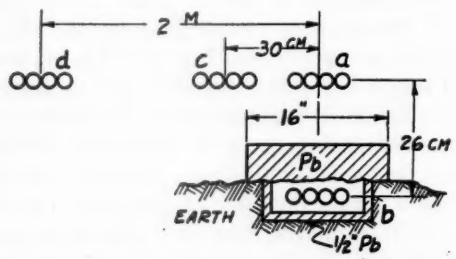

FIG. 8. Arrangement of counters for absorption experiment.

but may be as small as 24 or as large as 40 depending on the value of γ chosen. Thus when the variation of the spreading function ρ with pressure is taken into account, a change in the shape of the decoherence curve with elevation can be understood and the large apparent difference in altitude variation of narrow and extensive showers becomes much reduced and perhaps eliminated.

It is evident that more detailed calculations of the counting rate C are needed. If, however, the narrow showers differ in character from the extensive ones, then such calculations require a knowledge of the spreading function for narrow showers, as well as of the distribution $f(N)$. Even if ρ for narrow showers is different from that given by Eq. (10), it should depend upon pressure in the same manner if elastic scattering is the cause of the angular divergence of the showers.

THE ABSORPTION OF NARROW SHOWERS

Some experiments have also been performed to test the penetrating power of the narrow showers. Four counter trays each of area 320 cm² were arranged as shown in Fig. 8. The lower tray was placed below the level of the ground and shielded below and on the side by ½ inch of lead in addition. The whole arrangement was placed inside a box with a thin top of 0.5 g/cm² located immediately over trays *a*, *c*, *d*. Triple coincidences were recorded for counters *a*, *b*, *c* and for counters *a*, *b*, *d*. The difference in the counting rates as a function of the thickness of the lead between trays *a* and *b* is taken as a measure of the absorption of the narrow showers; the counting rate *a*, *b*, *d* is the result of the extensive showers alone. The results of this experiment are shown in the semilogarithmic plot of Fig. 9. The absorption of the extensive showers is in agreement with that measured by other observers.[10] The penetrating power of the narrow showers is greater than that of the extensive ones. The absorption corresponds to a mean free path of 9 cm of lead or about 100 g/cm²; for extensive showers the mean free path is 67 g/cm².

We have also measured the absorption of 41 g/cm² of aluminum and that of 73 g/cm² of aluminum. These points have been plotted in Fig. 9, first on the assumption that the absorption is mass proportional and second with the thickness measured in radiation units. For extensive showers the iron and aluminum points agree approximately with the absorption in lead when the thicknesses of the absorbers are expressed in radiation units. For the narrow showers the converse is true and the iron and aluminum points fall approximately on the lead curve only if the thicknesses are expressed in g/cm².

There are thus two important differences between the absorption of narrow and extensive showers. (1) The narrow showers are more penetrating than extensive ones and (2) the absorption is mass proportional for narrow showers but for extensive showers equal absorption occurs for equal thicknesses in radiation units.

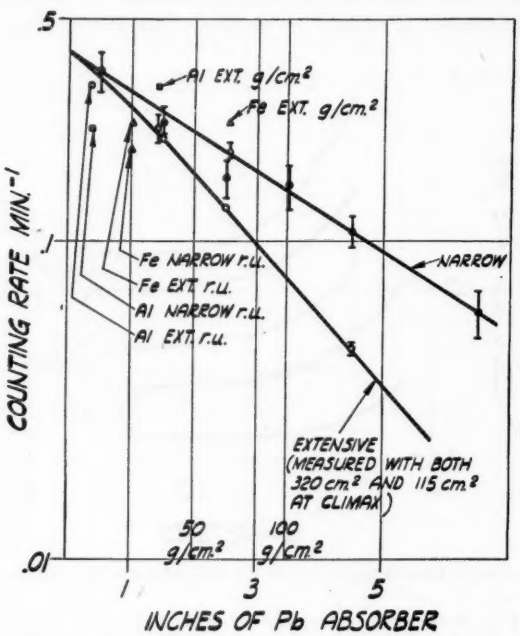

FIG. 9. Absorption of narrow and extensive showers.

[10] For example, G. T. Reynolds and W. D. Hardin, Phys. Rev. 74, 1549 (1948).

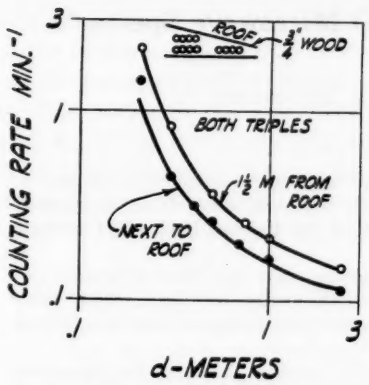

FIG. 10. Test of roof effect.

SUBSIDIARY EXPERIMENTS

Several additional observations were also made. In order to test the effect of the roof of the counter housing, an experiment was made in a house with a roof of ¾ inch of wood. Triple coincidences were recorded from three counter trays arranged as shown in the insert to Fig. 10. The decoherence curve was measured with the three trays placed as close to the roof as possible and then with the trays 1.5 meters below the roof. The counting rates when the trays were far from the roof were larger by a constant factor than those with the counters close. It seems likely that some production of ionizing rays occurs in the roof. With the roof 1.5 meters above the counters, the rays produced diverge and separate sufficiently to produce additional counts; when the roof is close the spreading is not large enough to cover both trays. We conclude that roof effects are best minimized by placing the counters as close as possible to the roof.

A rough check was made to find the effects of changing the number of counters in coincidence and hence of changing the minimum number of rays necessary to record a shower. In all cases so far described, only two rays were necessary. Four coincidence trays of 320 cm² area were used and in addition an anticoincidence tray of 640 cm² area was placed at a distance of 2.5 meters to eliminate the extensive showers. The four trays were arranged either as two telescopes (*A*), as one telescope and two single trays (*B*) or as four single trays (*C*). The average distance between any two trays was about 30 cm. Table II gives the counting rates observed. The observations were made at sea level.

The change in counting rate is thus a very sensitive function of the number of counters. This is another indication that the shower distribution function decreases rapidly with increasing number of rays. If a power-law expression is possible, the exponent γ must

TABLE II. Narrow showers as a function of number of counters.

Arrangement (see text)	Minimum number of rays	Counting rate min.⁻¹	Standard deviation min.⁻¹
A	2	0.151	0.008
B	3	0.024	0.003
C	4	0.010	0.0014

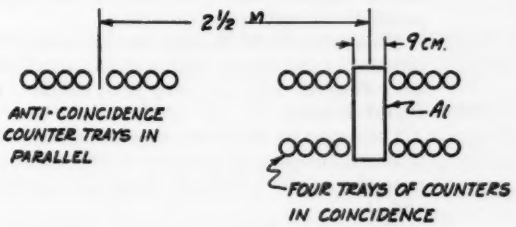

FIG. 11. Arrangement of counters to test effect of material between telescopes.

be large. It is not possible to determine γ quantitatively in this manner without a knowledge of the spreading function ρ because of the effect of the lower limit of the integral in Eq. (9). For extensive showers the lower limit can be taken as zero, and the values of γ obtained in this way agree, as Cocconi has shown, with the values found from the variation with area.

Since the variation with the number of counters is so rapid, it seems likely that the telescopic arrangement of trays used does have some directional selectivity and that the counters are not often discharged by rays coming at large angles with the vertical. This fact, in turn, agrees with the small ratio in the number of triple and quadruple counts as shown by the data of Fig. 2. From simple geometrical estimates, a ratio as small as that observed is possible only if the rays from narrow showers are concentrated about the vertical direction.

Finally an experiment was performed with the counters placed as shown in Fig. 11, similar to arrangement *A* of Table II. Nine cm of aluminum was interposed between the two telescopes as shown. The counting rate was found to be unchanged within the 7 percent statistical error of the measurements. We again conclude that the rays causing the counts are concentrated about the vertical direction.

ACKNOWLEDGMENTS

The authors wish to express their thanks to C. J. Abrams of the Climax Molybdenum Company and to Marcel Schein and E. F. Fahy for their generous hospitality and the use of laboratory facilities at Climax, Colorado. The observations at Denver were made possible through the kindness of B. Cohn and M. Iona of the University of Denver.

The Paschen-Back Effect in NH_3 and N_2O Microwave Spectra*

C. K. JEN
Cruft Laboratory, Harvard University, Cambridge, Massachusetts
(Received August 5, 1949)

The Paschen-Back effect in the microwave spectra of NH_3 and N_2O has been investigated in this experiment with a resonant cavity spectroscope. These molecules are known to possess relatively small values of nuclear electric quadrupole coupling and thus favor the realization of the Paschen-Back effect without prohibitively high magnetic fields.

The results for $N^{14}H_3$, representing a case of one-nuclear (N^{14}) coupling, show the effects of gradual decoupling of the nuclear spin from molecular rotation. The existence of the "forbidden" lines, whose intensities diminish with increasing field, indicates that the decoupling is not quite complete even in a field of 10,000 oersteds.

The results for $N^{14}N^{14}O^{16}$, representing a case of two-nuclear (N^{14}, N^{14}) coupling, show that the decoupling is almost complete at a field of 10,000 oersteds. An asymmetry of the Paschen-Back pattern for a $\Delta J \neq 0$ transition is ascribed to the non-linear dependence of the nuclear quadrupole coupling energy upon M_J and M_I.

The measured results are found to be in good agreement with quantum mechanical calculations. Also, consistent with the theory of the structure of the Paschen-Back pattern, it is shown that the molecular g-factors and the nuclear quadrupole coupling factors can be determined directly from experimental data.

I. INTRODUCTION

IN a previous paper,[1] the writer has investigated the Zeeman effect in microwave molecular spectra. It was shown that, if a molecular spectral line possesses a multiplet structure on account of a coupling energy between the nuclear spin and molecular rotation, the Zeeman effect of the multiplet structure can be accounted for by the combined magnetic contributions due to the nuclear and molecular g-factors. The underlying assumption for the Zeeman effect is that the energy change caused by the interaction of the external magnetic field with the nuclear and molecular magnetic moments is very much smaller than the energy differences in the multiplet structure. Under these conditions, the Zeeman splitting is a linear function of the field strength. As the external magnetic field is increased to the extent that the magnetic interaction energy becomes comparable with that of the multiplet separation, significant departures from linearity result. Further increase of the field accentuates still more the role of the magnetic energy relative to the multiplet separation energy, until the field is strong enough to decouple completely the nuclear spin from the molecular rotation. Following the usage in atomic spectra, the phenomenon representing the transition from the state characterized by the Zeeman effect to that of complete decoupling is called the Paschen-Back effect.

The Paschen-Back effect in molecular spectra can play an important role in elucidating the nature of spin-rotation coupling relations in a manner analogous to its role in atomic spectra. It affords a direct means for determining the molecular g-factor, which is responsible for the principal splitting in the completely decoupled state. Also, it gives a further check on the correctness of the theory of the Zeeman effect.

As regards the experimental realization of the Paschen-Back effect, the magnetic field required is essentially determined by the ratio of the spin-rotation coupling to the combined g-factor. It is evident, for any given resolution of the apparatus, that this ratio must be fairly small in order that the requisite magnetic field may not be prohibitively high. In practice, not very many molecules known in microwave spectra can satisfy this condition. The molecules NH_3 and N_2O are fairly typical of those whose electric quadrupole couplings are small enough to make the Paschen-Back effect realizable. They are thus taken as the subject of investigation for the present experiment.

II. A NEW MICROWAVE CAVITY SPECTROSCOPE

The essential features of a microwave resonant cavity spectroscope, together with circuit arrangements and principles of operation, have been presented in (I). For this and subsequent work, however, a new cavity has been constructed which is an integral part of the electromagnet assembly. The new apparatus embodies a number of mechanical improvements for the cavity and an electromagnet supplying a variable magnetic field up to 10,500 oersteds with approximately one percent spatial inhomogeneity.

Figure 1 shows, on the right-hand side, a cylindrical cavity soldered to one end of a magnetic pole piece and, on the left-hand side, a tuning plunger made to slide through another pole piece. The cavity, made of copper, is machined to an internal diameter of 1.949 inches. The hole at the bottom of the cavity is to couple microwave energy into the cavity from a wave guide which passes through the magnetic pole piece. This

* The research reported in this document was made possible through support extended Cruft Laboratory, Harvard University, jointly by the Navy Department, ONR, the Signal Corps of the U. S. Army, and the U. S. Air Force, under ONR Contract N5ori-76, T. O. 1.

[1] C. K. Jen, Phys. Rev. 74, 1396 (1948), hereafter referred to as (I).

coupling hole has a diameter of 0.166 inch and is offset from the center of the cavity by 0.25 inch. The tuning plunger consists of a long beryllium copper rod attached to a copper disk, which, in the assembled position, is able to move axially in the cavity with a very small clearance from the cavity wall. The rear side of the disk (facing the rod) is painted with powdered graphite in a ceramic binder, to attenuate extraneously coupled oscillation modes.

In Fig. 2, the cavity is shown in place between the pole pieces in the assembled position (the cavity being now soldered to the other pole piece as well). A circular loop of insulated wire, for the measurement of the magnetic field strength, is embedded in the wall of the cavity and is connected to an external fluxmeter by a pair of twisted leads. A large mocrometer head, which moves the tuning plunger and the sylphon bellows, controls the cavity tuning. The cavity setting, as measured by the micrometer reading, corresponds to a definite frequency scale for any given mode of oscillation. For very small plunger displacements, corresponding to minute changes in resonance frequency, a demountable precision dial indicator is coupled to the micrometer head, as shown in the picture. Other incidentals such as two pump leads and a mica window at the flange end of the wave guide may also be seen.

Figure 3 gives an over-all view of the whole apparatus when the center section, shown in Fig. 2, is assembled with the rest of the electromagnet. The wave guide leading from the bottom of the magnet indicates the manner of the microwave coupling to other parts of the measuring equipment.

III. EXPERIMENTAL RESULTS FOR $N^{14}H_3$ INVERSION SPECTRUM

The Paschen-Back effect in various $N^{14}H_3$ inversion lines has been found, except for differences in the relative complexity of patterns, to be not fundamentally different from one line to another. As might be expected from its low J-number, the $JK=11$ line shows a simple and more readily resolved pattern. This line is thus an appropriate subject for the present analysis.

Figure 4 shows the frequency separation between the centers of the two branches of σ-components as a function of the field strength. It is seen that a linear relation is maintained up to 3000 or 4000 oersteds. For still higher fields, there is a slight non-linearity and a gradual approach to a new straight line, whose slope corresponds to a g-factor approximately equal to the molecular g-factor (g_{mole}) obtained in (I). The transition is very gradual, as would be expected from the approximate equality between the combined g-factor, which controls the Zeeman splitting, and the molecular g-factor, which controls the Paschen-Back splitting in the decoupled state.

The lower picture in Fig. 5 is a reproduction of the oscilloscopic pattern[2] for the $JK=11$ line at a constant field of 8500 oersteds. The intensities of the strong lines (main π-line at the center and two strong σ-lines on each side of the center) were found to be essentially independent of field, whereas those of the weak lines diminished very noticeably with increasing field. However, the weak lines were found to be still detectable even in a field of 10,000 oersteds.

IV. THEORY OF THE PASCHEN-BACK EFFECT IN MOLECULES WITH ONE-NUCLEAR COUPLING

In order to interpret the experimental results described above, a brief theory of the Paschen-Back effect applicable to a symmetric top or linear molecule with one-nuclear coupling is sketched below. The total Hamiltonian[3] may be written as

$$\mathcal{H}=\mathcal{H}_R+\mathcal{H}_H+\mathcal{H}_Q, \tag{1}$$

where $\mathcal{H}_R$ = Hamiltonian for molecular rotation,

$$\mathcal{H}_H=-g_{\text{mole}}\mu_0\mathbf{J}\cdot\mathbf{H}-g_N\mu_0\mathbf{I}\cdot\mathbf{H},$$
$$\mathcal{H}_Q=C\{3(\mathbf{J}\cdot\mathbf{I})^2+\tfrac{3}{2}\mathbf{J}\cdot\mathbf{I}-\mathbf{J}^2\mathbf{I}^2\}$$

and

$$C=-eQ\frac{\partial^2 V}{\partial z^2}\left(1-\frac{3K^2}{J(J+1)}\right)\frac{1}{2I(2I-1)(2J-1)(2J+3)},$$

g_{mole}, g_N = molecular, nuclear g-factors,

$\mathbf{J}$, $\mathbf{I}$ = molecular, nuclear angular momentum vector operators associated with J, I quantum numbers,

K = quantum number for molecular angular momentum along figure axis,

Q = electric quadrupole moment of the nucleus for the state $M_I=I$ (M = magnetic quantum number),

FIG. 1. The microwave cavity and the magnet pole pieces (unassembled view).

[2] A photograph of the entire pattern is not feasible because of the narrow field of the cavity resonance.

[3] The nuclear magnetic dipole interaction with the molecular rotation field is neglected.

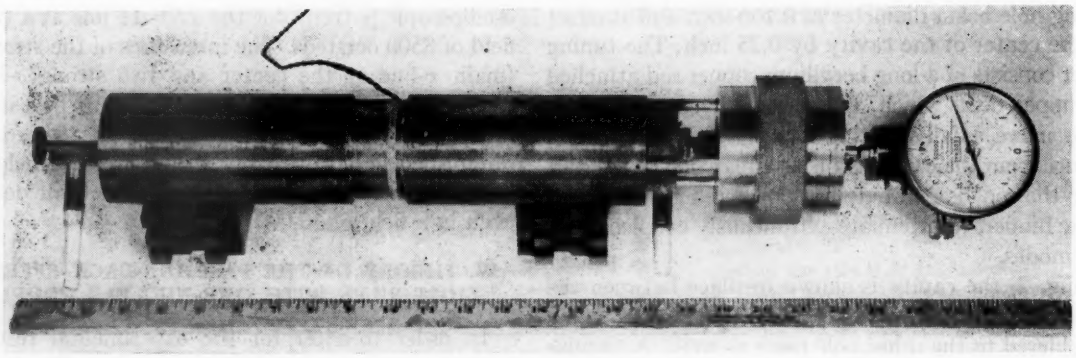

FIG. 2. The microwave cavity and the magnet pole pieces (assembled view).

V = electric potential at the nucleus in question due to all surrounding charges,
z = ordinate along figure axis,
μ_0 = nuclear magneton.

The first term, $\mathcal{H}_R$, on the right-hand side of Eq. (1) represents the Hamiltonian for the rotational state JK (or $JK\delta$, where δ is used for describing inversion or other types of doubling). The second term, $\mathcal{H}_H$, contains the sum of the magnetic energy operators for the molecular and nuclear magnetic interactions. The last term, $\mathcal{H}_Q$, represents the nuclear quadrupole interaction.

In treating the problem for intermediate fields, a representation designated by JIM_JM_I, in which the matrices for $\mathcal{H}_R$ and $\mathcal{H}_H$ are already diagonal (whereas the matrix for $\mathcal{H}_Q$ is not), can be used and then a unitary transformation can be made such that the matrix for $\mathcal{H}$ is diagonal in the transformed representation. The matrix elements for $\mathcal{H}_Q$ are non-vanishing only for the following transitions:

$$\begin{aligned} &\Delta M_J=0, \quad \Delta M_I=0; \\ &\Delta M_J=\pm 1, \quad \Delta M_I=\mp 1; \\ &\Delta M_J=\pm 2, \quad \Delta M_I=\mp 2. \end{aligned} \tag{2}$$

The matrix elements of $\mathcal{H}_H$ and $\mathcal{H}_Q$[4,5] can be shown to be as follows:

$$(M_JM_I|\mathcal{H}_H|M_JM_I)=-(M_Jg_{\text{mole}}+M_Ig_N)\mu_0H, \tag{3}$$

$$(M_JM_I|\mathcal{H}_Q|M_JM_I)=(C/2)\{J(J+1)-3M_J^2\}\times\{I(I+1)-3M_I^2\}, \tag{4}$$

$$\begin{aligned}&(M_J\pm 1M_I\mp 1|\mathcal{H}_Q|M_JM_I) \\ &=(3C/4)(2M_J\pm 1)(2M_I\mp 1) \\ &\times[(J\mp M_J)(J\pm M_J+1)(I\pm M_I)(I\mp M_I+1)]^{\frac{1}{2}},\end{aligned} \tag{5}$$

$$\begin{aligned}&(M_J\pm 2M_I\mp 2|\mathcal{H}_Q|M_JM_I) \\ &=(3C/4)[(J\mp M_J)(J\mp M_J-1)(J\pm M_J+1) \\ &\times(J\pm M_J+2)(I\pm M_I)(I\pm M_I-1) \\ &\times(I\mp M_I+1)(I\mp M_I+2)]^{\frac{1}{2}}.\end{aligned} \tag{6}$$

The solution for the eigenvalues is obtained by solving the secular equation of the $(2I+1)$th or $(2J+1)$th order (depending on which is smaller). The solution is very simple for an almost infinitely high field (for an assurance of complete decoupling), because only the diagonal elements as shown in Eqs. (3) and (4) need to be considered. The result is

$$\begin{aligned}W(H\to\infty)=&W_R(JK\delta)-(M_Jg_{\text{mole}}+M_Ig_N)\mu_0H \\ &+(C/2)\{J(J+1)-3M_J^2\}\{I(I+1)-3M_I^2\}.\end{aligned} \tag{7}$$

The calculations for the line intensities can be more conveniently carried out by the perturbation method. For brevity, let α denote M_JM_I with J and I as con-

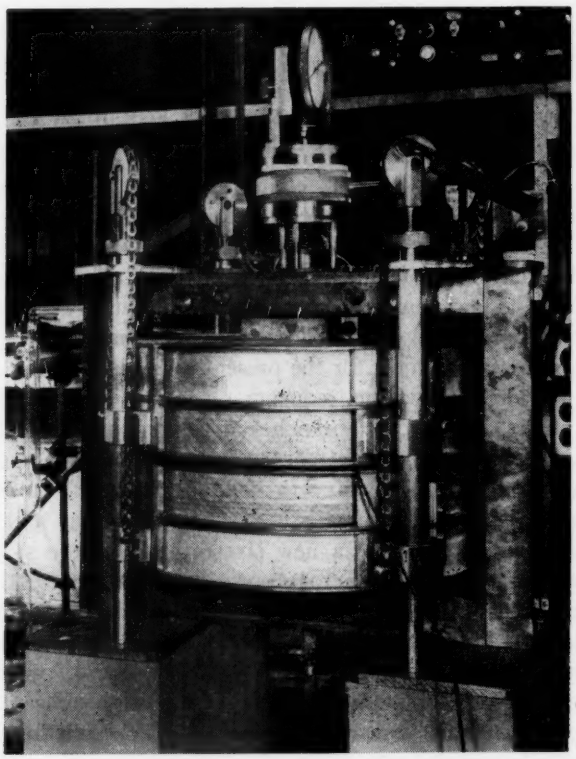

FIG. 3. The microwave cavity spectroscope for measuring Zeeman and Paschen-Back effects.

[4] Kellogg, Rabi, and Ramsey, Jr., Phys. Rev. **57**, 677 (1940).
[5] E. U. Condon and G. H. Shortley, *The Theory of Atomic Spectra* (Cambridge University Press, London, 1935).

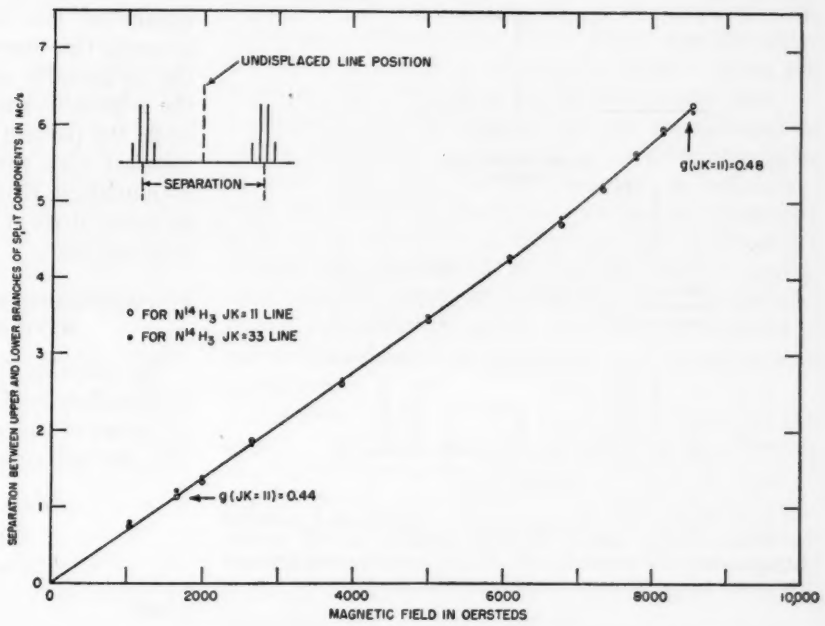

FIG. 4. Zeeman and Paschen-Back splitting for $N^{14}H_3$ lines as a function of the magnetic field.

stants, and β denote $M_{J'}M_{I'}$ with a constant J' not necessarily equal to J, and I' always equal to I. Further, let A and B represent states in an intermediate magnetic field which would go over, respectively, to the states represented by α and β at infinite field. The intensity of transition is known to be proportional to $|(A|\mathbf{P}|B)|^2$, where $\mathbf{P}$=electric moment vector. This matrix element $(A|\mathbf{P}|B)$ is, to the first-order preturbation, as follows:[5,6]

$$(A|\mathbf{P}|B)=(\alpha|\mathbf{P}|\beta)+\sum_{\beta'\neq\beta}\frac{(\alpha|\mathbf{P}|\beta')(\beta'|H_Q|\beta)}{W_0(\beta)-W_0(\beta')}+\sum_{\alpha'\neq\alpha}\frac{(\beta|\mathbf{P}|\alpha')(\alpha'|H_Q|\alpha)}{W_0(\alpha)-W_0(\alpha')}, \quad (8)$$

where each W_0 has the following form

$$W_0(\alpha)=W_R(JK\delta)+W_H(M_JM_I)=W_R(JK\delta)-(M_Jg_{\text{mole}}+M_Ig_N)\mu_0H, \quad (8a)$$

which is the unperturbed energy consisting of the rotational energy plus the magnetic energy in an uncoupled state. In addition to the rules given in Eq. (2) for the non-vanishing of the matrix elements of $\mathcal{H}_Q$, the following selection rules for the non-vanishing of the matrix elements of $\mathbf{P}$, such as $(\alpha|\mathbf{P}|\beta)$, are also essential

$$\Delta J=0,\pm1,\quad \Delta M_J=0,\pm1,\quad \Delta M_I=0. \quad (9)$$

If for two states, α and β, the selection rules in Eq. (9) are satisfied, then $(\alpha|\mathbf{P}|\beta)$ in Eq. (8) is finite while the summation terms vanish. The intensity of the transition between A and B is independent of the field strength to this degree of approximation. Such transitions are said to be "allowed" in the decoupled state. On the other hand, if the conditions in Eq. (9) are not satisfied, $(\alpha|\mathbf{P}|\beta)$ would certainly vanish, but the summation terms will not necessarily be zero. Wherever the latter terms contribute something, the transition between A and B would have a finite intensity, in spite of the fact that it is "forbidden" by the selection rules in Eq. (9). Such contributions are, however, necessarily field-dependent, because the denominator in each summation term is seen to be proportional to H from Eq. (8a). The intensity of such "forbidden" lines vary, to this approximation, inversely as the square of magnetic field strength.

The characteristics of a Paschen-Back pattern in intermediate fields, when one nuclear quadrupole coupling is involved, will be illustrated by a concrete example in Section V. However, a few salient features of the general problem can be brought out by treating the case of an almost infinitely high field. Using Eqs. (7) and (9), the following results for the transition frequencies are obtained.

(a) The $J\rightarrow J$ transition frequencies $(H\rightarrow\infty)$ are:

$$\nu_\pi=\nu_R, \quad (10)$$

$$\nu_\sigma\pm(M_JM_I)=\nu_R\pm\{g_{\text{mole}}(\mu_0H/h)+(3C/2h)(2M_J+1)[I(I+1)-3M_I^2]\}, \quad (11)$$

where $M_J\neq J$ and h=Planck's constant. The π-transition is a single line at the rotation frequency ν_R. The σ-transition consists of a fine structure with $2J(I+1)$ components in each branch (+ or −). The two branches of the σ-transitions are symmetrical with respect to ν_R and the components of each branch are symmetrical

[6] For conciseness, a small effect has been neglected resulting from the wave function not being renormalized after perturbation. Actual numerical calculations presented in Section V have, however, taken this into account.

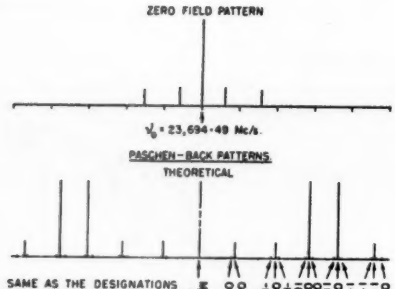

FIG. 5. Theoretical and experimental Paschen-Back patterns for $N^{14}H_3$ $JK=11$ line at $H=8500$ oersteds. (In the middle diagram, each line represents the over-all intensity of a group of transitions whose positions are indicated by the dots.)

with respect to its center of gravity. The effect of the nuclear g-factor is necessarily absent in the decoupled state because $\Delta M_I=0$. The molecular g-factor is related to the σ-transitions, by Eq. (11), as follows:

$$g_{\text{mole}}=\frac{h\{\nu_\sigma^+(M_JM_I)-\nu_\sigma^-(M_JM_I)\}}{2\mu_0H}, \tag{12}$$

or

$$=\frac{h\{\nu_\sigma^+(\text{c.b.})-\nu_\sigma^-(\text{c.b.})\}}{2\mu_0H}, \tag{13}$$

where c.b. denotes the center of each branch. The constant C, which is proportional to the quadrupole coupling factor, is related to the fine structure separation, again by Eq. (11), as follows:

$$C=\pm\frac{2h\{\nu_\sigma^\pm(M_J'M_I')-\nu_\sigma^\pm(M_JM_I)\}}{3\{(2M_J'+1)[I(I+1)-3(M_I')^2]-(2M_J+1)[I(I+1)-3M_I^2]\}}. \tag{14}$$

(b) The $J\rightarrow J+1$ transition frequencies ($H\rightarrow\infty$) are:

$$\nu_\pi(M_JM_I)=\nu_R+(1/2h)\{C'[(J+1)(J+2)-3M_J^2]-C[J(J+1)-3M_J^2]\}[I(I+1)-3M_I^2] \tag{15}$$

and

$$\nu_\sigma^\pm(M_JM_I)=\nu_R\pm\left\{g_{\text{mole}}\frac{\mu_0H}{h}+\frac{3C'}{h}M_J[I(I+1)-3M_I^2]\right\}+(1/2h)\{C'[(J+1)(J+2)-3(M_J^2+1)]-C[J(J+1)-3M_J^2]\}[I(I+1)-3M_I^2], \tag{16}$$

where C' has the same expression as C, with J replaced by $J'=J+1$. It is seen that the π-transition has a fine structure with $(J+1)(I+1)$ components, while each branch of the σ-transition has $(2J+1)(I+1)$ components. One important feature of these transitions is the asymmetric nature of the patterns. The pattern for the π-transition is not symmetrical with respect to ν_R, while the pattern for the σ-transitions is neither symmetrical with respect to ν_R nor with respect to the π-transitions. Expressions similar to Eqs. (12)–(14) can be easily derived for this case also, but they will not be given here.

V. CALCULATIONS FOR $N^{14}H_3$ AND COMPARISON WITH EXPERIMENTAL RESULTS

The solution for the $N^{14}H_3$ eigenvalue problem in intermediate magnetic fields is relatively easy, because the order of the secular equation is cubic [$I(N^{14})=1$]. The determinantal equation is

$$\begin{vmatrix}\mathcal{E}_{11}-E & \mathcal{E}_{12} & \mathcal{E}_{13}\\ \mathcal{E}_{21} & \mathcal{E}_{22}-E & \mathcal{E}_{23}\\ \mathcal{E}_{31} & \mathcal{E}_{32} & \mathcal{E}_{33}-E\end{vmatrix}=0, \tag{17}$$

where

$$\mathcal{E}_{11}=-\{(M+1)g_{\text{mole}}+g_N\}\mu_0H-(C/2)\{J(J+1)-3(M+1)^2\},$$

$$\mathcal{E}_{22}=-Mg_{\text{mole}}\mu_0H+C\{J(J+1)-3M^2\},$$

$$\mathcal{E}_{33}=-\{(M-1)g_{\text{mole}}+g_N\}\mu_0H-(C/2)\{J(J+1)-3(M-1)^2\},$$

$$\mathcal{E}_{12}=\mathcal{E}_{21}=-[3C/(8)^{\frac{1}{2}}](1+2M)[(J+1+M)(J-M)]^{\frac{1}{2}},$$

$$\mathcal{E}_{23}=\mathcal{E}_{32}=-[3C/(8)^{\frac{1}{2}}](1-2M)[(J+1-M)(J+M)]^{\frac{1}{2}},$$

$$\mathcal{E}_{13}=\mathcal{E}_{31}=(3C/2)[\{J+1)^2-M^2\}(J^2-M^2)]^{\frac{1}{2}},$$

and $M=M_J+M_I$, $E=W-W_R(JK\delta)$.

The calculated results for E as a function of the magnetic field are plotted in Fig. 6, using constants previously obtained in (I). For direct comparison with experiment, transition frequencies between the two inversion levels[7] and their intensities according to Eq. (8) are calculated for a constant field of 8500 oersteds and plotted in the center picture of Fig. 5. It is seen that there is generally a good agreement between the theoretical and experimental results.[8] Each strong line in the experimental pattern is now recognized to represent one (or several) of the allowed transitions satisfying Eq. (9). The weak lines, having field-dependent intensities are "forbidden" by the same selection rules. The statement made in Section III, that the weak lines were barely detectable in a field of 10,000 oersteds,

[7] For convenience, transitions are indicated in Fig. 6 between the magnetic levels belonging to one inversion state instead of two magnetic levels, one belonging to each inversion state.

[8] The experimental intensity of the π-line at the center ($\Delta M_J=\Delta M_I=0$) should not be compared on the same basis with those of the σ-lines, because the cavity-mode responses do not give π- and σ-lines the same weight factor.

should mean that the decoupling is not quite complete even in this field.

The agreement between the theory and experiment in the case of the molecular g-factors is also quite satisfactory. Equation (12) or (13), which applies directly to the case of $N^{14}H_3$, states that the g_{mole} can be determined from the frequency separation between the centers of the two branches in the σ-transition at very high fields. The experimental results plotted in Fig. 4 show that the measured g-factor at high fields does approach asymptotically the value previously obtained in (I), $g_{mole}=0.48$.

The two strong lines in each branch of the experimental pattern for the σ-transition in Fig. 5 are interpreted, in the light of the theory, as two distinct groups of unresolved fine structure lines. The frequency separation between the two groups is, by Eq. (14), a measure of the nuclear quadrupole coupling factor. A determination of the coupling factor from the Paschen-Back pattern gives a result in essential agreement with the value determined from the multiplet structure at zero field.

VI. PASCHEN-BACK EFFECT IN N_2O SPECTRUM

The microwave rotational spectra of N_2O were studied first by Coles, Elyash, and Gorman,[9] later by Smith, Ring, and Gordy,[10] and more recently by Coles and Hughes.[11] The first group of observers determined the rotational frequencies of $N^{14}N^{14}O$ (O for O^{16} throughout this section) and $N^{15}N^{14}O$ and gave values for the nuclear electric quadrupole coupling factors for the end and center N^{14} nuclei. The second group of observers redetermined the quadrupole coupling factor for the end N^{14} nucleus by applying Bardeen and Townes' theory[12] of two-nuclear coupling to their own results. The last group published the frequency measurement of the two other isotopic species, $N^{14}N^{15}O$ and $N^{15}N^{15}O$.

The N_2O molecule is interesting from the standpoint of studying the Paschen-Back effect because, first, its quadrupole interaction is conveniently small, and second, it offers a variety of different quadrupole coupling types ($N^{14}N^{14}O$ for two-nuclear coupling, $N^{15}N^{14}O$ and $N^{14}N^{15}O$ for one-nuclear coupling at different positions, and $N^{15}N^{15}O$ for no coupling). The simplicity of a $J=0\rightarrow1$ transition is another favorable feature.

In this experiment, some detailed studies on the $N^{14}N^{14}O$ spectrum and a brief examination of the effects in $N^{15}N^{14}O$ have been made.[13] In the case of $N^{14}N^{14}O$, the end N^{14} nucleus has a quadrupole coupling factor $(eQ/h)(\partial^2V/\partial z^2)=-1.02$ mc/s[10] (to be compared with the value -4.18 mc/s for N^{14} in $N^{14}H_3$) and the center N^{14} has a factor of -0.27 mc/s.[9] Figure 7 shows the observed triplet structure for $N^{14}N^{14}O$ in zero field.

According to the theory,[12] the two lower-frequency triplet components are expected to have fine structures of their own, provided the resolution is sufficiently high. The theoretical results in zero field are illustrated by the spectrum drawn directly above the experimental pattern. Since one nucleus has a much stronger coupling than the other, the gross triplet structure is essentially due to the stronger coupling, while the fine structure is due to the weaker coupling, which can be regarded as a perturbation.

The effect on the $N^{14}N^{14}O$ spectrum of increasing the magnetic field from zero can be thought of as a Zeeman range at extremely low fields and then another range of gradual decoupling at somewhat higher fields. Although such transition effects have been observed to take place qualitatively, they could not be measured with certainty because of the presence of many components within a frequency range of about one mc/s.

In contrast with the low field phenomena, the Paschen-Back spectrum for $N^{14}N^{14}O$ at fields above $H=5000$ oersteds presented a strikingly simple pattern. There were two stronger σ-lines, one on each side of the center (position of the zero field strongest line), and two π-lines (one strong and one weak) slightly displaced in opposite directions from the center. The line intensities increased with the field strength, but became almost

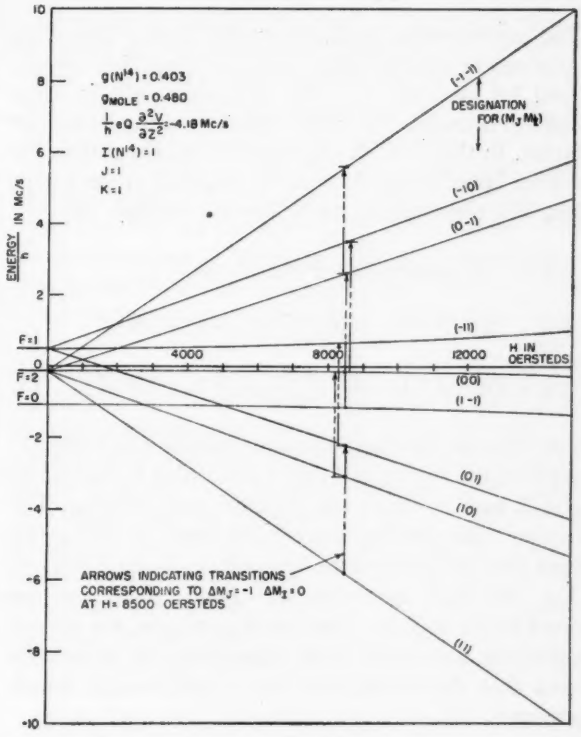

FIG. 6. Energy levels for $N^{14}H_3$ $JK=11$ state as a function of the magnetic field.

[9] Coles, Elyash, and Gorman, Phys. Rev. **72**, 973 (1947).
[10] Smith, Ring, and Gordy, Phys. Rev. **73**, 633 (1948).
[11] D. K. Coles and R. H. Hughes, Phys. Rev. **76**, 178 (1949).
[12] J. Bardeen and C. H. Townes, Phys. Rev. **73**, 97 (1948).
[13] The author is indebted to Professor E. B. Wilson, Jr. and Dr. D. K. Coles for generously supplying samples for this experiment.

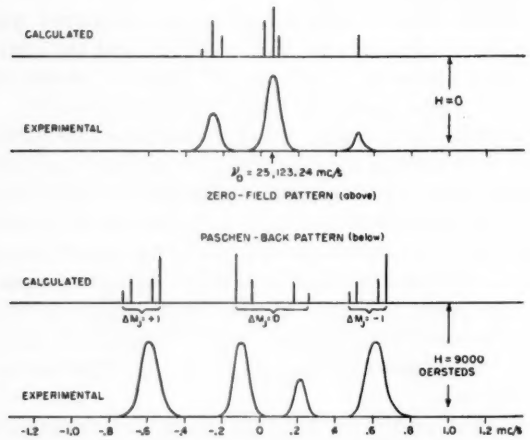

FIG. 7. Theoretical and experimental zero-field and Paschen-Back patterns for $N^{14}N^{14}O$ $J=0\rightarrow1$ rotational transition.

field-independent beyond $H=8000$ oersteds. The pattern at $H=9000$ oersteds is shown in the lower picture of Fig. 7. Use of still higher fields did not result in any noticeable change in the pattern.

The Paschen-Back effect in the $N^{15}N^{14}O$ spectrum at strong fields was found to be essentially the same as in the $N^{14}N^{14}O$ spectrum except that the line intensities reached their steady values at a lower field and that the π-line apparently remained single and was not appreciably displaced from the center.

VII. INTERPRETATION OF THE N_2O PASCHEN-BACK SPECTRUM

The experimental results described in the preceding section can be evaluated in terms of a simplified theory. It will be assumed that the magnetic field is large enough to decouple the nuclear spins from the molecular rotation. In the JIM_JM_I representation, the matrix for the total Hamiltonian is sensibly diagonal at very high fields. The eigenvalues can be directly written as[14]

$$W=W_0-\{M_Jg_{\text{mole}}+(M_{I_1}+M_{I_2})g_N\}\mu_0H$$
$$+(C_1/2)[J(J+1)-3M_J^2][I_1(I_1+1)-3M_{I_1}^2]$$
$$+(C_2/2)[J(J+1)-3M_J^2][I_2(I_2+1)-3M_{I_2}^2], \quad (18)$$

where all quantities have the same meaning as in Eq. (1) except for the subscipts 1 and 2 pertaining to the nuclei 1 and 2, each of which has a quadrupole coupling. The selection rules are also exactly the same as in Eq. (9), except that $\Delta M_I=0$ means here $\Delta M_{I_1}=0$ and $\Delta M_{I_2}=0$.

For the N_2O spectrum, $I_1=I_2=1$, $J=0$ for the ground state, and $J=1$ for the upper state, the energy expressions are even more simplified. It is readily shown that the $\pi(\Delta M_J=0)$ and $\sigma(\Delta M_J=\pm1)$ transitions are:

$$\pi\text{-lines:}\quad \nu_\pi(M_{I_1}M_{I_2})=\nu_R+(C_1/h)(2-3M_{I_1}^2)$$
$$+(C_2/h)(2-3M_{I_2}^2), \quad (19)$$

$$\sigma\text{-lines:}\quad \nu_\sigma^{\pm}(M_{I_1}M_{I_2})=\nu_R\pm g_{\text{mole}}\mu_0H/h$$
$$-(C_1/2h)(2-3M_{I_1}^2)-(C_2/2h)(2-3M_{I_2}^2), \quad (20)$$

where each C is the value of C (Eq. (1)) at $J=1$. The molecular g-factor (g_{mole}) and the quadrupole coupling parameters (C_1 and C_2) can be directly derived from Eqs. (19) and (20) with the following results:

$$g_{\text{mole}}=\frac{h\{\nu_\sigma^+(M_{I_1}M_{I_2})-\nu_\sigma^-(M_{I_1}M_{I_2})\}}{2\mu_0H}, \quad (21)$$

$$C_1=(h/3)\{\nu_\pi(0\pm1)-\nu_\pi(\pm1\pm1)\}, \quad (22)$$

$$C_2=(h/3)\{\nu_\pi(\pm10)-\nu_\pi(\pm1\pm1)\}. \quad (23)$$

It is noted from Eqs. (19) and (20) that both the π- and σ-lines in the Paschen-Back spectrum for the case of two-nuclear coupling have fine structures, resulting from the nuclear quadrupole interactions. The σ-lines are, for the $J=0\rightarrow1$ transition, asymmetrical relative to the π-lines because of non-linear dependence of the interaction energy upon M_J and M_I. Equation (21) states that the molecular g-factor can be deduced from the frequency separation between any σ-line and its "image," if the lines are resolved, or between "+" and "−" unresolved groups of lines. Equations (22) and (23) show that each quadrupole interaction factor can be determined directly from the fine structure, if there is sufficient resolution for the lines whose separation is caused by that interaction.

A comparison between theory and experiment can now be made. Again in Fig. 7, a theoretical spectrum is drawn directly above the experimental pattern for $H=9000$ oersteds, using the coupling factors cited in Section VI. The approximate agreement between theory and experiment indicates that the spin-rotation decoupling is almost complete for the field used. Since the fine structure of the σ-lines is not experimentally resolved and that of the π-line is only partially resolved, only the larger of the two coupling factors can be experimentally determined. This yields a result which is in essential agreement with the value assumed.

The experimental determination of g_{mole} can be obtained quite accurately, because, in contrast to the determination of the coupling factor, this does not depend upon the resolution of the fine structure. Further, a similar determination has been made from the Paschen-Back spectra for $N^{15}N^{14}O$, for which Eq. (21) would also apply by preserving the contributions of only one nucleus. The results of such determinations for g_{mole} in nuclear units are:

$N^{14}N^{14}O$ $\quad g_{\text{mole}}=0.087\pm0.004$

and

$N^{15}N^{14}O$ $\quad =0.085\pm0.004.$

[14] H. M. Foley, Phys. Rev. 71, 747 (1947).

Thus, the molecular g-factors for $N^{14}N^{14}O$ and for $N^{15}N^{14}O$ are essentially equal within the limits of experimental error.

VIII. CONCLUSION

The Paschen-Back effect for NH_3 and N_2O molecules has been shown to exist in the microwave spectra with only moderately strong magnetic fields. For both one- and two-nuclear couplings, the experimental results can be satisfactorily interpreted in terms of the quantum mechanical theory of perturbations.

The Paschen-Back effect in the microwave molecular spectra should prove to be useful in interpreting the nature of the spin-rotation coupling and in the direct determination of molecular g-factors.

PHYSICAL REVIEW VOLUME 76, NUMBER 10 NOVEMBER 15, 1949

Impulse Breakdown in the 10^{-9}-Sec. Range of Air at Atmospheric Pressure*,**

R. C. FLETCHER***
Laboratory for Insulation Research, Massachusetts Institute of Technology, Cambridge, Massachusetts
(Received August 1, 1949)

The formative lag of spark breakdown has been measured over the range from 0.5 to 50×10^{-9} sec. using transmission line circuits in conjunction with the micro-oscillograph. It is found to be a function only of the applied field (independent of gap-width) for the shorter times (high fields), but to increase for decreasing gap-widths for the longer times (low fields). A calculation of the formative lag is presented which is based on the assumption that it consists mainly of the time for a single electron avalanche to build up a space-charge field comparable with the applied field. This predicts the observed formative lags within the experimental accuracy of the measurements over the entire range used. The increasing times for decreasing gap-widths for the longer times is interpreted as the transition from a single avalanche to a multiple avalanche mechanism of breakdown. The critical field where this transition takes place for a given gap-width is computed and found to predict the observed critical fields within the experimental accuracy. The good agreement between theory and experiment enables a more reliable prediction than has previously been possible of the critical gap-width above which the threshold field is determined by a single avalanche mechanism.

A sharp drop in the rate of fall of the breakdown voltage is observed for the shorter times. It is suggested that this may be a change in the mechanism of electron release from the cathode.

I. INTRODUCTION

MANY experiments have been performed to measure the formative lag time of the atmospheric spark as a function of applied voltage.[1] Unfortunately this time is so short for a slight overvoltage that oscillograph measurements have previously been impossible, and other indirect schemes have had to be used. These, although often ingenious, have still limited the measurement of the formative lag to a rather small region of applied voltage (i.e., up to about 70 percent overvoltage), where the time varies extremely rapidly with the applied voltage. However, although individual measurements of the formative lag have differed from each other by as much as a factor of five, its order of magnitude and the general shape of its variation with overvoltage have been well established. In fact, the discovery that the order of magnitude of the formative lags was so short led to the suggestion that the Townsend theory had to be either modified or rejected in explaining the breakdown of atmospheric air.[2]

Proposed theories of the atmospheric spark have attempted to predict the observed threshold field and order of magnitude of the formative time.[2,3] Largely because accurate measurements of the formative time were not available, little attempt has been made to compare quantitatively the experimental and theoretical variation of the formative time with applied voltage. Raether has made the suggestion[4] that most of the formative lag consists of the time a single electron avalanche takes to build up to the magnitude where its space-charge field is comparable with the applied field. This suggestion was based on the "streamer" mechanism of breakdown, in which secondary avalanches, initiated before and behind the head of the initial avalanche by photon absorption, build up more rapidly in the enhanced field caused by the space charge. This creates two streamers of ionization which appear to move from the head of the initial avalanche towards the anode and the cathode at a much higher velocity than the velocity of the initial avalanche. Thus the complete spark channel should be established very soon after the space-charge field of the initial avalanche becomes of the order of the applied field. Raether showed that this suggestion explains the general shape

* Sponsored by the ONR, the Army Signal Corps, and the Air Force under ONR Contract N5ori-07801.
** From a doctorate thesis in physics, Massachusetts Institute of Technology.
*** National Research Council Predoctoral Fellow.
[1] A summary is given by R. Strigel, *Elektrische Stossfestigkeit* (Verlag. Julius Springer, Berlin, 1939), p. 34.
[2] J. Slepian, Elec. World **91**, 761 (1928); J. Franck and A. von Hippel, Zeits. f. Physik **57**, 696 (1929); L. B. Loeb, Science **69**, 509 (1929).
[3] L. B. Loeb and J. M. Meek, *The Mechanism of the Electric Spark* (Stanford University Press, Stanford University, California, 1941); H. Raether, Zeits. f. Physik **112**, 464 (1939).
[4] H. Raether, Elektrotech. Zeits. **63**, 301 (1942).

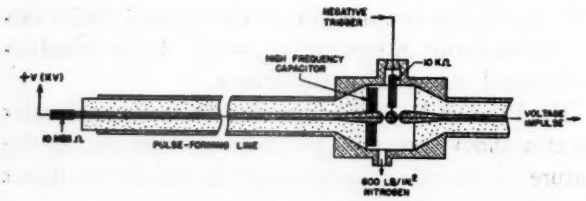

FIG. 1. Schematic sketch of u.h.s. impulse generator capable of delivering 20-kv impulses with rise times of 4×10^{-10} sec. The coaxial capacitor serves to sharpen the top of the impulse.

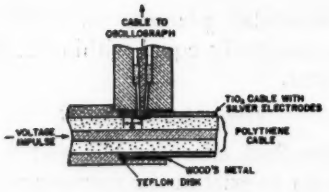

FIG. 2. Connections to u.h.s. voltage divider, consisting of two concentric coaxial transmission lines whose characteristic impedances produce a divider ratio of 100:1.

of the formative lag *vs.* overvoltage curve and the correct order of magnitude, but more exact comparison was not possible because of the limited range and accuracy of the measurements of the formative lag.

With the development of the micro-oscillograph[5] in the Laboratory for Insulation Research there arose the possibility of measuring the formative lag by oscillographic means with greater accuracy and over a wider range of times than has been previously possible. Thus, if the associated circuitry could be developed, the micro-oscillograph would be capable of measuring transients which change in times considerably less than 10^{-9} sec. Direct oscillographic measurement has the advantage that it reveals the shape of the voltage impulse being used to measure the breakdown. There is good reason to believe that many of the previous attempts to measure the formative lag were limited by oscillations or spikes on the voltage impulse and also perhaps by rise times which were too long compared to the time lags being measured.

The present investigation was conducted to measure the formative lag down to times of less than 10^{-9} sec., and to compare this measured value with a value calculated according to the suggestion of Raether. It was also thought that the oscillographic recording of the breakdown at high current levels might be of some interest.

II. EXPERIMENTAL ARRANGEMENT

In order to measure time lags down to less than one mμsec. it is necessary to have circuits capable of handling transients with frequency components in the ultra-high frequency range. These transients might justifiably be called ultra-high speed (u.h.s.) transients, and the associated circuits, ultra-high speed (u.h.s.) circuits. A brief discussion of the particular u.h.s. circuitry used in the present investigation follows, leaving a more detailed description of the required special techniques for a separate report.[5a]

Transmission lines are used as circuit connections throughout in order to eliminate the effects of stray inducatance and capacity. To generate the voltage impulse, a three-electrode trigger gap is arranged along the center conductor of a coaxial transmission line and kept under 600 p.s.i. of nitrogen (Fig. 1). The transmission line on one side of this gap is initially charged to a voltage $+V$ (of the order of 20 kv), while the other side is grounded. When the center electrode is triggered with a negative pulse the trigger gap breaks down and a voltage impulse of $V/2$ is sent down the previously grounded transmission line. A coaxial capacitor in parallel with the pulse-forming line serves to sharpen the voltage impulse. This impulse generator produces voltage impulses across the spark gap to be measured which have rise times of the order of 0.4 mμsec.

A voltage divider is required in order to view these kilovolt impulses with the micro-oscillograph. A successful design uses two concentric coaxial transmission lines, the characteristic impedances of which produce a divider ratio of 100 to 1 (Fig. 2). In order to do this the smaller impedance line is made of titanium dioxide ceramic (dielectric constant 85) while the larger impedance line is a standard 52-ohm polyethylene cable (RG17/U) (dielectric constant 2.25). Because the transition from the low to the high dielectric line excites the higher modes of the coaxial lines, the pick-off probe is placed far enough from the junction ($\frac{1}{4}$ in.) for these higher modes to be attenuated to negligible amplitudes. The ceramic line could be made conveniently only in short lengths (26 cm) so that there are reflections from the end in 16 mμsec. These reflections are confined to spikes by terminating the line with carbon resistors.

The spark gap to be tested is arranged along the center conductor of an air-dielectric coaxial transmission line with an inner conductor of 0.920 in. and an outer conductor of 2.265 in. in diameter. This is tapered to connect with the polyethylene cable so as to approximately preserve the 52-ohm characteristic impedance and still make a transition from a polyethylene to an air dielectric (Fig. 3). Circular holes are cut through the outer conductor in order to view the spark, allow for ultraviolet illumination, and permit free circulation of air. One electrode can be moved relative to the other

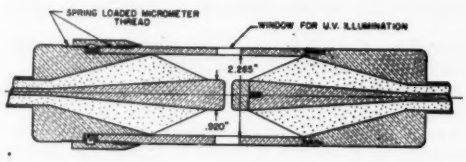

FIG. 3. Spark gap under test arranged along the center conductor of a transmission line to eliminate distortions due to stray inductance and capacity.

[5] G. M. Lee, Proc. Inst. Radio Eng. **34**, 121W (1946).
[5a] R. C. Fletcher, Rev. Sci. Inst. (to be published).

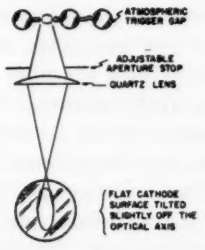
ATMOSPHERIC TRIGGER GAP
ADJUSTABLE APERTURE STOP
QUARTZ LENS
FLAT CATHODE SURFACE TILTED SLIGHTLY OFF THE OPTICAL AXIS

FIG. 4. Schematic sketch of ultraviolet illuminating system showing roughly the shape of illuminated area.

by means of a micrometer screw which enables the gap to be set to an accuracy of ± 0.0003 cm. The electrodes are made of brass and shaped to an approximately Rogowski profile. The faces of the electrodes are highly polished with alumina powder and then washed with acetone.

Ultraviolet illumination is provided by concentrating the light from an illuminating spark gap with an $f/2$ quartz lens on the cathode of the spark gap being tested. The illuminating gap is made the short leg of a three-electrode triggered spark gap, which is fired at least 60 mμsec. before the voltage impulse is applied across the test gap. The electrodes of the illuminating gap are pointed and the gap is made small (*ca.* $\frac{1}{8}$ in.) to cause the spark to be roughly spherical in shape and always confined to the same point in space. Although this illumination has to come from the side, by tilting the optical axis of the illuminating system slightly with respect to the plane of the electrodes, one may obtain an illumination of the center of the cathode which is roughly elliptical in shape and covers about $\frac{1}{4}$ the total area of the cathode, or about 1 cm^2, as indicated in Fig. 4. The intensity may be varied by adjusting the diameter of the aperture placed directly in front of the lens.

The spark gap is arranged in the testing circuit shown schematically in Fig. 5. Initially the two lines labeled "pulse-forming line" are charged to the voltages indicated. These serve to limit the pulses formed at the impulse generator and the illuminating gap to 75 and 150 mμsec., respectively.

The process is started by turning on the beam of the micro-oscillograph for about one millisecond by means of a mechanical switch which dips quickly in and out of a pool of mercury. A probe is inserted into the beam path, so that when the beam is first turned on, a voltage is induced on the probe, which, when amplified, fires a thyratron-ignition-coil trigger generator. The output of the ignition coil triggers the illuminating gap. This gap simultaneously begins building up a photon intensity in the spark gap, sets off a magnetron timing wave, and triggers the u.h.s. impulse generator. When the impulse generator fires, a portion of the impulse is fed into the sweep driver while the main part proceeds down a 40-ft. transmission line (RG17/U) through the voltage divider to the spark gap. Current through the spark gap is observed by feeding the other side of the gap into the oscillograph through another transmission line. The cables from the voltage divider and the spark gap are so arranged that their signals arrive at the micro-oscillograph simultaneously. Synchronization of these with the sweep was obtained by varying the length of line to the sweep driver.

The sweep circuit is a vacuum tube pentode (3D21) discharging the capacity of the deflection plate leads. It is driven by a thyratron driver (2D21). It was found that the plate of the sweep pentode began to recharge during the millisecond the oscillograph beam is turned on. To prevent this a hydrogen thyratron (3C45) discharge circuit had to be built which turns off the power supply voltage leading to the sweep pentode after the sweep has passed. This discharge circuit is triggered from the illuminating gap. Sweep speeds are obtained by this method which give full scale deflection continuously adjustable from 5 to 1000 mμsec., and which are synchronizable to ± 0.1 mμsec.

The voltage of the impulse applied across the gap is assumed to be the voltage V to which the pulse-forming line is initially charged, less 5 percent for the small part of the voltage picked off for triggering the sweep circuit. The voltage V is measured by means of the current through a 100-megohm resistor to an accuracy of ± 1 percent. Small oscillations on the top of the pulse (Fig. 7) probably decrease this accuracy for the shorter times.

III. EXPERIMENTAL RESULTS

In order to check the conditions under which later experiments were conducted, an initial measurement was made of the d.c. breakdown of air (at 760 ± 3 mm of Hg, 22 ± 1°C, and 40 ± 10 percent relative humidity), using the same voltmeter, spark gap, and general procedure as used in the later impulse measurements. The results of this d.c. measurement are plotted in Fig. 6, together with a weighted average for a number of measurements compiled by Schumann.[6]

Measurements of the impulse breakdown of air (the

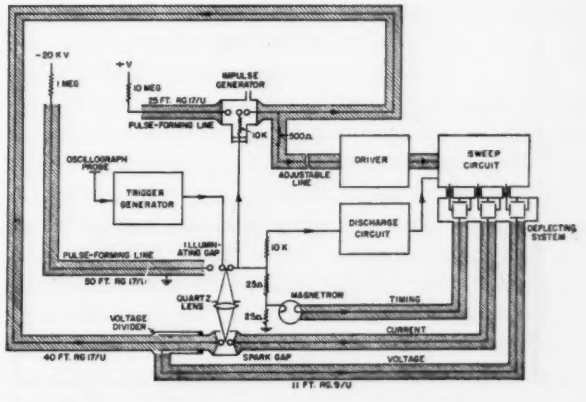

FIG. 5. Schematic diagram of u.h.s. circuit for studying impulse breakdown of air.

[6] W. O. Schumann, *Elektrische Durchbruchfeldstärke von Gasen* (Verlag. Julius Springer, Berlin, 1923), p. 26.

same conditions as for the initial measurement) were made on oscillograms obtained with the circuits described in Section II. Sketches of typical voltage traces for different conditions of applied field and gap-width are presented in Fig. 7. These sketches were prepared by tracing the image of the oscillograms formed by a micro-projector and correcting them for the effect of the known reflections in the transmission lines. It can be observed that the first evidence of breakdown after the applied voltage achieves its full size occurs at the time marked τ, which we shall define as the time lag of breakdown. The degree to which the breakdown proceeds during the rise time of the applied voltage is neglected in this definition of lag time. An estimation of the magnitude of this effect will be given later. Little additional information was obtained from the current oscillograms because of the high displacement current caused by the voltage impulse across the capacity of the spark gap.

The effect on the time lag of varying the ultraviolet illumination intensity was tested for a fixed gap-width of 1.55 mm and applied field of 82 kv/cm. For the greatest intensity used there was no detectable randomness, but as the intensity decreased the randomness increased. In Fig. 8 is plotted the logarithm of the fraction of time lags larger than τ as a function of τ. For each intensity about 35 lags were measured. It can be seen that the distribution seems to be exponential for all intensities measured, as has been found previously for longer times and lower ultraviolet intensities.[7,8] Using the experimental conclusion found by Strigel,[8] that every electron released from the cathode is successful in initiating the breakdown at this high an overvoltage (95 percent), and assuming that all of the statistical fluctuations are due to the fluctuations in the supply of initiating electrons from the cathode, we can use the observed distributions to calibrate our ultraviolet source in terms of the photoelectric current. Thus, if the distribution is $e^{-\tau/\sigma}$, $1/\sigma$ should be the rate at which electrons are released from the cathode. σ can be measured from the distribution curves to give a value of $0.0037/A^2$ mμsec., where A is the aperture diameter in inches of the ultraviolet illuminating system. This corresponds to a photoelectric current of $4.3A^2 \times 10^{-8}$ amp./cm^2.

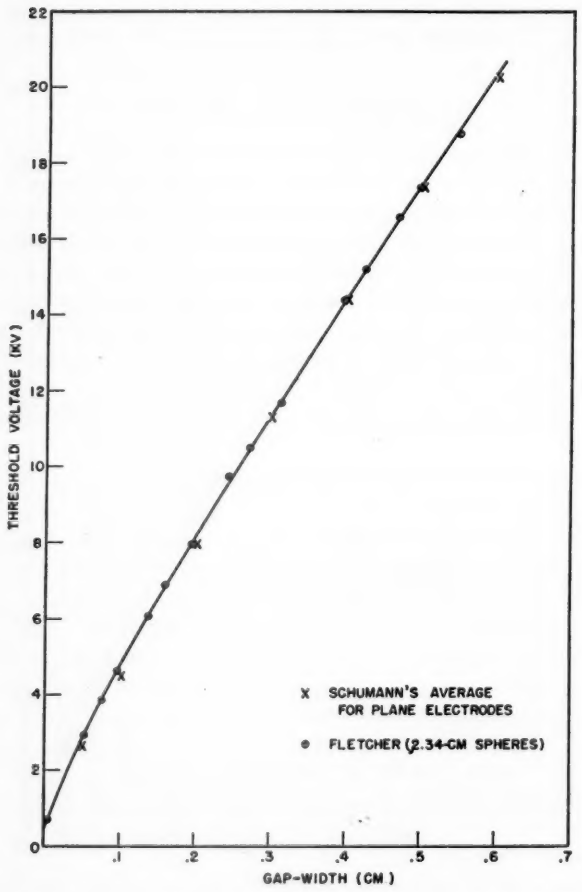

FIG. 6. D.c. threshold voltage measured under same conditions as the impulse breakdown measurements. Comparison is made with a weighted average for a number of measurements compiled by Schumann (see reference 6).

The non-statistical lag obtained for the higher intensities of ultraviolet illumination is considered the formative lag. This formative lag was measured for a variety of voltages and gap-widths for times between 0.5 and 50 mμsec. It was convenient to make runs at constant voltage rather than constant gap-width because both the adjustment of the impulse generator and the synchronization of the sweep circuit are a function of the impulse voltage. The results are plotted in Fig. 9 as a function of the applied field. For fields above 50 kv/cm the formative lag is a function of field alone independent of gap-width, while below 50 kv/cm the formative lag depends on the gap-width. Thus for fields less than the critical field (49 kv/cm), the constant voltage plot for $V=7.5$ kv begins to have longer formative lags than the other two voltages measured; for $E=42$ kv/cm the plot for $V=12.7$ kv begins to have longer formative lags.

IV. CALCULATION OF THE FORMATIVE LAG

In accordance with the suggestion of Raether[4] we shall attempt to compute the critical avalanche size as a means of calculating the formative lag. We shall consider the critical magnitude of the avalanche as the size which just reduces the field inside the avalanche to zero. This is the condition for plasma formation which must eventually be true for the whole discharge channel. Secondary avalanches may be initiated in front of and behind the initial avalanche before this space-charge field is achieved, but these secondary avalanches, building up at the same rate as the primary one, will have little effect until their rate of build-up is increased by the external space-charge fields of the

[7] K. Zuber, Ann. d. Physik **76**, 231 (1925); A. Tilles, Phys. Rev. **46**, 1015 (1934).
[8] R. Strigel, Wiss. Veroff. Siemens-Konzern **11(2)**, 52 (1932).

initial avalanche and until the exponential build-up of the initial avalanche is arrested by its internal field.

In order to compute the critical avalanche size let us consider the electron avalanche in more detail. In the short times with which we are here concerned the positive ions, being so much less mobile than the electrons, will remain practically where they are created. Thus the motion of the electrons entirely determines the distribution of both ions and electrons. When the avalanche first begins, the distributions are dominated mainly by the diffusion of electrons, since the densities of electrons and positive ions are small enough that the influence of the space-charge field is negligible. For this case the rate of build-up of electron and positive ion densities, n_- and n_+, are given by the following differential equations:

$$\begin{aligned} \partial n_-/\partial t &= \alpha v n_- - D\nabla^2 n_- + v(\partial n_-/\partial z), \\ dn_+/dt &= \alpha v n_-, \end{aligned} \tag{4.1}$$

where α is the first Townsend coefficient for ionization by electron impact, v is the drift velocity in the applied field E taken in the z direction, and D is the diffusion coefficient. These equations have the following exact

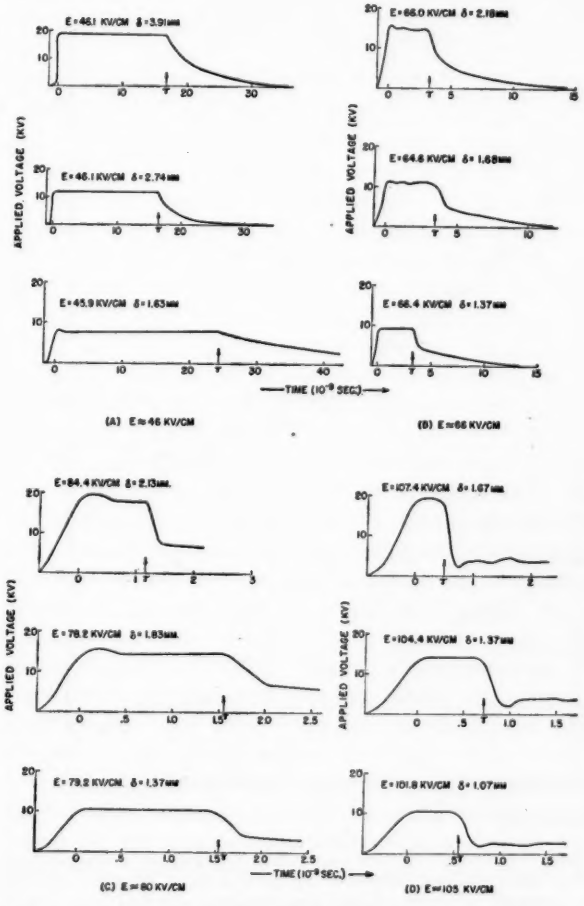

FIG. 7. Tracings of breakdown voltage for various conditions of applied field and gap-width.

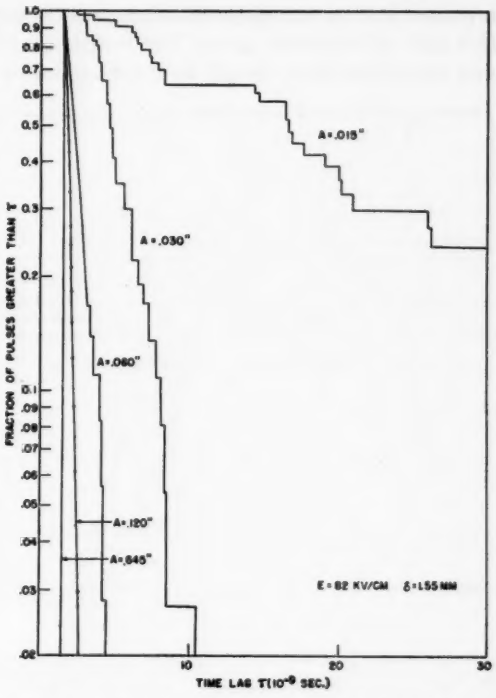

FIG. 8. Distribution of time lags for different diameter (A) aperture stops of ultraviolet illuminating system.

solutions:

$$n_- = (4\pi Dt)^{-\frac{1}{2}} \exp\left[-\frac{x^2+y^2+(z-vt)^2}{4Dt} + \alpha v t\right],$$

$$n_+ = \alpha v \int_0^t (4\pi Dt')^{-\frac{1}{2}} \exp\left[-\frac{x^2+y^2+(z-vt')^2}{4Dt'} + \alpha v t'\right] dt'. \tag{4.2}$$

It can be seen that the distribution of electrons is a normal Gaussian distribution, viewed in a coordinate system moving in the z direction with the velocity v. For this distribution the average distance of an electron from the center is well known to be $(6Dt)^{\frac{1}{2}}$, which can be considered the breadth of the avalanche.

The integral determining the positive ion distribution cannot be evaluated in terms of well-known functions. Its general behavior can be obtained by noting that the integrand is the electron distribution at the time t'. If the breadth of the avalanche at $t'=z/v$ is small compared to $1/\alpha$, the Gaussian part of the integrand will vary much more rapidly than the $e^{\alpha v t'}$. At the maximum of the Gaussian part of the integrand, $t'=z/v$, the slowly varying part can be taken in front of the integral sign, and the remaining integral can be expressed in terms of the error function

$$I(x) = \frac{2}{(\pi)^{\frac{1}{2}}} \int_0^x \exp(-x^2)dx.$$

It is convenient to introduce the characteristic length $a \equiv 4D/v$ and the distance $z_0 \equiv vt$. The length $a \equiv 4D/v$, to a first approximation, should be independent of the applied field E, since $D \sim (U_e)^{\frac{1}{2}}$ (where U_e is the average electron energy), $v \sim (E)^{\frac{1}{2}}$, and $U_e \sim E$ for the high fields considered here.[9] z_0 is the distance the center of

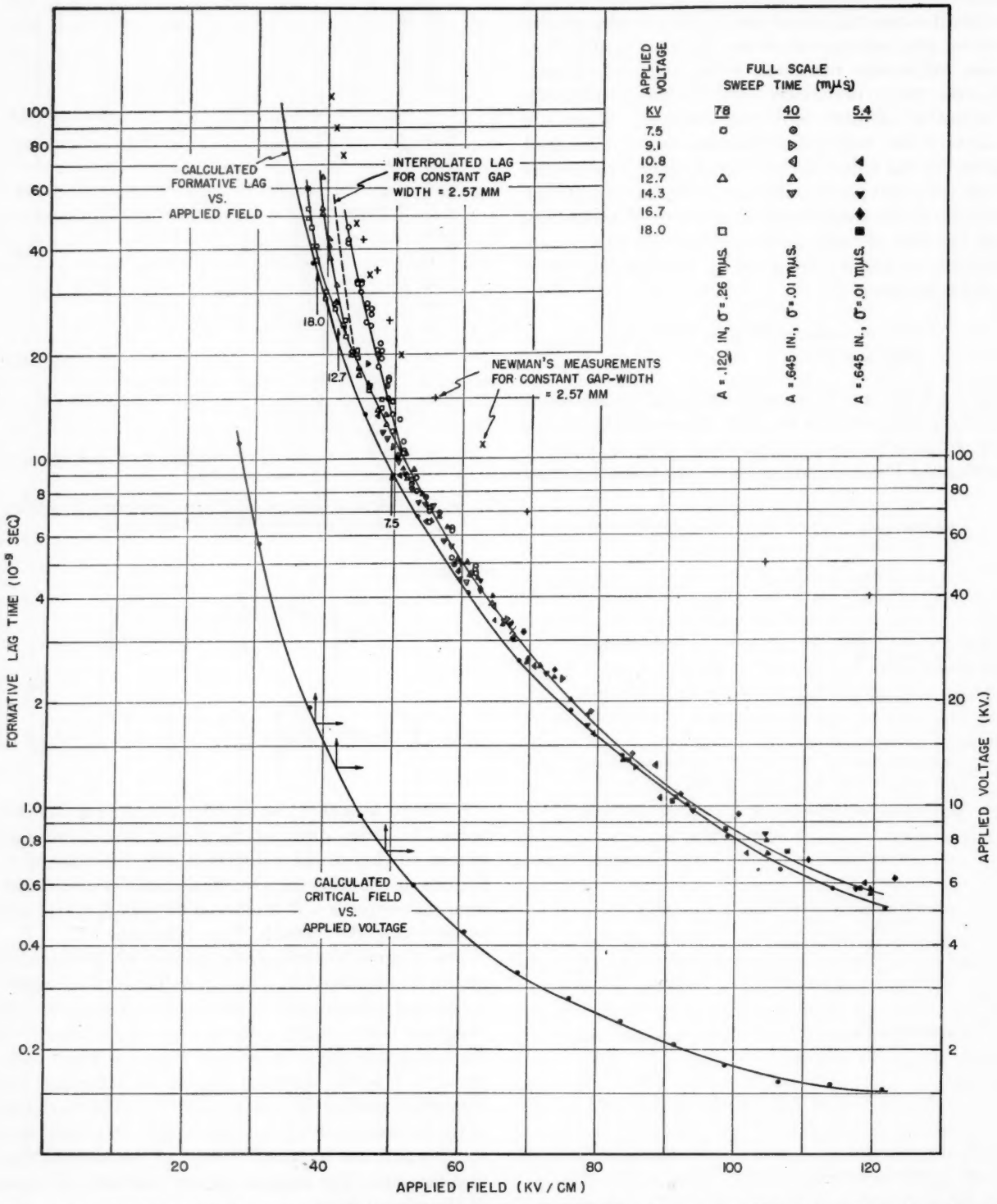

FIG. 9. Measurements of the formative lag plotted as function of applied field for different gap-widths (or applied voltages), and compared with a calculated formative lag and with the measurements of Newman (see reference 12). On the same graph are plotted the calculated critical fields, below which, for a given applied voltage, multiple avalanches (and thus longer formative lags) should be required for breakdown. The measurements are corrected for the finite rise time of applied voltage as discussed in Section V.

[9] L. B. Loeb, *Fundamental Processes of Electrical Discharge* (John Wiley and Sons, Inc., New York, 1939); A. von Engel and M. Steenbeck, *Elektrische Gasentladungen* (Verlag. Julius Springer, Berlin, 1932), Vol. I.

the electron cloud has moved. Then

$$n_-=(\pi a z_0)^{-\frac{1}{2}}\exp\left[-\frac{x^2+y^2+(z-z_0)^2}{az_0}\right]e^{\alpha z_0},$$

$$n_+=\begin{cases}\dfrac{\alpha}{2\pi a z}\exp\left[-\dfrac{x^2+y^2}{az}\right]\left[1+I\left(\dfrac{z_0-z}{(az)^{\frac{1}{2}}}\right)\right]e^{\alpha z}, & z<z_0\\ \dfrac{\alpha}{2\pi a z_0}\exp\left[-\dfrac{x^2+y^2}{az_0}\right]\left[1-I\left(\dfrac{z-z_0}{(az_0)^{\frac{1}{2}}}\right)\right]e^{\alpha z_0}, & z>z_0,\end{cases} \tag{4.3}$$

where the expression for n_+ is good only when the avalanche breadth $(3az_0/2)^{\frac{1}{2}}$ is small compared to $1/\alpha$.

In order to compare the two expressions for n_- and n_+, the densities can be plotted along the axis of the avalanche ($x=y=0$). It is convenient to do this in dimensionless coordinates, by plotting the densities in terms of the maximum electron density $n_0=(\pi a z_0)^{-\frac{1}{2}}e^{\alpha z_0}$, and the distances in terms of $(az_0)^{\frac{1}{2}}$, which is approximately the avalanche breadth. Thus, if $w\equiv(z-z_0)/(az_0)^{\frac{1}{2}}$ and $b=\alpha(az_0)^{\frac{1}{2}}$, in the vicinity of the avalanche head ($z\simeq z_0$), Eqs. (4.3) become

$$n_-=n_0e^{-w^2},$$
$$n_+=\begin{cases}\frac{1}{2}bn_0[1+I(-w)]e^{bw}, & w<0\\ \frac{1}{2}bn_0[1-I(w)], & w>0.\end{cases} \tag{4.3a}$$

These equations are plotted in Fig. 10 for different values of the parameter $b=\alpha(az_0)^{\frac{1}{2}}$, which is approximately the ratio of the avalanche breadth to the ionizing distance $1/\alpha$. At the highest values of $\alpha(az)^{\frac{1}{2}}$ the approximation made in evaluating the integral of Eq. (4.2) is no longer good, but the general features of the curves should be correct. As $\alpha(az_0)^{\frac{1}{2}}$ increases, the cloud of electrons tends to overlap more and more the cloud of positive ions. Thus the center of mass of the electron cloud is at $z=z_0$, and its spread $(\langle x^2+y^2+(z-z_0)^2\rangle_{Av})^{\frac{1}{2}}$ is $(3az_0/2)^{\frac{1}{2}}$. The center of mass of the positive ions is approximately at $z=1/\alpha$, while its spread is $(3az_0/2)^{\frac{1}{2}}$ for $\alpha(az_0)^{\frac{1}{2}}>1$ and $\simeq 1/\alpha$ for $\alpha(az_0)^{\frac{1}{2}}<1$.

As the densities of electrons and positive ions increase due to ionization, the space charge develops a field E_s, which changes the distribution calculated above. The rate-of-build-up equation then becomes too complicated to solve exactly, and an approximation method has to be used. The simplest approximation would be to assume that the distribution is unaffected by the space-charge field. The critical avalanche size N_c could then be obtained by calculating the internal space-charge field from this distribution, and setting it equal to the applied field.

A somewhat better approximation can be obtained by the following scheme: Assume the distribution is unaffected by the space-charge field up to the time t_t at which the space charge first becomes important. At this time the space-charge field E_t can be computed from the diffusion-dominated distribution found above. For times larger than t_t assume the field is proportional

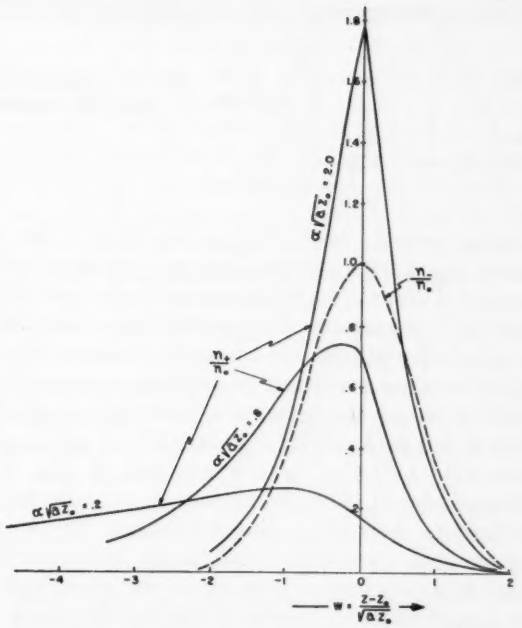

FIG. 10. Distribution of electron and positive ion densities along the axis of the electron avalanche for different values of the ratio of avalanche radius $(3az_0/2)^{\frac{1}{2}}$ to ionization distance $1/\alpha$. Densities are plotted in terms of the maximum electron density n_0, and distance from the center of electron cloud is plotted in terms of $(az_0)^{\frac{1}{2}}$, approximately the avalanche radius.

to the number of electrons N and inversely proportional to the square of the avalanche radius r_s, as would be true for a spherical distribution of charge; i.e., if $r_s=r_t$, $E_s=E_t$, and $N=N_t$ at $t=t_t$, then

$$E_s=E_t\frac{N}{N_t}\frac{r_t^2}{r_s^2}. \tag{4.4}$$

The radius r_s to be used in this equation can be obtained by integrating the drift velocity due to the space-charge field E_s. The calculations which follow are made according to this scheme.

The quantities r_t, E_t, and N_t can be computed from the condition that, at $t=t_t$, the drift velocity v_t due to the space-charge field becomes equal to the diffusion velocity $=-(D/n_-)\nabla' n_-$ (where the prime refers to the moving coordinate system). The diffusion velocity can be evaluated from Eq. (4.2) to give

$$v_t=r_t/2t_t, \tag{4.5}$$

where r_t can be taken as $(3avt_t/2)^{\frac{1}{2}}$. If we put $t_t=\ln N_t/\alpha v$ and assume $v\sim(E)^{\frac{1}{2}}$,[9] Eq. (4.5) yields a relation for E_t in terms of N_t:

$$E_t=\frac{3}{8}\frac{a\alpha}{\ln N_t}E. \tag{4.6}$$

A second relation between E_t and N_t can be obtained by calculating the space-charge field from the distribution given by Eq. (4.2). To do this it will be convenient

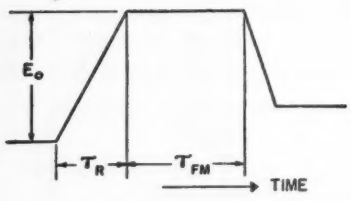

FIG. 11. Idealized shape of applied impulse.

to make several simplifying assumptions.[9a] We will assume that all the electrons are in a sphere of radius $(3az_0/2)^{\frac{1}{2}}$. This predicts fields due to the electrons which depart by a maximum of 60 percent from the fields of the actual distribution. We will further assume that the positive ions are contained in a sphere whose center is $1/\alpha$ distant from the center of the electron sphere and whose radius is $(3az_0/2)^{\frac{1}{2}}$ for $\alpha(3az_0/2)^{\frac{1}{2}}>1$ and $1/\alpha$ for $\alpha(3az_0/2)^{\frac{1}{2}}<1$ (following the analysis of Eq. (4.2) presented above). The assumption of a sphere for the distribution of positive ions for $\alpha(3az_0/2)^{\frac{1}{2}}<1$ is a poor one, but under this condition the maximum field is mainly determined by the denser electron cloud, so that a more exact knowledge of the ion distribution is not necessary. With these assumptions the equation for the space-charge field (taken at the point of maximum retarding field $z=z_0-(3az_0/2)^{\frac{1}{2}}$) is

$$E_t=\frac{e}{4\pi\epsilon_0}N_t\frac{1}{(3a/2\alpha)\ln N_t}\times\begin{cases}1+(3/2)a\alpha\ln N_t-[(3/2)a\alpha\ln N_t]^{\frac{1}{2}}, & (3/2)a\alpha\ln N_t<1\\ 1/[(3/2)a\alpha\ln N_t]^{\frac{1}{2}}, & (3/2)a\alpha\ln N_t>1\end{cases}\tag{4.7}$$

where e is the electronic charge and ϵ_0 is the dielectric constant of free space (rationalized m.k.s. units). Using Eqs. (4.6) and (4.7) to eliminate E_t, we can then obtain an implicit equation to determine N_t:

$$N_t=\frac{9\pi\epsilon_0}{4e}Ea^2\begin{cases}[1+(3/2)a\alpha\ln N_t-[(3/2)a\alpha\ln N_t]^{\frac{1}{2}}]^{-1}, & (3/2)a\alpha\ln N_t<1\\ [(3/2)a\alpha\ln N_t]^{\frac{1}{2}}, & (3/2)a\alpha\ln N_t>1.\end{cases}\tag{4.8}$$

For $N>N_t$ the avalanche radius r_s will be determined mainly by the drift velocity v_s due to the space-charge field. If we assume this velocity to be proportional to $(E_s)^{\frac{1}{2}}$,[9] r_s is given by the equation

$$r_s=r_t+\int_{t_t}^{t}v(E_s/E)^{\frac{1}{2}}dt.\tag{4.9}$$

Substituting E_s from Eq. (4.4) and differentiating, we obtain

$$r_s dr_s=v\left(\frac{E_t}{E}\right)^{\frac{1}{2}}r_t\frac{e^{\frac{1}{2}\alpha vt}}{(N_t)^{\frac{1}{2}}}dt.$$

This can be integrated to give

$$r_s^2=r_t^2+4\left(\frac{E_t}{E}\right)^{\frac{1}{2}}\frac{r_t}{\alpha}\left[\left(\frac{N}{N_t}\right)^{\frac{1}{2}}-1\right].$$

For all of the values in the region where we will use this equation, $N\gg N_t$ and $r_s\gg r_t$, so that

$$r_s^2\simeq 4\left(\frac{E_t}{E}\right)^{\frac{1}{2}}\frac{r_t}{\alpha}\left(\frac{N}{N_t}\right)^{\frac{1}{2}}.\tag{4.10}$$

The final expression for the space-charge field in terms of the avalanche size N can be obtained by the use of Eqs. (4.4), (4.6), and (4.10) to give

$$E_s=(3/16)a\alpha E(N/N_t)^{\frac{1}{2}},\tag{4.11}$$

where N_t can be computed from Eq. (4.8).

The critical avalanche size N_c, which drops the internal field of the avalanche to zero, will be attained when $E_s=E$. From Eq. (4.11) this can be seen to be

$$N_c=(256/9)N_t/(a\alpha)^2.\tag{4.12}$$

The formative lag is calculated from this by the equation

$$\tau_F=(1/\alpha v)\ln N_c.\tag{4.13}$$

In order to obtain numerical answers from these equations we will use Sanders's values[10] for α (extrapolated from lower pressures), take the value $a=3\times10^{-4}$ cm calculated from Raether's observation[11] of the avalanche breadth, and assume $v=0.224\times10^7(E)^{\frac{1}{2}}$ cm/sec., which is adjusted to the avalanche velocity observed by Raether[11] at fields near the threshold and extrapolated to the higher fields by the expected dependence on the square root of the applied field.[9] This predicts the values τ_F plotted in Fig. 9 to compare with the experimentally observed values.

V. DISCUSSION OF THE FORMATIVE LAG

Before considering how much significance should be placed on the comparison of the computed formative lag with the experimental values, let us examine the effect on the observed formative lag, as defined above, of a finite rise time of applied voltage. For simplicity let us consider a linearly rising applied field of rise time τ_R and designate the measured formative lag by τ_{FM} as shown in Fig. 11. Further, we shall assume that the ultraviolet illumination is intense enough so that the entire time lag is formative, which was the actual condition under which the experiment was conducted. With the same type of analysis used in the previous section the total time to bring about breakdown is given by the equation

$$\ln N_c=\alpha(E)v(E)\tau_{FM}+\int_0^{\tau_R}\alpha\left(E\frac{t}{\tau_R}\right)v\left(E\frac{t}{\tau_R}\right)dt.\tag{5.1}$$

[9a] Calculations using this same type of analysis were first made by Slepian, reference 2.

[10] F. H. Sanders, Phys. Rev. 44, 1020 (1933).

[11] H. Raether, Zeits. f. Physik 107, 91 (1937).

Since the calculated formative lag is $\tau_F=\ln N_c/\alpha(E)v(E)$, it can be expressed in terms of the measured value by the equation

$$\tau_F=\tau_{FM}+\frac{1}{\alpha(E)v(\alpha)}\int_0^{\tau_R}\alpha\left(E\frac{t}{\tau_R}\right)v\left(E\frac{t}{\tau_R}\right)dt. \quad (5.2)$$

The integral can be evaluated with the use of the empirical relations, $\alpha\sim(E-B)^2$ and $v\sim(E)^{\frac{1}{2}}$,[9] where B is a constant of the order of 24 kv. With these

$$\tau_F=\tau_{FM}+\frac{2}{7}\tau_R\frac{E^2-(14/5)BE+(7/3)B^2}{(E-B)^2}. \quad (5.3)$$

This expression was used to correct the measured points, and the corrected points are the ones plotted in Fig. 9. The correction amounted to an addition to the measured value of a practically constant value of 0.1 mμsec., which even for the smallest times amounted to only 20 percent.

The calculation of the formative lag reveals that the formative lag should be a function of field alone, independent of gap-width (or applied voltage). This is found to be true for the high fields, but not for the lower fields. For a given gap-width (or applied voltage) below a certain critical field the time lags become larger than for a larger gap-width (or smaller voltage). This critical field is believed to be the field for which the initial avalanche takes the entire gap-width to achieve the critical avalanche size. For a smaller field than this critical field a single avalanche is unable to create a high enough space-charge field to cause breakdown. More than one avalanche is required to bring about this condition. This requires the longer formative time which is observed.

To check this idea the critical field (E_c) can be computed according to the analysis of the previous section. Thus E_c should be given by the implicit equation

$$\delta=\ln N_c/\alpha(E_c) \quad \text{or} \quad V=E_c\delta=E_c\ln N_c/\alpha(E_c). \quad (5.4)$$

A plot of this calculated critical field *vs.* applied voltage is given in Fig. 9. The arrows indicate the expected critical fields for the three applied voltages used in the measurements of the longer times. The agreement with observation is well within the experimental and theoretical accuracy, confirming the validity of the interpretation of the behavior of the formative lag for the lower fields.

For the longest gap-widths used (or largest applied voltages) the observed formative lags should check the calculated values down to 39 kv/cm. It can be seen from Fig. 9 that the calculated values follow the observed values very closely, being if anything, a few percent too low. This small discrepancy is in the right direction to be explained by the neglect in the calculation of the time after the critical avalanche size has been reached until visible current is produced. However, not too much significance should be placed on the discrepancy since the velocity used in the calculation was extrapolated from a value observed by Raether to which he ascribed an accuracy of only ± 15 percent.[11] This would introduce the same percent accuracy into the calculation of the formative lag. The agreement with experiment is well within this expected accuracy.

It should be pointed out, though, that the observed agreement does not serve to distinguish between the radial space-charge field emphasized by Loeb and Meek[3] and the axial field used here. The $\ln N_c$ is insensitive to the details of the particular assumptions made in computing it. Thus a change in the value of N_c by a factor of 10 changes the calculated time lag by only 12 percent. This insensitivity was what permitted such rough assumptions made in the calculation to give good agreement with experiment. A constant value of $N_c=10^8$ would serve to predict the observed formative lag and critical field about as well as the computed variation in N_c due to the space-charge field. The main value of the computation is to establish that the correct order of magnitude for the N_c is given by considering the space-charge field of a single avalanche to be the dominating factor governing the breakdown.

In Fig. 9 comparison of the observed time lag is made with the measurements of Newman,[12] who seems to have taken the most precautions among previous workers against parasitic oscillations in his applied impulse voltage. Newman's data were taken for a gap-width the breakdown voltage of which was 10 kv, or $\delta=2.57$ mm. The broken line in Fig. 9 is interpolated from the present measurements for a constant gap-width of $\delta=2.57$ mm. Newman's measurements are about 10^{-8} sec. longer than the micro-oscillograph measurements at the same field. This could be explained by assuming that Newman defined his lag time from the bottom of his rising impulse (as seems probable from his experimental arrangement) instead of from the top as defined here, and by further assuming the rise time of his applied impulse to be of the order of 10^{-8} sec.

It is conceivable that, if the photoelectric current released by the ultraviolet illumination were too large, the experimentally determined formative lag would be decreased, making the observed agreement between computed and observed formative time lag appear as merely fortuitous. This might occur if there were a high probability of a second electron being released close to a point where the initiating electron was released, in a time small enough to influence the initial avalanche. If we assume that interaction is possible if the second electron is released a distance away from the point of release of the initial electron equal to the avalanche radius r_s, and if we further assume that interaction can occur if the second electron is released in a time $1/\alpha v$ after the first electron, the condition imposed on the

[12] M. Newman, Phys. Rev. **52**, 652 (1937).

photoelectric current is

$$(S/\pi r_s^2)\sigma \gg 1/\alpha v, \tag{5.5}$$

where S is the total illuminated area of the cathode. With the use of Eqs. (4.10), (4.6), and (4.12), the avalanche radius r_s where $N=N_c$ can be shown to be equal to $4/\alpha$, whence the condition on σ becomes

$$\sigma \gg 16\pi/S\alpha^2 v. \tag{5.6}$$

The computed value of $16\pi/S\alpha^2 v$ varies from 5×10^{-2} mμsec. at $E=38$ kv/cm, to 6.3×10^{-4} mμsec.at $E=53$ kv/cm, down to 8.5×10^{-7} mμsec. at $E=122$ kv/cm. The measurements were carried out with $\sigma=0.26$ mμsec. for $E<50$ kv/cm and $\sigma=0.01$ mμsec. for $E>50$ kv/cm. Thus the photoelectric current was on the average a factor of one hundred lower than that which would be expected to affect the formative time lag.

VI. DETERMINATION OF THE CRITICAL GAP-WIDTH

If the interpretation of the formative lag for lower fields is correct, it should be possible to predict the critical gap-width (δ_c) for which a single avalanche determines the threshold. This has been attempted previously by a number of writers,[4,13] but until recently[14] all have had to rely on a comparison of an approximate calculation of the critical field with the observed threshold field. Because of the approximate nature of the calculations, the critical gap-width has been predicted to be anywhere from 0.013 cm to 1.3 cm. With the present data it is possible to check an approximate calculation, in which, by itself, one would not have too much confidence, with two kinds of experimental observations, in which one would have considerably more confidence, to obtain a more reliable value of the critical gap-width.

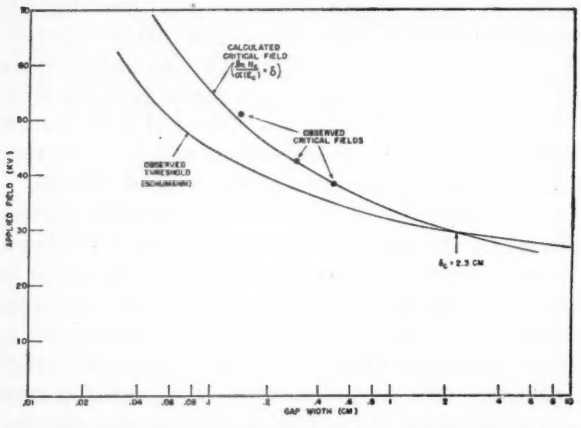

FIG. 12. Determination of the critical gap-width above which the threshold should be determined by a single avalanche.

The critical gap-width will occur when the critical field is equal to the threshold field. In Fig. 12 the calculated critical field and the observed threshold field (Schumann[6]) are plotted as a function of gap-width. The two curves are seen to cross at $\delta_c=2.3$ cm, which should be the critical gap-width.

The fact that E_c drops below E_T for $\delta>\delta_c$ indicates that it is not sufficient to drop the internal field to zero to bring about breakdown for $\delta>\delta_0$. The additional condition is that electrons must be regenerated behind the head of the avalanche. Apparently this condition requires a relatively higher field for $\delta>\delta_c$ than is required for the smaller gap-widths. This may be in part caused by the additional supply of electrons available at low gap-widths from photo-emission from the cathode which are not available at the lower gaps because of absorption in the gas. These considerations indicate that the actual δ_c may be higher than that determined from Fig. 12, and not lower as suggested by previous writers.

VII. DISCUSSION OF HIGH CURRENT DISCONTINUITY

Examination of the voltage traces of Fig. 7 reveals that for the three highest fields shown the breakdown current has a discontinuity in its rate of increase. Thus it starts out with a very rapid rate of rise and then rather suddenly changes to a slower rate of rise at a current which is of the order of magnitude of 75 amp. It is of interest to discover the cause of this discontinuity.

The first expected discontinuity in the initial electron avalanche occurs when the avalanche achieves its critical size, and the anode and cathode streamers begin. The current which is observed in the external circuit at this discontinuity should be $eN_c v/\delta$. With the use of the calculated value of N_c the current computed from this relation is found not to exceed 10 ma over the entire range of measurements. This is much too low to account for a discontinuity of the order of 75 amp. In addition, one would expect the onset of the streamers to cause an increase in the rate of rise of current rather than a decrease.

The next discontinuities to be expected would be the arrival of either the cathode-directed or anode-directed streamers at one of the electrodes. It is difficult to estimate the current to be expected from these streamers. However, since the electrons which cause the current from the streamers have not yet reached the electrodes, the observed current should be all displacement current which should be unaffected by an insulator on either of

[13] L. B. Loeb and J. M. Meek, reference 3, p. 48; L. H. Fisher, Phys. Rev. 69, 530 (1946).

[14] The recent measurements by L. H. Fisher and B. Bederson (Phys. Rev. 75, 1615 (1949)) of the formative lag near the threshold offers a new method of determining δ_c. Their published data are not inconsistent with the views herein expressed if the regenerative mechanism of the modified Townsend discharge is considered to be photo-emission from the cathode and/or photo-ionization of the gas.

the electrodes. In order to test this possibility some oscillograms were taken with a disk of polystyrene first on the cathode and then on the anode. Three voltage traces, all for the same applied field, are shown in Fig. 13 to indicate the effect of an insulated electrode. It is observed that the current at the discontinuity is the same whether the insulator is on the cathode or the anode and that this current is about $\frac{1}{3}$ that observed without the insulator. This indicates that the current at the discontinuity must be at least partly conduction current. Therefore the discontinuity cannot be due to the arrival of either of the streamers at the electrodes.

A possible explanation of the discontinuity may be that a change occurs in the mode of release of electrons from the cathode. This might conceivably take place in the following way: If electron regeneration from the cathode is initially by an intense photon bombardment of the cathode with photons released by the ionization processes in the streamer, when the current builds up high enough to drop the applied field due to the generator impedance, the number of bombarding photons will drop accordingly. The field will therefore drop only to an equilibrium value for which the photoelectric current is just able to hold the field at this value. To decrease the field further another mechanism for electron release must enter. This might be by positive ion bombardment, a much slower mechanism. This would qualitatively explain the observed discontinuity. However, verification requires further experimental work.

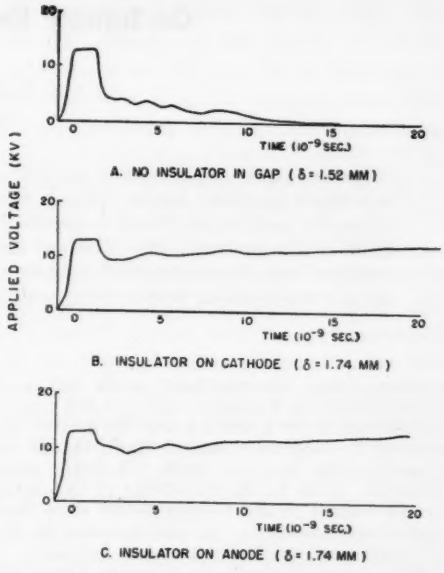

FIG. 13. Voltage traces for a spark gap with and without a 0.40-mm thick polystyrene disk, all for the same applied field (83 kv/cm).

ACKNOWLEDGMENT

The author is grateful to Professor A. von Hippel for making available to him the facilities of the Laboratory for Insulation Research and for his guidance and encouragement. He also wishes to acknowledge the constant cooperation and assistance of the members of the Laboratory.

On Infinite Relativistic Particle Matrices*

WALTER WESSEL
USAF Institute of Technology, Dayton Ohio

(Received May 19, 1948)

Besides the known tensors of integral and half-odd-integral rank (spinors) there exists a new form of relativistic covariant entities with an infinite number of components, discovered in 1944 by Dirac. An especially simple type of them is generated by operations underlying a theory of the electron recently proposed by the present author. This way the representations are obtained immediately in matrix form, the matrices being of an unexpectedly simple type. Half of them have continuous spectra. They permit the setting up of wave equations having always positive energy.

* The present paper was completed at the end of 1947, but could not immediately be published. As far as it is concerned with the representations of the Lorentz-group, the matter has already been settled by V. Bargmann, Ann. of Math. **48**, 568 (1947) and Harish-Chandra, Proc. Roy. Soc. **A189**, 372 (1947), whose papers in the meantime came to the knowledge of the author. With regard to this work it should be pointed out more clearly, that these Lorentz-representations, i.e., the matrices M_k, Π_k in our terms, although mathematically the most interesting part, are only six of the sixteen elements of our theory. Our primary aims are not to construct these representations but (*a*) to translate the Poisson-brackets given in an earlier paper into commutation relations and (*b*) to find matrix representations for the κ_k and especially for the ι_k-matrices, that serve to set up the wave equation $\iota_k p^k = -m(\mathrm{I}, \mathrm{K})c$. The connection of our starting point (*a*) with Harish-Chandra's representation would be achieved, as far as the M_k, Π_k-matrices are concerned, by the unitary transformation that is indicated in its first steps by formula (37). This "normal representation" has been fully developed in the meantime and appears simultaneously in Zeits. f. Naturforschung **4a** (1949). The construction of the matrices mentioned under (*b*) needs a slight generalization of Harish-Chandra's method, because the six M_k, Π_k matrices behave like a subgroup in the 16-element-scheme. The connection between the invariants of the Lorentz-group, *viz.*, J^2, I (Harish-Chandra) resp. $-Q$, R (Bargmann) with our I, K is given by

$$-Q = J^2 = \mathrm{I}^2 - \mathrm{K}^2 - 1, \quad R = I = \mathrm{IK}.$$

The factorization of R resp. I is essential for the construction of irreducible representations of the whole 16 elements, because only I, not K commutes with all of them.

A short report of the present paper together with a first attack upon the mass problem appeared recently (Sommerfeld-Festheft). Zeits. f. Naturforschung **3a**, 559 (1948). In a simultaneous paper of Bopp (Zeits. f. Naturforschung **3a**, 564 (1948)) the underlying physical ideas have much been improved. The continuous spectrum of the ι-components has already been noticed by E. L. Hill, Phys. Rev. (2) **73**, 910 (1948), but it is a main result of our paper (see formula (23)) that ι^4 can be used in a discontinuous and even one side bounded form. Next to I it is just the key for the classification (see our Table III).

SOME years ago Dirac[1] discovered a new type of vector called "expansor" by him with an infinite number of components, which by a Lorentz-transformation undergo a *unitary* substitution. It is expected that expansors will be of great importance in particle-theory, as they provide a method of dealing with continuous entities more amenable to quantum theory than the usual methods of field theory, "quantization" not merely considered as an introduction of Planck's constant but essentially as the selection of an enumerable manifold from a continuous one. In its general form Dirac's theory looks rather complicated mainly by the particular behavior of the fourth world-coordinate. Meanwhile the author met with the same thing from another point of view, considering just radiation-reaction-forces. The method arrived at furnishes immediately the matrices of the representations and subsequently of the transformations from both a restricted and enlarged type of Dirac's. Starting with spinors rather than vectors of integral rank, we include integral as well as half-odd-integral representations. At the same time there is a wide restriction or ordering of the immense manifold of components by the existence of an invariant, which makes the representation split up into a number of non-combining ones, whose matrices can be written down in an unexpectedly simple way. Besides being Hermitian, as Dirac's theory implies, they have eigenvalues of a noteworthy type.

Representations of the Lorentz-transformation are induced[2] by a scheme of commutation-relations between six quantities, which by a suitable transformation may be combined into the components of a six-vector. In this form their commutation-rules generalize those of a moment of momentum and may be considered as the respective ones of the magnetic and relativistic electric momentum of a moving particle. For convenience we shall speak of the momentum components instead of the mathematical quantities. Denoting them by M_1, M_2, M_3, Π_1, Π_2, Π_3, we have[2]

$$M_1M_2 - M_2M_1 = iM_3, \quad \Pi_1\Pi_2 - \Pi_2\Pi_1 = -iM_3,$$
$$M_1\Pi_2 - \Pi_2M_1 = i\Pi_3, \tag{1}$$

together with the relations obtained from these by cyclic permutation of 123 and with

$$M_1\Pi_1 - \Pi_1M_1 = M_2\Pi_2 - \Pi_2M_2 = M_3\Pi_3 - \Pi_3M_3 = 0. \tag{2}$$

There is a very singular consequence of these equations, which looks almost like a contradiction between quantum-mechanics and relativity-theory. Of course,

[1] P. A. M. Dirac, Proc. Roy. Soc. London **A183**, 284 (1944).

[2] B. L. van der Waerden, *Die gruppentheoretische Methode in der Quantenmechanik* (Verlag. Julius Springer, Berlin, 1932).

[3] See also P. A. M. Dirac, Proc. Roy. Soc. London **A155**, 447 (1936).

the relations are invariant under a Lorentz-transformation, i.e., they reproduce themselves, if one substitutes for the components their combinations relative to another system of reference. Now by the rules of quantum-mechanics the measurable values of any physical quantity are given by the eigenvalues of its representing matrix. However, because of the minus-sign on the second triplet of equations required by the relativistic invariance, the eigenvalues of the Π_k, $k=1, 2, 3$ are purely imaginary.

For proof introduce the quantities $\Pi=\Pi_1+i\Pi_2$ and $M=M_1+iM_2$, whose commutation with Π_3 gives

$$\Pi\Pi_3-\Pi_3\Pi=M, \quad M\Pi_3-\Pi_3M=-\Pi. \tag{3}$$

Bringing Π_3 into diagonal form and labelling the Π, M with its eigenvalues π', π'', $\cdots$, say, one has

$$(\pi''-\pi')\Pi_{\pi'\pi''}=M_{\pi'\pi''}, \quad (\pi''-\pi')M_{\pi'\pi''}=-\Pi_{\pi'\pi''}. \tag{4}$$

There may be more indices of the Π, M, say $I, J, \cdots$, a certain manifold of π's belonging to each of them. This does not prevent the conclusion, that for non-vanishing $\pi'-\pi''$

$$\Pi_{\pi'\pi''}=\frac{M_{\pi'\pi''}}{\pi''-\pi'} \tag{5}$$

for every $I, J, \cdots$, and in consequence, by the second Eq. (4), $M_{\pi'\pi''}=0$ or

$$(\pi''-\pi')^2=-1. \tag{6}$$

Thus the π are purely imaginary (save perhaps for a common additive constant, which may be shown actually to disappear).

In Dirac's theory of the electron this difficulty does not interfere, because his commutation-rules are of an entirely different ("anti-commutative") character. Moreover, there is no *intrinsic* magnetic and electric momentum at all. Different authors already have attempted to introduce one, as has Breit,[4] on the basis of experimental evidence. If one does not insist on the scheme (1), this may be realized without difficulty, since the Dirac-current can be decomposed in a well-known manner into a convective and a polarization parts. But now the author met with the same necessity from classical considerations[5] culminating in a system of Poisson-brackets for the momentum-components to be converted into commutation-rules. These Poisson-brackets are of the form (1) and by no means of an "anti-commutative" character, and so the question arose: Are there hermitian matrices, which fulfill the relations (1) or, in mathematical terms, are there unitary representations of the Lorentz-group?

At first sight the conclusion (4)–(5), which forbids them, looks quite stringent. There is only one way to escape it: The division by the factor $\pi''-\pi'$ is impossible, if the π-values are continuous (because then the left-hand sides of (4) become integrals with δ-functions) and this seems almost absurd. One might not expect, by "reasons of four-dimensional symmetry," the eigenvalues of the Π to be different from those of the M (we shall so term henceforth the Π_k, M_k, $k=1, 2, 3$, for brevity), which according to the first triple-set of Eqs. (1) are always discontinuous. But really one can only conclude that the Π-components among themselves and the M-components among themselves must have equal eigenvalues, because they can be completely exchanged by a rotation of the coordinate-system. A Lorentz-transformation never completely exchanges an M and a Π; either the transformation reproduces them or it yields a linear combination of two non-commuting ones. Now the eigenvalues of non-commuting matrices are not additive, and so the eigenvalues of these linear combinations need not be of a mixed character. The same thing comes in play at rotations, where it prevents the continuous alteration of quantized observables. There is another question, whether the sum of a matrix with a discontinuous spectrum and a second matrix with a continuous one may have discontinuous eigenvalues. A similar question arises in connection with the second triple-set of Eqs. (1), where two continuous-valued Π-components by mere multiplication and subtraction have to yield the discrete-valued M-components. But there is an elementary example of a matrix with a continuous spectrum, which even by simple multiplication with itself gets a discontinuous one. Imagine a particle reflected along a straight line between two rigid walls, represented by a potential-hole of suitable steepness, a "reflection-oscillator," so to say. It is just the case assumed to be realized, in first approximation, by the electrons inside a metallic conductor. The momentum (p) of such an oscillator, due to Heisenberg's uncertainty principle, must have a continuity of measurable values, its coordinate-values being bounded. Indeed the correspondence-principle shows that the "reflection-oscillator" will have a fully developed series-spectrum, in spite of its seemingly uniform motion. At the same time, evidently, its energy-spectrum is quantized, and so p^2 will have a discrete spectrum, whereas p has a continuous one.

After all, there is even a strong reason to guess that the eigenvalues of the Π may not be exhausted by their known finite representations. Confining oneself to the M one has $\mathbf{M}^2=M_1^2+M_2^2+M_3^2$ as a quantity which commutes with all the M_k, $k=1, 2, 3$. Therefore every value of $\mathbf{M}^2$ yields an independent representation of the M_k, which is necessarily finite, as $\mathbf{M}^2$ is definite. But $\mathbf{M}^2$ is no longer commutable with the Π_k-components, and so it may not serve to reduce the M, Π-system as a whole. However, there are now two invariants, viz. $\mathbf{M}^2-\mathbf{\Pi}^2$ and the scalar product $\mathbf{M\Pi}$, which commute with all M_k and Π_k, and these now are indefinite. So

[4] G. Breit, Phys. Rev. **72**, 984 (1947).

[5] W. Wessel, FIAT Report No. 1131, henceforth referred to as l.c. Appeared also Zeits. f. Naturforschung **1**, 622 (1946), with different numeration of formulas.

TABLE I. Commutation table.

	I	K	ι_1	ι_2	ι_3	ι_4	κ_1	κ_2	κ_3	κ_4	M_1	M_2	M_3	Π_1	Π_2	Π_3
I	0	0	0	0	0	0	0	0	0	0	0	0	0	0	0	0
K	0	0	κ_1	κ_2	κ_3	κ_4	ι_1	ι_2	ι_3	ι_4	0	0	0	0	0	0
ι_1	0	$-\kappa_1$	0	$-M_3$	M_2	$-\Pi_1$	$-K$	0	0	0	0	ι_3	$-\iota_2$	$-\iota_4$	0	0
ι_2	0	$-\kappa_2$	M_3	0	$-M_1$	$-\Pi_2$	0	$-K$	0	0	$-\iota_3$	0	ι_1	0	$-\iota_4$	0
ι_3	0	$-\kappa_3$	$-M_2$	M_1	0	$-\Pi_3$	0	0	$-K$	0	ι_2	$-\iota_1$	0	0	0	$-\iota_4$
ι_4	0	$-\kappa_4$	Π_1	Π_2	Π_3	0	0	0	0	K	0	0	0	$-\iota_1$	$-\iota_2$	$-\iota_3$
κ_1	0	$-\iota_1$	K	0	0	0	0	M_3	$-M_2$	Π_1	0	κ_3	$-\kappa_2$	$-\kappa_4$	0	0
κ_2	0	$-\iota_2$	0	K	0	0	$-M_3$	0	M_1	Π_2	$-\kappa_3$	0	κ_1	0	$-\kappa_4$	0
κ_3	0	$-\iota_3$	0	0	K	0	M_2	$-M_1$	0	Π_3	κ_2	$-\kappa_1$	0	0	0	$-\kappa_4$
κ_4	0	$-\iota_4$	0	0	0	$-K$	$-\Pi_1$	$-\Pi_2$	$-\Pi_3$	0	0	0	0	$-\kappa_1$	$-\kappa_2$	$-\kappa_3$
M_1	0	0	0	ι_3	$-\iota_2$	0	0	κ_3	$-\kappa_2$	0	0	M_3	$-M_2$	0	Π_3	$-\Pi_2$
M_2	0	0	$-\iota_3$	0	ι_1	0	$-\kappa_3$	0	κ_1	0	$-M_3$	0	M_1	$-\Pi_3$	0	Π_1
M_3	0	0	ι_2	$-\iota_1$	0	0	κ_2	$-\kappa_1$	0	0	M_2	$-M_1$	0	Π_2	$-\Pi_1$	0
Π_1	0	0	ι_4	0	0	ι_1	κ_4	0	0	κ_1	0	Π_3	$-\Pi_2$	0	$-M_3$	M_2
Π_2	0	0	0	ι_4	0	ι_2	0	κ_4	0	κ_2	$-\Pi_3$	0	Π_1	M_3	0	$-M_1$
Π_3	0	0	0	0	ι_4	ι_3	0	0	ι_4	κ_3	Π_2	$-\Pi_1$	0	$-M_2$	M_1	0

they may yield non-combining systems, being finite for themselves, but not limiting the Π_k- and M_k-values.

Indeed there are such representations, but one may not easily find them proceeding from the system (1), because the continuous character of the Π is unfavorable to their diagonal transformation, extending as it does also to the invariants. On the other hand reduction goes almost by itself, if one introduces the group of Eqs. (1) as a subgroup into the system the author arrived at in the above mentioned paper. One has only to interpret the Poisson-brackets as commutation-relations.

We shall not begin here with the somewhat remote starting point of our former considerations, but rather at once with the complete scheme of commutation-rules. Our electron, in addition to its magnetic momentum, will have a spin-angular momentum and a velocity to be discerned, following Dirac, from the velocity of its center of gravity. Let ι be a four-vector proportional to the four-velocity, but not bounded by the condition $\iota_\lambda \iota^\lambda = -1$ ($\lambda = 1 \cdots 4$), and similarly let κ be a vector, whose spacial components are proportional to the spin-angular momentum, also unbounded and both dimensionless. Further let I and K be two invariants connected with the invariants of M, Π by

$$\mathrm{I}^2 - \mathrm{K}^2 = \mathbf{M}^2 - \mathbf{\Pi}^2, \quad \mathrm{IK} = \tfrac{1}{2}(\mathbf{M\Pi} + \mathbf{\Pi M}). \tag{7}$$

Then there exists a group-like system of commutation-rules between these quantities of such a nature that a combination of two of them always gives a third one, and a Lorentz-transformation of all the components reproduces the whole system. The invariance is proved[5] for the Poisson-brackets and persists in the re-interpretation. For convenience, the system will be given in the form of a "group-table," the rows labeled with the first factor (a) and the columns with the second factor (b) of the operation

$$[ab] = ab - ba \tag{8}$$

and the value of $[ab]/i$ inserted at their crossing. (See Table I.)

The system is not a group in the mathematical sense (for lack of a unity element), being not even a ring (for failure of associativity), but one may speak quite well of subgroups, central, etc. The invariant 1 is the "central" and in consequence will split up the representation generally. Secondly, of course, one will choose one of the M-components, M_3 say, as a diagonal matrix, being certain that its eigenvalues will be discrete ones. In the third place, limiting oneself to the "subgroup" of Eqs. (1) and (2) expressed at the right lower corner of the present scheme, one might think of the introduction of K and Π_3 as quantities commuting with both I and M_3 and with one another, but by the reasons just mentioned this is impracticable. Going through the "group-table" one now sees that together with I, K, and Π_3 also ι_3, ι_4 and κ_3, κ_4 commute with M_3. None of them commutes with K, so that this quantity may be dropped. Left with I, M_3, ι_3, ι_4, κ_3, κ_4, one finds that they form two sets of mutually commuting elements, namely I, M_3, ι_3, κ_4 and I, M_3, κ_3, ι_4. Thus, the elements of one of these sets may be brought simultaneously in diagonal form and their eigenvalues may be used to label the rows and columns of all matrices. It will be shown that ι_3 and κ_4 have continuous spectra too, whereas κ_3 and ι_4 have discrete ones. Therefore, we will have a I, M_3, κ_3, ι_4-representation or, as I commutes with all elements, a set of non-combining M_3, κ_3, ι_4 representations.

At this point it seems no longer possible to avoid introducing the spinors of the previous paper. These spinors, although otherwise disliked for their entangled connection with world-vectors, are here in their proper place. They express the sixteen elements through eight real quantities (four complex spinors) in either bilinear or quadratic homogeneous forms, which exhibit at once their spectral character. The reduction of the elements to half their number involves a set of supplementary

conditions studied explicitly l.c.,[5] but unimportant for the present purpose except for its compatibility with the scheme of Table I.[6] To be brief, we shall now refer repeatedly to the foregoing paper and, concerning the spinor-calculus, to the paper of Laporte and Uhlenbeck.[7] Replace the factor Γ of l.c. (5.10) by i and the round brackets by the square brackets of formula (8). They read then,

$$[\psi_\mu \chi^\nu]=\delta_\mu{}^\nu, \quad [\psi_{\dot\mu}\chi^{\dot\nu}]=-\delta_{\dot\mu}{}^{\dot\nu} \tag{9}$$

and are compatible in this form. Indeed, if an ordinary spinor ψ_μ is expressed in terms of two real quantities, say, a, b, in the form $\psi_\mu=a+ib$, its $\psi_{\dot\mu}$ is obtained by change of i into $-i$. With a, b as Hermitian matrices, ψ will transform correctly if one also understands $\psi_{\dot\mu}$ as $a-ib$. In other words, denoting as usual by a $\dagger$ the process of changing the rows and columns of a matrix and substituting all their i by $-i$, the matrix $\psi_{\dot\mu}$ is to be considered as $\psi_\mu{}^\dagger$, and so

$$[\psi_\mu{}^\dagger \chi^{\nu\dagger}]=[\chi^\nu \psi_\mu]^\dagger=-\delta_\mu{}^\nu. \tag{10}$$

Introduce now the real and imaginary parts in the form

$$\begin{aligned} p_1&=\frac{1}{\sqrt2}(\psi_1+\psi_{\dot1}), \quad & q_1&=\frac{1}{i\sqrt2}(\chi^1-\chi^{\dot1}),\\ p_2&=\frac{1}{i\sqrt2}(\psi_1-\psi_{\dot1}), \quad & q_2&=\frac{1}{\sqrt2}(\chi^1+\chi^{\dot1}). \end{aligned} \tag{11}$$

Then by (9) the p, q are canonical in the quantum-mechanical sense:

$$[p_m q_n]=\frac{1}{i}\delta_{mn}, \quad m,n=1,2. \tag{12}$$

Having exhausted only the spinors with the index 1, a second system p_3, p_4, q_3, q_4 will be introduced, also transforming the spinors with the index 2. Note that index 4 does not play a singular role, the p_k, q_k not being the components of a world-vector. With these p_k, q_k, $k=1\cdots4$, the I, K, M, Π, ι, κ are now to be expressed as the I, J, $\mathfrak{M}$, $\mathfrak{P}$, j, k of the former paper, Greek type indicating dimensionless quantities. For instance M_3 takes the form (note $\psi^1=\psi_2$, $\psi^2=-\psi_1$)

$$\begin{aligned} \mathrm{M}_3=\mathrm{M}_{12}&=-\frac{1}{2i}(m_{12}-m_{\dot1\dot2}), && \text{l.c. (4.11)}\\ &=-\tfrac12(\psi_1\chi^1-\psi_2\chi^2+\psi_{\dot1}\chi^{\dot1}-\psi_{\dot2}\chi^{\dot2}), && \text{l.c. (4.7)}\\ &=-\tfrac12(p_1q_2-p_2q_1)+\tfrac12(p_3q_4-p_4q_3). && (13) \end{aligned}$$

[6] Beside the eight conditions indicated l.c. there is a supernumerary one, the number of independent elements being seven, as has been shown by W. Kofink, Ann. d. Physik (V) **38**, 421 (1940). Indeed Eq. (3.26) resp. (4.26) l.c. has a dual one to be formed by jM^* instead of jM.

[7] O. Laporte and G. E. Uhlenbeck, Phys. Rev. **37**, 1380, 1552 (1931).

TABLE II.

n_1	n_3	n_2	n_4
ι	0	ι	0
$\iota-1$	1	$\iota-1$	1
$\iota-2$	2	$\iota-2$	2
.	.	.	.
.	.	.	.
.	.	.	.
0	ι	0	ι

Having the form of angular momentum components, the brackets may be brought into quadratic forms by the contact-transformation

$$\begin{aligned} p_1&=\frac{1}{\sqrt2}(\bar p_1-\bar q_2), \quad & q_1&=\frac{1}{\sqrt2}(\bar p_2+\bar q_1),\\ p_2&=\frac{1}{\sqrt2}(\bar p_2-\bar q_1), \quad & q_2&=\frac{1}{\sqrt2}(\bar p_1+\bar q_2),\\ &\text{etc.,} \end{aligned} \tag{14}$$

generated by the function

$$\begin{aligned} &S(q_1\cdots q_4, \bar p_1\cdots\bar p_4)\\ &\quad=\sqrt2\sum_{k=1}^{4}\bar p_k q_k-\bar p_1\bar p_2-\bar p_3\bar p_4-q_1q_2-q_3q_4, \end{aligned} \tag{15}$$

in the well-known manner ($p_k=\partial S/\partial q_k$, $\bar q_k=\partial S/\partial \bar p_k$). So we have

$$\begin{aligned} \mathrm{M}_3=&-\tfrac14(\bar p_1{}^2+\bar q_1{}^2)+\tfrac14(\bar p_2{}^2+\bar q_2{}^2)\\ &+\tfrac14(\bar p_3{}^2+\bar q_3{}^2)-\tfrac14(\bar p_4{}^2+\bar q_4{}^2), \end{aligned} \tag{16}$$

and it is seen at once that the eigenvalues of M_3 are all positive and negative integral and (note the factor $\frac14$) half-odd-integral numbers. Owing to the change of signs there is no "zero-point" term, as of course must be expected from the first triple-set of (1). Likewise the other three representative quantities I, κ_3, and ι_4 just amount to quadratic forms. Writing for abbreviation

$$H_k=\tfrac12(\bar p_k{}^2+\bar q_k{}^2), \quad k=1,2,3,4, \tag{17}$$

one obtains ($\iota^4=-\iota_4$)

$$\begin{aligned} \mathrm{M}_3&=\tfrac12(-H_1+H_2+H_3-H_4),\\ \mathrm{I}&=\tfrac12(H_1-H_2+H_3-H_4),\\ \kappa_3&=\tfrac12(H_1+H_2-H_3-H_4),\\ \iota^4&=\tfrac12(H_1+H_2+H_3+H_4). \end{aligned} \tag{18}$$

The fourth quantity is positive definite, which will be of both mathematical and physical importance. The other three exhaust the possibilities of two negative signs. Obviously all have discrete eigenvalues, and by reasons of rotational transformability M_1, M_2 and κ_1, κ_2 will be discrete-valued too.

Correspondingly, the Π_3, K, ι_3, κ^4 are continuous, re-establishing in this way the "relativistic symmetry." The quantity $\kappa^4=-\kappa_4$ appears immediately, without

the preceding transformation, in the form

$$\kappa^4=\tfrac{1}{4}\sum_{k=1}^{4}(p_k^2-q_k^2), \tag{19}$$

which evidently has no discrete eigenvalues, the term $-q^2$ corresponding to a potential-peak instead of a potential-hole. The invariant K and the component Π_3 become

$$\left.\begin{matrix}\mathrm{K}\\ \Pi_3\end{matrix}\right\}=\pm\tfrac{1}{2}(\bar{p}_1\bar{p}_2-\bar{q}_1\bar{q}_2)+(\bar{p}_3\bar{p}_4-\bar{q}_3\bar{q}_4), \tag{20}$$

and a transformation to principal axes shows that they are also composed of terms of the form p^2-q^2. The component $\iota_3=-\frac{1}{2}(\bar{p}_1\bar{q}_2+\bar{p}_2\bar{q}_1)+(\bar{p}_3\bar{q}_4+\bar{p}_4\bar{q}_3)$ is not so easily transformed. But

$$\iota_2=-\tfrac{1}{2}(\bar{p}_1\bar{p}_4-\bar{q}_1\bar{q}_4)+\tfrac{1}{2}(\bar{p}_2\bar{p}_3-\bar{q}_2\bar{q}_3) \tag{21}$$

has again the form (20), and from this the continuous character of the ι_1- and ι_3-components may be inferred.

Let us introduce the eigenvalues explicitly putting

$$H_k=n_k+\tfrac{1}{2},\quad n_k=0,1,2,\cdots,\quad k=1,2,3,4. \tag{22}$$

As the $\mathrm{M}_3\cdots\iota^4$ shall be used as indices themselves, we shall drop their subscripts, writing simply† μ, κ for M_3, κ_3 and, to spare the "zero-point" term, $\iota=\iota^4-1$. So we have from (18)

$$\begin{aligned}\mu&=\tfrac{1}{2}(-n_1+n_2+n_3-n_4),\\ \mathrm{I}&=\tfrac{1}{2}(n_1-n_2+n_3-n_4),\\ \kappa&=\tfrac{1}{2}(n_1+n_2-n_3-n_4),\\ \iota&=\tfrac{1}{2}(n_1+n_2+n_3+n_4).\end{aligned} \tag{23}$$

Obviously the eigenvalues of I are all integral and half-odd-integral numbers, both positive and negative including zero. Every I by its character, integer or not, determines a set of ι, κ, μ of the same character. Furthermore, every given value of ι admits only a finite number of combinations of n_1, n_2, n_3, n_4. Thus the definiteness of ι^4 enables one to unfold every representation step by step. The value of ι may be written according to (23) in the forms $\iota=n_2+n_4+\mathrm{I}$ or $\iota=n_1+n_3-\mathrm{I}$, depending on the sign of I, showing that always

$$\iota\geqq|\mathrm{I}|. \tag{24}$$

For a more detailed study we may confine ourselves to the most simple case

$$\mathrm{I}=0. \tag{25}$$

Hence, $n_1+n_3=n_2+n_4$ and $\iota=n_1+n_3$, for instance. Given the value of ι one has the possible arrangements shown in Table II. Every left-side arrangement can be combined with every right-side one, there being $(\iota+1)^2$ combinations. Thus ι^4 is $(\iota+1)^2$ or $(\iota^4)^2$-fold degenerate.

† In the forthcoming paper Zeits. f. Naturforschung **4a** the letter κ denotes the maximum value of M_3.

Eliminating n_3 and n_4, for instance, one gets from (23)

$$\kappa=n_1+n_2-\iota,\quad \mu=-n_1+n_2. \tag{26}$$

Accordingly κ will have its maximum value if n_1 and n_2 have theirs (and inversely), or

$$-\iota\leqq\kappa\leqq\iota \tag{27}$$

according to Table II. The terminal values are realizable just once, with $\mu=0$. Furthermore, still following Table II, one sees that $\kappa=\iota-1$ and $\kappa=1-\iota$ are both realizable twofold with $\mu=-1$, 1, or $\kappa=\iota-2$ and $\kappa=2-\iota$ threefold with $\mu=-2$, 0, 2, etc., down to $\kappa=0$ with $\mu=-\iota$, $-\iota+2$, $-\iota+4$, $\cdots$, $\iota-2$, ι, so that the μ-values attached to a value of κ may be written

$$|\kappa|-\iota,\ |\kappa|-\iota+2,\ \cdots,\ \iota-|\kappa|-2,\ \iota-|\kappa|. \tag{28}$$

Briefly stated: a multiplication of two matrices a and b in the ι, κ, μ-representation will be accomplished by the process

$$(\iota'\kappa'\mu'|ab|\iota''\kappa''\mu'')=\sum_{0}^{\infty}{}^{\iota}\sum_{-\iota}^{\iota}{}^{\kappa}\sum_{|\kappa|-\iota}^{\iota-|\kappa|}{}^{\mu}(2)\times(\iota'\kappa'\mu'|a|\iota\kappa\mu)(\iota\kappa\mu|b|\iota''\kappa''\mu''), \tag{29}$$

the index (2) indicating steps of two units in the index. Similarly in the case $\mathrm{I}=\frac{1}{2}$:

$$\sum_{n_1-n_2+n_3-n_4=1}=\sum_{\frac{1}{2}}^{\infty}{}^{\iota}\left\{\sum_{\frac{1}{2}}^{\iota}{}^{\kappa}\sum_{-\iota+\kappa-\frac{1}{2}}^{\iota-\kappa-\frac{1}{2}}{}^{\mu}(2)+\sum_{-\frac{1}{2}}^{-\iota}{}^{\kappa}\sum_{-\iota-\kappa+\frac{1}{2}}^{\iota+\kappa+\frac{1}{2}}{}^{\mu}(2)\right\}. \tag{30}$$

In the preceding expressions exchange of κ and μ is possible. To write down the matrices we make the usual transformation

$$\bar{p}=\frac{1}{\sqrt{2}}(P+Q),\quad \bar{q}=\frac{i}{\sqrt{2}}(P-Q), \tag{31}$$

for every k. Any H, formula (22), with eigenvalues m, n will then be made diagonal by

$$P_{mn}=(m+1)^{\frac{1}{2}}\delta_{m+1,n},\quad Q_{mn}=(m)^{\frac{1}{2}}\delta_{m-1,n}, \tag{32}$$

being different H_k to be distinguished by different m_k, n_k. For convenience we shall give the six representative matrices explicitly:

$$\begin{aligned}\mathrm{M}_1&=\tfrac{1}{2}(-P_1Q_3-P_3Q_1+P_2Q_4+P_4Q_2),\\ \mathrm{M}_2&=(i/2)(P_1Q_3-P_3Q_1+P_2Q_4-P_4Q_2),\\ \mathrm{M}_3&=\tfrac{1}{2}(-P_1Q_1+P_2Q_2+P_3Q_3-P_4Q_4).\\ \Pi_1&=-\tfrac{1}{2}(P_1P_4+Q_1Q_4+P_2P_3+Q_2Q_3),\\ \Pi_2&=(i/2)(P_1P_4-Q_1Q_4-P_2P_3+Q_2Q_3),\\ \Pi_3&=-\tfrac{1}{2}(P_1P_2+Q_1Q_2-P_3P_4-Q_3Q_4).\end{aligned} \tag{33}$$

Note that $P^\dagger=Q$, $Q^\dagger=P$, guaranteeing the hermitian character of the M, II. The arrangement of the factors is arbitrary.

Inserting the P, Q from (32) one has for instance

$$\Pi_1=-\tfrac{1}{2}\{[(m_1+1)(m_4+1)]^{\frac{1}{2}}\delta_{m_1+1,n_1}\delta_{m_2n_2}\times\delta_{m_3n_3}\delta_{m_4+1,n_4}+\cdots\}, \tag{34}$$

TABLE III.

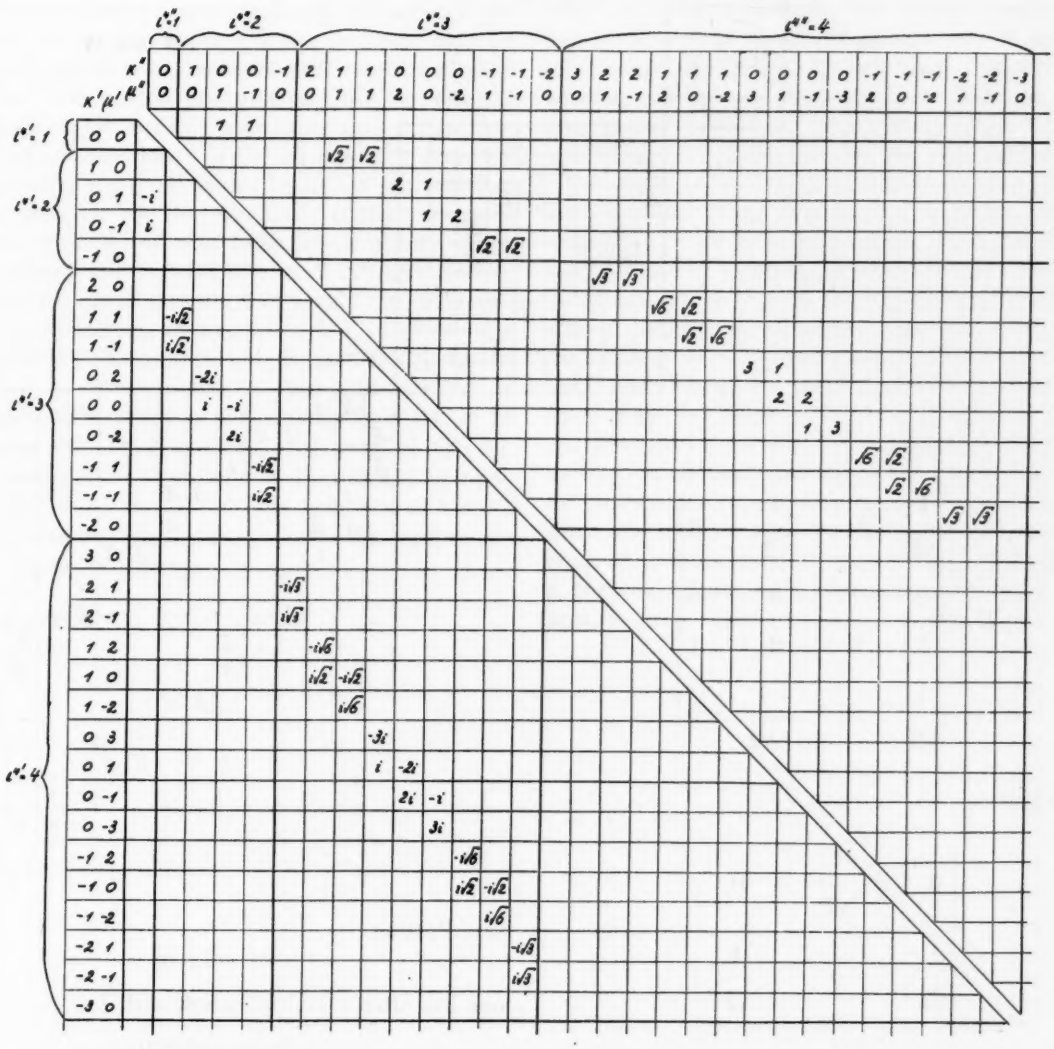

the . . . indicating three similar terms. Here the m_k, n_k are to be substituted by the I, ι, κ, μ according to (23). Inverting these formulas we have, putting I=0 and indicating m and n by one and two accents respectively:

$$\begin{aligned} m_1&=\tfrac{1}{2}(\iota'+\kappa'-\mu'), & m_2&=\tfrac{1}{2}(\iota'+\kappa'+\mu'),\\ m_3&=\tfrac{1}{2}(\iota'-\kappa'+\mu'), & m_4&=\tfrac{1}{2}(\iota'-\kappa'-\mu'),\\ n_1&=\tfrac{1}{2}(\iota''+\kappa''-\mu''), & n_2&=\tfrac{1}{2}(\iota''+\kappa''+\mu''),\\ n_3&=\tfrac{1}{2}(\iota''-\kappa''+\mu''), & n_4&=\tfrac{1}{2}(\iota''-\kappa''-\mu''). \end{aligned} \tag{35}$$

The rather extended terms are reduced to half their number of factors by the commutability of Π_1 and κ (see Table I), involving κ-diagonal character of Π_1 at least for all non-vanishing values of κ, and actually throughout. Thus Π_1 attains the form

$$\Pi_1=-\tfrac{1}{4}\delta_{\kappa'\kappa''}\{[(\iota'+\kappa'-\mu'+2)(\iota'-\kappa'-\mu'+2)]^{\frac{1}{2}} \times\delta_{\iota'-\mu'+2,\iota''-\mu''}\delta_{\iota'+\mu',\iota''+\mu''}+\cdots\} \tag{36}$$

and may easily be written down row by row, the root being constant in every row. The structure of the Π-matrices will become clear from Table III, where the upper triangle refers to $-2\cdot\Pi_1$ and the lower to $-2\cdot\Pi_2$, the missing triangles being the Hermitian complements. The ι-, κ- and μ-matrices, of course, are immediately given by either the head or the left margin of the Π-representations. A complete representation may now be gained simply from Table I, if one disposes of Π_3 or one further M-component. There is some interest in considering M_1, for instance. As it commutes with ι, only its quadratic submatrices are different from zero. Table IV gives $2\cdot M_1$ with the same meaning of rows and columns as Table III. Evidently the M-submatrices are further reducible, finite representations of the rotation group (as they are) being characterized by matrices of rank $2j+1$, $j=0, 1, 2, \cdots$ instead of $(\iota+1)^2$, $\iota=0, 1, 2, \cdots$. Thus e.g. $(1\kappa'\mu'|M_1|1\kappa''\mu'')$ will be decomposed by a unitary transformation $U^\dagger\cdot M_1 U$

TABLE IV.

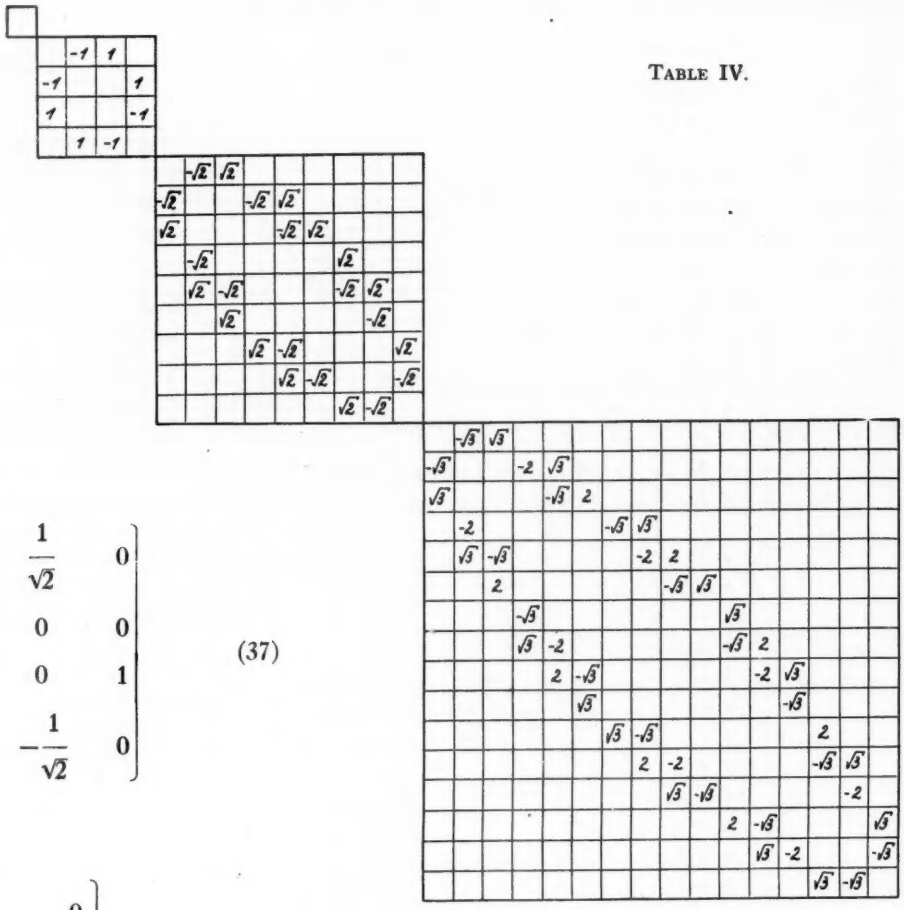

with

$$U=\begin{pmatrix} \frac{1}{\sqrt{2}} & 0 & \frac{1}{\sqrt{2}} & 0 \\ 0 & -1 & 0 & 0 \\ 0 & 0 & 0 & 1 \\ \frac{1}{\sqrt{2}} & 0 & -\frac{1}{\sqrt{2}} & 0 \end{pmatrix} \tag{37}$$

into (0) and

$$\begin{pmatrix} 0 & \frac{1}{\sqrt{2}} & 0 \\ \frac{1}{\sqrt{2}} & 0 & \frac{1}{\sqrt{2}} \\ 0 & \frac{1}{\sqrt{2}} & 0 \end{pmatrix}.$$

By the same transformation $(1\kappa'\mu'|\mathrm{M}_3|1\kappa''\mu'')$ goes over into (0), (1 0−1). In this way every submatrix can be decomposed again into a step-matrix, labeled by μ and its maximum value. Yet for the present purpose it seems more interesting to have evidence of the connection between μ and κ, and so this transformation may first be set apart. Physically it may appear strange to find magnetic and angular momenta combined in the way indicated by these matrices, but in the case $\mathrm{I}=\frac{1}{2}$ one will have $\kappa=(\frac{1}{2}, -\frac{1}{2})$ together with $\mu=(-\frac{1}{2}, \frac{1}{2})$, and this will be correct for a negative electron.

Given the representations of the Lorentz-transformation, explicit transformation formulas may easily be worked out. Let us begin with an infinitesimal transformation (ϵ) to a system of reference moving in direction 1,

$$\mathrm{M}_3'=U^{\dagger}\mathrm{M}_3U=\mathrm{M}_3+\epsilon\Pi_2, \tag{38}$$

say. Putting

$$U=1+\epsilon u \tag{39}$$

one has after a multiplication with $U^{\dagger}$

$$\mathrm{M}_3u=u\mathrm{M}_3+\Pi_2. \tag{40}$$

According to Table I this equation will be obeyed by

$$u=-i\Pi_1. \tag{41}$$

A finite transformation with $\varphi=N\epsilon$ will now be effectuated by an N-fold repetition of this process. So we have at the limit $\epsilon=0$, $N=\infty$:

$$U=\lim_{N=\infty}\left(1-i\frac{\varphi}{N}\Pi_1\right)^N=\exp(-i\varphi\Pi_1). \tag{42}$$

Similarly a rotation will be obtained through M instead of Π. The exponential matrices being infinite (and actually containing an infinite number of elements in every row and column) will transform an "expansor" $A\mathrm{I}\iota\kappa\mu$ of Dirac's type according to

$$A'=\exp(-i\Pi)A \tag{43}$$

in a unitary way.

At present we must restrict ourselves to these mathematical preliminaries, as every application in the sense

proposed l.c. will need rather laborious work. As is well known Dirac's theory agrees excellently with experience, and every attempt to improve it can be tested only by very subtle effects, e.g., the term-shift recently studied by Bethe,[8] and related phenomena. Only two general advantages of the present apparatus may be emphasized. First, as mentioned in the introductory remarks, the continuous spectrum shown by half of our matrices seems to account for the essentially continuous, non-quantum character of the radiation-damping-process and its natural line-breadth in a more intrinsic manner than does the usual procedure of Hohlraum quantization. It is satisfactory, that κ_k, $k=1, 2, 3$, corresponding to the spin-angular momentum, is quantized, whereas ι_k, $k=1, 2, 3$, corresponding to the four-velocity, is continuous. Very probably the ordinary velocity, to be represented by the Hermitian real part of $(\iota^4)^{-1}\iota_k$, $k=1, 2, 3$ will still be continuous. This should be more comprehensible than the puzzling behavior of Dirac's velocity matrices, which always have the eigenvalues $\pm c$ (=velocity of light).

[8] H. Bethe, Phys. Rev. **72**, 339 (1947).

Moreover our matrix I allows one to set up Hamilton-functions (wave-equations) with definite energy. In the rest-system of the center of gravity ($p=0$) the energy will have the form $E=(u^4)^{-1}m_0c^2$ (m_0=rest-mass, u^4=4-component of four-velocity). Now, in Dirac's theory one is provided with two operators to be connected with the mass, both having eigenvalues $+1$ and -1 and non-commuting with the Hamilton-operator as a whole. Thus, E can be positive of negative, and transitions may occur in external fields. Here we have also two invariants, I and K, of which I commutes with ι^4. Thus $E=(\iota^4)^{-1}m_0c^2$ with $m_0=m_0(\mathrm{I})$ will be hermitian and of correct transformation character. Owing to the definiteness of ι^4, however, any positive even function $m_0(\mathrm{I})$ will now always yield a positive E. With odd m_0 there may be $E>0$ or $E<0$; yet by the exclusive character of I there will be no transitions in any case, as long as m_0 does not depend on K. Of course this simple example is only an informative one and does not solve the difficult mass-problem. Indeed the physical point of view arrived at in the last section of the former paper would make one expect a term with $(\iota^4)^{-1}(\mathrm{I}^2+\mathrm{K}^2)^{\frac{1}{2}}$ rather than $(\iota^4)^{-1}$.

PHYSICAL REVIEW VOLUME 76, NUMBER 10 NOVEMBER 15, 1949

Sound Propagation in Chemically Active Media*

LEONARD LIEBERMANN
University of California, Marine Physical Laboratory, San Diego, California
(Received August 8, 1949)

A fluid containing chemically active ingredients in equilibrium may exhibit unique physical properties: the compressibility may depend on the rate of compression; similarly the specific heat may depend on the rate of temperature change. This rate dependence arises from the finite reaction rate of the chemical components. One phenomenon resulting from this behavior is the anomalous absorption and dispersion of sound. Expressions are given relating the chemical reaction rate, the equilibrium constant, and other chemical parameters, to the acoustical properties of the fluid. As an illustration of these relationships the unusual sound absorption in aqueous $MgSO_4$ solution is discussed. Calculation shows that the partial compressibility associated with the ionization process is of the correct magnitude to explain the observed absorption.

I. INTRODUCTION

A FLUID containing chemically active components may possess unusual physical properties which are not commonly encountered in ordinary fluids. One of these unique properties may be illustrated by the following experiment: Suppose a container is filled with a substance containing chemically active ingredients in equilibrium; the chemical reaction must be one whose equilibrium constant is pressure dependent. Means are provided for observing the instantaneous change in volume with pressure and hence of measuring the coefficient of compressibility. Such an experiment will yield the unusual result that the coefficient of compressibility depends on the *rate* of compression (or dilatation).

The explanation for this result is fairly obvious: the chemical reaction contributes in part to the volume change, but its contribution depends on how far the reaction has proceeded toward equilibrium and hence on the rate of compression. Furthermore, it is entirely possible for the compressibility measurement to be performed in a time too short for the chemical reaction to participate, in which case the measured compressibility will be only that of the reactants considered as inert. Hence, a chemically active fluid may be said to have two compressibilities: a static, or equilibrium compressibility, and a dynamic compressibility whose value depends on the compression rate and which approaches a limiting value at high rates of compression.

In an analogous manner a chemically active substance whose equilibrium is temperature dependent may possess dynamic and static specific heats. The static specific heat of the substance is measured after equilibrium is attained and is identified with the value obtained in conventional measurements. The dynamic specific heat will depend on the rate of change of temperature and will approach a limiting value at high rates of change. The difference between the limiting value and the static value is simply the partial specific heat of the chemical reaction.

An acoustic wave is a familiar example of a process in which rapid compressions and temperature changes occur. In acoustics then, the distinction between the static and dynamic properties which exists in a chemically active medium may be expected to become extremely important. Long ago, Albert Einstein[1] interpreted the excessive sound absorption occurring in a partially dissociated gas such as nitrogen tetraoxide, as a result of the dissociation reaction. It may also be expected that chemical reactions occurring in liquids might also influence the propagation of sound waves. Particularly interesting, are the possibilities for determining the reaction rates of rapid chemical processes from the study of acoustic behavior.

The ensuing sections deal with relationships between chemical and acoustic properties, which will be useful in studies of this kind. As an illustration of the application of these relationships, a calculation is made of the anomalous sound absorption in an aqueous $MgSO_4$ solution which is compared with observation.

II. PARTIAL COMPRESSIBILITY AND SPECIFIC HEAT OF A CHEMICALLY ACTIVE SUBSTANCE

A. Static Considerations

In order to obtain the dynamic compressibility and specific heats it is convenient to consider first static values. These may be obtained with the aid of the well-known thermodynamic relationships,[2]

$$(\partial \Delta F/\partial P)_T = \Delta V, \tag{1a}$$

$$(\partial \Delta F/\partial T)_P = -\Delta S. \tag{1b}$$

The first expression relates the isothermal change in free energy, ΔF, to the molar volume change, ΔV; the second relates the isobaric change in free energy to the molar entropy change, ΔS. From these two expressions the van't Hoff equation and its isothermal analog

$$(\partial \ln K/\partial T)_P = \Delta H/RT^2, \tag{2a}$$

$$(\partial \ln K/\partial P)_T = -\Delta V/RT \tag{2b}$$

* This work represents one of the results of research carried out under contract with the Bureau of Ships, Navy Department.

[1] Albert Einstein, Sitz. Berliner Akad., 380 (1920).
[2] For example, see: Gilbert N. Lewis and Merle Randall, *Thermodynamics* (McGraw-Hill Book Company, Inc., New York, 1923).

are obtained, where ΔH is the molal heat content, and K the equilibrium constant of the chemical reaction.

Compressibility is defined as $-\partial V/V\partial P$. This definition may also be written as

$$\beta_0' \equiv -(1/V)(\partial V/\partial \ln K)_T(\partial \ln K/\partial P)_T, \quad (3)$$

where β_0' will be defined as the static isothermal *partial* compressibility. It follows then from Eq. (2b) that

$$\beta_0' = (\partial V/\partial \ln K)\Delta V/VRT. \quad (4)$$

The partial compressibility can be reduced to a less general form depending on the nature of the chemical reaction: Consider the ideal reversible reaction $A \rightleftarrows B$; for example, a substance possessing two states (such a model has been proposed for both the shear and bulk viscosities of liquids). The equilibrium constant, K, is then, $N/(1-N)$, where N is the molal fraction in the excited state. From Eq. (4) we have for this case

$$\beta_0' = (dV/dN)(1-N)N\Delta V/VRT.$$

But ΔV is by definition, dV/dN. Hence,

$$\beta_0' = (V/RT)(\Delta V/V)^2 N(1-N). \quad (5a)$$

Or, since $\Delta F = -RT \ln K$, the compressibility may also be written as

$$\beta_0' = (V/2RT)(\Delta V/V)^2/(1+\cosh \Delta F/RT). \quad (5b)$$

Another simple reaction is $AB \rightleftarrows A+B$; for example, a partially dissociated gas or liquid. In this case, ideally

$$\beta_0' = (V/RT)(\Delta V/V)^2 N(1-N)/(2-N). \quad (6)$$

Hence, the molar change in volume, ΔV, and the free energy (or the equilibrium constant) serve to determine the value of the partial compressibility at any fixed temperature. For a maximum compressibility there exists an optimum degree of dissociation; complete dissociation ($1-N \rightarrow 0$) and negligible dissociation ($N \rightarrow 0$) would both be expected to exhibit small compressibilities.

In an analogous fashion a partial molal specific heat may be calculated for a chemically active substance. The molal specific heat is defined as

$$C_0' \equiv \Delta H \partial N/\partial T.$$

It follows from Eq. (2a) that

$$C_0' = [(\Delta H)^2/RT^2] dN/d \ln K. \quad (7)$$

For the two-state reaction, $A \rightleftarrows B$,

$$C_0' = [(\Delta H)^2/RT^2] N(1-N) = (\Delta H)^2/2RT^2(1+\cosh \Delta F/RT). \quad (8a)$$

Similarly, for the dissociation reaction, $AB \rightleftarrows A+B$,

$$C_0' = [(\Delta H)^2/RT^2] N(1-N)/(2-N), \quad (8b)$$

which completes the analogy.

B. Kinetics of Compressibility and Specific Heat

It is convenient to begin kinetic considerations by once again referring to a specific reaction, for example $AB \rightleftarrows A+B$. According to the law of mass action the recombination rate will be kN^2, and the dissociation rate, $kK(1-N)$, where k is the familiar reaction rate constant. At equilibrium it is clear that,

$$dN/dt = kN^2 - kK(1-N) = 0.$$

If the equilibrium of a reaction is only slightly perturbed, for example, by the application of a pressure change, it may easily be shown that the rate of return toward equilibrium is, to a first-order approximation:

$$d(\Delta N)/dt = \kappa(\Delta N - \Delta N_0),$$

where ΔN_0 represents the magnitude of the small perturbation; the newly introduced quantity, κ, will be defined as the *equilibrium* reaction rate. Although the form of the above equation holds for all chemical reactions the relationship between the conventional reaction rate, k, and the equilibrium reaction rate, κ, depends on the specific reaction. For example, $\kappa = k(K+1)$ for the reaction $A \leftrightarrows B$; $\kappa = k(2N+K)$ for the reaction $AB \rightleftarrows A+B$.

If the applied perturbation, ΔN_0, is a constant, the above gives as a solution

$$\Delta N = \Delta N_0[1-\exp(-\kappa t)].$$

Hence $1/\kappa$ may be regarded as the time constant, or relaxation time, of the reaction in the vicinity of equilibrium.

Any perturbation, produced in the chemical reaction by a sound wave, will vary periodically with time, for example, as $\exp i\omega t$. In this case the solution to the above equation gives for the amplitude of the perturbation

$$\Delta N = \Delta N_0/(1+i\omega/\kappa).$$

However, ΔN is proportional to $\Delta \ln K$. Hence from Eq. (3) it follows for a periodic pressure variation, that

$$\beta' = \beta_0'/(1+i\omega/\kappa), \quad (9a)$$

where β' is the *dynamic* isothermal partial compressibility. Similarly for a periodic temperature variation it follows from Eq. (6) that

$$C' = C_0'/(1+i\omega/\kappa), \quad (9b)$$

where C' is the dynamic partial molal specific heat.

The complex character of the dynamic compressibility may be interpreted in terms of a phase lag between applied pressure and compression (or rarefaction). The real part of the dynamic compressibility is in phase with the pressure; the imaginary part lags the applied pressure by $\pi/2$. At low frequencies the magnitude of the real part predominates; at high frequencies the imaginary part is greater, diminishing toward zero with increasing frequency but less rapidly

than the real part. The above interpretation holds in a similar manner for the dynamic specific heat.

In the following section it will be shown how the complex character of the dynamic partial compressibility and dynamic partial specific heat results in the absorption of energy from an acoustic wave propagated through a medium.

III. Sound Absorption and Chemical Reaction

That the existence of imaginary quantities in the expression for the specific heat or compressibility implies the dissipation of sound energy, can be simply shown as follows: A plane acoustic wave in an absorptive medium can be represented in the form

$$a=a_0\exp[i\omega(t-x/c)-\alpha x],$$

where a is the amplitude of the sound wave at a distance x, and α is the amplitude absorption coefficient. The expression may also be written in the form

$$a=a_0\exp[i\omega(t-x/v)],$$

where $1/v=1/c+\alpha/i\omega$. It is convenient to define the complex refractive index as c/v; it follows then that the imaginary part of the square of the refractive index is $-2i\alpha c/\omega$. Hence, the imaginary part of the refractive index is associated with absorption of sound.

The complex refractive index for any medium may be calculated with the aid of the well-known relation.

$$v^2=\gamma/\beta\rho, \tag{10}$$

where γ is the ratio of the specific heats and ρ is the density. The compressibility, β, is the dynamic compressibility of the medium as a whole. However, published values for the compressibilities of materials are invariably static compressibilities. The static compressibility, β_0, is related to β by

$$\beta=\beta_0-\beta_0'+\beta_0'/(1+i\omega/\kappa). \tag{11}$$

Analogously,

$$C_P=C_0-C_0'+C_0'/(1+i\omega/\kappa), \tag{12a}$$

$$C_V=C_0-\Delta-C_0'+C_0'/(1+i\omega/\kappa), \tag{12b}$$

where Δ is C_P-C_V. Hence, the square of the refractive index is given by

$$(c/v)^2=\frac{C_0}{C_0-\Delta}\cdot\frac{C_0-\Delta-C_0'+C_0'/(1+i\omega/\kappa)}{C_0-C_0'+C_0'/(1+i\omega/\kappa)}\cdot\frac{\beta_0-\beta_0'-\beta_0'/(1+i\omega/\kappa)}{\beta_0}. \tag{13}$$

Collecting imaginary terms it is found approximately that,

$$2\alpha=\left[\frac{C_0'\Delta}{C_0^2}+\frac{\beta_0'}{\beta_0}\right]\frac{\omega^2\kappa}{c(\omega^2+\kappa^2)}. \tag{14}$$

The first term in this equation results from temperature-induced changes in the chemical reaction; the second term is associated with the effect of pressure on the reaction. At low frequencies, ($\kappa\gg\omega$), absorption is proportional to the square of the frequency; in the critical region, ($\kappa=\omega$), absorption increases much less rapidly with frequency; at extremely high frequencies absorption is independent of frequency provided other dissipative processes are absent. Actually the dissipation resulting from the viscosity of the medium cannot be neglected at high frequencies which again results in a square dependence on frequency in this region. These relationships between chemical absorption, viscous dissipation, and frequency are summarized in Fig. 1.

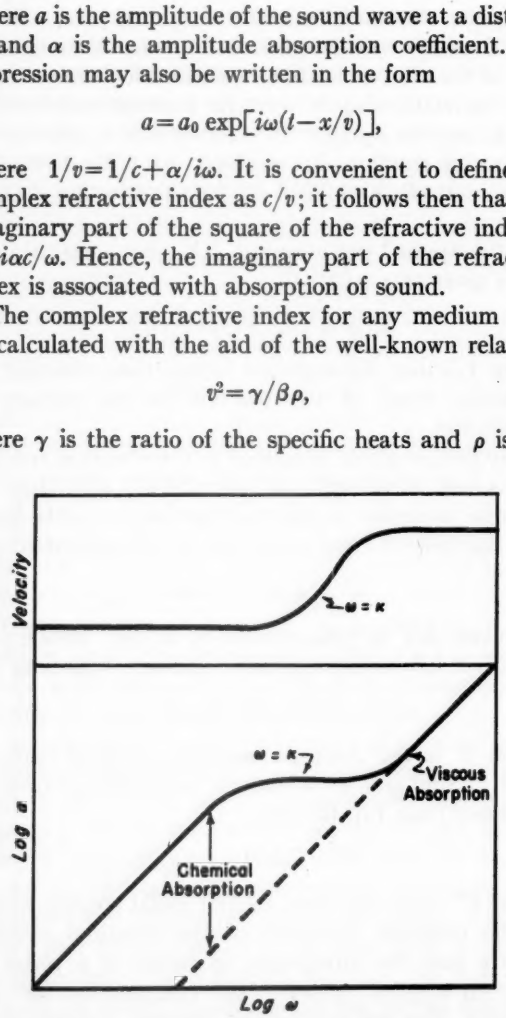

FIG. 1. These curves illustrate the dependence of sound absorption and velocity on frequency in a chemically active fluid. Except for the critical region ($\omega=\kappa$) absorption is proportional to the square of the frequency and the velocity is independent of frequency. Increasing the equilibrium reaction rate, κ, decreases the magnitude of the chemical absorption (but not the velocity shift) as well as displaces the critical region to higher frequencies.

The real part of the refractive index is also frequency dependent; expressed in another way, dispersion of the velocity of sound may be exhibited by a chemically active fluid. The real part of the refractive index is approximately

$$(c/v)^2=1+2\alpha\kappa c/\omega^2. \tag{15}$$

Hence, the sound velocity in a chemical medium is constant at low frequencies, and increases in the critical region becoming constant again at higher frequencies as illustrated in Fig. 1. Clearly, data on velocity dispersion will yield the same kind of chemical information as can be derived from sound absorption data. However, the total change in velocity is usually an extremely small fraction and may not easily be observed. Particularly difficult would be the elimination of velocity variations resulting from uncontrolled temperature changes in the medium.

In the following section a calculation is made illustrating the utilization of absorption data to obtain the partial molar compressibility and chemical reaction rate of a chemical reaction.

IV. ILLUSTRATION OF SOUND ABSORPTION RESULTING FROM A CHEMICAL REACTION

It was found recently[3] that the absorption of sound in sea water behaves in an anomalous fashion. The quantity $2\alpha/\omega^2$ was observed to be constant at frequencies up to 100 kc and to decrease by a factor of 50 becoming constant again at frequencies above 1000 kc. Significantly, this effect was not found in fresh water although the absorption of sea water and fresh water are practically identical at frequencies above 1000 kc. Obviously the anomalous absorption could be attributed to a process involving one of the dissolved substances in the ocean.

Sufficient measurements were made to establish the frequency dependence of the absorption in the ocean in the form

$$2\alpha/\omega^2 = A\kappa/(\kappa^2+\omega^2)+B. \tag{16}$$

It will be noted that this frequency dependence is identical with that predicted by Eq. (14). From this identity,

$$A \equiv C_0'(C_P-C_V)/cC_0^2+\beta_0'/\beta_0 c$$

obtains. The coefficient A was found to be 2.9×10^{-10} sec./cm; the reaction rate, κ, of the process responsible for the absorption, was 0.9×10^6/sec.

Recently, Robert W. Leonard[4] was able to repeat these sea water measurements in the laboratory. By synthesizing artificial sea water he was able to show that $MgSO_4$ was the dissolved substance in sea water which was chiefly responsible for the absorption anomaly. It was found that a pure $MgSO_4$ solution having the same molal concentration (0.02 mole/liter) as is found in the ocean, gave somewhat higher absorption than the synthesized sea water which also included NaCl, $MgCl_2$, and $CaSO_4$. It appears from Leonard's data that the quantity A for the $MgSO_4$ solution is 10^{-9} sec./cm and κ is 1.5×10^6/sec.

The chemical reaction in $MgSO_4$ solution responsible for this sound absorption is one of several normally present; as a group these are termed ionization. The nature of the particular reaction is uncertain, for ionization processes in solution are complicated and not well understood. For the present purpose identification of the reaction is not required and in subsequent discussions it will be referred to simply as an ionization process.

The partial specific heat of the solution may be obtained directly from the temperature dependence of the heat of dilution eliminating the need for evaluating Eq. (8b). Such observations have been made by Plake[5] for $MgSO_4$ at two temperatures, 20° and 10°C. These data give only an approximate value for C_0' but the accuracy is adequate. Plake's heat of dilution data yields 1.2×10^{-3} cal./g/°C for C_0'. Using (C_P-C_V) equal to 6×10^{-3}, and $C_0=1$ and $c=1.5\times10^5$ the first term of A is found to be 4.5×10^{-11} sec./cm. It is clear that the partial molal specific heat of $MgSO_4$ can only account for about 5 percent of the observed absorption. This conclusion is sustantiated by a few observations on the temperature dependence of the absorption. The specific heat term in Eq. (14) is proportional to (C_P-C_V) which diminishes rapidly with decreasing temperature and vanishes in the neighborhood of a few degrees centigrade. However, these measurements of absorption show no such marked sensitivity to the temperature.

Inasmuch as the first term of Eq. (14) is not adequate to explain the absorption, the effect of the compressibility term will now be considered. Compressibilities of dilute solutions have been investigated with the aid of sound velocity measurements using Eq. (10). The results of these measurements can be expressed in terms of the quantity ϕ which is defined as

$$\phi \equiv (\beta_S-\beta_0)/m,$$

where β_0 and β_S refer to the compressibility of the solution and of the solvent and m is the molar concentration of the solute. Bachem[6] determined ϕ for $MgSO_4$ over a range of concentrations and found the approximate empirical relationship,

$$\phi = \phi_0 - 35\times10^{-7}m^{\frac{1}{2}}. \tag{17}$$

The empirical relationship above does not give explicitly the partial compressibility arising from the ionization process. This portion of the compressibility may be distinguished from the whole with the aid of Eq. (6). Reinterpreting Eq. (6) for ideal ionic dissociation in solution, it predicts that the partial molal compressibility arising from the ionization reaction should approach 0 with negligible concentration; furthermore, this compressibility may be expected to increase approximately as the square root of the concentration for dilute solutions. Hence it seems reasonable that the second term of Eq. (17) represents the partial molal compressibility associated with ionization; the first term ϕ_0 represents the partial molal compressibility of the completely ionized solute. It follows that for $MgSO_4$,

$$\beta_0' = -35\times10^{-7}m^{\frac{1}{2}}.$$

It is to be noted that the sign of β_0' is negative although ϕ is positive; the molal compressibility of a solution is decreased by the addition of a solute, but increasing the concentration lessens the effect.

[3] Leonard Liebermann, J. Acous. Soc. Am. **20**, 868 (1948).
[4] Leonard, Combs, and Skidmore, J. Acous. Soc. Am. **21**, 63 (1949). Dr. Leonard has kindly made available the data which was shown on a slide at the thirty-sixth meeting of the Acoustical Society of America in Cleveland, Ohio (November 4–6, 1948).
[5] Ewald Plake, Zeits. f. physik Chemie **A162**, 257 (1932).
[6] Ch. Bachem, Zeits. f. Physik **101**, 541 (1936).

The partial dynamic compressibility calculated from the above with a concentration of 0.02 mole/liter yields for A, 1.3×10^{-9}. Hence the magnitude of A calculated by means of the dynamic compressibility, is in good agreement with the value obtained from the observed sound absorption in $MgSO_4$. Clearly the partial compressibility of the $MgSO_4$ ionization reaction is of the correct magnitude to explain this unique sound absorption.

V. ABSORPTION PROCESSES IN SOLUTIONS

The preceding discussion relating sound absorption and chemical reaction has been chiefly phenomenological, with little concern for the nature of the molecular processes which produce these acoustic effects. Possibly a few pertinent facts and relationships which are summarized below may well be significant as a basis for a molecular description of sound absorption in solutions.

One of the several possible ionic interactions present in ionization has been treated theoretically by Debye and Falkenhagen[7] in their theory of electrical conductivity in solutions. In this theory the normal interaction between the solute and solvent ions in solution is assumed to be perturbed by the application of an external electric field; this perturbation between ion and solvent, of course, proceeds with a specific reaction rate. Hence, application of an alternating electric field results in a dependence of conductivity on the field frequency in a manner exactly analogous to the preceding acoustic treatment. It has already been pointed out that $MgSO_4$ absorption data lead to a reaction rate for one of the reactions associated with the ionization process, namely, $\kappa=1.5\times10^6$/sec. The value of κ from the frequency dependence of electrical conductivity for $MgSO_4$ is of the approximate order of magnitude which suggests a possible similarity meriting further study.

As pointed out previously, the partial compressibility and the partial specific heat have been found empirically for most salts to vary approximately as the $\frac{3}{2}$ power of the concentration of the solute. The reaction rate, κ, may also depend on the concentration as can be inferred from the earlier discussion of reaction kinetics. For a dissociation reaction, which seems reasonable in this case, κ is approximately proportional to the concentration.** Hence, sound absorption in solution may be predicted to vary as the square root of the solute concentration. Interestingly, the Debye-Falkenhagen theory predicts the same dependence of conductivity on the concentration.

It may be expected that other salts possessing compressibility properties similar to $MgSO_4$ would also exhibit similar acoustic properties. Salts which exhibit similar compressibilities are $CdSO_4$, $CuSO_4$, $MnSO_4$, and $ZnSO_4$; Na_3PO_4 exhibits a somewhat greater compressibility. Provided their reaction rates are nearly identical to $MgSO_4$, which is a likely possibility, these salts may be expected to be acoustically similar. Univalent salts such as NaCl uniformly exhibit a smaller partial compressibility and would be expected to be less active acoustically. In spite of this it is somewhat surprising that the 25-fold increase in concentration of NaCl over $MgSO_4$ found in sea water does not compensate for the lower partial compressibility of the former and produce comparable sound absorption. Further, the quantity, A, for NaCl is 40 times greater than for $MgSO_4$. Clearly in order to explain the lack of absorption of the former the reaction rate must also be considerably greater; at least 200 times greater than that of $MgSO_4$ to produce a negligibly small absorption. This conclusion regarding the greater reaction rate in NaCl is in agreement with chemical expectations: The increase in κ resulting from the greater concentration of the NaCl is 25; the increase arising from the difference in ionization constants is nearly 10, which leads to a reaction rate similar to that deduced above.

Finally it deserves mention that the unique compressibility properties exhibited by a $MgSO_4$ solution bear a close resemblence to that property of pure liquids known as the dilatational (compressional) viscosity.[8] Actually, there exists at present no experiment by which these two properties, dilatational viscosity, and partial compressibility associated with a chemical reaction, could be disinguished. Quite likely the distinction is purely a formal one requiring some theoretical clarification but in no way excluding these chemical reactions from the class of mechanically dissipative processes known as viscous forces.

[7] Peter Debye and Hans Falkenhagen, Physik. Zeits. **29**, 121, 401 (1928). Also see[6] Hans Falkenhagen, *Electrolytes* (Clarendon Press, Oxford, 1934), pp. 181–192.

** For the two state reaction, $A\rightleftarrows B$, the equilibrium reaction rate, κ is independent of the concentration.

[8] Leonard Liebermann, Phys. Rev. **75**, 1415 (1949).

The Energy Level Density and Partition Function of Nuclei

D. TER HAAR*
Purdue University, Lafayette, Indiana
(Received July 18, 1949)

In this paper the nuclear energy level densities given by van Lier and Uhlenbeck, and by Bohr and Kalckar are compared with those given by Wergeland. It is shown that Wergeland's formula agrees slightly better with observational data. Wergeland's energy level density is then used to calculate the partition function of nuclei at a temperature of 1 Mev since this partition function enters into a discussion of the equilibrium theory of the origin of the chemical elements.

IN many problems it is necessary to have a formula for the density of the energy levels of a nucleus. As examples we may mention the statistics of nuclear reactions[1] or the discussion of the equilibrium theory of the origin of the chemical elements.[2] It is therefore important to have as accurate an expression for the level density as possible. Bethe[3] assumed that the nucleus might be treated as a Fermi-Dirac gas of Z protons and N neutrons in a spherical box, the volume of which is the volume of the nucleus, and proportional to $A=N+Z$. Van Lier and Uhlenbeck[4] have generalized Bethe's procedure by considering a gas of Fermi-Dirac particles, where the density of the energy levels of the *individual* particles is left undefined. It turns out that the level density of the nucleus is given by

$$\rho(A, E)dE=[1/E(48)^{\frac{1}{2}}]\exp[\pi(2E/3\Delta)^{\frac{1}{2}}]dE, \quad (1)$$

where E is the excitation energy, $\rho(A, E)$ the density of the levels for a nucleus of atomic weight A in the neighborhood of the energy E, and Δ the spacing of the individual energy levels at the top of the Fermi distribution. It is seen that ρ depends on A and the density of the individual levels only through Δ. It is therefore not surprising that Bohr and Kalckar[5] obtained the same formula under the assumption of equidistant individual levels. For Δ, it seems a good approximation to use

$$\Delta=10/A \text{ Mev}. \quad (2)$$

Recently, Wergeland[6] has attacked the problem from a different point of view. Instead of using the approximation that the nucleons are free, he uses the liquid drop model of the nucleus. The total energy of the nucleus is no longer the sum of the individual energies of the constituent nucleons but equal to the sum of the energies of the excited proper vibrations of the drop. In this way, Wergeland obtains for the level density:

$$\rho(A, E)dE=1.14A^{1/7}E^{-5/7}\exp(0.9A^{2/7}E^{4/7})dE, \quad (3)$$

where all energies are expressed in Mev.

In order to compare the two formulas, we have calculated the level spacings for various values of A and E. The results are given in Table I. The first number given is that obtained from Eq. (1), and the second value that obtained from Eq. (3).

It is seen from Table I that Wergeland's formula (3) gives a better estimate for the energy level distance at about 10 Mev than formula (1) since from experimental data (slow neutrons) follows that the level distance should be of the order of magnitude of a few ev.[7] This is not surprising since one should expect better results from the liquid drop model than from the free particles model.

Since the level density following from formula (1) is so much larger than that given by formula (3), it is of interest to repeat the calculations of Beskow and Treffenberg[2] of the partition function of a nucleus at a temperature $T=\theta/k$, where $\theta=1$ Mev. The partition function is given by the formula

$$\Gamma=\sum g\exp(-E/\theta), \quad (4)$$

where the summation must be extended over all excited states and g is the statistical weight of the level.

TABLE I. Energy level distances in ev for different values of A and E.

A \ E	0.1 Mev	0.5 Mev	1 Mev	5 Mev	10 Mev	50 Mev	100 Mev
50	10^5	5.10^4	2.10^4	100	1	10^{-9}	10^{-16}
	5.10^4	5.10^4	3.10^4	1000	100	10^{-4}	10^{-9}
100	5.10^4	10^4	2000	0.5	5.10^{-4}	10^{-16}	10^{-27}
	4.10^4	3.10^4	2.10^4	300	10	10^{-7}	10^{-13}
150	3.10^4	3000	300	10^{-2}	10^{-6}	10^{-22}	10^{-34}
	3.10^4	2.10^4	10^4	100	2	10^{-8}	10^{-16}
200	2.10^4	1000	100	10^{-4}	10^{-8}	10^{-27}	10^{-41}
	2.10^4	2.10^4	6000	40	0.5	10^{-10}	10^{-17}
250	10^4	400	20	10^{-5}	10^{-10}	10^{-31}	10^{-47}
	2.10^4	10^4	5000	20	0.2	10^{-11}	10^{-19}

* This paper was written while the author was temporarily at Yerkes Observatory, Williams Bay, Wisconsin.

[1] V. Weisskopf, Phys. Rev. **52**, 295 (1937).

[2] G. Beskow and L. Treffenberg, Arkiv f. Mat. Astr. o. Fys. 34A, No. 13 (1947).

[3] H. A. Bethe, Phys. Rev. **50**, 332 (1936).

[4] C. van Lier and G. E. Uhlenbeck, Physica **4**, 531 (1937).

[5] N. Bohr and F. Kalckar, Kgl. Danske Vid. Sels. Mat.-fys. Medd. **14**, No. 10 (1937).

[6] H. Wergeland, Fra Fysik. Verden, 223 (1945).

[7] See e.g., H. A. Bethe and G. Placzek, Phys. Rev. **51**, 450 (1937).

TABLE II. Values of the partition function for different values of A.

A	50	100	150	200	250
$\log_{10}\Gamma$	2.6	6.1	9.6	13.1	16.5
$\log_{10}\Gamma'$	2.2	2.6	2.9	3.2	3.5
B & T	3	6.5	10	13.5	17

Formula (4) can be written in the form:[2]

$$\Gamma\cong 1+\int_{\Delta/2}^{\infty}\rho(A,E)\exp(-E/\theta)dE, \tag{5}$$

where the 1 can be neglected in all practical instances.

Using expression (1) for $\rho(A,E)$, Γ is given by

$$\Gamma=\int_{\Delta/2}^{\infty}(1/E(48)^{\frac{1}{4}})\exp[\pi(2E/3\Delta)^{\frac{1}{2}}-E/\theta]dE. \tag{6}$$

The integrand varies very little up to its maximum which occurs for

$$E_{\max}=\pi^2\theta^2/6\Delta, \tag{7}$$

and the integral is therefore in good approximation given by

$$\{(1/E(48)^{\frac{1}{4}})\exp[\pi(2E/3\Delta)^{\frac{1}{2}}-E/\theta]\}_{E=E_{\max}}\times(E_{\max}-\Delta/2),$$

or, using Eqs. (2) and (7) and substituting numerical values:

$$\Gamma\cong 0.14\exp(0.16A), \tag{8}$$

which agrees very closely with the values plotted by Beskow and Treffenberg[2] (compare also Table II).

Using formula (3) on the other hand, we have

$$\Gamma'=\int_{\Delta/2}^{\infty}1.14A^{1/7}E^{-5/7}\exp[0.9A^{2/7}E^{4/7}-E/\theta]dE. \tag{9}$$

The maximum now occurs for

$$E_{\max}'=0.5A^{2/3}\theta^{7/3}\text{ Mev}, \tag{10}$$

and the integral is approximately equal to

$$\Gamma'\cong 0.9A^{\frac{1}{4}}\exp(0.1A^{\frac{1}{4}}), \tag{11}$$

which is much smaller than the Γ of Eq. (8), due to the fact that formula (3) gives a wider spacing of the levels. In Table II we have given the values of $\log_{10}\Gamma$ and $\log_{10}\Gamma'$ as calculated from Eqs. (8) and (11) for different values of A; in the last row, we have inserted the values of $\log_{10}\Gamma$ as given by Beskow and Treffenberg.[2]

From Table II it is immediately seen that Beskow and Treffenberg have grossly overestimated the influence of the excited states of the nucleus in calculating their partition function, using formula (1) for the energy level density. It remains to be seen whether this overestimation will invalidate their conclusions as to the relative abundances of the chemical elements in the stellar models discussed by them,[8] but it might be worth while to reinvestigate this point and to recalculate their abundance curve, using Γ' instead of Γ, and perhaps also using a different value for θ.

[8] G. Beskow and L. Treffenberg, Arkiv f. Mat. Astr. o. Fys. 34A, No. 17 (1947).

Letters to the Editor

PUBLICATION of brief reports of important discoveries in physics may be secured by addressing them to this department. The closing date for this department is five weeks prior to the date of issue. No proof will be sent to the authors. The Board of Editors does not hold itself responsible for the opinions expressed by the correspondents. Communications should not exceed 600 words in length

Theory of the Formation of Powder Patterns on Ferromagnetic Crystals

CHARLES KITTEL
Bell Telephone Laboratories, Murray Hill, New Jersey
October 6, 1949

MAGNETIC powder patterns or "Bitter patterns" are sometimes formed on the surfaces of ferromagnetic crystals when a liquid suspension of fine ferromagnetic particles is placed on the crystal. Powder patterns are the most powderful tool available for the study of the nature of ferromagnetic domains,[1] yet there has not been an adequate discussion of the mechanism by which the powder particles collect at domain boundaries to form the lines which are observed under the microscope. It is frequently said that the colloid particles collect in the regions in which the maximum inhomogeneity in the local magnetic field occurs. This is an inadequate statement, and in particular fails to account for the enhancement of some lines when a uniform magnetic field is applied normal to the surface under examination, and the disappearance of other lines under the same conditions.

The particles in the suspension are small enough so that they remain indefinitely in suspension. The particle distribution is accordingly governed by the Boltzmann distribution law. The magnetic energy of a particle of effective susceptibility $\chi=(\mu-1)/4\pi$ in a field H is $-\frac{1}{2}\chi H^2V$, where V is the volume of the particle. In thermal equilibrium the density of particles is given by

$$p(H)=p(0)e^{\chi H^2V/2kT}, \tag{1}$$

where $p(0)$ is the density at a point for which $H=0$. It is seen that there will be a marked tendency for the particles to concentrate in regions in which H^2 is large.

On the surfaces of crystals there are strong local fields of diverse origin. The fields of greatest interest are caused by long narrow strips of poles formed by the intersection of Bloch walls with the crystal surface. Suppose that the poles produce a magnetic field $\mathbf{\Delta H}$ in their vicinity; we then apply from outside a uniform field $\mathbf{H}$. The particle density over the line of poles will be greater than that in other places by the factor

$$\exp[[2\mathbf{H}\cdot\mathbf{\Delta H}+(\Delta H)^2]\chi V/2kT].$$

When $\mathbf{H}$ is in the same direction as $\mathbf{\Delta H}$, the line is enhanced with respect to the density in the absence of the applied field; if $\mathbf{H}$ is opposite to $\mathbf{\Delta H}$, the line is weakened and may be made to disappear. The operation of this effect is beautifully illustrated by Fig. 17 in the paper by Williams, Bozorth, and Shockley.[1]

In the absence of an external field it is necessary that $(\Delta H)^2\chi V \gg 2kT$ for a well-defined line to collect. For magnetite spheres the effective susceptibility is essentially determined by the demagnetizing factor and we have $\chi\cong\frac{3}{4}\pi$. We require, for particles of volume 10^{-12} cc,

$$|\Delta H|\gg[2kT/\chi V]^{\frac{1}{2}}\cong[4\times10^{-13}/10^{-12}]^{\frac{1}{2}}\cong 0.6 \text{ oersted},$$

which may be expected to be exceeded near a Bloch wall.

If the particles in the suspension are small enough to behave as single domains,[2] that is, as small permanent magnets, then the distribution law will be

$$p(H)=p(0)[\sinh(\mu H/kT)]/(\mu H/kT), \tag{2}$$

where μ is the magnetic moment of a particle. This relation is obtained by integrating the Boltzmann factor $\exp[\mu H\cos\theta/kT]$ over all solid angles. The effect of an applied field is exhibited in some cases by this density function, although in a less striking manner. In the colloidal suspensions employed in practice the particle size is relatively large, so that distribution law (1) is applicable. An account of other aspects of the theory will be found in reference 3. In the derivation of both distribution functions we have neglected field inhomogeneities over the volume of a single particle, the effects of mutual interactions among the particles, and the reorientation of spins in a wall under the action of the external magnetic field. These approximations are not likely to change the general nature of the results.

[1] Williams, Bozorth, and Shockley, Phys. Rev. **75**, 155 (1949); H. J. Williams and W. Shockley, Phys. Rev. **75**, 178 (1949).
[2] C. Kittel, Phys. Rev. **70**, 965 (1946).
[3] C. Kittel, Rev. Mod. Phys. **21**, 541 (1949).

Nuclear Moments of Mg^{25}

M. F. CRAWFORD, F. M. KELLY,* A. L. SCHAWLOW,** AND W. M. GRAY***
McLennan Laboratory, University of Toronto, Toronto, Canada
October 3, 1949

THE Mg I lines 5184, 5173, and 5167A ($3s3p\ ^3P^0_{2,1,0}-3s4s\ ^3S_1$) and the Mg II resonance line 2796A ($3s\ ^2S_{1/2}-3p\ ^2P^0_{3/2}$) have been excited in an atomic beam light source and their hyperfine structures resolved with a Fabry-Perot etalon. The structures show that for Mg^{25} $I=5/2$ and the nuclear magnetic moment is negative and equal to -0.96 ± 0.07 nuclear magnetons.

The line 5167A ($3s3p\ ^3P_0-3s4s\ ^3S_1$) was studied with 21-, 54-, and 73-mm etalons. The interferometer plates were coated with evaporated silver[1] to give a reflectivity of 80 percent and a transmission of 17.5 percent in the green. The 21-mm etalon patterns showed no structure. The 54-mm patterns showed two weak components which are assigned to Mg^{25}, a strong component due to Mg^{24}, and indications of a component due to Mg^{26} very close to Mg^{24}. The separations of the Mg^{25} components relative to the Mg^{24} components are $+0.0303\pm0.0004$ and -0.0341 ± 0.0006 cm^{-1} where the positive sign indicates a higher wave number.

For all three lines the Mg^{24} and Mg^{26} components were resolved with a 73-mm etalon in which the silver films had a 90 percent reflectivity. The separations of the Mg^{26} component relative to the Mg^{24} component are -0.0138 ± 0.0003, -0.0122 ± 0.0015, and -0.0138 ± 0.0004 cm^{-1} for the lines 5167, 5173, and 5184A, respectively. As predicted by the specific mass effect, the isotope shifts in all three lines are equal within the assigned errors.

The resolution of the Mg^{24} and Mg^{26} components in 5167A permits an accurate determination of the center of gravity of the three components due to Mg^{25}, on the assumption that it is midway between the Mg^{24} and Mg^{26} components. Thus the interval rule can be used to determine the I value. The separations of the two Mg^{25} components, measured in the 54-mm pattern, from their center of gravity are -0.0272 and $+0.0372$ cm^{-1}. The ratio of these separations is 1.37 ± 0.07. This ratio should be 1.40 for $I=5/2$ and 1.29 for $I=7/2$. Thus the spin of Mg^{25} is 5/2 and the inverted splitting of $^3S_1$ shows that the magnetic moment is negative.

The over-all separation of the Mg^{25} components, 0.0644 ± 0.0010 cm^{-1}, is equal to $6A(^3S_1)$, where $A(^3S_1)$ is the h.f.s. interval factor. Thus $A(^3S_1)=0.0107$ cm^{-1}, and gives $\mu(Mg^{25})=-0.97\pm0.05$ n.m. by the method used for P IV by Crawford and Levinson.[2]

The line 2796A ($3s\ ^2S_{1/2}-3p\ ^2P_{3/2}$) was studied with 21-, 30-, and 50-mm etalons using aluminum coated plates with reflectivities of 80 percent. The 21-mm pattern showed a strong com-

ponent due to Mg^{24} and a weak component $+0.095$ cm^{-1} from the Mg^{24} component. The 30-mm pattern showed the weak component resolved into two, the stronger of which had the higher frequency. The separations of these from the Mg^{24} component are $+0.1021 \pm 0.0004$ and $+0.0786 \pm 0.0007$ cm^{-1}. The stronger is assigned to Mg^{26} and the weaker is one of the two components expected from Mg^{25}. The 50-mm pattern indicated a faint component on the high frequency side of the strong component which in this pattern arises from an overlap of the Mg^{24} and Mg^{26} components in adjacent orders; but its position could not be accurately measured.

The ratio of the intensities of the Mg^{26} component and the neighboring Mg^{25} component, corrected for their mutual influence and the background due to Mg^{24}, was measured from the 30-mm pattern and is 1.7 ± 0.2. The assigned error is large because the background intensity due to Mg^{24} is comparable to the intensity of both the Mg^{25} and Mg^{26} components. Using the known relative abundances[3] of the isotopes and the intensity formula, values of this ratio can be predicted for both positive and negative moments and various I values. For a negative moment and $I=1/2$, $3/2$, $5/2$, and $7/2$ the predicted values are 1.49, 1.78, 1.91, and 1.99, respectively. Positive values of the moment give ratios greater than 2.55. Thus the measured value confirms a negative magnetic moment. It is not sufficiently accurate to determine I, but is compatible with $I=5/2$.

If the center of gravity of the Mg^{25} components is assumed to be midway between the Mg^{24} and Mg^{26} components the interval factor of $^2S_{1/2}$ of Mg II can be evaluated and used to calculate the magnetic moment. The position of the Mg^{25} component, corrected for the influence of the Mg^{26} component, relative to the center of gravity is 0.0274 ± 0.0015 cm^{-1}. For $I=5/2$ this separation gives $a_{3s}=0.0231$ cm^{-1} when allowance is made for the small structure of $^2P_{3/2}$. $\mu(Mg^{25}) = -0.93 \pm 0.05$ n.m. is obtained from a_{3s} by the Goudsmit formula.[4] However, the uncertainty in μ would be increased to 10 percent if the assumed position of the center of gravity is in error by 0.001 cm^{-1}.

The values of the magnetic moment determined from the h.f.s. splittings of $^3S_1$ of Mg I and $^2S_{1/2}$ of Mg II agree within the assigned errors. The weighted mean is -0.96 ± 0.07 nuclear magnetons. The Fermi-Segrè[5] correction has been applied and the effect of the finite size of the nucleus[6,7] is negligible.

The spin and the negative sign of the magnetic moment agree with the predictions of the shell structure in nuclei.[8,9] The magnitude of the magnetic moment falls near the average curve for similar nuclei in a Schmidt diagram,[8] but as for most of these nuclei it does not agree with the value predicted by an individual particle model.

* Holder of a fellowship from the National Research Council of Canada.
** Now at Columbia University, New York, New York.
*** Holder of a fellowship from the Research Council of Ontario. Now at the University of Reading, Reading, England.

[1] S. Tolansky, *Multiple Beam Interferometry of Surfaces and Films* (Oxford University Press, New York, 1948).
[2] M. F. Crawford and J. Levinson, Can. J. Research **A27**, 156 (1949).
[3] J. R. White and A. E. Cameron, Phys. Rev. **74**, 991 (1948).
[4] S. Goudsmit, Phys. Rev. **43**, 636 (1933).
[5] E. Fermi and E. Segrè, Zeits. f. Physik **82**, 729 (1933).
[6] J. E. Rosenthal and G. Breit, Phys. Rev. **41**, 459 (1932).
[7] M. F. Crawford and A. L. Schawlow, Phys. Rev. **76**, 1310 (1949).
[8] E. Feenberg and K. C. Hammack, Phys. Rev. **75**, 1877 (1949).
[9] L. W. Nordheim, Phys. Rev. **75**, 1894 (1949).

Nuclear Moments of $_{39}Y^{89}$

M. F. Crawford and N. Olson
McLennan Laboratory, University of Toronto, Toronto, Canada
October 3, 1949

LINES in the first, second, and third spectra of yttrium have been examined for hyperfine structure,[1-4] but none has been observed. The only result obtained from these investigations was that the magnetic moment of $_{39}Y^{89}$ is small. From the observed half-width, 0.1 cm^{-1}, of the Y III resonance line 2817A ($5s\,^2S_{1/2} - 5p\,^2P_{3/2}$) Wittke[3] estimated an upper limit of 0.05 cm^{-1} for the h.f.s. splitting of $5s\,^2S_{1/2}$, and from this calculated $\mu \leq 0.1$ n.m., on the supposition that $I=\frac{1}{2}$.

In the present investigation, the Y III resonance line 2817A ($5s\,^2S_{1/2} - 5p\,^2P_{3/2}$) has been resolved into two components. The observed intensity ratio is 3:1, and the fainter component is of lower frequency. Thus $I=\frac{1}{2}$, and the magnetic moment is negative. The magnetic moment calculated from the observed separation of the two components is $\mu = -0.14$ n.m.

The Y III spectrum was excited in the electrodeless discharge described by Crawford and Levinson.[5] YCl_3 was introduced into the quartz discharge tube. The tube was then evacuated, and argon admitted. The pressures used were in the range of 0.1 to 1.0 mm Hg at room temperature (26°C). Gaseous impurities in the discharge tube were removed by calcium shavings placed in a side branch. Graded seals connected the discharge tube to the pumping system, and liquid air traps placed between the stopcocks and the discharge tube prevented contamination by vapors from the stopcock grease. The discharge tube, with the exception of the windows, was immersed in liquid air. Even with liquid air cooling the Y III lines were easily excited.

The structure of 2817A was resolved with a 3-cm Fabry-Perot etalon, with aluminum coated plates. The etalon was placed between the collimator and the dispersing prism of the spectrograph, which had an $F/4$ off-axis paraboloidal mirror as the camera objective. The structure of the other resonance line of Y III could not be measured because an argon line was superimposed on it.

The effects of different excitation conditions and argon pressures on the half-intensity width and the intensity of the components were studied. It was possible to obtain half-widths of 0.05 cm^{-1} with intensity adequate to give in a two-hour exposure a photographic density suitable for accurate intensity measurements. The plates were calibrated for intensity measurements by the step-slit continuous spectrum method. The intensity ratio of the two components was found to be independent of excitation conditions and argon pressures. Thus the structure observed must be h.f.s.

The separation of the components, when corrected for their small overlap as determined from the analysis of the intensity contours, is 0.060 ± 0.005 cm^{-1}. This separation is very nearly equal to the difference between the splittings of the $^2S_{1/2}$ and $^2P_{3/2}$ levels. A calculation shows that the splitting of the $^2P_{3/2}$ level is 1/15 that of the $^2S_{1/2}$ level. Therefore the $^2S_{1/2}$ splitting is 0.064 ± 0.005 cm^{-1}. The magnetic moment calculated from this separation by the Goudsmit formula,[6] with a Fermi-Segrè correction,[7] is $\mu = -0.14$ n.m. The correction for the finite size of the nucleus[8] is negligible compared to the experimental error in μ.

The spin and the sign of the magnetic moment of $_{39}Y^{89}$ are consistent with the predictions of the single particle model[9-11] for a configuration in which 50 neutrons form closed shells and the last 5 protons are in the $3p$ shell. Thus one concludes that at $Z=39$ the $2s$ and $3p$ proton levels have not crossed. The magnitude of the magnetic moment of $_{39}Y^{89}$ is in fair agreement with that predicted for the single particle model, and is additional evidence that the observed and predicted magnetic moments are in much better agreement for nuclei with completed shells plus or minus one proton, or plus or minus one neutron than for other nuclei. Pb^{207} and Bi^{209} are the two outstanding exceptions and they are adjacent to the radioactive elements.

[1] H. Schüler and T. Schmidt, Naturwiss. **22**, 838 (1934).
[2] D. T. Williams and L. P. Graneth, Phys. Rev. **54**, 338 (1938).
[3] H. Wittke, Zeits. f. Physik **116**, 547 (1940).
[4] P. G. Kruger and C. N. Challacombe, Phys. Rev. **47**, 509 (1935); **48**, 111 (1935).
[5] M. F. Crawford and J. Levinson, Can. J. Research **A27**, 156 (1949).
[6] S. Goudsmit, Phys. Rev. **43**, 636 (1933).
[7] E. Fermi and E. Segrè, Zeits. f. Physik **83**, 729 (1933).
[8] M. F. Crawford and A. Schawlow, Phys. Rev. **76**, 1310 (1949).
[9] E. Feenberg and K. C. Hammack, Phys. Rev. **75**, 1877 (1949).
[10] L. W. Nordheim, Phys. Rev. **75**, 1894 (1949).
[11] Maria G. Mayer, Phys. Rev. **75**, 1969 (1949); Haxel, Jensen, and Suess, Phys. Rev. **75**, 1766 (1949).

The Nuclear Spin of He^3

A. E. Douglas and G. Herzberg
Division of Physics, National Research Council of Canada, Ottawa, Canada
October 5, 1949

THE nuclear g-factor of He^3 has been determined by Anderson and Novick[1] by means of the nuclear magnetic resonance method. Assuming a nuclear spin of $\frac{1}{2}$, they obtained for the nuclear magnetic moment the value 2.131 n.m. Even though the spin value $\frac{1}{2}$ appears most probable, to our knowledge no experimental determination of this quantity has yet been made. Since at least in one important case, that of B^{10}, a direct determination of the spin[2] has led to a value widely different from the one expected from theory, it appears to be of interest to determine the spin of He^3 unambiguously.

We have determined the spin of He^3 from the intensity alternation in the band spectrum of the He_2^3 molecule. An 88 percent sample of He^3 was excited by a slightly condensed discharge through a small Geissler tube. The spectrum was taken in the first order of a 21-foot grating and exhibited several He_2 bands. The band chosen for more detailed measurements is the one at 6400A representing a $^3\Sigma^+_\mu - {}^3\Pi_g$-transition. It involves only low lying states which are not likely to be perturbed or affected by l-uncoupling. The triplet spliting is negligible. Figure 1 reproduces the photometer curve of part of the P branch showing clearly the intensity alternation. A relative intensity scale obtained by means of a rotating sector is indicated at the left. It can be seen from Fig. 1 that the intensity ratio of successive lines is approximately 3:1. Actual measurement of the original record (using several groups of three successive lines and determining the ratio of the mean of the two outer ones to the central line of each group) gives the intensity ratio 2.8:1. Semiquantitative evaluations of other bands also give ratios close to 3:1. The theoretical ratios for the spins $\frac{1}{2}$, 1, and $\frac{3}{2}$ are 3:1, 2:1, and 1.67:1 respectively. The nuclear spin of He^3 is therefore unequivocally established to be $\frac{1}{2}$, in agreement with theoretical predictions. The nuclear spin of He^3 is thus the same as that of H^3 recently determined from the hyperfine structure of the magnetic resonance spectrum by Nelson and Nafe[3] and from the intensity alternation in H_2^3 by Dieke and Tomkins.[4]

In the 6400A band of He_2^4 the lines with odd K are missing in the P and R branch (since the nuclear spin is zero and since He^4 follows Bose statistics). In the corresponding He_2^3 band the lines with odd K are the strong ones (see Fig. 1) showing that the He^3 nuclei follow *Fermi statistics*, in agreement with expectation for a nucleus consisting of an odd number of nucleons.

As shown by Fig. 1 the lines of He^3He^4 also appear in the spectrum. In agreement with expectation there is no intensity alternation in the He^3He^4 band.

We are greatly indebted to the U. S. Atomic Energy Commission for the loan of the He^3 and to Dr. W. B. Lewis, Director of the Chalk River Laboratory, for arranging for this loan.

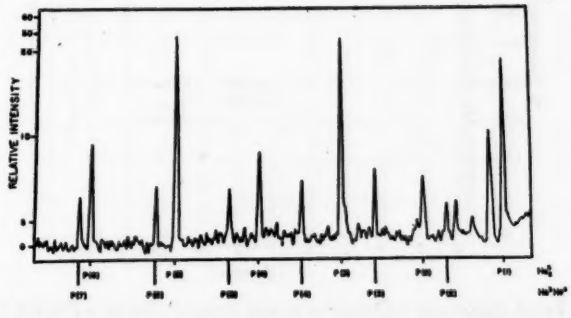

FIG. 1. Photometer curve of a portion of the P branch of He_2^3 and He^3He^4.

[1] H. L. Anderson and A. Novick, Phys. Rev. 73, 919 (1948).
[2] Gordy, Ring, and Burg, Phys. Rev. 74, 1191 (1948).
[3] E. B. Nelson and J. E. Nafe, Phys. Rev. 75, 1194 (1949).
[4] G. H. Dieke and F. S. Tomkins, Phys. Rev. 76, 283 (1949).

Inversion Spectrum of Ammonia

A. H. Sharbaugh, T. C. Madison, and J. K. Bragg
General Electric Research Laboratory, Schenectady, New York
October 6, 1949

THIRTY-SEVEN previously unreported ammonia absorption lines have been measured and identified. A Stark-modulation spectrograph with a one-foot absorption cell was used at room temperature with a modified 2K-33 tube[1] as the source. The assignments were made on the basis of the line intensities and a new empirical formula. The frequencies of the lines together with their assigned rotational quantum numbers are given in Tables I and II. The frequencies reported for the $N^{14}H_3$ lines are accurate to about ± 0.1 mc/sec.; and those for $N^{15}H_3$ to about ± 0.5 mc/sec. The experimental error of the $N^{15}H_3$ lines is determined by the fact that this isotope concentration is only 0.38 percent in unenriched ammonia as used in this study.

TABLE I. $N^{14}H_3$ absorption lines.

Frequency (mc/sec.) ± 0.1	Assignment (J, K)
16798.3	9, 5
16841.3	7, 1
17291.6	7, 2
17378.1	8, 4
18017.6	7, 3
18127.2	12, 9
18162.6	11, 8
18178.0	13, 10
18285.6	10, 7
18313.9	14, 11
18391.6	6, 1
18499.5	9, 6
18535.1	15, 12
18808.7	8, 5
18842.9	16, 13
18884.9	6, 2
19838.4	5, 1
21818.1	14, 11
23777.4	16, 14
24680.1	17, 15

TABLE II. $N^{15}H_3$ absorption lines.

Frequency (mc/sec.) ± 0.5	Assignment (J, K)
17097.2	7, 3
17548.4	9, 6
17855.3	8, 5
17943.4	6, 2
18258.8	7, 4
18788.2	6, 3
19387.5	5, 2
19702.1	8, 6
19708.2	9, 7
19793.4	7, 5
19810.8	10, 8
19984.6	6, 4
20009.9	11, 9
20131.6	4, 1
20272.3	5, 3
20683.0	4, 2
26243.0	9, 9

On the basis of the increased number of accurately measured lines now available, a new empirical formula

$$\nu(\text{mc/sec.}) = 23785.8 - 151.450J(J+1) + 211.342K^2 + 0.503027J^2(J+1)^2 - 1.38538J(J+1)K^2 + 0.949155K^4 - 0.001259997J^2(J+1)^3 + 0.005182367J^2(J+1)^2K^2 - 0.007088534J(J+1)K^4 + 0.003210437K^6, \quad (1)$$

given in Eq. (1), has been developed which includes sixth power terms in contrast to the older fourth power expressions. (See for example, references 2 and 3.) To gain some idea of the improvement in the prediction of new absorption frequencies, the positions of all the currently available assigned lines[2-4] were computed with the empirical expressions of references 2 and 3 as well as with the sixth power expression given here. The average deviation from experiment was found to be 45, 26, and 7 mc/sec., respectively, for the empirical equations of references 2, 3, and the present sixth power one.

The authors gratefully acknowledge the assistance of Miss Virginia G. Thomas and Mrs. Dorothy M. Hoffman in the computational work involved in developing the empirical formula.

[1] See A. H. Sharbaugh and J. Mattern, Phys. Rev. 75, 1102 (1949).
[2] Strandberg, Kyhl, Hillger, and Wentink, Phys. Rev. 71, 326 (1947).
[3] J. W. Simmons and W. Gordy, Phys. Rev. 73, 713 (1948).
[4] W. E. Good and D. K. Coles, Phys. Rev. 71, 383 (1947).

The Optical Properties of Semiconductors. I. The Reflectivity of Germanium Semiconductors

K. LARK-HOROVITZ AND K. W. MEISSNER
Purdue University, West Lafayette, Indiana
October 3, 1949

IN recent years it has been possible to prepare semiconducting alloys of germanium with known number of carriers of predictable sign.[1] The electrical behavior of these semiconductors is determined by the number and type of impurity centers and it was therefore of great interest to investigate also the optical properties of such materials. The reflectivity of silicon of indeterminate origin has been investigated before.[2]

Germanium alloys, both of the *N* type (electron conductor) and *P* type (hole conductor) have been selected. Two of these samples had a small number of carriers ($\sim 10^{16}$/cm^3) whereas the other two samples had high impurity content ($\sim 5.10^{18}$/cm^3) and form a degenerate electron gas at low temperatures.[3]

In the range from 0.6μ to 12μ a rock salt spectrometer was used. A Nernst filament held in a water jacket provided with a suitable window was the radition source. The radiation was focused by a concave aluminum mirror onto the sample from which it was reflected to another concave aluminum mirror which finally focused it on the entrance slit of the spectrometer. The semiconductor sample was mounted in exactly the same plane as a comparison aluminum mirror. The reflectivity was determined for various settings of the spectrograph by the intensity measured with a sensitive thermocouple and galvanometer, expressed in terms of the reflectivity of the aluminum mirror[4] (deposited by evaporation on an optical flat). The semiconductor samples were optically polished and their flatness determined by interference methods. Between 0.6μ and 0.8μ the reflectivity of all the samples is between 47 percent and 51 percent.[5] The reflectivity then decreases and remains almost constant about 35 percent up to about 40μ. From this reflectivity value the dielectric constant was calculated to be about 16 in agreement with the value necessary to calculate[6] resistivity due to impurity scattering in the material.

In the range from 8.7μ to 152μ the method of residual rays was used in a form similar to the one described by J. Strong.[7] The radiation source was a globar heating element enclosed in a water-cooled jacket and specially prepared thermocouples with sensitive galvanometers were used for the measurements of radiation intensities. The samples were held on a rotating disk provided with 12 circular openings. One of these openings holds an aluminum mirror for relative reflection measurements. In the residual ray apparatus it was possible to select radiations from the incident continuous radiation at 8.7μ, 20μ, 30μ, 41μ, 52μ, 117μ, and 152μ.

TABLE I. Reflectivity of germanium semiconductors in the infra-red in percent.

Sample type	Resistivity at ~20°C	8.7μ	20μ	30μ	41μ	52μ	117μ	152μ
1 *P* type	0.005Acm	35.4	33.8	33.2	40.3	53	79	46
2 *P* type	0.5Acm	37.3	41.0	36.7	38.5	38	41	36
3 *N* type	0.006Acm	36.5	34.5	30.6	29.0	29	81	50
4 *N*-type	~3Acm	37.2	37.2	37.2	38.5	38	34	39

Table I gives a summary of the results obtained for the various wave-length for the different samples.

It can be seen that the highly conducting samples 1 and 3 show a high reflectivity at 117μ which decreases again at 152μ, but is still considerably higher than the reflectivity of the high resistance samples which remains essentially constant through the whole wave-length range. Systematic investigation of low resistance samples also as a function of temperature is under way now.

Experiments have also been carried out with silicon samples of various impurity content and the results agree with earlier investigations. Of particular interest is the reflectivity of silicon samples which have been heat-treated and which show a definite indication of the formation of a silicate layer on the surface. This investigation will be discussed in detail somewhere else.

[1] K. Lark-Horovitz, "Preparation of semiconductors," NDRC report 14-585 (1945).
[2] Forsterling and S. Freedericksz, Ann. d. Physik **40**, 201 (1913); Ingersoll, Astrophys. J. **32**, 286 (1910); Pfesdorf, Ann. d. Physik **81**, 906 (1926).
[3] V. Johnson and K. Lark-Horovitz, Phys. Rev. **71**, 374, 909 (1947).
[4] The reflectivity for such aluminum mirrors is 90 percent at 0.6μ and increases between 2μ and 91μ regularly from 97 percent to 99 percent as verified by measurements of K. B. Hunt in this laboratory (M.S. thesis, Purdue (1945)).
[5] For a germanium film H. M. O'Bryan (I.O.S. **26**, 122 (1936)) has found in the visible a reflectivity of about 36 percent. This checks with recent observations by V. Bottom in this laboratory who found for a film deposited on a plate of optically polished fused silica 37 percent whereas the reflectivity as determined from the optical constants for bulk material was found to be 45 percent using sodium light. However, measurements by J. Thornhill in this laboratory indicate that germanium films may show the ordinary structure of the bulk material, but their mobility as determined from Hall effect and conductivity is too small by a factor of 1000, indicating the presence of electron traps.
[6] K. Lark-Horovitz and V. A. Johnson, Phys. Rev. **69**, 258 (1946).
[7] J. Strong, Phys. Rev. **37**, 1565 (1931); K. W. Meissner and K. B. Hunt, Research Report OPRD-WPB-74 (1945).

Optical Properties of Semiconductors. II. Infra-Red Transmission of Germanium*

M. BECKER AND H. Y. FAN
Purdue University, West Lafayette, Indiana
October 3, 1949

THE extinction coefficient k of germanium for infra-red light has been determined by previous measurements[1] up to about 1.2μ. For silicon, values of k are given by Ingersoll's[2] measurements up to 2.25μ. All previous measurements on the optical constants of these materials were made either using reflected light or using light transmitted through a thin film of the material. Properties of thin films are often not the same as those of the bulk material. (See I.) Light reflection depends upon the surface condition. It is therefore preferable, wherever possible, to use light transmitted through bulk samples for the determination of optical constants of the material.

We have found that bulk material of germanium as thick as several cm gives appreciable transmission over broad regions of the infra-red spectrum.

Transmission measurements on bulk germanium samples were made with a Gaertner rocksalt monochromator using a Western

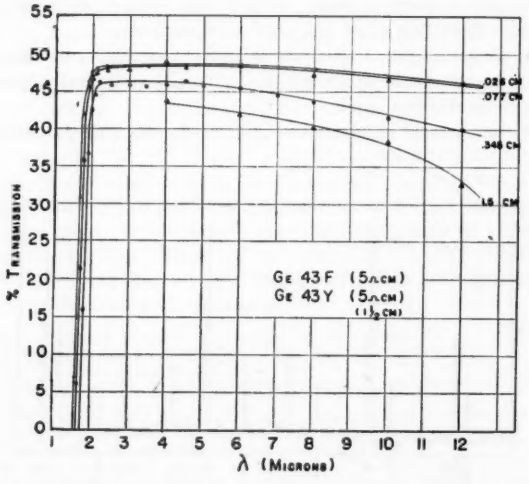

FIG. 1. Percentage transmission of high resistivity Ge as a function of wave-length for various thicknesses. The 1.5-cm sample is from melt 43 Y; the others are from melt 43 F.

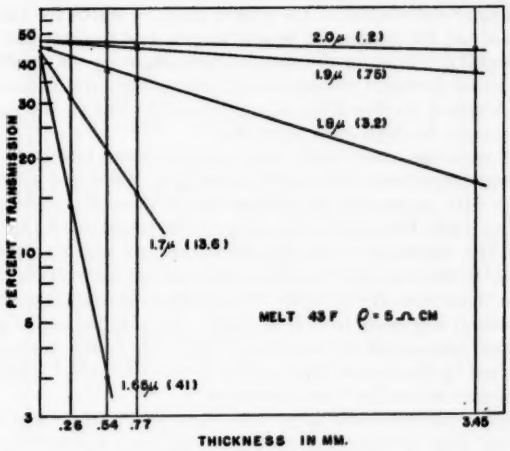

FIG. 2. Percentage transmission of germanium as a function of thickness for various wave-lengths. The figures in the parentheses give the absorption coefficient in cm^{-1} for each wave-length.

Union concentrated arc, or a Nernst glower as light sources, and a vacuum thermopile as detector. Curves for three samples of different thicknesses, 0.26 mm, 0.77 mm, and 3.45 mm, of N-type germanium from the same melt are shown in Fig. 1. The samples are single crystals with reistivity of about 5 ohm cm.[3] Figure 2 gives the logarithm of percentage transmission plotted against sample thickness for different wave-lengths. To determine the absorption coefficient from transmission measurements it is necessary for the samples to have the same reflecting power R. To insure this both surfaces of the samples were optically polished. It is seen from Fig. 2 that at wave-lengths where the absorption is small and the transmission is determined primarily by surface reflections, there is no irregular variation of transmission for the different samples. This shows that the surfaces of the samples as prepared do have nearly the same reflecting power.

If the transmitted light is given by

$$I/I_0=(1-R)^2e^{-\epsilon l}, \quad l=\text{thickness of material},$$

then ϵ and R are determined from the slope and intercepts of the straight lines in Fig. 2. However, when the transmission is high, multiple reflections ot both surfaces have to be taken into account. Starting from known formulas[4] and taking into account the finite width of the spectrum used in the measurement of each point, it can be shown that

$$I/I_0=[(1-R)^2+4R\sin^2x]/(e^{\epsilon l}-R^2e^{-\epsilon l}),$$

where $x=\tan^{-1}[2k/(n^2+k^2-1)]$, n being the index of refraction. The term involving x is negligible in the range of our measurements. Using this expression to analyze the experimental data we find that the reflecting power $R=0.35$ (in agreement with results in I), is constant within the spectrum covered by our measurements. The absorption coefficient, $\epsilon=4\pi kv/c$, is plotted in Fig. 3.

The absorption increases rapidly for wave-lengths below 2μ. For measurements below 1.6 much thinner samples have to be used. For wave-lengths above 2 the absorption is so small that much thicker samples, i.e., several cm, should be used for accurate measurement. A single crystal 15 mm thick was cut from a melt of about the same resistivity, 5 ohm cm. The transmission curve for this sample is included in Fig. 1 and the absorption coefficient, calculated using $R=0.35$, is given in Fig. 3. The absorption coefficient curves for the two similar melts agree in shape and in order of magnitude. The discrepancy may be due to inaccuracy on account of insufficient thickness of samples used.

Similar measurements were made on samples from a melt of much lower resistivity, 0.015 ohm cm. These samples are polycrystalline with 2 or 3 grain boundaries in the light beam. The curve of absorption coefficient is also shown in Fig. 3. The absorption is seen to be higher than that of high resistivity single crystal samples. The reflecting power is constant for the spectrum covered and is the same, $R=0.35$, as for the high resistivity samples.

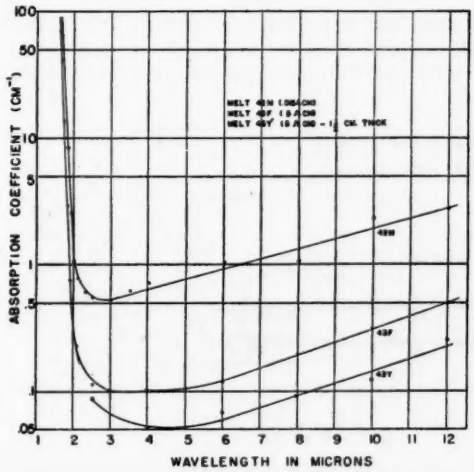

FIG. 3. Absorptivity of germanium as a function of wave-length for different resistivities. The curve for 43 Y is drawn assuming the same reflectivity as the other melts since only one thick piece was available.

* Signal Corps Contract W36-039-sc-38151; Progress Report (February, May, 1949). A summary of this work was presented at the Ad Hoc Crystal Meeting at M.I.T. (June, 1949).

[1] W. H. Brattain and H. B. Briggs, Phys. Rev. **75**, 1705 (1949).

[2] L. R. Ingersoll, Astrophys. J. **32**, 286 (1910).

[3] The authors wish to thank Mr. W. E. Taylor for preparing the single crystal, high resistivity melts.

[4] R. B. Barnes and M. Czerny, Phys. Rev. **38**, 338 (1931).

Optical Properties of Semiconductors. III. Infra-Red Transmission of Silicon*

M. BECKER AND H. Y. FAN
Purdue University, West Lafayette, Indiana
October 3, 1949

LIKE germanium, bulk silicon also shows appreciable transmission in the infra-red. This can be directly demonstrated photographically since high transmission begins at 1.0μ. Type I–Z photographic plates are sensitive to 1.3μ. Spot images of a parallel light beam can be photographed on such plates through a piece of silicon 0.3 mm thick in a few seconds of exposure. (In the case of germanium, high transmission begins at 1.6μ, beyond the sensitivity of the plates. Thirty-six hours of exposure through germanium does not affect the plate at all.)

Using basically the same experimental arrangement described in the companion letter on germanium, transmission measurements were made on low resistivity ($\rho=0.03$ ohm cm) P-type silicon from liquid air temperature to 380°C. The reflecting power deduced from these measurements is constant for the spectral region covered: $R=0.27$, in agreement with earlier measurements by K. Lark-Horovitz and K. W. Meissner. Figure 1 shows the absorption curves for different temperatures. The absorption is seen to decrease with decreasing temperature over the entire spectrum covered by the measurements. The values of extinction coefficient obtained by Ingersoll[1] are several orders of magnitude higher than our results. This may very well be due to the fact that the material used in these early experiments was very impure. For instance, germanium strongly doped with aluminum (~0.005 ohm cm) shows absorptions at least several orders of magnitude higher than the data presented in the companion letter.

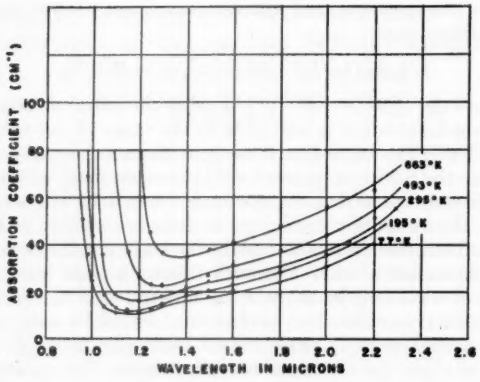

FIG. 1. Temperature dependence of the infra-red absorptivity of low resistivity silicon as a function of wave-length.

The sharp increase of absorption for both germanium and silicon toward short wave-lengths is apparently due to quantum transitions from the filled to the conduction band. The energy gap between these bands as determined from intrinsic conductivity measurements is about 0.76 ev for germanium and about 1.1 ev for silicon. The absorption band is then expected to begin at about 1.6μ and 1.1μ respectively. Our measurements show that at room temperature absorption begins to rise at about 2μ for germanium and at about 1.2μ for silicon. The results for silicon shown in the figure indicate a definite temperature dependence.

For wave-lengths longer than required for excitation between bands absorption can be caused by free electrons and holes. Such absorption can be calculated according to the Drude-Zener theory which gives the conductivity

$$\sigma(\nu)=nk\nu=[\gamma^2/(\nu^2+\gamma^2)]\sigma_0,$$

where σ_0 is the d.c. conductivity, and γ is related to the mobility, b, by

$$\gamma=e/2\pi mb,$$

n being the number of carriers.

The values of b for the samples used were determined by Hall effect and resistivity measurements. The absorption so calculated is only about one-tenth of the observed values for silicon. For germanium the calculated absorption is two to three orders of magnitude too small. This fact has yet to be explained.

* Work supported by the Signal Corps.

[1] L. R. Ingersoll, Astrophys. J. 32, 286 (1910).

Protons from the Bombardment of He^3 by Deuterons*

L. D. WYLY,** V. L. SAILOR,*** AND D. G. OTT
Sloane Physics Laboratory, Yale University, New Haven, Connecticut

September 26, 1949

THE $He^3(d, p)He^4$ reaction has long been a tantalizing gap in experimental studies of nuclear transmutations. The expected Q-value for the reaction can be calculated from the masses of the particles, and is 18.368 ± 0.042 Mev according to the mass tables of Bainbridge.[1] This is larger than any other known Q-value for a d, p reaction. Recently Hatton and Preston[2] observed the reaction at 90° and found a single group of protons which had approximately the expected range. They found no excited states of He^4.

A study of $He^3(d, p)He^4$ has been made at Yale University using a 1.13-cm^3 sample of helium gas containing 88 percent He^3 and 12 percent He^4.† The objectives of this study were to determine the angular distribution of the proton yield, to search for excited states of the He^4 nucleus at several angles, and to determine experimental Q-values for the reaction by measuring the ranges of the emitted protons. Comparison of the experimental Q-value with the calculated Q-value gives an experimental point on the range-energy curve for high energy protons.

The apparatus used in the experiment is shown in Fig. 1. The deuteron beam was collimated by two $\frac{1}{8}$-in. holes and approximately 0.03 μa entered the helium target through a calibrated aluminum foil. The mean beam energy in the target was 3.17 ± 0.05 Mev. The thickness of the aluminum chamber wall was 158 ± 7 mg/cm^2 which was thick enough to stop protons from all reactions except those from $He^3(d, p)He^4$. Protons from the target could be observed at any angle from 0° to 130°. A description of the spectrometer apparatush as been given previously.[3] The solid angle presented by the counter aperture corresponded to the Livingston and Bethe[4] criteria for "good geometry."

The proton yield was large indicating an exceptionally large reaction cross section. Curves of yield *vs.* total absorption were obtained at 0°, 45°, and 90°. Two typical curves obtained at 0° are shown in Fig. 2. Curve A was taken with the discriminator set to accept all pulses slightly larger than noise. For curve B the discriminator was adjusted so that only the largest pulses would record. Curves of type A were used to determine the extrapolated range at each angle. The extrapolated range was converted to mean range according to the procedure outlined by Livingston and Bethe,[4] account being taken of the fact that a small part of the absorbing path was in air and the remainder in aluminum. The proton energy was obtained from the mean range by using the range-energy curves of Bethe.[5] Table I lists for each angle the corrected mean ranges, the proton energies, the experimental Q-values and the proton energy expected from the 18.368-Mev Q-value. The proton ranges taken with the calculated proton energies give experimental determinations of the proton range-energy relation. These points agree with the range-energy curve of Bethe to within ±1 percent, which is the precision of the experiment.

TABLE I. Summary of experimental ranges, proton energies, and Q-values for $He^3(d, p)He^4$ compared with expected proton energies calculated from $Q=18.368$ Mev.

Angle of observation	Mean range (cm)	Proton energy (Mev)	Experimental Q (Mev)	Calculated proton energy (Mev)
0°	423±5	20.6±0.17	18.45±0.17	20.53
45°	367±6	19.2±0.2	18.5±0.2	19.08
90°	269±6	16.1±0.2	18.5±0.2	15.96

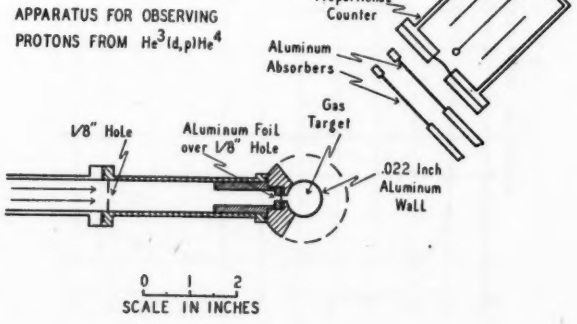

FIG. 1. Target chamber and counter. The target chamber was constructed from an aluminum cylinder; only two gaskets were necessary. Counter and absorbers could be rotated about target so that protons from the target could be observed at any angle from 0° to 130°.

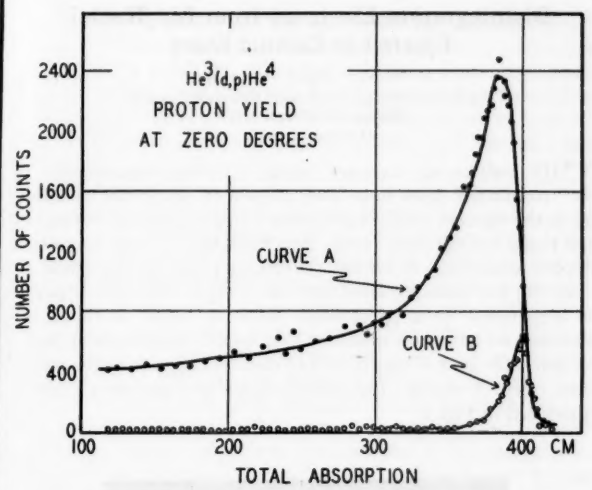

FIG. 2. Proton yield curves for 0° observations. Curves *A* and *B* were taken with different settings of pulse height discriminator. The total absorption is in cm air-equivalent but 26 cm must be added to account for variation in stopping power of aluminum with energy.

At each of the three angles of observation only one group of protons was found. If any other groups are present in the range of absorption studied, their yield is less than 6 percent of the yield of the observed group. Thus no excited states of He^4 lying between ground and 11.4 Mev were produced by the reaction in amounts of as much as 6 percent.

The angular variation of the proton yield was studied at 15° intervals from 0° to 120° with a bombarding energy of 3.17 Mev. At each angle the absorption was set to give the maximum yield. The data were corrected to account for geometrical peculiarities of the chamber including the curvature of the chamber wall. This latter correction proved difficult to evaluate and introduces an uncertainty in the results of as much as 25 percent between the extreme cases of 90° and 0°. The corrected data were transformed to the center of mass system using the usual conversion factors for angle and solid angle. The experimental results are plotted as circles in Fig. 3, in which the yield at each angle has been normalized to the 90° yield and the angle is transformed to the center of mass system. A rough fit to the points is given by the curve which is of the form $1.22+0.60P_2+0.23P_4$, where P_2 and P_4 are the respective Legendre polynomials. It is apparent that the distribution is not isotropic. The yield at 0° is more than twice the yield at 90°.

We would like to express our gratitude to Professor E. C. Pollard, who first proposed the problem and who made the necessary arrangements for performing the experiment. We are also indebted to Professor W. W. Watson for his active interest and assistance.

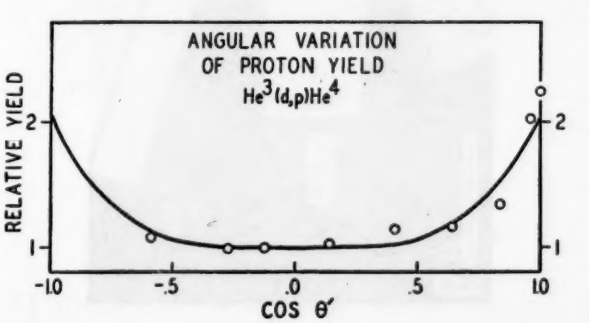

FIG. 3. Angular distribution of proton yield in center of mass system. The deuteron energy was 3.17 Mev. Experimental points are circles having diameters approximately equal to the counting statistics. The solid curve is of the form $1.22+0.60\ P_2+0.23P_4$.

* Assisted by the Joint Program of the ONR and the AEC.
** Now at Georgia School of Technology, Atlanta, Georgia.
*** Now at Brookhaven National Laboratory, Upton, Long Island, New York.
† The He^3 sample was purchased from the AEC.

[1] H. T. Bainbridge, Preliminary Report No. 1, Nuclear Science Series, NRC.
[2] J. Hatton and G. Preston, Nature **164**, 145 (1949).
[3] L. D. Wyly, Phys. Rev. **76**, 104 (1949).
[4] M. S. Livingston and H. A. Bethe, Rev. Mod. Phys. **9**, 245 (1937).
[5] H. A. Bethe, Brookhaven National Laboratory Report No. BNL-T-7.

Note on Methane in the Infra-Red Solar Spectrum

ROBERT R. MCMATH, ORREN C. MOHLER, A. KEITH PIERCE, AND LEO GOLDBERG
McMath-Hulbert Observatory University of Michigan, Pontiac, Michigan
September 23, 1949

IN earlier papers,[1] the writers have described a series of investigations of the infra-red solar spectrum from 1.0μ to 3.6μ, which are being carried out at the McMath-Hulbert Observatory with the McGregor spectrometer and Cashman PbS cells. The program of solar observations has recently been enlarged, as the result of a cooperative arrangement with the Mt. Wilson Observatory. In accordance with this arrangement, the McMath-Hulbert Observatory has constructed and attached to the Snow solar telescope on Mt. Wilson a near-duplicate of the McGregor spectrometer. Various members of the McMath-Hulbert staff are engaged in operating the spectrometer, the cost of which has been financed under a contract with the Office of Naval Research.

In connection with a systematic program of identification of solar and telluric lines in the infra-red, the laboratory absorption spectrum of CH_4 in the region 1.0μ–3.6μ has recently been recorded at Lake Angelus. A d.c. carbon arc was employed as the source of continuous spectrum, and the absorption cell, 25 cm in length, was filled with methane at a pressure of two atmospheres. The dispersion of the tracings, about 3.5 mm/A, is more than sufficient for complete resolution of the rotational structures of the CH_4 bands.

Strong telluric bands of methane have already been recognized as important features of the infra-red solar spectrum between 1.66μ and 3.5μ. Migeotte[2] first called attention to the spectroscopic evidence for atmospheric methane by his identification of the fundamental ν_3 band at 3.3μ. Simultaneously, McMath, Mohler, and Goldberg[3] recorded the overtone band, $2\nu_3$, at 1.66μ and the *Q*-branches of the combination bands $\nu_3+\nu_2$, $\nu_3+\nu_4$, and $\nu_1+\nu_4$ at 2.20μ, 2.32μ, and 2.37μ, respectively. Other combination bands that might be expected to appear in the solar spectrum are $\left\{\begin{matrix}\nu_1+\nu_2+\nu_4\\ \nu_2+\nu_3+\nu_4\end{matrix}\right\}$ at 1.71μ and 1.73μ and $\nu_2+\nu_4$ at 2.43μ.[4] The latter bands, according to Moorhead,[5] do not exhibit *Q*-branches.

The rotational structure of ν_3 and of its first overtone is so extremely regular that the members of the positive and negative branches may be detected in the solar spectrum without reference to the laboratory spectrum of CH_4. The dispersion of the solar tracings is sufficiently high, however, that the splitting of the high series members, due to Coriolis interaction, is plainly visible. On the other hand, the combination bands of CH_4, especially those involving the neighboring frequencies ν_2 and ν_4, are strongly perturbed, and exhibit highly complicated and irregular rotational structures.[6]

The new laboratory tracings of the CH_4 spectrum verify the complexity of the combination bands. The spectrum between 2.15μ and 2.45μ consists of hundreds of individual lines distributed in apparently random fashion between 2.15μ and 2.45μ. Detailed analysis of the spectrum will undoubtedly disclose that the lines are actually arranged in many overlapping series, including, perhaps, several faint bands for which quantum numbers have not higherto been assigned.

A comparison between the laboratory records and solar tracings obtained both at Lake Angelus and at Mt. Wilson shows that all of the CH_4 bands observed in the laboratory are also present in the solar spectrum. Since the bands originate in the earth's atmosphere, the line intensities show a strong dependence upon solar altitude. The two bands at 1.7μ are very weak and require about three air masses (3.3 cm of CH_4 at NTP) for visibility in the solar spectrum. On the other hand, the lines of the four combination bands in the 2μ region are both strong and numerous even on noon-day tracings. About 330 lines of CH_4 in the spectral region 2.15μ–2.45μ appear on solar tracings obtained both at Lake Angelus and at Mt. Wilson with various air masses ranging from 1 to 13. We estimate that between one-third and one-half this number would be produced by a single air mass. Furthermore, about 50 percent of all telluric lines in this spectral region are accounted for by CH_4. The majority, if not all, of the remaining lines, are due to H_2O. It is expected that the water vapor lines can be identified by comparisons between solar tracings obtained under varying concitions of humidity.

We acknowledge with gratitude the continuance of grants-in-aid by McGregor Fund of Detroit.

[1] See summary article by Robert R. McMath and Leo Goldberg, Proc. Am. Phil. Soc. (in press).
[2] M. Migeotte, Phys. Rev. **73**, 519 (1948).
[3] McMath, Mohler, and Goldberg, Phys. Rev. **73**, 1203 (1948).
[4] G. Herzberg, *Infrared and Raman Spectra* (D. van Nostrand Company, Inc., New York, 1945), p. 308.
[5] J. G. Moorhead, Phys. Rev. **39**, 83 (1932).
[6] A. H. Nielsen and H. H. Nielsen, Phys. Rev. **48**, 864 (1935).

Atmospheric HDO

H. A. Gebbie, W. R. Harding, and C. Hilsum
Royal Naval Scientific Service, Admiralty, England
and
V. Roberts
Telecommunications Research Establishment, Ministry of Supply, England
October 4, 1949

THE appearance of the ν_2 absorption of HDO in the solar spectrum has been reported by Adel.[1] In the course of measurements made to determine the absolute transmission of the atmosphere for a horizontal path of 2264 yards over sea, we have found an absorption at 3.67 microns that corresponds to the

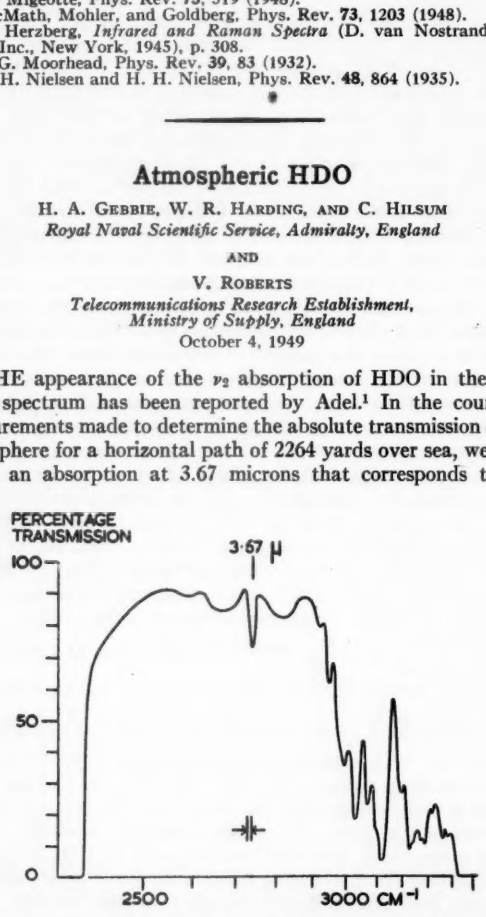

FIG. 1. Atmospheric transmission 2.7–4.3 microns. Path length 2264 yards; precipitable water 17 mm.

Q-branch of ν_1 HDO. Absorptions corresponding to the P and R branches are also observed.[2] Figure 1 shows a typical transmission curve taken with a lithium fluoride prism.

A full account of the work will be published in due course.

[1] A. Adel, Astrophys. J. **93**, 506 (1941).
[2] E. F. Barker and W. W. Sleator, J. Chem. Phys. **3**, 660 (1935).

Disintegration Electrons from Li_3^8 Nuclei Ejected in Cosmic Stars

E. Pickup and L. Voyvodic
Division of Physics, National Research Council, Ottawa, Ontario, Canada
October 3, 1949

THE well-known hammer tracks occurring occasionally in cosmic-ray stars have been shown[1] to be almost certainly due to the ejection of Li_3^8 nuclei which disintegrate at the end of their range leaving Be_4^8, which then splits up into two oppositely directed α-particles. A further convincing proof of this would be to see the Li_3^8 disintegration electron coming from the origin of the α-particles. In a particularly sensitive batch of Ilford G5 emulsions we have now observed four cosmic stars showing hammer tracks, in each of which the Li_3^8 disintegration electron can be clearly seen. A mosaic of photo-micrographs of one such event is reproduced in Fig. 1.

FIG. 1. Photograph of mosaic of photo-micrographs of a 5-pronged cosmic star found in an Ilford G5 emulsion, with Li_3^8 nucleus ejected. This shows the characteristic hammer track, and also the Li_3^8 disintegration electron. The zenithal direction for the event is indicated on the photograph.

Figure 1 shows a 5-pronged star with a Li_3^8 fragment of energy about 17 Mev, two other fragments which end in the emulsion (probably a 2.5-Mev proton and a 22-Mev α-particle), and two probable high energy protons in a downward direction, although we cannot definitely rule out the possibility of one or both of the two latter being mesons. There is no sign of an incident charged particle.

Grain counting on the Li_3^8 electron gave 36 grains/100 microns (253 microns before leaving the emulsion), while a μ-meson decay electron in the same plate gave 37 ± 2 grains/100 microns. For three random light tracks in this plate the counts were 35, 36 and 36 ± 2 grains/100 microns. In another case the Li_3^8 fragment was ejected in a 23-pronged star, which contained only one lightly ionizing fragment, and at least two others heavier than Li_3^8. This event occurred in a plate from another box. The grain counts for the Li_3^8 electron (600 microns before leaving the emulsion) and a π-μ-meson decay electron (800 microns) in the same plate were 34 ± 2 and 36 ± 2 grains/100 microns respectively,and the average count on eleven light random tracks was 32 ± 2 grains/100 microns. The other two Li_3^8 events occurred in 4- and 5-pronged stars, but the disintegration electrons were rather too steep in the emulsion for accurate grain counting. Owing to the possible spread in energy values of the Li_3^8 electron and the meson decay electron it is not possible with these few results to compare the relative ionization values measured with that expected theoretically, but it may be noted that the grain density in the two cases discussed appears slightly lower for the Li_3^8 electron.

The electrons show characteristic scattering, but no measurements have been made. The initial directions of the disintegration electrons relative to that of the α-particles appear fairly random for the four cases observed.

It is hoped to discuss further details of these, and other Li_3^8 events found in C2 emulsions, including examples of B_5^{11}, cosmic-neutron disintegrations in boron loaded emulsions, in a later paper. However, one further point of interest may be made now. Referring to the event in Fig. 1, grain counting (using a long μ-meson in the same plate as a reference) shows that the two lightest tracks in the 5-pronged star would not have been observed in the less sensitive C2 emulsions, and this event would have been described as a 3-pronged star. Similarly, the other 5-pronged star containing a Li_3^8 fragment showed three light tracks, which would not have been detected in C2 emulsions. Thus, it is by no means certain that most of these events can be described in terms of a simple, light element, neutron reaction as was thought might be the case,[1] although there will undoubtedly be some examples of simple, neutron induced reactions.[2]

We are indebted to the Trans-Canada Airlines for carrying our emulsions,[3] to Misses S. Young, B. Mear, and B. Woodruff for the preliminary searching, and to Mr. D. Rushton for preparing the mosaic.

[1] See Franzinetti and Payne, Nature 161, 735 (1948).
[2] As suggested in the above reference; also, in boron loaded plates, examples of events produced by cosmic neutrons similar to the B_5^{11}, fast neutron reaction (E. Pickup, Phys. Rev. 74, 495 (1949). Cases of these have been observed (H. Yagoda and N. Kaplan, Phys. Rev. 75, 1328 (1949); E. Pickup, (unpublished work)).
[3] They were flown at an average height of about 14,000 feet.

Gamma-Ray of K^{40}

G. A. Sawyer and M. L. Wiedenbeck
Randall Laboratory of Physics, University of Michigan, Ann Arbor, Michigan
October 7, 1949

THE gamma-ray activity of K^{40} has been determined by means of a scintillation counter calibrated with a known activity of K^{42}.

The source of the K^{40} radiation was 4 pounds of KCl placed in a cylindrical shell around a crystal of stilbene. The light output of the stilbene was piped through a Lucite rod to two adjacent photo-multiplier tubes, cooled with dry ice (see Fig. 1). The high noise background characteristic of a single photo-multiplier was eliminated since only coincidences between the photo-multipliers were measured. As a result the real counts from the K^{40} (about 0.5 count per second) were more than twice the background.

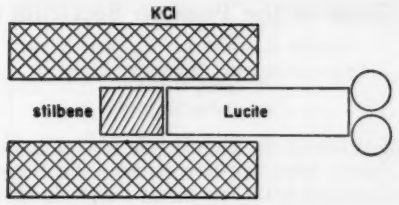

FIG. 1. Geometry used with scintillation counter.

The gamma-ray activity of the K^{40} was then determined by mixing into the 4 pounds of KCl a known activity of K^{42}, also in the form of the chloride. In the decay of K^{42} a single gamma-ray of 1.51 Mev is emitted in 25 percent of the disintegrations.[1] This is almost identical in energy with the 1.55-Mev gamma-ray associated with the decay of K^{40}.[2,3] Thus the ratio of K^{40} activity to K^{42} activity could be obtained directly without corrections for counter efficiency, solid angle subtended, or absorption of the gamma-rays. The activity of the K^{42}, obtained from Carbide and Carbon Chemicals Company, Oak Ridge, Tennessee, was measured by beta-ray counting in a known geometry on five samples of varying strengths placed on thin Nylon backing of 0.6 mg/cm^2. supplementary experiments indicated that the correction for window absorption, scattering from the backing, etc., was less than one percent. Correction was always made for decay of the K^{42}, which has a 12.4-hour half-life.[1] The activities obtained from these five samples are given in Table I.

TABLE I. Source strength of K^{42}.

Source weight in mg	Disintegrations/ g/sec. $\times10^{-6}$
2.30	1.25
2.30	1.17
3.20	1.19
3.55	1.17
4.95	1.21

Five progressively larger amounts of the K^{42} were thoroughly mixed into the K^{40} source and in each case the resulting counting rates were measured. The data obtained are given in Table II.

TABLE II. Counting rate of K^{42}.

K^{42} in mg added to K^{40}	Counts/g/sec.
62	43.0
214	46.2
382	47.2
712	45.6
1262	46.2

The decay of the K^{42} was followed through six half-lives and gave no indication of appreciable impurity. Attempts to detect gamma-gamma-coincidences also gave negative results.

The gamma-activity of K^{40} was found to be 3.6 ± 0.3 gamma-rays/g of ordinary potassium/sec., in good agreement with the values of Gleditsch and Graf[2] (3.6 ± 0.8 gamma-rays/g/sec.) and Ahrens and Evans[4] (3.3 gamma-rays/g/sec.). Further work on the decay scheme of K^{40} is in progress.

[1] K. Siegbahn, Arkiv. f. Mat. Astr. o. Fys. 34B, No. 10 (1946).
[2] E. Gleditsch and T. Graf, Phys. Rev. 72, 640 (1947).
[3] O. Hirzel and H. Wäffler, Helv. Phys. Acta 19, 216 (1946).
[4] L. H. Ahrens and R. D. Evans, Phys. Rev. 74, 279 (1948).

On the Shape of the Positron Spectrum of Cu^{61} *

GEORGE E. OWEN AND C. SHARP COOK
Physics Department, Washington University, St. Louis, Missouri
September 26, 1949

IN considerations of the allowed beta-spectra according to the Fermi theory, there has been evidence[1] for the existence of an excess of particles in the low energy region. In spite of corrections[2] the allowed spectra continue to exhibit an excess of low energy particles. This deviation has been attributed to the finite thickness of the source. Although many quoted source thickness values have appeared to be quite small, deposition of sources from solution has been observed to lead to considerable non-uniformity in the process of crystallization, etc. Thus the quoted figures are merely average values and not true values over the entire surface of the source.

Since the supposedly allowed positron spectrum of Cu^{61} has a low energy excess in evidence below 500 kev, any decrease in the number of low energy particles to be gained through the use of thinner sources should be readily apparent in this spectrum. To check the existance of this marked deviation in the Cu^{61} spectrum, a method has been developed by which carrier-free sources of Cu^{61} can be evaporated onto a backing, providing very thin and uniform sources.

Cu^{61} was prepared by a $(d, 2n)$ reaction on Ni^{61}. The active copper was then electroplated onto a 0.01-inch diameter tungsten wire.[1] This tungsten was then used as the heated filament from which the Cu^{61} was evaporated onto a source backing of 0.00025-inch aluminum foil. The image was formed by an aluminum mask fitted over the source backing. This aluminum backing was necessary since thinner Zapon foils, when placed at the required ½-inch distance, will not withstand the excessive heat from the hot filament.

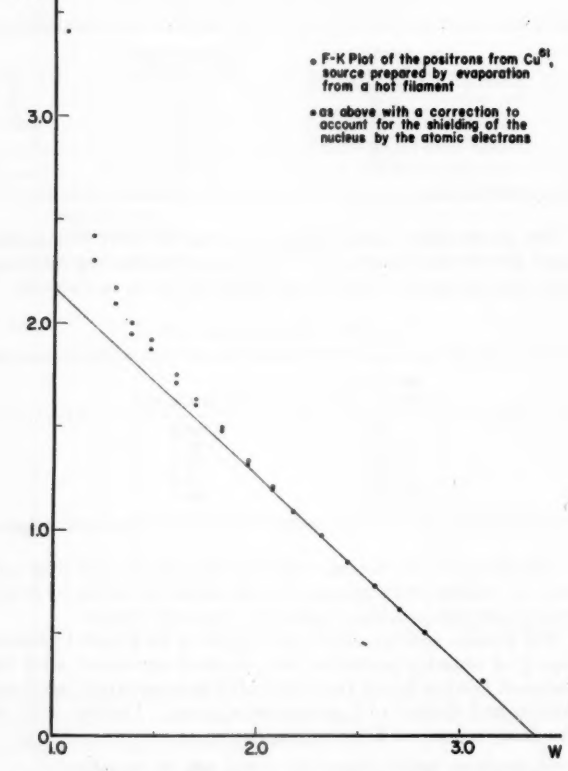

FIG. 1. F−K plot of the spectrum of an evaporated source of Cu^{61} showing the effect of applying the shielding correction of Rose.

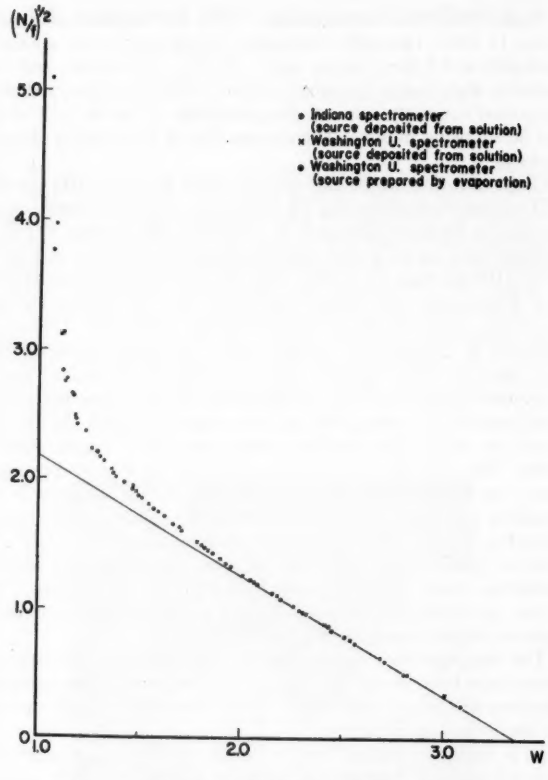

FIG. 2. Comparison of the F−K plots of Cu^{61} taken under conditions as discussed in the text.

Using the relative shapes and intensities of the 47-kev and 330-kev lines of I^{131}, a series of independent experiments has indicated that distortions at energies greater than 47 kev resulting from back-scattering are negligible.[3]

After preparation by evaporation, the source of Cu^{61} *could not be seen visually and could only be detected by its activity.* The fact that all the atoms plated onto the wire are radioactive copper atoms allowed an estimation of the thickness by calculations derived from the amount of activity present on the source backing. These give a calculated thickness of 10^{-4} microgram per square centimeter. This is considerably less than one complete atomic layer and corresponds to a random distribution of single atoms.

The positron spectrum was then studied in a 6-cm radius of curvature spectrometer set to a resolution giving 1.2 percent at half-maximum for an internal conversion line.[4]

Figure 1 shows the F−K plot with and without the shielding correction of Rose.[5] It is evident that the deviation below 500 kev remains.

Figure 2 illustrates the comparison of the F−K plots of the Cu^{61} spectrum as obtained from two different spectrometers and three different sources:

A. The 40-cm radius of curvature Indiana spectrometer using a source of less than 40 $\mu g/cm^2$ prepared from solution on a Zapon backing
B. The 6-cm radius of curvature spectrometer at this laboratory using a source of less than 40 $\mu g/cm^2$ prepared from solution on a Zapon backing
C. The same 6-cm radius spectrometer using the source of $(10)^{-4}$ $\mu g/cm^2$ prepared by evaporation.

It is significant that all the spectra taken under such widely different conditions have produced identical results. Also it is difficult to account for this consistant deviation by instrumental distortions.

This work has been assisted by the Joint Program of the ONR and AEC.

* Since the submission of the manuscript for the accompanying letter to the editor, the positron and negatron spectra of Cu^{64} have been studied using identical techniques. The resulting F−K plots show no deviation from a straight line as low as 50 kev. This suggests the possibility of the existence of a forbidden spectrum or complex disintegration in the case of Cu^{61}. However, the possibility of a forbidden transition does not seem reasonable in view of the fact that the *ft*-value for this isotope predicts an allowed transition.

[1] C. S. Cook and L. M. Langer, Phys. Rev. **73**, 601 (1948); **74**, 227 (1948).
[2] G. E. Owen and H. Primakoff, Phys. Rev. **74**, 1406 (1948); C. S. Wu and R. D. Albert, Phys. Rev. **75**, 1107 (1949).
[3] Further details of this experiment will be published.
[4] G. E. Owen and C. S. Cook, Rev. Sci. Inst. **20**, 768 (1949).
[5] M. E. Rose, Phys. Rev. **49**, 727 (1936); C. Longmire and H. Brown, Phys. Rev. **75**, 1102 (1949).

A. Germanium Counter

KENNETH G. MCKAY
Bell Telephone Laboratories, Murray Hill, New Jersey

September 29, 1949

WHEN insulating crystals, such as diamonds, are used as crystal counters of nuclear particles, a complicating factor is the trapping of mobile charge carriers in the crystal. This results in a broad pulse height distribution and the development of internal space charge fields. These effects can be greatly minimized for bombarding particles of high specific ionization by using a very thin crystal together with a high electric field. A method of obtaining the equivalent of this is to use a barrier layer in a semiconductor. The properties of the barrier layer in germanium under a point contact are such that one can calculate under what circumstances it could be used as a counter.[1]

Figure 1 shows the equivalent circuit to be considered where R_b, C_b represent the constituents of the barrier impedance, R_i, C_i those of the amplifier input, and R_s the series resistance of the body of the germanium. By applying a reverse bias to the barrier, we can insure that $R_b \gg R_s$ and thus neglects R_s completely. The equivalent circuit then reduces to a simple parallel RC circuit where $R=R_bR_i(R_b+R_i)^{-1}$ and $C=C_i+C_b$. Bombardment of the barrier by an alpha-particle produces free electrons and positive holes in the barrier region which are then swept out by the barrier field aided by the applied field. The time taken to sweep the carriers out of the barrier region is assumed to be short compared with the RC relaxation time, so that this action is equivalent to the production of an impulse current across the barrier layer, resulting in a peak voltage across the barrier of $v=Q/C$ where Q is the effective charge transported across the barrier. We require that C be small enough to give an adequate signal-to-noise ratio thus limiting the maximum area of the barrier that can be employed. The noise power per unit cycle from a barrier varies inversely with the frequency and increases with increasing bias.[2] Consequently, it is important to eliminate the low frequency noise components and to operate at as low a bias as possible. We also require that the relaxation time RC be long compared with the amplifier rise time. The relaxation time of a barrier in *N*-type high back-voltage germanium is of the order of 0.1μ sec. or less,

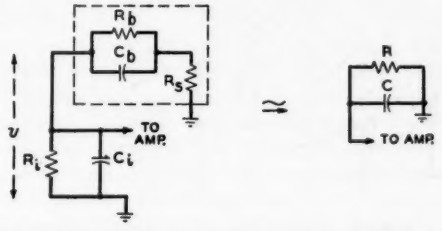

FIG. 1. Equivalent circuit of germanium crystal and amplifier input.

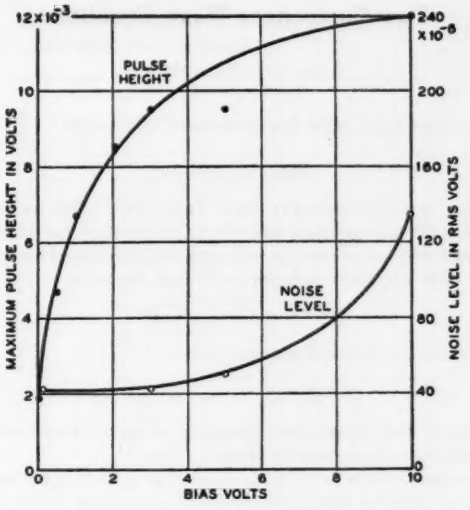

FIG. 2. Observed maximum pulse height and noise level as a function of applied bias.

thus requiring rather wide band amplification. This relaxation time can be increased by reducing the barrier capacity to less than the amplifier input capacity which condition also results in the maximum pulse voltage.

Experimentally this condition was realized by setting a phosphor bronze point contact down on the face of a piece of *N*-type high back-voltage germanium. A large area ohmic contact was made to the opposite face of the germanium. The point was biased negatively with respect to the germanium and was connected to the input of an amplifier covering the frequency range of 100 kc to 15 mc. The barrier capacity was less than 1 $\mu\mu$f and the total input capacity was 17 $\mu\mu$f. The point exhibited a typical rectifier current-voltage characteristic, and the contact area was photo-sensitive. An uncollimated polonium alpha-source was placed near the contact area. The resultant pulses, as displayed on an oscilloscope, showed a broad distribution in pulse height owing presumably to the passage of some alpha-particles near the edges of the sensitive region. However, the maximum pulse height was well defined and is shown in Fig. 2 as a function of bias. The pulse shape agreed with that calculated from the circuit constants; the pulse rise time was apparently limited by the amplifier from which we can only conclude that it was less than 0.05 μsec. It should be noted that pulses are observed at zero bias as a result of the action of the barrier field alone. The maximum observed pulse height corresponds to the passage of 10^6 electronic charges across the barrier per alpha-particle. The current multiplication factor at the collector point has not been determined.[1] The sensitive region has a diameter of between 10^{-3} and 10^{-2} cm.

In another test a commercial Western Electric Type 400 B germanium rectifier was cut open and the wax impregnation removed. It was inserted in the circuit and the results obtained were essentially the same as those described above.

The fast rise and recovery times should commend this counter for high speed or coincidence counting. It will respond effectively only to particles with a high specific ionization, thus discriminating against betas etc. The small sensitive volume renders it spatially selective. Trapping apparently does not play an observable role. The sensitive area could be increased by using a different geometry or by using a $P-N$ junction, the maximum area being subject to the restrictions discussed above.[3] After bombardment by about 10^{13} alphas/cm^2, the counting efficiency should change but the original condition can be restored by a suitable heat treatment.

[1] J. Bardeen and W. H. Brattain, Phys. Rev. **74**, 230 (1948).
[2] J. A. Becker and J. N. Shive, Elec. Eng. **68**, 215 (1949).
[3] Shockley, Pearson, and Sparks, Phys. Rev. **76**, 180 (1949).

Two-Component Wave Equations

J. SERPE
University of Liège, Belgium
October 4, 1949

IN a recent note Jehle[1] has considered the system

$$\gamma^k(\partial_k - i\varphi_k)\psi = \mu\psi^* \tag{1}$$

involving a two-component wave function ψ and its complex conjugate ψ^*; the notation $\partial_k (k=0, 1, 2, 3)$ is used for $\partial/\partial x_k$; φ_k is a real external four-potential, μ a real constant; the four matrices γ^k and their complex conjugates γ^{k*} obey the rules

$$\tfrac{1}{2}(\gamma^{k*}\gamma^\lambda + \gamma^{\lambda*}\gamma^k) = -g^{k\lambda}1, \tag{2}$$

where 1 denotes the unit matrix, and

$$g^{00}=1, \quad g^{11}=g^{22}=g^{33}=-1, \quad g^{k\lambda}=0 \quad \text{if} \quad k\neq\lambda.$$

Kilmister[2] has investigated an aspect of the relationship of such two-component equations to Dirac's system.

The object of this letter is to show that Jehle's equations may be used to describe Majorana particles[3] interacting with a pseudovector field.

We first split ψ and γ^k into their real and imaginary parts, putting

$$\psi = \psi_R + i\psi_I, \tag{3}$$

$$\gamma^k = \gamma_R{}^k + i\gamma_I{}^k. \tag{4}$$

Since ψ_R and ψ_I have two components we may write the wave function as a four-row real matrix

$$\Psi = \begin{vmatrix} \psi_R \\ \psi_I \end{vmatrix}. \tag{5}$$

In this way the system (1) may be written

$$\Gamma^k(\partial_k - \Gamma\varphi_k)\Psi = \mu\Psi, \tag{6}$$

where

$$\Gamma^k = \begin{vmatrix} \gamma_R{}^k & -\gamma_I{}^k \\ -\gamma_I{}^k & -\gamma_R{}^k \end{vmatrix}, \qquad \Gamma = \begin{vmatrix} \cdot & \cdot & -1 & \cdot \\ \cdot & \cdot & \cdot & -1 \\ 1 & \cdot & \cdot & \cdot \\ \cdot & 1 & \cdot & \cdot \end{vmatrix}. \tag{7}$$

Using Eqs. (7) and (2), we find that the Γ^k obey Dirac's anticommutation relations, i.e.:

$$\tfrac{1}{2}(\Gamma^k\Gamma^\lambda + \Gamma^\lambda\Gamma^k) = -g^{k\lambda}1. \tag{8}$$

The Γ^k are real. Moreover it can be seen on the examples given by Jehle that Γ^1, Γ^2, Γ^3 and $i\Gamma^0$ may be taken as Hermitian; they give then a Majorana representation of Dirac's matrices. We also see that Γ anticommutes with the four Γ^k and that $\Gamma^2=-1$. Thus

$$\Gamma = \pm i\Gamma^5, \tag{9}$$

where

$$\Gamma^5 = i\Gamma^0\Gamma^1\Gamma^2\Gamma^3. \tag{10}$$

Both signs in Eq. (9) may occur, as can be seen directly on the two special examples given by Jehle.

Finally, Jehle's system becomes

$$\Gamma^k(\partial_k \pm i\Gamma^5\varphi_k)\Psi = \mu\Psi. \tag{11}$$

This equation, with Ψ quantized, may describe Majorana particles of "charge" ± 1 interacting with a pseudovector field φ_k. Considered from this point of view, it is covariant for the complete Lorentz group including reflections.

Jehle's formulation of Majorana's theory is easily extended to the case where there is an interaction with a real scalar field S and a real pseudoscalar field P. In this more general case, the wave equation can be written (assuming unit "charges")

$$\gamma^k(\partial_k - i\varphi_k)\psi = (\mu + S + iP)\psi^*. \tag{12}$$

[1] H. Jehle, Phys. Rev. **75**, 1609 (1949).
[2] C. W. Kilmister, Phys. Rev. **76**, 568 (1949).
[3] E. Majorana, Nuovo Cimento **14**, 171 (1937).

The Effect of Nuclear Shells upon the Pattern of the Atomic Species

WILLIAM D. HARKINS
University of Chicago, Chicago, Illinois
September 6, 1949

THE principle of regularity and continuity of atomic species, as developed by the writer, continues the thorium radioactive series down through the stable species to helium 4, and the uranium series to neon 22 and on to hydrogen 2. Harkins and Popelka[1] have shown that all of the species of the uranium series from Pb 206 to H 2 are stable, with the exception of Sr 90, which is adjacent to, but not at the end of the 50-neutron shell. In the thorium-helium series 5 are unstable, but all of these are near, but not at, the end of the 50- or 82-neutron shells.

The purpose of the present communication is to exhibit other effects of these "magic numbers" upon the pattern of the stable atomic species. It is shown that the *neutron magic numbers* have a much greater effect than the corresponding proton numbers.

Figure 1 gives the pattern in such a form as to emphasize the limits of the valley of stability, which, on account of the existence of series, are somewhat irregular. The "magic" neutron numbers are represented by lines which are somewhat curved. The lower limit of stability is of interest. Up to MN 20 it lies on the x axis $N/P=1$, or the isotopic number $I=0$. Above that no stable species lies below the straight line from $_{20}{}^{20}Ca_0{}^{40}$ to $_{80}{}^{116}Hg_{36}{}^{196}$, where the values represent $_P{}^N E_I{}^A$, where E is the element in question, P is the proton or atomic number, I, the isotopic number, or number of extra neutrons and A the atomic mass.

Figures 2a and 2b present the simplest plot. This gives all of the stable species. Also the naturally radioactive species of the U and Th series above $_{81}$Tl. The most abundant species are designated by a line around the symbol, and those below or slightly above 1 percent of the element by an open circle. Above $P=32$ these rare isotopes have the lowest neutron content, below this often the highest.

Very marked is the fact that for neutron $MN=50$ there are 6 species and 3 of these are the most abundant for the element. For neutron $MN-82$ (MN=magic number) there are 7 species with 5 the most abundant for the element.

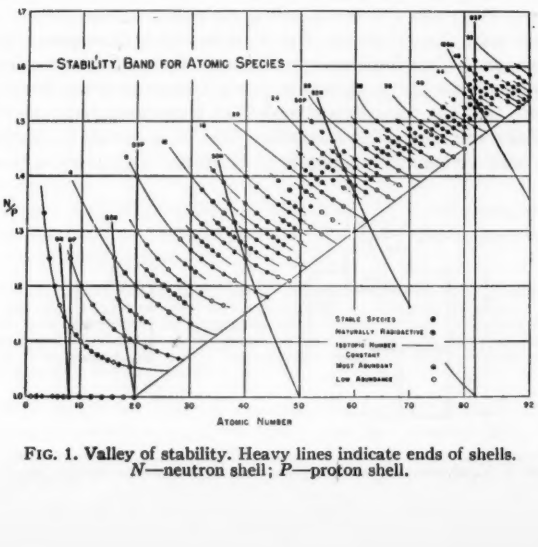

FIG. 1. Valley of stability. Heavy lines indicate ends of shells. N—neutron shell; P—proton shell.

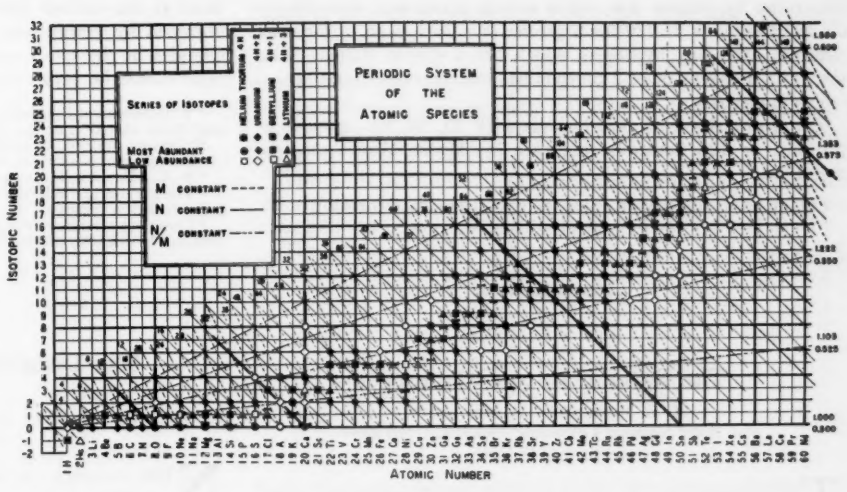

FIG. 2a. Stable atomic species to atomic number $P=60$. Heavy lines indicate ends of shells. N—neutron shell; P—proton shell.

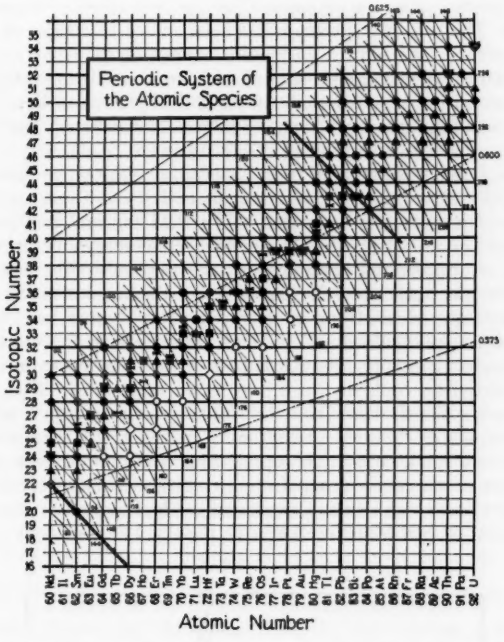

FIG. 2b. Stable atomic species. Atomic number $P=60$ to 81. Heavy lines indicate ends of shells. N—neutron shell; P—proton shell.

The most marked effect of a proton MN is shown at calcium = 20 where $_{20}Ca_{28}^{48}$ would presumably not exist if it were not at the end of a proton shell. This distorts the pattern. The region of few isotopes is just below this, but the neutron MN 20 gives 4 species with 2 of them the most abundant for the element. The 82-proton and 126-neutron magic numbers extend into the region of natural radioactivity, but even there the former is represented by 3 stable isotopes and the latter by 2, and both of these 2 are the most abundant isotopes.

A chart which emphasizes the effect of "magic numbers" on existence and isotopic number (extra neutrons) of the most abundant isotope is presented in Fig. 3, where the values for the *odd* elements are connected by a line, and those for the even elements are not so connected. It is remarkable that for $P=9$ to 30 the number of extra neutrons (I) is represented by higher values for odd than for even elements, but for 32 to 77 the values of I for even elements lie above the line for odd elements. The shift occurs just where the region of abundant species changes to that of rare species. Just at Ni_{28}, where the shift occurs, the number of extra neutrons becomes specially low (2).

The remarkable feature of the figure is the break which occurs just above the 50- and the 82-*neutron shells*. Here element 43, *which has no stable isotope*, lies just above the end of the 50-neutron shell, and 61, again with no stable isotope, just above the end of the 82-neutron shell. Neither the proton shells nor the 20- or 126-neutron shells have such a marked effect upon the relations discussed here.

In a paper submitted in July the abundance of nuclear species is considered in terms of even and odd P and even and odd N. This shows in a much more marked way the effects of the proton "magic numbers." This method of treatment of even and odd P was introduced in 1915 (1920 for even and odd N) by the writer, but even yet prominent workers classify according to even or odd $A=P+N$, which obscures certain of the relations, since odd +odd=even.

The effect of a proton magic number may be illustrated by tin at the ends of the 50-proton shell. Since the number of protons is greater than 30 it is a somewhat rare element. However, the effect of the end of the shell is shown by the fact that *it is much more abundant than any other element from $P=41$ to $P=92$*, and is, for example, 24 times more abundant than cadmium ($P=48$), which has the next lower even atomic number.

In 1915–17 the writer developed what has become known as Harkins rule, that the elements of even number are very much more abundant than those of odd number. However, the remainder of the rule is usually forgotten. This is that the atomic species which contain an even number of neutrons are very much more abundant than those in which the number is odd.

Thus 2 is the most important of the magic numbers. This is

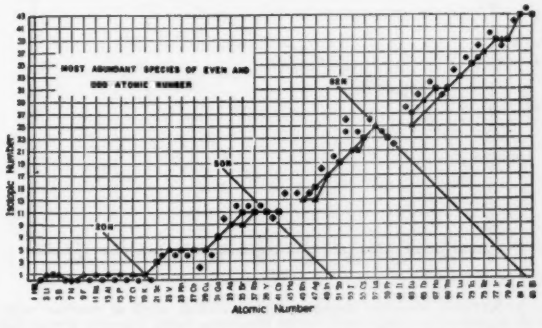

FIG. 3. Most abundant isotopes of the elements of odd and of even atomic number. Heavy lines indicate ends of shells. N—neutron shell; P—proton shell.

illustrated by helium p_2n_2 *whose cosmic abundance, according to the latest estimate, is 120 times greater than that of all of the other elements,* excluding hydrogen, which has a simple nucleus. This shell of 2 neutrons or of 2 protons has not received the attention which it merits.

For a discussion of closed shells with 20, 50, 82 neutrons or protons, or 126 neutrons, a paper by Maria Mayer may be consulted.[2]

[1] W. D. Harkins and M. Popelka, Jr., Phys. Rev. **76**, 989 (1949).
[2] M. G. Mayer, Phys. Rev. **74**, 235 (1948).

The Ratio of L_I to K Capture*

M. E. Rose and J. L. Jackson**
Oak Ridge National Laboratory, Oak Ridge, Tennessee
September 29, 1949

THE phenomenon of orbital electron capture from the L_I shell was observed recently by Pontecorvo, Kirkwood, and Hanna[1] in A^{37}. The experimental value of the ratio of probabilities for L_I to K capture was reported to be between 8 and 9 percent. As was mentioned in reference 1 a computed ratio of only 6 percent is obtained using relativistic wave functions with Slater screening constants.[2]

It is possible to use a much better representation of the screening and we have calculated the L_I to K capture ratio using (1) relativistic wave functions computed on the Eniac by J. Reitz[3] with a potential function obtained from a Thomas-Fermi field with exchange and (2) self-consistent field wave functions.[4] In the case of the relativistic wave functions the small screening for the $1s$ wave function was not considered and an extrapolation had to be carried out since the $2s$ wave functions are available for $Z=29$, 49, 84 and 92 only. Since the ratio is not very sensitive with Z (see Fig. 1), this extrapolation seems safe enough. The Hartree wave functions used for A included the effect of exchange and the neglect of non-relativistic effects makes a rather trivial error in the case of A. The results are:

	L/K ratio
(1) relativistic wave functions	8.2 percent
(2) Hartree wave functions	8.1 percent

and the agreement with the observed value is all that could be desired.

The L/K ratio for other values of Z may be obtained from Fig. 1, curve (1) for medium and heavy atoms and curve (2) for light atoms. In Fig. 1 the square of the ratio of the $2s$ to $1s$ wave functions at the nuclear radius is shown. The L/K capture ratio is obtained by multiplying by the square of the ratio of neutrino energies in the two cases,[2] but in almost every case this latter ratio should be very close to unity.

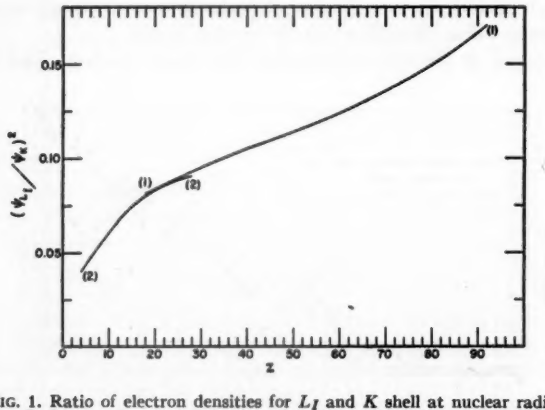

FIG. 1. Ratio of electron densities for L_I and K shell at nuclear radius *versus* Z. Curve (1): relativistic wave functions with Thomas-Fermi field plus exchange. Curve (2): Hartree self-consistent field wave functions. To obtain ratio of L_I to K capture multiply by square of ratio of neutrino energies in the two cases, $(E_{L_I}/E_K)^2$.

* This document is based on work performed under Contract No. W-7405, eng 26 for the AEC at the Oak Ridge National Laboratory.
** Present address, New York University.
[1] Pontecorvo, Kirkwood, and Hanna, Phys. Rev. **75**, 982 (1949).
[2] R. E. Marshak, Phys. Rev. **61**, 431 (1942).
[3] The authors are indebted to Dr. Reitz for a pre-publication copy of these wave function tables.
[4] Complete references are to be found in D. R. Hartree, Reports on Progress in Physics, XI (1946–47).

The Disintegration Scheme of Tm^{170}

J. S. Fraser
Radiation Laboratory, McGill University, Montreal, Quebec, Canada
September 27, 1949

NEW evidence for the complexity of the beta-ray spectrum of 127-day Tm^{170} has been obtained by the use of a thin lens spectrometer supplemented by β-γ-coincidence measurements. The beta-ray spectrum has been shown to consist of two components; one with a maximum energy of (970±5) kev as reported previously, and a second with an endpoint of (886±5) kev comprising approximately 10 percent of the transitions. The single weak gamma-ray,[1–4] largely internally converted, has been found to have an energy of (83.9±0.2) kev.

The source was prepared from "Specpure" Tm_2O_3 irradiated in the Chalk River pile to give a specific activity of 5 mc/mg. The source thickness was estimated to be 0.25 mg/cm² and it was mounted on a 0.03 mg/cm² Nylon film rendered conducting by a layer of evaporated aluminum (0.02 mg/cm²). The counter window was made up of Nylon films to a thickness of 0.055 mg/cm² and passed electrons of energy greater than 7 kev. Good statistics were obtained and the high energy end of the spectrum was studied carefully. The Kurie plot of the beta-spectrum using the relativistic coulomb correction factor is shown in Fig. 1. If the assumption is made that the higher energy group is of the allowed shape, then the discontinuity in the Kurie plot is indicative of a weak beta-ray group of lower maximum energy. Subtraction of the main group from the total yields a reasonably straight line which when extrapolated to the energy axis gives an end point of (900±20) kev (curve C, Fig. 1). The rise of the curve

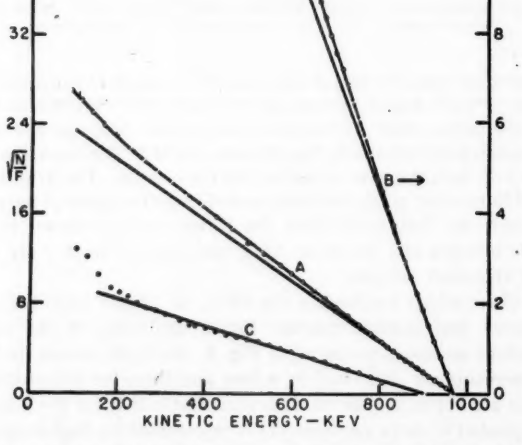

FIG. 1. Kurie plot of the Tm^{170} beta-spectrum. Curve A is the curve of the experimental points, curve B is the high energy end plotted with an expanded ordinate scale, and curve C is obtained by subtracting the main group.

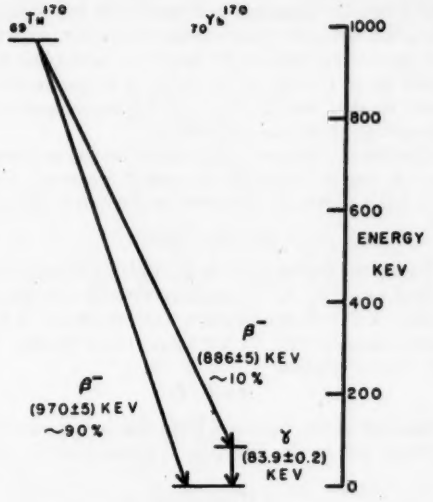

FIG. 2. Tentative decay scheme for Tm^{170}.

above the straight line at energies less than 240 kev is assumed to be due to scattering within the source.

A second source of 0.1 mg/cm² on a 0.5 mg/cm² aluminum backing was used to check the efficacy of the method of grounding the first source. The locations of the conversion lines and the end point agreed, within the accuracy of calibration, with those obtained with the first source. The effects of scattering in the source were slightly decreased in the thinner source.

The energy of the gamma-ray was computed from the K, L, and M conversion lines on the beta-spectrum at 22.6, 73.5, and 81.2 kev respectively as well as from the L and M photo-electron lines using a 15.3 mg/cm² lead radiator. A search for other gamma-rays[4] using a 40-mc source with lead and uranium radiators yielded a negative result.

The significant result obtained from the coincidence experiments was the very low ratio of beta-gamma-coincidences to beta-rays. A brass-cathode gamma-counter and a 2.1 mg/cm² mica end-window beta-counter were used in conjunction with a coincidence mixer of 0.45-microsecond resolving time. An aluminum absorber, 16 mg/cm², was placed before the beta-counter to avoid registering coincidences between conversion electrons and x-rays.

For the simple decay scheme previously proposed,[2,3] the ratio of the beta-gamma-coincidence rate, $N_{\beta\gamma}$, to the beta-counting rate should be equal to ϵ_γ, the efficiency of the gamma-counter in the experimental geometry. For the decay scheme depicted in Fig. 2 this ratio will be $N_2(1-\alpha)/(N_1+N_2)\epsilon_\gamma$, where N_1 refers to beta-particles in the group going to the ground state, N_2 to the lower energy group and α is the ratio of converted gamma-rays to N_2. The value of ϵ_γ for 84-kev gamma-rays was measured by calibrating the coincidence apparatus with Co^{60} gamma-rays and by referring to a semi-empirical efficiency curve for a similar counter.[5] The result was $\epsilon_\gamma=(2.9\pm0.2)\times10^{-4}$. The average of the two experimental values obtained for the ratio $N_{\beta\gamma}/N_\beta$ is $(3.05\pm1.0)\times10^{-6}$. The inference is that the factor $N_2(1-\alpha)/(N_1+N_2)$ is of the order 0.01. The Kurie plot analysis of the beta-spectrum leads to a value of approximately 0.1 for the ratio $N_2/(N_1+N_2)$. Thus $\alpha\cong0.9$.

The conversion coefficients were also measured from the ratios of the height of the lines above the continuum to the area corresponding to the group N_2. The line heights were corrected approximately for window absorption after a method described by Witcher,[6] using Nylon absorbers before the counter window. The results are $\alpha_K=0.08$, $\alpha_L=0.55$, and $\alpha_M=0.17$ so that $\alpha=0.80$.

The low beta-gamma-coincidence rate obtained here is in fair agreement with that obtained by Ketelle[7] who states that the gamma rays are in coincidence with not more than 10 percent of the beta-rays.

The result would be consistent with the simple decay scheme only if the gamma-ray were converted more than 90 percent whereas the experimental value would be about 8 percent referred to the simple scheme. A decay scheme which is consistent with all of the present results is given in Fig. 2.

The resolving power of the coincidence-absorption method used by Graham and Tomlin[3] is probably too low to distinguish between the two proposed decay schemes.

The author wishes to express his appreciotion to Professor J. S. Foster, for his help and advice throughout this work and to Dr. D. G. Douglas for valuable discussions and assistance.

[1] G. T. Seaborg and I. Perlman, Rev. Mod. Phys. 20, 585 (1948).
[2] D. Saxon and J. Richards, Phys. Rev. 76, 186 (1949).
[3] R. L. Graham and D. H. Tomlin, Nature 164, 278 (1949).
[4] P. J. Grant and R. Richmond, Nature 163, 840 (1949).
[5] G. F. von Droste, Zeits. f. Physik 100, 529 (1936).
[6] C. M. Witcher, Phys. Rev. 61, 32 (1941).
[7] B. H. Ketelle (private communication to the author).

Erratum: Altitude Dependence of Penetrating Particles Slowed Down After Traversing 15 Cm of Lead

[Phys. Rev. 76, 851 (1949)]

MARCELLO CONVERSI
Institute for Nuclear Studies, University of Chicago, Chicago, Illinois

THE numbers per hour of mesons (M) and of X-particles (X) stopped in the absorber must be multiplied by the factor 1.6×10^{-7} (not 1.1×10^{-7} as stated in the paper) in order to obtain the corresponding absolute numbers per sec., g, sterad. The ordinate of Fig. 1 must be multiplied, accordingly, by (1.6/1.1).

The "true anticoincidences" at 30,000 feet, in the fourth line of Table I, are 925±30 per hour (not 985±30).

Magnetic Multipole Internal Conversion

N. TRALLI AND I. S. LOWEN*
Physics Department, Washington Square College, New York University, New York, New York

September 30, 1949

IN a previous letter[1] on the calculation of magnetic internal conversion coefficients in the Pauli approximation curves of the ratio of the coefficients in the K shell to those in the L shell

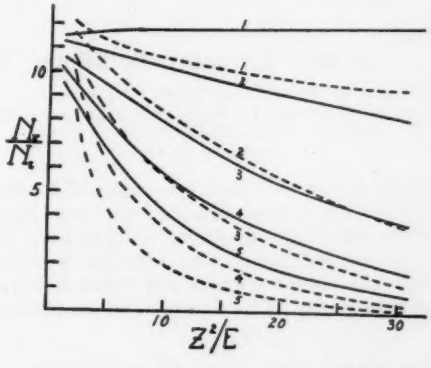

FIG. 1. Curves for N_K/N_L as a function of Z^2/E. Solid line, magnetic multipole; broken line, electric multipole.

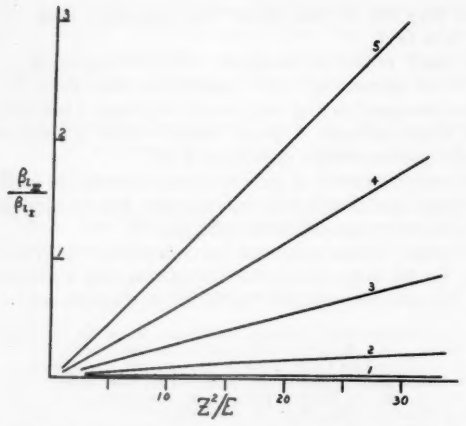

FIG. 2. Curves for the ratio of the magnetic internal coefficient for the L_{III} sub-shell to those for the L_I sub-shell as a function of Z^2/E.

versus Z^2/E for $Z=35$ and E, the gamma-ray energy in kev, were given for multipole orders $l=1, 2, 3$. The calculations have been extended to cover multipole orders 4 and 5. Figure 1 shows the complete set of curves. For the sake of comparison, the curves of Hebb and Nelson[2] for the electric multipole conversion ratios are included.

In Fig. 2 the ratio of the magnetic internal conversion coefficients for the L_{III} sub-shell to those for the L_I sub-shell has been plotted against Z^2/E for $Z=35$. Since, in this approximate theory, the magnetic internal conversion for the L_{II} sub-shell is less than 5 percent of that for the L_I sub-shell, these curves provide an additional method for determining the type of magnetic multipole radiation.

The curves of Figs. 1 and 2 are valid for low Z and low gamma-ray energy. However, the exact calculations of Rose and his co-workers[3] show that, in the K shell, the approximate method gives very poor results for the internal conversion coefficients for Z as low as 40 and energies as low as 150 kev. Of course, if one is concerned with lower values of Z, say about 25, and smaller gamma-ray energies, better agreement of approximate with exact calculations may be expected. In any case it is possible that the ratios given by the approximate method may be better than the values of the internal conversion coefficients. This point will be settled when the exact calculations for the L shell are completed. Until then the curves should be used with extreme caution.

* Deceased.
[1] I. S. Lowen and N. Tralli, Phys. Rev. **75**, 529 (1949).
[2] M. H. Hebb and E. Nelson, Phys. Rev. **58**, 486 (1940).
[3] M. E. Rose *et al.* Phys. Rev. (to be published).

A New Gyromagnetic Effect

S. J. BARNETT AND LOUIS A. GIAMBONI
University of California, Los Angeles, California, and California Institute of Technology, Pasadena, California
September 30, 1949

THE existence of this effect was suggested to one of us by Professor Albert Einstein a number of years ago. Not long afterward the quantitative theory was developed, and experiments instituted to test its validity. Circumstances, however, made it necessary to stop the work temporarily before it was completed, and only recently has its continuance become practicable, with the same magnetic materials and much the same experimental procedure, but with great improvements in many particulars.

A long circular cylinder of the substance under investigation is magnetized along its axis to intensity of magnetization J_s near saturation, so that the moments of all the magnetic elements point essentially in the same direction, Z.

In a direction X, normal to Z, a small magnetic intensity with frequency f, much below the resonance frequency, is applied. When the rod is absent the intensity in the space it is to occupy is

$$H_x=H_{ox}\sin 2\pi ft.$$

This causes the intensity of magnetization (always practically parallel and equal to J_s) to oscillate through the small angle θ in the plane XZ, thus producing a small intensity of magnetization J_x, synchronous with H_x and proportional thereto. The angle θ is given by the relation

$$\theta=J_x/J_s.$$

The rotation of the elements gives rise to a gyromagnetic intensity in the rod in the direction Y (normal to X and Z) such that[1]

$$H_y=\rho d\theta/dt$$

where ρ is the gyromagnetic ratio.

If the rod is infinite in length, there results an intensity of magnetization in the direction Y given by the formula

$$J_y=\rho f/2\pi\cdot[(\mu-1)/(\mu+1)]^2(H_{ox}\cos 2\pi ft)/(J_s)$$

where μ is the transverse permeability of the material.

From this formula, after correction for end effects due to the finite length of the cylinder, and after direct measurements of J_s and the other quantities involved, the quantity ρ can be calculated. It is assumed that, as is the case of the actual experiments, eddy currents are negligible.

In this way, for compressed Permalloy powder (from the Bell Telephone Laboratories), at frequencies of 22 kc and 30 kc, and in longitudinal fields varying in strength from 0 to 2700 gausses, it has been found that the (corrected) formula is satisfied throughout the region of approximate saturation when

$$\rho=(1.01\pm 0.06)m/e.$$

The formula does not, of course, hold in the region between $J_s=0$ and approximate saturation. As would be expected, J_y is zero when J_s is zero; and it increases to a maximum somewhat before approximate saturation is reached. It then follows the formula into the strongest fields.

In view of the magnitude of the experimental error, there is no certain disagreement between these results, obtained with very intense fields, and the results obtained from the Barnett effect, with rotation frequencies equivalent to exceedingly minute magnetic intensities, and from the Einstein-de Haas effect, with weak and moderate intensities. This value is about $1.05\ m/e$.[2]

Experiments have also been made on compressed iron powder (from the Bell Telephone Laboratories), but the fields obtainable have not been sufficiently intense to produce approximate saturation. The observable early part of the curve between J_y and J_s closely resembles that for Permalloy, and the part nearest saturation suggests a value of ρ approximately equal to $(1.06\pm 0.10)m/e$. The standard value of ρ for iron is $1.03m/e$.[2]

We expect to publish soon a much more nearly complete account of this work.

For important assistance we are indebted to the Carnegie Institution of Washington, the National Research Council and the U. S. Navy, ONR. The experimental work has been done in the Norman Bridge Laboratory of the Institute.

[1] S. J. Barnett, Phys. Rev. **6**, 239 (1915); and Proc. Am. Acad. **68**, 229 (1933).
[2] S. J. Barnett, Proc. Am. Acad. **73**, 401 (1940); Proc. Am. Acad. **75** 109 (1944); and Phys. Rev. **66**, 224 (1944).